U.S. DEPARTMENT OF COMMERCE/Environmental Science Services Administration

Monograph 1

A World Atlas of Atmospheric Radio Refractivity

QC
973
.I48

Bradford R. Bean

DATA LIBRARY
Woods Hole Oceanographic Institution

MBL/WHOI
0 0301 0040078 1

U. S. DEPARTMENT OF COMMERCE
ENVIRONMENTAL SCIENCE SERVICES ADMINISTRATION

A World Atlas of Atmospheric Radio Refractivity

B. R. Bean, B. A. Cahoon, C. A. Samson, and G. D. Thayer

Institute for Telecommunication Sciences and Aeronomy
Institutes for Environmental Research
Boulder, Colo.

ESSA Monograph 1

UNITED STATES GOVERNMENT PRINTING OFFICE, WASHINGTON : 1966

U.S. DEPARTMENT OF COMMERCE
JOHN T. CONNOR, *Secretary*

ENVIRONMENTAL SCIENCE SERVICES ADMINISTRATION
ROBERT M. WHITE, *Administrator*

Institutes for Environmental Research
GEORGE S. BENTON, *Director*

This work was supported in part by the
U.S. Navy Weather Research Facility,
Contract Number 7560: NABUSTDS 65 Ser. 300.

Library of Congress Catalog Card Number: Map 66–74

For sale by the Superintendent of Documents, U.S. Government Printing Office, Washington, D.C. 20402. Price $2.25

Preface

This atlas has been prepared for the radio engineer who wants an estimate of the behavior of the radio refractive index at any point on the earth. It has many limitations, which the authors have tried to point out in the text, but should provide useful information for engineering design and predictions of tropospheric radio circuits.

The work upon which this atlas is based has been in progress for several years in the Radio Meteorology Section of the Central Radio Propagation Laboratory, National Bureau of Standards, Boulder, Colo.* Many people have contributed to this research effort through the years, and it is not feasible to acknowledge them all individually. Those most directly involved with the preparation of material for this atlas include W. B. Sweezy and W. A. Williams, who were responsible for most of the computer programming; Mrs. B. J. Weddle, who assisted in processing and cataloging of the data; T. D. Stevens, who did most of the compiling, checking, and plotting of the maps, graphs, and tables; and L. P. Riggs, J. D. Horn, and Mrs. G. E. Richmond (deceased), who contributed to the atlas project in its early stages.

The National Weather Records Center of the U. S. Weather Bureau in Asheville, N. C., supplied the meteorological data upon which this atlas is based, and also performed the preliminary conversions of these data to refractivity parameters.

Finally, we thank the personnel of the U. S. Navy Weather Research Facility at Norfolk, Va., who foresaw a need for such an atlas and have arranged for support of the project over a period of years.

*Now the Institute for Telecommunication Sciences and Aeronomy (ITSA), Environmental Science Services Administration.

Contents

Page

Preface iii
Abstract ix
1. Introduction 1
2. Discussion of Basic Data 2
3. World Maps of $N(z)$ 4
3.1. Development 4
Figure 1. Three-part exponential fit to mean N-profile: Koror 5
Figure 2. Three-part exponential fit to mean N-profile: Dakar 6
3.2. Discussion of $N(z)$ Map Contours 4
3.3. Reliability of Contours of $N(z)$ Maps 6
3.4. Problem Areas of $N(z)$ Maps 7
Figure 3. Five-year mean wet refractivity term: February 8
Figure 4. Five-year mean wet refractivity term: May 9
4. World Maps of $\overline{\triangle N}$ 10
4.1. Development 10
4.2. Discussion of Contours and Reliability of $\overline{\triangle N}$ Maps 10
5. World Maps of Extreme N-Gradients 12
5.1. Development 12
5.2. Discussion of Gradient Map Contours (Subrefraction) 12
5.3. Discussion of Gradient Map Contours (Superrefraction and Ducting) 14
5.4. Discussion of Cumulative Distributions of Ground-Based Gradients 15
Figure 5. Five-year mean vertical refractive gradient profile: Aden 16
Figure 6. Five-year mean vertical refractive gradient profile: Nicosia 17
5.5. Reliability and Limitations of Ground-Based Refractivity Gradient Data 17
6. World Maps of Mean Tropopause Altitudes 19
7. Appraisal of Results 20
7.1. Accuracy of $N(z)$ Maps 20
Table 1. Standard errors of 5-year mean values of monthly mean N_s for 40 stations 20
Figure 7. Correlation of $\overline{\triangle N}$: monthly mean N-profiles versus monthly mean exponential model 21
Table 2. Absolute errors in recovering mean N from map contours for 32 stations 21
Table 3. Approximate total standard errors, σ_T, for $N(z)$ maps in appendix A 22
7.2 Accuracy of $\overline{\triangle N}$ Maps 23
Figure 8. Correlation of $\overline{\triangle N}$: monthly mean N-profiles versus monthly mean weather summary data 22
7.3. Accuracy of Gradient Maps 24
8. Conclusions 25
9. References 26
10. Appendix A. World Maps of $N(z)$ Parameters 29
Table A-1. Cumulative distribution levels of surface refractivity 30
Figure A-1. Location of $N(z)$ data stations 32
Figure A-2. Mean sea-level dry term, D_o: February 33
Figure A-3. Mean sea-level wet term, W_o: February 33
Figure A-4. Dry-term tropospheric scale height in km, H_1: February 34
Figure A-5. Dry-term stratospheric scale height in km, H_2: February 34
Figure A-6. Wet-term scale height in km, H_w: February 35
Figure A-7. Mean density tropopause altitude in km, z_t: February 35
Figure A-8. Mean sea-level dry term, D_o: May 36
Figure A-9. Mean sea-level wet term, W_o: May 36
Figure A-10. Dry-term tropospheric scale height in km, H_1: May 37
Figure A-11. Dry-term stratospheric scale height in km, H_2: May 37
Figure A-12. Wet-term scale height in km, H_w: May 38
Figure A-13. Mean density tropopause altitude in km, z_t: May 38
Figure A-14. Mean sea-level dry term, D_o: August 39

Page

Figure A-15. Mean sea-level wet term, W_o: August 39
Figure A-16. Dry-term tropospheric scale height in km, H_1: August 40
Figure A-17. Dry-term stratospheric scale height in km, H_2: August 40
Figure A-18. Wet-term scale height in km, H_w: August 41
Figure A-19. Mean density tropopause altitude in km, z_t: August 41
Figure A-20. Mean sea-level dry term, D_o: November 42
Figure A-21. Mean sea-level wet term, W_o: November 42
Figure A-22. Dry-term tropospheric scale height in km, H_1: November 43
Figure A-23. Dry-term stratospheric scale height in km, H_2: November 43
Figure A-24. Wet-term scale height in km, H_w: November 44
Figure A-25. Mean density tropopause altitude in km, z_t: November 44
Figure A-26. Standard prediction error of the exponential fit to the mean wet-term profile: February 45
Figure A-27. Standard prediction error of the exponential fit to the mean wet-term profile: May 45
Figure A-28. Standard prediction error of the exponential fit to the mean wet-term profile: August 46
Figure A-29. Standard prediction error of the exponential fit to the mean wet-term profile: November 46
Figure A-30. Areas of doubtful applicability of three-part exponential model of $N(z)$ for $z < 6$ km 47

11. Appendix B. World Maps of $\overline{\triangle N}$ 48
Table B-1. Mean surface refractivity 49
Figure B-1. Location of $\triangle N$ data stations 52
Figure B-2. Monthly mean $\triangle N$: January 53
Figure B-3. Monthly mean $\triangle N$: February 53
Figure B-4. Monthly mean $\triangle N$: March 54
Figure B-5. Monthly mean $\triangle N$: April 54
Figure B-6. Monthly mean $\triangle N$: May 55
Figure B-7. Monthly mean $\triangle N$: June 55
Figure B-8. Monthly mean $\triangle N$: July 56
Figure B-9. Monthly mean $\triangle N$: August 56
Figure B-10. Monthly mean $\triangle N$: September 57
Figure B-11. Monthly mean $\triangle N$: October 57
Figure B-12. Monthly mean $\triangle N$: November 58
Figure B-13. Monthly mean $\triangle N$: December 58
Figure B-14. Annual mean of sea-level refractivity, $\overline{\overline{N}}_o$ 59
Figure B-15. Annual mean of refractivity gradient between surface and 1 km, $\overline{\overline{\triangle N}}$ 59
Figure B-16. Slope of regression line of $\overline{\triangle N}$ versus $\overline{N}_s$, b 60
Figure B-17. Correlation coefficient of $\overline{\triangle N}$ versus $\overline{N}_s$ 60
Figure B-18. Standard prediction error of the regression line of $\overline{\triangle N}$ versus $\overline{N}_s$ 61
Figure B-19. Standard prediction error of the regression line of $\overline{\triangle N}$ versus $\overline{N}_s$ as a percent of $\overline{\overline{\triangle N}}$ 61
Figure B-20. Areas of doubtful applicability of using $\overline{N}_s$ to predict $\overline{\triangle N}$ 62

12. Appendix C. World Maps and Cumulative Distribution Charts of Gradients of Ground-Based Atmospheric Layers 63
Figure C-1. Percent of time gradient ≥ 0 (N/km): February 64
Figure C-2. Percent of time gradient ≥ 0 (N/km): May 64
Figure C-3. Percent of time gradient ≥ 0 (N/km): August 65
Figure C-4. Percent of time gradient ≥ 0 (N/km): November 65
Figure C-5. Gradient (N/km) exceeded 10 percent of the time for 100-m layer: February 66
Figure C-6. Gradient (N/km) exceeded 2 percent of the time for 100-m layer: February 66
Figure C-7. Gradient (N/km) exceeded 10 percent of the time for 100-m layer: May 67
Figure C-8. Gradient (N/km) exceeded 2 percent of the time for 100-m layer: May 67
Figure C-9. Gradient (N/km) exceeded 10 percent of the time for 100-m layer: August 68
Figure C-10. Gradient (N/km) exceeded 2 percent of the time for 100-m layer: August 68
Figure C-11. Gradient (N/km) exceeded 10 percent of the time for 100-m layer: November 69
Figure C-12. Gradient (N/km) exceeded 2 percent of the time for 100-m layer: November 69
Figure C-13. Percent of time gradient ≤ -100 (N/km): February 70
Figure C-14. Percent of superrefractive layers thicker than 100 m: February 70
Figure C-15. Percent of time gradient ≤ -100 (N/km): May 71
Figure C-16. Percent of superrefractive layers thicker than 100 m: May 71

Page

Figure C-17. Percent of time gradient ≤ -100 (N/km): August 72
Figure C-18. Percent of superrefractive layers thicker than 100 m: August 72
Figure C-19. Percent of time gradient ≤ -100 (N/km): November 73
Figure C-20. Percent of superrefractive layers thicker than 100 m: November 73
Figure C-21. Percent of time gradient ≤ -157 (N/km): February 74
Figure C-22. Percent of ducting layers thicker than 100 m: February 74
Figure C-23. Percent of time gradient ≤ -157 (N/km): May 75
Figure C-24. Percent of ducting layers thicker than 100 m: May 75
Figure C-25. Percent of time gradient ≤ -157 (N/km): August 76
Figure C-26. Percent of ducting layers thicker than 100 m: August 76
Figure C-27. Percent of time gradient ≤ -157 (N/km): November 77
Figure C-28. Percent of ducting layers thicker than 100 m: November 77
Figure C-29. Percent of time trapping frequency $<$ 3000 Mc/s: February 78
Figure C-30. Percent of time trapping frequency $<$ 1000 Mc/s: February 78
Figure C-31. Percent of time trapping frequency $<$ 300 Mc/s: February 79
Figure C-32. Percent of time trapping frequency $<$ 3000 Mc/s: May 79
Figure C-33. Percent of time trapping frequency $<$ 1000 Mc/s: May 80
Figure C-34. Percent of time trapping frequency $<$ 300 Mc/s: May 80
Figure C-35. Percent of time trapping frequency $<$ 3000 Mc/s: August 81
Figure C-36. Percent of time trapping frequency $<$ 1000 Mc/s: August 81
Figure C-37. Percent of time trapping frequency $<$ 300 Mc/s: August 82
Figure C-38. Percent of time trapping frequency $<$ 3000 Mc/s: November 82
Figure C-39. Percent of time trapping frequency $<$ 1000 Mc/s: November 83
Figure C-40. Percent of time trapping frequency $<$ 300 Mc/s: November 83
Figure C-41. Lapse rate of refractivity (N/km) exceeded 25 percent of time for 100-m layer: February 84
Figure C-42. Lapse rate of refractivity (N/km) exceeded 10 percent of time for 100-m layer: February 84
Figure C-43. Lapse rate of refractivity (N/km) exceeded 5 percent of time for 100-m layer: February 85
Figure C-44. Lapse rate of refractivity (N/km) exceeded 2 percent of time for 100-m layer: February 85
Figure C-45. Lapse rate of refractivity (N/km) exceeded 25 percent of time for 100-m layer: May 86
Figure C-46. Lapse rate of refractivity (N/km) exceeded 10 percent of time for 100-m layer: May 86
Figure C-47. Lapse rate of refractivity (N/km) exceeded 5 percent of time for 100-m layer: May 87
Figure C-48. Lapse rate of refractivity (N/km) exceeded 2 percent of time for 100-m layer: May 87
Figure C-49. Lapse rate of refractivity (N/km) exceeded 25 percent of time for 100-m layer: August 88
Figure C-50. Lapse rate of refractivity (N/km) exceeded 10 percent of time for 100-m layer: August 88
Figure C-51. Lapse rate of refractivity (N/km) exceeded 5 percent of time for 100-m layer: August 89
Figure C-52. Lapse rate of refractivity (N/km) exceeded 2 percent of time for 100-m layer: August 89
Figure C-53. Lapse rate of refractivity (N/km) exceeded 25 percent of time for 100-m layer: November 90
Figure C-54. Lapse rate of refractivity (N/km) exceeded 10 percent of time for 100-m layer: November 90
Figure C-55. Lapse rate of refractivity (N/km) exceeded 5 percent of time for 100-m layer: November 91
Figure C-56. Lapse rate of refractivity (N/km) exceeded 2 percent of time for 100-m layer: November 91
Table C-1. Median and minimum trapping frequency (Mc/s) of ducting layers 92
Figure C-57. (a) Cumulative probability distributions of dN/dh for ground-based 100-m layer: Aden, Arabia (February, May) 93
Figure C-57. (b) Cumulative probability distributions of dN/dh for ground-based 100-m layer: Aden, Arabia (August, November) 94

Page

Figure C-58. Cumulative probability distributions of dN/dh for ground-based 100-m layer: Amundsen-Scott, Antarctica ... 95
Figure C-59. Cumulative probability distributions of dN/dh for ground-based 100-m layer: Balboa (Albrook), Panama C. Z. ... 96
Figure C-60. Cumulative probability distributions of dN/dh for ground-based 100-m layer: Bangui, Central African Republic ... 97
Figure C-61. Cumulative probability distributions of dN/dh for ground-based 100-m layer: Bordeaux, France ... 98
Figure C-62. (a) Cumulative probability distributions of dN/dh for ground-based 100-m layer; Dakar, Republic of Senegal (February, May) ... 99
Figure C-62. (b) Cumulative probability distributions of dN/dh for ground-based 100-m layer: Dakar, Republic of Senegal (August, November) ... 100
Figure C-63. Cumulative probability distributions of dN/dh for ground-based 100-m layer: Denver, Colo. ... 101
Figure C-64. Cumulative probability distributions of dN/dh for ground-based 100-m layer: Ezeiza, Argentina ... 102
Figure C-65. Cumulative probability distributions of dN/dh for ground-based 100-m layer: Fort Smith, Northwest Territories, Canada ... 103
Figure C-66. Cumulative probability distributions of dN/dh for ground-based 100-m layer: Hilo, Hawaii ... 104
Figure C-67. Cumulative probability distributions of dN/dh for ground-based 100-m layer: Long Beach, Calif. ... 105
Figure C-68. Cumulative probability distributions of dN/dh for ground-based 100-m layer: Lourenco Marques, Portuguese East Africa ... 106
Figure C-69. Cumulative probability distributions of dN/dh for ground-based 100-m layer: Nandi, Fiji Islands ... 107
Figure C-70. Cumulative probability distributions of dN/dh for ground-based 100-m layer: New York, N. Y. ... 108
Figure C-71. Cumulative probability distributions of dN/dh for ground-based 100-m layer: Nicosia, Cyprus ... 109
Figure C-72. Cumulative probability distributions of dN/dh for ground-based 100-m layer: Ostersund, Sweden ... 110
Figure C-73. Cumulative probability distributions of dN/dh for ground-based 100-m layer: Perth, Australia ... 111
Figure C-74. Cumulative probability distributions of dN/dh for ground-based 100-m layer: Saigon, Viet Nam ... 112
Figure C-75. Cumulative probability distributions of dN/dh for ground-based 100-m layer: San Juan, P. R. ... 113
Figure C-76. Cumulative probability distributions of dN/dh for ground-based 100-m layer: Ship Station "C" ... 114
Figure C-77. Cumulative probability distributions of dN/dh for ground-based 100-m layer: Tashkent, U.S.S.R. ... 115
Figure C-78. Cumulative probability distributions of dN/dh for ground-based 100-m layer: Vladivostok, U.S.S.R. ... 116

13. Appendix D. World Charts of Tropopause Heights ... 117
Figure D-1. Tropopause heights (km), based on temperature lapse rate: February ... 117
Figure D-2. Tropopause heights (km), based on temperature lapse rate: May ... 118
Figure D-3. Tropopause heights (km), based on temperature lapse rate: August ... 118
Figure D-4. Tropopause heights (km), based on temperature lapse rate: November ... 119

14. Appendix E. Sample Listing of the Computer Output for San Juan, P. R., and Amundsen-Scott, Antarctica ... 120
Table E-1. Mean N-profiles: San Juan, P. R. ... 121
Table E-2. Mean N-profiles: Amundsen-Scott, Antarctica ... 123
Table E-3. Cumulative distributions of ground-based gradients: Amundsen-Scott, Antarctica ... 125
Table E-4. Analysis of ground-based superrefractive and ducting layers: Amundsen-Scott, Antarctica ... 127

Abstract

This atlas presents world maps and graphs of upper-air radio refractivity, $N(z)$ (where z is the altitude), mean monthly $\triangle N$ (the difference between the refractivity at the surface and at 1 km above the surface), extreme values of gradients of refractivity observed in the lowest layer of the atmosphere (including maps of minimum trapped frequency ducting gradients), and monthly mean tropopause heights. All refractivity values were derived from radiosonde data. The $N(z)$ maps are presented in terms of a three-part exponential model, with separate exponentials for the water vapor and air density terms of $N(z)$, with the latter separated into tropospheric and stratospheric terms. The $\triangle N$ data were derived by interpolation from fixed pressure-level data.

1. Introduction

There has been a need in radio engineering for a method whereby the radio refractivity, N, at some height, z, or the gradient of N with respect to height, dN/dz, could be accurately estimated for any world location during any season of the year. Previous studies have attempted to solve this problem by determination of the value of surface refractivity, N_s, and the use of an exponential decay with height [Bean et al., 1960a][1], or by presenting seasonal means and distributions of N at fixed pressure levels in the atmosphere for various radiosonde stations [U. S. Navy, 1955–59; Michaelis and Gossard, 1958]. However, these results did not provide any means whereby $N(z)$ could be obtained at any arbitrary location, i.e., places for which meteorological measurements were not available. In addition, specific information on the gradient of the refractive index has not been available previously on a worldwide basis, especially for the very important layers of the atmosphere at or near the surface where the presence of superrefractive or ducting gradients can produce anomalous propagation of microwaves.

This atlas presents maps, charts, and discussions of the worldwide variations in the radio refractive index. With the aid of this atlas, estimates of the following parameters may be readily determined for any part of the world: the refractivity at any height, $N(z)$; the average gradient of N over the first kilometer above the surface, ΔN; and the gradient of N in the lowest layer of the atmosphere (with emphasis on subrefractive, superrefractive, and ducting layers and the probability of trapping of radio waves by ducting layers). The world distribution of $N(z)$ is presented in the form of a three-part exponential model, with separate exponential terms for the water-vapor term, the density term in the troposphere, and the density term in the stratosphere; the parameters used to represent this $N(z)$ model are the reduced-to-sea-level values of surface water vapor and density terms, the scale heights of the three exponential terms, and the transition height between the tropospheric and stratospheric density exponentials. Seasonal maps of mean tropopause heights, which were obtained in the course of the data reduction required for the three-part exponential model, are also presented.

[1] Literature references on page 26.

2. Discussion of Basic Data

The radio refractive index of the atmosphere, n, exceeds unity by at most 450 parts per million; it is therefore customary to utilize the radio refractivity, N, given by [2]

$$N = (n-1) \times 10^6. \qquad (1)$$

The radio refractivity of air for frequencies up to 30,000 Mc/s is given by Smith and Weintraub [1953]:

$$N = 77.6 \frac{P}{T} + 3.73 \times 10^5 \frac{e}{T^2}, \qquad (2)$$

where P is the total atmospheric pressure in millibars (mb), T is the absolute temperature in degrees Kelvin (K), and e is the partial pressure of water vapor in millibars. [For the development of this equation from theory, c.f. Bean, 1962]. The P/T term in (2) is frequently referred to as the "dry term" (even though there is a small water vapor component in the total pressure) and the e/T^2 term, as the "wet term."

The radiosonde is in general use throughout the world to measure the pressure, temperature, and relative humidity of the upper air. These data can be used to obtain the corresponding vertical profile of radio refractivity. However, there are a number of disadvantages in the use of radiosonde data for the purpose of obtaining N-profiles; perhaps the most important of these is the relatively slow response (large lag constants) of the radiosonde temperature and humidity sensors [Bunker, 1953; Wagner, 1960, 1961; Bean and Dutton, 1961]. Also of some importance is the method of selecting levels for which data are reported. The procedure followed by most meteorological services consists of reporting temperature, humidity, and height at certain fixed pressure levels, called "mandatory levels" (e.g., 850 mb), plus a sufficient number of additional "significant" levels to provide a profile of temperature and relative humidity such that linear segments between levels will not depart from the original data at any point by more than 1°C or 10 percent relative humidity. Such tolerances, although acceptable for most meteorological purposes, may result in errors of as much as 30 N-units (under extreme conditions) in a linear-segment N-profile constructed from radiosonde data. Some punched-card refractivity data are available which were calculated from significant levels chosen with an even wider tolerance, 2°C and 30 percent relative humidity [Bean and Cahoon, 1961a]. In spite of these deficiencies, this atlas is based entirely upon radiosonde data, since no other worldwide, long-term upper-air data are available. (More detailed measurements, obtained primarily from wiresonde and aircraft refractometer flights, are available only for a very few locations and for very limited periods of time.)

The first step toward obtaining a broad sample of upper-air refractivity data was the selection (by geographic-climatic considerations and period of record available) of 112 radiosonde stations from the worldwide network.[3] Wherever possible, a total of 5 years of data was obtained for each of the 4 representative "seasonal" months of February, May, August, and November.

Five-year means were selected for use in the preparation of this atlas for two reasons: (a) a large number of stations, including all of those in the U.S.S.R., have available records dating back only to the International Geophysical Year (IGY), 1958; (b) 5 years seemed to represent the best compromise between the number of stations and the length of record, since the total amount of data which could be processed was naturally limited. A large number of stations is desirable for mapping purposes (better coverage), while longer periods of record yield more stable (accurate) estimates of long-term means (of climatic variables). For each radiosonde ascent, the reported values of pressure, temperature, and humidity at each mandatory or significant level were converted by means of (2) to radio refractivity values (by the National Weather Records Center, Asheville, N. C.). These data, when received at ITSA, were used to obtain four monthly *mean N-profiles* for the available period of record for each of the 112 stations. The procedure followed was to obtain for each profile the values of N at a number of standard height levels by assuming separate exponentials for the dry and wet terms between each reported level. The mean N-profile for the

[2] Throughout this atlas, the term atmosphere should be understood to mean the nonionized atmosphere, i.e., excluding the ionosphere.

[3] A list of these stations is included in appendix A.

standard height levels was then computed as the arithmetic mean of the individually interpolated values of N at each standard height for all of the profiles in the sample. In this way, 5-year mean values of refractivity were obtained for a large number of levels, ranging from the surface to 30 km (or more) above the surface, for a worldwide sample of stations. Over 18,000 individual values of mean N were determined in this way.

In addition to these calculations, the approximate height of the tropopause was determined for each profile; this was the height of the bottom of the lowest atmospheric layer which met the following criteria:

(a) the layer thickness was $\geqq$ 2 km,

(b) the temperature gradient $\geqq -2°C$/km.

The 2-km thickness could be made up of two or more consecutive layers from the radiosonde data. Mean monthly values of tropopause heights were obtained for the period of record for each station by averaging the individual profile tropopause heights; maps of these tropopause heights are shown in appendix D.

The monthly mean value of the average N-gradient between the surface and 1 km above the surface has been recognized as a radiometeorological parameter of some importance [Saxton, 1951; Bean and Meaney, 1955; CCIR, 1965]. Therefore, maps are included of the mean value of this parameter for all 12 months, with a more comprehensive network of stations than was available from the complete radiosonde data sample discussed above. For this purpose a sample of 268 stations was chosen from those available in the Monthly Climatic Data for the World and the National Summary of Climatological Data (U.S.A.).[4] These publications list monthly mean values of pressure, temperature, and relative humidity or dew point for the surface and some of the mandatory pressure levels from radiosonde data. For stations near sea level, the 900-mb level is very close to 1 km above the surface, but for most stations outside of the U.S.A. the 850-mb level was the lowest reported; the altitude of this pressure level varies between roughly 1.3 and 1.5 km above sea level. However, it was felt that interpolation from the 850-mb data, using separate exponentials for the wet and dry terms, would yield fairly accurate values of monthly mean N at the required 1-km height.

The radiosonde-derived data described in the preceding paragraphs constitute the basic data from which this atlas has been prepared. In the following sections the methods of reduction and presentation of these data are discussed, as well as the consistency and reliability of the results so obtained.

[4] Data from these two publications (published by the National Weather Records Center, Asheville, N.C., under the sponsorship of the World Meteorological Organization [WMO] and the U.S. Weather Bureau) will hereafter be referred to as "weather summary data."

3. World Maps of $N(z)$

3.1. Development

In order to prepare worldwide maps of upper atmospheric N from the 5-year mean N-profiles described previously, it was decided to reduce the quantity of necessary $N(z)$ maps by abstracting each mean profile in terms of a model atmosphere which would use three negative exponential functions of altitude. The three functions which are used to represent each mean profile are a single exponential for the wet term, W, and two exponentials for the dry term, D. Two exponential functions are necessary for the dry term because of the change in the lapse rate of the temperature from the normal 6.5°C/km in the troposphere to the nearly isothermal stratosphere where the temperature may increase with height. Least-squares fits were obtained for log $\overline{W}$ versus height over the interval 0 to 3 km above the surface. The ranges to be covered by the two fits for the dry term were determined from the mean tropopause heights and their standard deviations which had been obtained during the analysis of the N-profiles in each sample. The tropospheric dry term, D_1, was fit over the interval 0 to the tropopause height minus one standard deviation, and the stratospheric dry term, D_2, was fit from the tropopause height plus one standard deviation to the upper limit of data for that profile. In both cases, log $\overline{D}$ was fit to height using least squares. The resulting model atmosphere is given by

$$\overline{N}(z) = \overline{D}_o \exp\left(-\frac{z}{H_1}\right) + \overline{W}_o \exp\left(-\frac{z}{H_w}\right), \qquad (3)$$

$z \leq z_t$,

$$\overline{N}(z) = \overline{D}_o \exp\left(-\frac{z_t}{H_1} - \frac{(z - z_t)}{H_2}\right) + \overline{W}_o \exp\left(-\frac{z}{H_w}\right), \qquad (4)$$

$z > z_t$;

$\overline{D}_o$ and $\overline{W}_o$ are the mean sea-level values of the dry and wet terms (reduced from the surface values using the free-atmosphere scale heights), H_w is the wet-term scale height, H_1 is the tropospheric dry-term scale height, H_2 is the stratospheric dry-term scale height, and z_t is the altitude above mean sea level of the point of transition between the tropospheric and stratospheric dry-term exponentials. The altitude, z_t, may thus be thought of as an effective density tropopause.

Examples of the application of this model to actual mean refractivity profiles are given in figures 1 and 2: a very good fit (Koror) and one of the worst fits encountered (Dakar). The good fit obtained in figure 1 is especially significant since Koror represents a climatic type (equatorial station with a very high mean surface refractivity, 387.6) for which exponential models of N were previously thought to be unsatisfactory [Misme et al., 1960]. Dakar (fig. 2) is an example of the climatic type (characterized by a persistent low-level temperature inversion with dry subsiding air above) where this model (or any other simple model) of N versus z is inadequate to explain the N-structure at low latitudes. It was found that the behavior of the wet term (measured on figs. 1 and 2 by S_w, the rms error over the first 3 km) was a good indicator of whether or not the data would provide a good fit to the profile. However, it can be noted in figure 2 that, even though the rms wet-term error below 3 km is 14.6 N-units, the profile at Dakar above an altitude of 6 km is well represented by the three-part exponential.

Maps were prepared for each of the 4 "seasonal" months of the parameters necessary to utilize the three-part exponential in estimating upper-air refractivity. These are the reduced-to-sea-level values, $\overline{D}_o$ and $\overline{W}_o$; the three scale heights, H_w, H_1, and H_2; and the transition altitude, z_t. The surface values of $\overline{N}$ can be recovered by substituting the elevation of the surface above sea level at the desired location in (3), which amounts to inverting the process used to reduce the surface values of $\overline{N}$ to sea level. The series of maps given in appendix A can be used to estimate the mean value of N at any desired altitude for each of the seasonal months at any world location except those areas outlined in figure A-30 (which summarizes the wet-term rms error values found in figures A-26 through A-29).

3.2. Discussion of $N(z)$ Map Contours

The world maps of $N(z)$ parameters reveal a number of interesting trends. Some of these are:

(1) The D_1 scale height, H_1:

(a) is smaller than average over the arctic seas in winter because of dense stratified air;

(b) remains higher than average over land areas during their warm seasons due to a steep temperature lapse rate with height.

(2) The D_2 scale height, H_2:

shows a minimum in the equatorial region because of the colder temperatures found above the tropical tropopause.

(3) The wet scale height, H_w:

(a) is larger than average in the general area of the equatorial heat belt during all seasons. This indicates a steep temperature gradient with a very small lapse of *absolute* humidity with height in the turbulently mixed deep layer of warm air. However, in some tropical areas

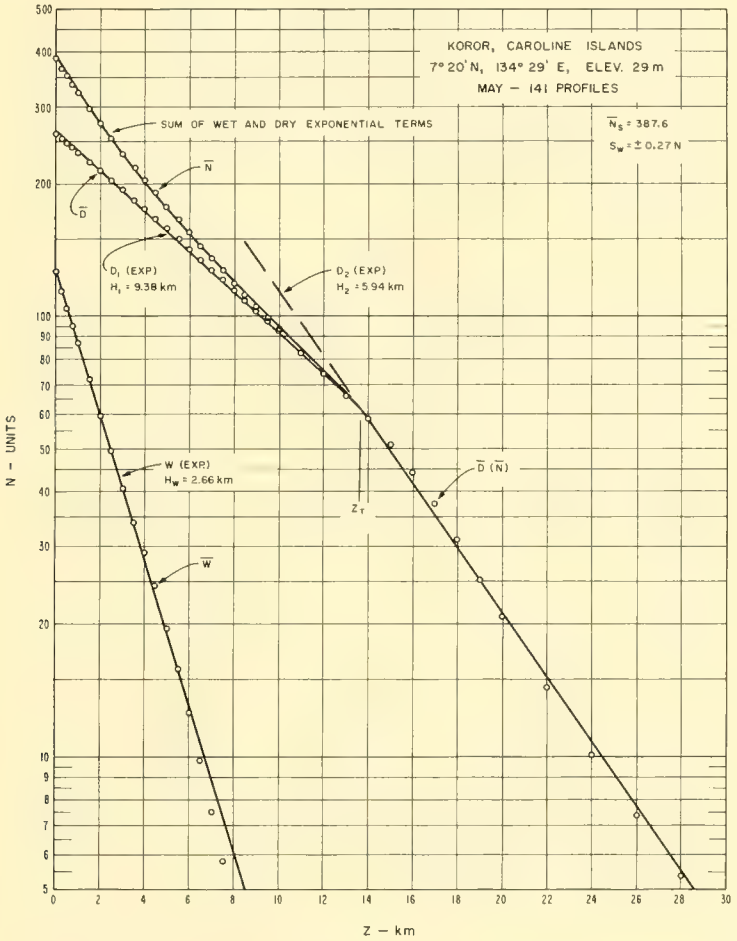

FIGURE 1. *Three-part exponential fit to mean* N*-profile: Koror.*

definite changes may occur in H_w because of seasonal shifting of small, but persistent, anticyclonic circulations which modify to a considerable vertical extent the normal zonal transport of water vapor in those latitudes. The seasonal differences of H_w in the Coral Sea area seem to confirm the existence of such a cellular structure northeast of Australia [Hutchings, 1961].

(b) is larger than average over two types of convectively heated continental interiors:

(1) high-latitude land masses where the sea-level wet term is less than 20 N-units;

(2) temperate desert steppe regions where the sea-level wet term is between 20 and 60 N-units.

(c) is lower than average in areas where subsidence or tradewind ducting persistently occurs below 3 km.

(4) The dependence of the dry sea-level values, D_o, upon temperature (because $D_o = 77.6\ P/T$) is revealed in such features as the 332 high in Siberia during February and the 260 low in the Sahara Desert during May and August.

(5) The wet sea-level values, W_o, are also

very dependent upon temperatures because of the larger water content possible at high temperatures. There are two exceptions:

(a) Large interior deserts, where mountains block the normal moisture flow, tend to have low wet-term values relative to their temperatures.

(b) In August, when the monsoonal moisture is trapped south of the Himalayas, India shows unusually high wet-term values.

(6) The intersection height, z_t, is closely related to the height of the tropopause, but in areas where an isothermal layer precedes the stratospheric increase of temperature, the D_2

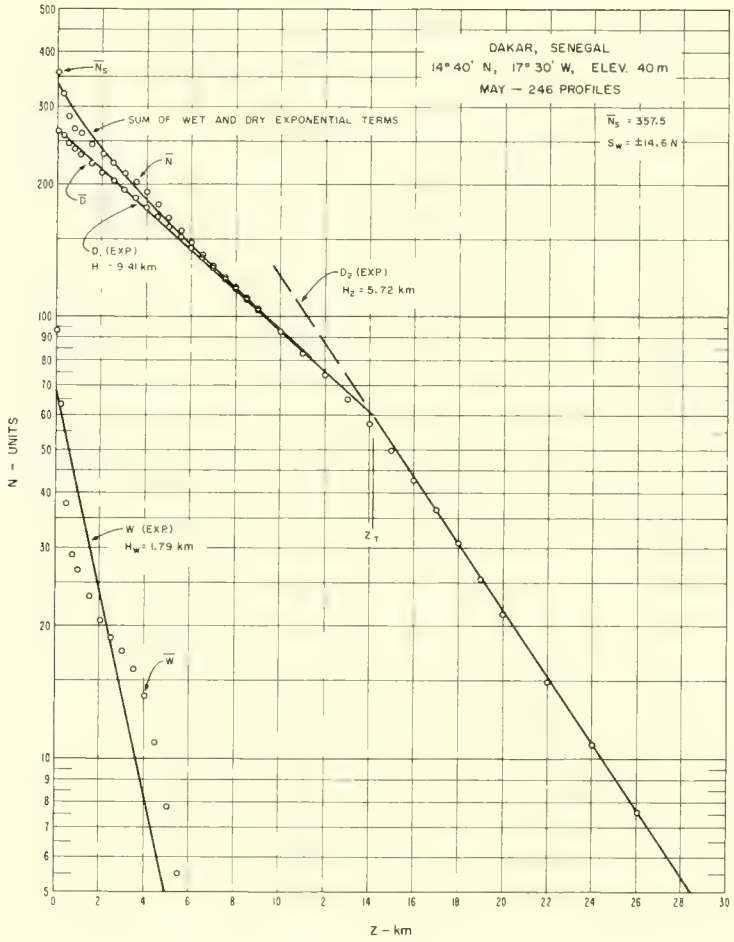

FIGURE 2. *Three-part exponential fit to mean* N*-profile: Dakar.*

curve may intersect the D_1 curve as much as 2 km below the tropopause heights given in figures D-1 through D-4 (see appendix D).

3.3. Reliability of Contours of $N(z)$ Maps

Although radiosonde stations are the only worldwide source of upper-air meteorological data, many areas of the world had few, if any, radiosonde reporting stations before 1957. As a result of the IGY, many new stations were established, especially in the lower latitudes; however, radiosonde data are still not available for a number of large areas, such as Brazil, China, and the Indian Ocean. High latitudes also show a noticeable sparsity of upper-air data; fortunately, there is a fairly small and uniform transition in most parameters at these far-south and far-north latitudes. Even in the U.S.A., where the first radiosonde network was established in 1938, radiosonde stations are still several hundred miles apart.

The maps were hand-contoured by interpolation between the widely-spaced plotted data points, using a technique similar to that used in the analysis of synoptic weather maps. Each

map was then carefully checked by another analyst to make certain all data points had been properly considered. The contours were modified in some areas on the basis of other information or considerations not accounted for in the machine-analyzed radiosonde data. For instance, supplementary surface data [Knoll, 1941; Serra, 1955; Bean and Cahoon, 1957; UNESCO, 1958; Bean et al., 1960b; Air Ministry, 1961; Dodd, 1965] were considered in the contouring of those parameters (D_o and W_o) dependent upon surface observations. Also, if spurious "high" centers of the wet term (such as the isolated values found at Tananarive, Malagasy Republic) were produced at high elevation stations by reduction-to-sea-level procedures, these values were smoothed to some extent. It was also found that the wet scale heights derived from mean N-profile data for stations at altitudes greater than 1 km tend to give more unrealistic sea-level wet terms than the average wet-term scale height of 3.0 km suggested by Hann [List, 1958]. When this "standard atmosphere" scale height was substituted for Hw, the maximum error of $N(z)$ values calculated from (3) or (4) for all stations above 1 km which are listed in table A-1 was 6.2 percent of the true 5-year mean value at Tananarive in August; the second largest error was 5.5 percent at Nairobi in February.

Another contouring check was made of all modified contours; a third analyst reviewed the smoothing to be sure it was consistent with the original plotted data as well as with the supplementary information.

To further check the contouring, calculated $N(z)$ values (using (3) and (4) with values read from figs. A-1 through A-25) were compared with actual observed values at 32 representative stations. The results of this check (reported in detail in table 2 of sec. 7) emphasize that, although some error undoubtedly results in $N(z)$ values below 1 km due to contouring, it is not a problem for $N(z)$ values at 3 km or above.

3.4. Problem Areas of $N(z)$ Maps

The use of wet and dry scale heights in a biexponential radio refractive index model has proved to be a good indicator of climatic differences [Bean, 1961; Misme, 1964]. The dry term, or atmospheric density component of refractivity, decreases with height in a uniform manner throughout the troposphere so that its scale height is an accurate indicator of the degree of density stratification, but the water-vapor component (the wet term) is not so well-behaved. Because the saturation vapor pressure, e_s, is itself an exponential function of temperature (which generally decreases linearly with height), one of the best wet-term models is probably an exponential curve [Reitan, 1963; Dutton and Bean, 1965]. However, an exponential model of the wet term must be used with discretion because humidity is extremely variable, both vertically and horizontally (because of its high dependence upon the temperatures within the different air masses, as well as various terrain and land-water effects).

To show actual physical changes in H_w, the wet scale height, it would be desirable to present contoured values based not only on a large number of stations, but also on data representative of various times of day. Figures A-6, A-12, A-18, and A-24 present the seasonal values of H_w, but worldwide maps of the diurnal variability of the wet scale heights are not yet available.

There are three specific areas of the world where the assumption of an exponential distribution of the wet term is largely invalid and can be used only with reservations. Two of the areas have one thing in common — a low sea-level wet term. At continental stations in high latitudes where strong temperature inversions persist during winter months, the wet term at 3 km may be as large as, or even larger than, that at the surface (because of the increase of water vapor "capacity" with temperature), and the result is a negative or a very large positive value of the wet scale height, neither of which is physically realistic. At any tropical desert station where the sea level wet term is < 30 N-units, deceivingly high wet scale heights also may result. Fortunately, because of the small contribution of the wet term in these cases, the total N-error remains small. The wet-term profiles at nine stations with low values of W_o were examined, and the largest error at any height was 3.7 percent of the true 5-year $N(z)$ value at Niamey (a desert station) in February (fig. 3). In the arctic areas (represented by Barrow, Alaska, in this same figure) the maximum error never exceeded 1.5 percent of the total $N(z)$ value.

The third area presents a more serious problem because it exists in a subtropical climate (15°-35° north and south of the equator) where the wet term contributes from $\frac{1}{4}$ to $\frac{1}{3}$ of the total N. The sharp decrease of humidity and increase of temperature which is found in atmospheric layers between the surface and 3 km in the subsidence regions of semipermanent subtropical highs destroys the exponential distribution of the wet term. In fact, in regions such as this, the exponential fit may be valid only at two or three points. This can be noted in figure 4, where the mean wet term for May is graphed, and the H_w value from the least-squares fit from 0-3 km of log $\overline{W}$ versus height is indicated, for

four dissimilar stations: Dakar (low-level subsidence), Antofagasta (intermediate subsidence-trade wind ducting), Hilo (trade wind inversion), and Balboa (steep exponential gradient). A check of figure A-30 reveals that the first three of these stations are located in areas where, because the rms of the wet-term error exceeds 5 N-units for at least 1 month, the three-part exponential model is not recommended.

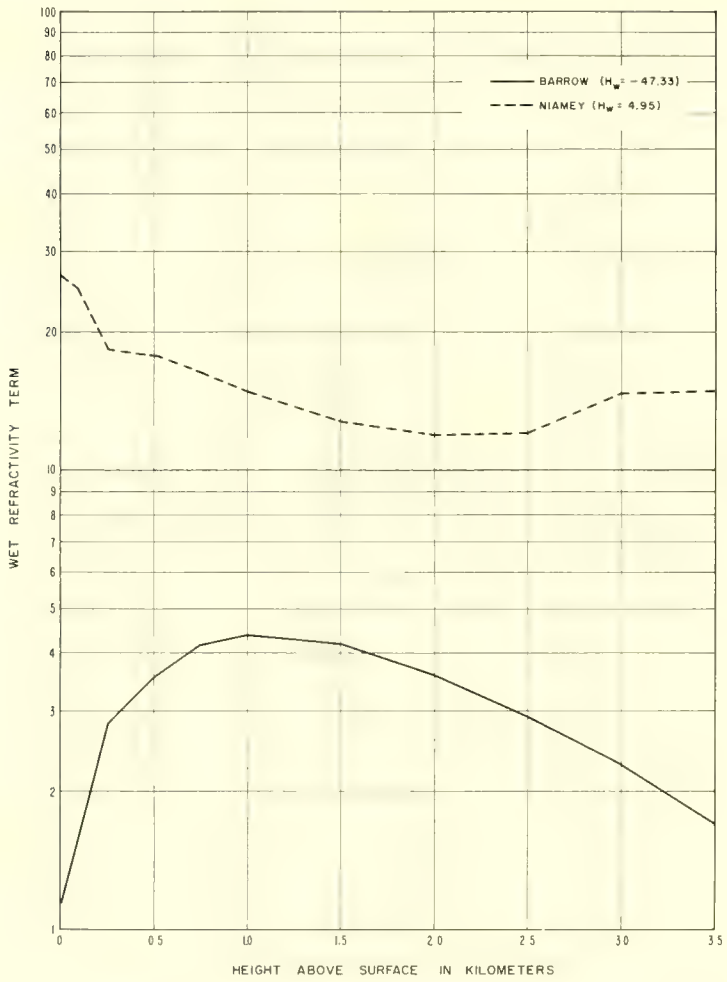

FIGURE 3. *Five-year mean wet refractivity term: February.*

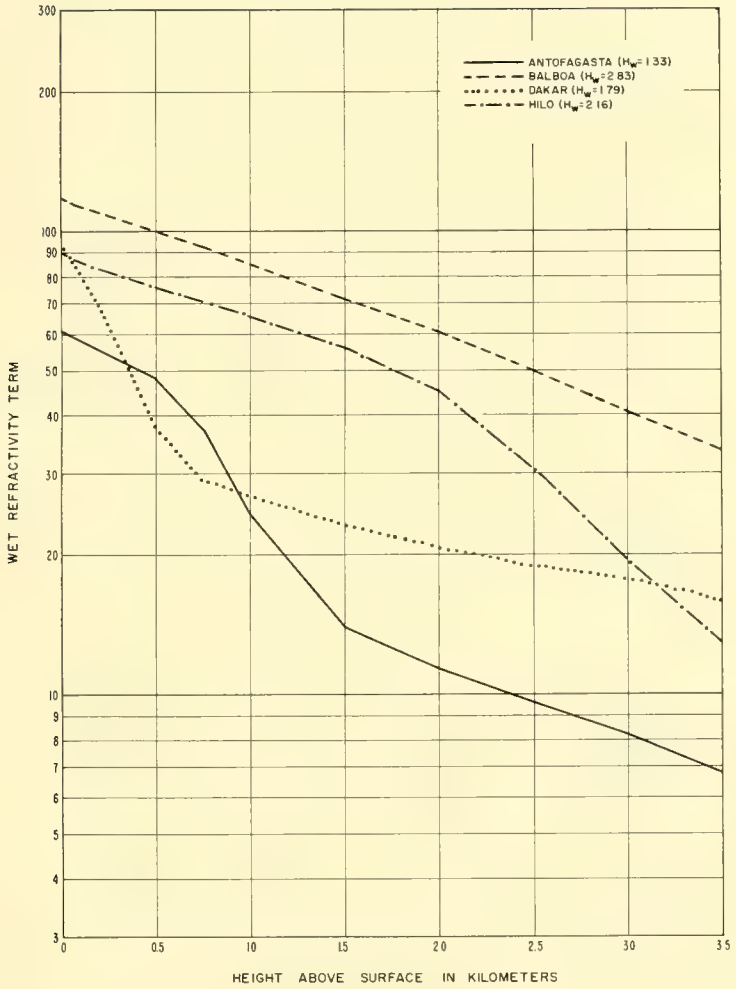

FIGURE 4. *Five-year mean wet refractivity term: May.*

4. World Maps of $\overline{\Delta N}$

4.1. Development

Twelve maps of monthly mean ΔN were prepared from the 5-year mean values obtained by interpolation of mandatory pressure level radiosonde data for the 268 stations listed in table B-1 and located in figure B-1 in appendix B. These maps, contoured in the same manner as the $N(z)$ maps (sec. 3.3), are figures B-2 through B-13.

Previous work has shown that a good correlation may exist between ΔN and surface N on a monthly mean basis [Bean and Thayer, 1959; Bean and Cahoon, 1961b; CCIR, 1965]. In fact, in many areas of the world this seasonal correlation is very high, and in such areas a regression line might provide better estimates of monthly mean ΔN than the maps in appendix B (if the mean value of surface N were available for that particular month of that year for the desired location). This regression line could also be used with the N_s distribution data from table A-1 to provide estimates of the ΔN distribution. Correlations were therefore calculated for the 12 monthly mean values of ΔN and surface N for each of the stations in the sample. The equations resulting from these calculations were put into the form of deviations from the annual means:

$$\overline{\Delta N} = b\,(\overline{N}_s - \overline{\overline{N}}_s) + \overline{\overline{\Delta N}} \pm \text{S.E.}, \qquad (5)$$

where N_s is the surface value of N, the single bar represents a monthly mean value, the double bar represents the annual mean, b is the slope of the regression line, and S.E. is the standard error of estimate. The equations were put in this form because the intercept of the equations in the ordinary form is equal to $\overline{\overline{\Delta N}} - b\overline{\overline{N}}_s$, which is too unwieldy for contouring on maps. Maps, which appear in appendix B, were prepared of the slope (b), the annual means ($\overline{\overline{\Delta N}}$ and $\overline{\overline{N}}_0$), and the standard error of prediction and correlation coefficient of the regression lines.[5]

4.2. Discussion of Contours and Reliability of $\overline{\Delta N}$ Maps

The world $\overline{\Delta N}$ maps of this atlas do not show as much detail as may be found in other publications which consider only specific areas [Bean et al., 1960b; du Castel, 1961; Rydgren, 1963; CCIR, 1963]. It was necessary in this study to omit some of the available radiosonde data in areas with relatively dense weather networks (e.g., the U.S.A. and Europe) in order to obtain a more nearly uniform worldwide coverage. Even with this coverage, the map scale size precluded the contouring detail which would be necessary if localized terrain effects were to be included; for example, mountainous locations (higher than 1 km) probably have lower values of ΔN than those indicated in figures B-2 through B-13. Some dissimilarity in the contour patterns between the maps in appendix B and other $\overline{\Delta N}$ maps may also be found because of the differences in the time period used in the samples; such disagreements emphasize the fact that 5 years of data are not adequate for reliable means in many areas.

The map contours of worldwide $\overline{\Delta N}$ indicate that:

(1) Low values of ΔN are characteristic of:

(a) large desert and steppe regions such as the Sahara, the Australian interior, the southwestern U.S.A., and the Asian region southeast of the Caspian Sea all year;

(b) high plateau areas during all seasons except winter.

(2) High values of ΔN are found in:

(a) all areas where large masses of subsiding air prevent the normal diffusion of water vapor, creating an unusually large N-gradient between the moist surface air and the very dry air at 1 km. Specific examples are:

(1) continental west coasts at latitudes 20°–35° in the summer hemisphere and 10°–25° in the winter. In fact, the true $\overline{\Delta N}$ may be higher than indicated on the maps at locations such as Dakar, Senegal, where a very thick (~250 m) surface or near-surface ducting layer occurs much of the time;

(2) tropical ocean areas where a trade-wind inversion leads to a persistent elevated ducting layer below 1 km. [Note: In a few cases where the entire thickness of an elevated layer lies between 1 km and the height of the 850-mb level, the interpolation method gives a map value which may be 5 to 10 N-units too high.]

(b) southeast Arabia and the Gulf of Persia during July and August, when orographic subsidence traps moisture from the southwest monsoon in the gulf and lowlands between the mountains.

[5] N_0 is an approximate sea-level value of N_s, defined by the equation $N_0 = N_s e^{0.1z}$, where z is the elevation above sea level in km.

(c) Siberia and the Canadian interior in winter because of the intense surface temperature inversion.

(d) the Mediterranean and Black Seas during summer when convective mixing greatly increases the near-surface humidity.

(e) India in the spring, when increased heating over land produces a low-pressure region which leads to onshore winds and humid weather conditions until the onset of the monsoon.

In winter a combination of high and low $\overline{\Delta N}$ values appear near the tip of southwest Africa as the subsidence from the South Atlantic High causes a large moisture gradient to appear off the coast, whereas a small humidity gradient is characteristic of the dry plateau region inland.

5. World Maps of Extreme *N*-Gradients

5.1. Development

The gradient of N near the surface of the earth is of particular importance in many applications of telecommunications; e.g., extreme values of these initial gradients are responsible for much of the unusual behavior of radio systems. Superrefractive gradients (defined here as values between –100.0 N/km and –156.9 N/km) are responsible for greatly extended service horizons, and may cause interference between widely separated radio circuits operating on the same frequency. Ground-based radio ducts (layers having a negative gradient larger in absolute value than 156.9 N/km) can cause prolonged spacewave fadeouts within the normal radio horizon [Bean, 1954] and allow radar to track objects many hundreds of kilometers beyond the normal radio horizon. On the other hand, subrefractive gradients (zero or positive gradients) produce greatly reduced radio horizons, and may result in diffraction fading on normally line-of-sight microwave paths.

In the process of obtaining the mean N-profile for each station and month, cumulative distributions were prepared of the gradients occurring between the surface and the 50-m and 100-m levels. Each gradient was calculated as the simple difference between the surface N and the value at 50 or 100 m above the surface, divided by the height interval. For 99 out of the 112 stations in the mean N sample, cumulative distributions were also prepared of the gradients and thicknesses of all observed ground-based superrefractive or ducting layers, regardless of the thickness of the layer (except that no layer less than 20 m thick was included, because the gradients obtained in such cases are not considered to be reliable). In addition, cumulative distributions were prepared of the minimum trapped frequency for each of the observed ducts in the sample. (This sample size averaged 208 pieces of data for each month; for all months the smallest sample was 30 and the largest, 620). The minimum trapped frequency refers to the approximate lower limit of frequencies that will be propagated in a duct in a waveguide-like mode, and is given by [Kerr, 1951]

$$f_{\min} = \frac{1.2 \times 10^5 \text{ (c/s)}}{(t)^{3/2} \left[-\frac{dn}{dz} - \frac{1}{r} \right]^{1/2}}, \qquad (6)$$

where $f_{\min}$ is the minimum trapped frequency in c/s, t is the total thickness of the duct in km, dn/dz is the average gradient over the duct (n/km), and r is the radius of the earth in km. Equation (6) is derived under the assumption of a constant gradient throughout the duct, but moderate departures from this assumption do not seem to affect the results greatly. The $f_{\min}$ corresponds to an absolute attenuation of the guided energy of about 3 dB/km (5 dB/mile) [Kerr, 1951].

The maps in appendix C were prepared from the cumulative distributions discussed above. The distributions of gradients for the 0 to 100-m layer were used to obtain maps of the positive (subrefractive) gradient exceeded for 10 and 2 percent of the observations at any location, and the percent of observations with 0 or positive N-gradients. Maps were also prepared of the extreme values of negative gradients observed; these are referred to as "lapse rates" of N (i.e., decrease with height, a term normally used in referring to atmospheric temperature gradients; it is used here to avoid the awkwardness of referring to a very strong negative gradient as being "less than" a given negative value). Included in appendix C are maps of the lapse rate of N exceeded for 25, 10, 5, and 2 percent of the observations for the 100-m layer. Cumulative probability distribution charts of the gradients at 22 representative world locations are also presented.

Other maps in appendix C were prepared from the distributions of superrefractive and ducting layer gradients, thicknesses, and $f_{\min}$ values for ducts. These include the percent of time that the lapse rate of N in the ground-based layer is equal to or larger than 100 N/km and equal to or larger than 157 N/km (ducting gradient), the percent of superrefractive layers that were more than 100 m thick, and the percent of ducting layers that were more than 100 m thick (the last two refer to the percent of thick layers out of the number of observed layers of that type). The distributions of $f_{\min}$ values were used to prepare maps of the percent of all observations which showed ground-based ducts having an $f_{\min}$ value of less than 3000 Mc/s, 1000 Mc/s, and 300 Mc/s.

5.2. Discussion of Gradient Map Contours (Subrefraction)

Ground-based subrefractive layers may be

found in the same tropical and subtropical locations as superrefractive layers, because a small change in relative humidity at high temperatures produces a very noticeable change in absolute humidity, and the N-change (either positive or negative) with height is highly dependent upon the variation of absolute humidity. For instance, subrefractive gradients occur quite often during the afternoon at stations which experience superrefraction or ducting during the night and early morning. Other stations may have nocturnal subrefraction during winter and superrefraction during the same hours in summer. However, subrefraction, unlike superrefraction, rarely occurs at surface temperatures below 10°C (the only exception would be locations greater than 1 km above sea level).

The surface conditions conducive to subrefractive gradients are of two rather opposite types:

(a) temperature $>$ 30°C; relative humidity $<$ 40 percent;

(b) temperature 10° to 30°C; relative humidity $>$ 60 percent.

Type (a) is usually found during the daylight hours of months when intense solar heating occurs at warm, dry continental locations and forms a very nearly homogeneous surface layer (no decrease of density with height) which may be several hundred meters thick. Since a moist parcel of air is less dense than a dry parcel at the same temperature and pressure, the intense convection which occurs within such a layer of absolutely unstable air tends to concentrate the available water vapor near the top of the layer, because a moist adiabatic upper boundary is formed where the superadiabatic lapse rate changes abruptly to a subadiabatic or very stable lapse rate. The result is an increase (sometimes as large as 50 percent of the surface value) with height of the wet term through the ground-based layer. This increase, coupled with no change in the dry term, leads to a subrefractive (or positive) gradient.

This layer may retain its subrefractive nature throughout the early evening hours at stations where conditions are favorable for the development of a temperature inversion. As the ground cools rapidly, the air very near the ground cools and becomes more dense, but the water vapor which is trapped between the two stable layers causes the positive wet-term gradient from surface to the top of the original layer to remain large enough to overbalance the slightly decreasing gradient of the dry term. This evening subrefraction is an outgrowth of type (a); however, it may resemble type (b) at the surface because it can be found with a temperature as low as 20°C and a relative humidity as high as 60 percent.

Type (b) occurs most often during night and early morning hours, and is characteristic of coastal trade-wind and sea-breeze areas where differential heating of land and sea results in the advection of air which is warmer and more humid than the normal surface layer. In this type, both dry and wet terms may increase with height, creating a surface layer of subrefraction which is generally more intense in gradient than type (a) but not so thick. This form of subrefraction might also be found for short periods in *any* location where frontal passages or other synoptic changes create the necessary conditions.

Type (a) subrefraction is hard to evaluate from figures C-1 through C-4 because its percentage occurrence at any specific location is so dependent upon the time of day represented by the radiosonde data at that location. For instance, because the local radiosonde observation times in the southwestern U.S.A. were 0800 and 2000 for the data period used in this atlas, only the subtype (a) of evening subrefraction is recorded. Because conditions are more suitable for inversions in February and May, these months appear to have surface-based subrefractive layers more often than August. However, a detailed check of midafternoon observations near White Sands, N. Mex., reveals that midday subrefractive conditions are quite prevalent during much of August and September. The same diurnal problem is found in northern Africa and the desert region south and east of the Caspian Sea, where many of the stations take observations between 0300 and 0600 LST. Furthermore, even at those stations which do have midday data, the "motorboating" problem (i.e., humidities too low to be measured by the radiosonde — see sec. 5.5) during the warmest seasons at very dry locations probably masks out a large percentage of subrefractive occurrences; e.g., the occurrence of subrefraction recorded in November and February for the interior of Australia (where afternoon observations are included) is probably too low.

Figures C-1 through C-4 reveal that type (b) subrefraction can be expected 10 to 20 percent of the time in the western Mediterranean Sea and the Red Sea area, and also in the Indonesian-Southwest Pacific Ocean region. These locations seem to indicate a slight seasonal trend, with a higher probability of occurrence during winter months. Another region with a 10 to 20 percent level of subrefractive gradient occurrence is the Ivory Coast and Ghana lowlands of Africa where onshore winds prevail all year.

Occurrences of type (b) subrefraction exceed 5 percent at these locations and times of year:

(1) Southeast coast of U.S.A. all months;

(2) Hawaiian Islands all months except May;
(3) South Africa all months except November;
(4) Southeast coast of South America in November and February;
(5) Southern California in November;
(6) North Indian Ocean in May;
(7) Isthmus of Panama in November.

5.3. Discussion of Gradient Map Contours (Superrefraction and Ducting)

Superrefractive and ducting gradients in ground-based layers are most often associated with temperature inversions (temperature increasing with height within the layer), not only because a positive temperature height-gradient causes a negative N-gradient, but also because the low eddy diffusion qualities associated with a temperature inversion often lead to a steep negative gradient of humidity through the inversion. However, previous investigations [Bean, 1959] have shown that there are at least two other typical situations encountered in the formation of strong ground-based gradients: The first of these is the arctic situation, where, with surface temperatures below about —20°C, a strong temperature inversion (typical of continental arctic air masses) produces a superrefractive or ducting layer, while the vapor pressure may actually increase with height. More often, in this case, the wet term is negligible throughout the layer. The second case is typical of very humid tropical areas when the surface temperature is 30°C or greater. In these locations (which are usually coastal) a common occurrence is a slight decrease of temperature with height, accompanied by a very strong lapse of *absolute* humidity. Such profiles may show only a slight decrease of *relative* humidity with height, but, because the saturation vapor pressure is nearly an exponential function of temperature, the resulting vapor pressure gradient may be very large, thus causing a steep N-gradient.

Figures C-41, C-45, C-49, and C-53 show that persistent ducting (D) or superrefractive (SR) initial gradients can be found more than 25 percent of the time for at least two seasons in seven general areas of the world:

(1) Dakar - Fort Lamy transitional strip in Africa (D: all seasons),

(2) northern Arabian Sea including coastal areas of the Gulf of Aden and the Persian Gulf (D: all seasons),

(3) India, Bay of Bengal, southeast Asia, Indonesia, and north tip of Australia (SR: all seasons),

(4) southwest coast of North America, including portions of the North Pacific (SR: February, May, November),

(5) Gulf of Mexico and Caribbean region (SR: May, August, November),

(6) northwest coast of Africa and western Mediterranean (SR: May, August),

(7) Antarctica (D: May, August).

Area (1): Tropical west coast locations in the vicinity of 15°–22°N or S are affected annually by three or four latitudinal weather zones [Trewartha, 1961]. In winter the Dakar-Fort Lamy region is under the influence of dry anticyclonic Saharan air, but even at the time of low sun, the prevailing surface air movement is onshore from the southwest. The vertical depth of this maritime current is more shallow than in summer, but during the early morning hours, the surface relative humidity is 80 to 90 percent compared with 40 to 60 percent in the dry subsiding air above. Even with radiational cooling, the night temperatures throughout the marine layer (from 50 to 600 m thick) still remain over 20°C. This combination of temperature and humidity creates trapping conditions for frequencies below 300 Mc/s about 30 percent of the time in February (fig. C-31).

The weather zones advance rapidly northward [Thompson, 1965], so that by July the Dakar-Fort Lamy strip is in the wet tropical regime associated with the fluctuating, unstable Intertropical Convergence Zone (ITC). The marine current of the westerlies becomes much deeper, but the ducting layers are shallower and can exist only intermittently between the turbulent, showery periods common to the region. Figures C-22, C-24, C-26, and C-28 indicate that more than 30 percent of the ducting layers are over 100 m thick for all seasons except summer.

Area (2): The coastal areas of Arabia experience high surface humidities all year from monsoonal and sea-breeze effects, but during May and August these values are reinforced by temperatures above 25°C in a marine layer which may extend up to a height of 800 to 900 m before it meets the overrunning dry northeasterlies [Tunnell, 1964]. The percentage occurrence of ducts at Bahrain seems much higher than at Aden because all observations at Bahrain were taken at 0300 LST (when the surface humidity is at its maximum of 75 to 90 percent), whereas the Aden observations, taken twice a day, include as many observations at 1500 LST (when the relative humidity value is much less) as at 0300 LST. For instance, 50 of the 66 ducts recorded in August at Aden were from early morning observations. However, the fact that ducting gradients at Bahrain trap frequencies below 300 Mc/s over 75 percent of the time as compared to 5 percent at Aden (fig. C-37) is due to another factor: the thickness of the moist marine layer, when ducting is present

at Bahrain, is greater than 300 m over half the time.

Area (3): A moist surface layer is also found in the monsoonal areas. Its temperature is 25 to 30°C and, during occurrences of ducting, the surface relative humidity ranges from 85 to 100 percent, but the trapping incidence is much less than in either area (1) or (2). The surface layer is shallower and its gradient is less intense because the humidity decrease between it and the air mass directly above it is only 10 to 20 percent. Because brief periods of stable weather occur even between surges of the summer monsoon, the ducting incidence remains over 10 percent for all of area (3).

Area (4): Along the western coast of North America, from Southern California to Central Mexico, the most important month for unusual radio propagation due to surface conditions is February, when frequencies below 300 Mc/s are trapped 10 percent of the time. During the period studied, 30 percent of the superrefractive gradients were at least 300 m thick in all 4 months. Closer examination of the ducting structure in Mazatlan reveals that if near-surface layers (bases of 100–300 m) were included, the percentage of occurrence would be increased by 20 to 40 percent for all months except August. During February, May, and November the surface temperature of 20 to 30°C remains nearly constant through the ducting layer, but the relative humidity decreases from a surface value of 70 to 80 percent to values ranging from 20 to 40 percent. The dry air in the upper layer results from subsidence in the eastern margin of the Pacific high pressure cell, which shifts northwestward in August, thus decreasing the ducting incidence in Mazatlan but increasing it in lower California and the Hawaiian Islands (figs. C-21, C-23, C-25, C-27).

Area (5): The center of most intense ducting in the Caribbean Sea and Gulf of Mexico changes with the seasons (figs. C-41 through C-56). The smallest percentage of superrefractive ground-based gradients is found in February, with the stronger gradients concentrated near the east coast of Central America. By May the superrefractive area has shifted eastward into the Caribbean and northward into Florida. In August it includes parts of the eastern U.S. but is still most intense in the Swan Island area, and in November the area encompasses all of the Caribbean. The ground-based superrefractive layers are thicker than 100 m approximately 70 percent of the year, but the ducting layers are never intense enough to exceed the 1-percent trapping level for 300 Mc/s.

Area (6): The cause of superrefraction in the western Mediterranean and northwest Africa is very similar to that in area (4). During the summer season, subsidence along the eastern edge of the Atlantic high-pressure cell superimposes a dry layer over the marine surface layer; during the winter season, the major subsidence area shifts southward, the temperatures throughout the surface layer are 5 to 10°C lower, and the percentage of superrefraction and trapping incidence decreases.

Area (7): During the long Antarctic night, intense radiation from the snow-covered ground keeps the surface temperature much lower than that in the air several hundred meters above. This temperature inversion of 10 to 25°C is the cause of all the ducting gradients in May and August, which trap frequencies <1000 Mc/s at least 40 percent of the time (see appendix E).

5.4. Discussion of Cumulative Distributions of Ground-Based Gradients

Data from 22 representative stations were selected as a sample of the kinds of ground-based gradient distributions from the surface to 100 m which occur in various climates and locations throughout the world.

Interesting similarities which exist among the gradient distributions imply that the refractivity climate of any station may be related more to the season or month of the year than to any particular latitudinal location. For instance, consider the interesting relationships between Bangui (a tropical station), Bordeaux (temperate), and Amundsen-Scott (arctic). The gradient distribution at Amundsen-Scott in February resembles that of Bordeaux in February, but its August distribution slope resembles that of Bangui in May. However, Bangui's distribution slope and range in August resembles Bordeaux in May. Amundsen-Scott forms another interesting climatic triad with Saigon and Long Beach. In August the distribution slope and range of Amundsen-Scott is very similar to that of Saigon (a tropical station), but the negative gradient intensity is about 100 N-units greater at all percentage levels. However, Saigon in May, before the monsoon, resembles Long Beach in February.

It was expected that a pronounced diurnal effect would exist in the gradient structure near the surface, so two stations, Aden, Arabia, and Nicosia, Cyprus, where data were available at two thermally opposite times of day—2 and 3 a.m. and 2 and 3 p.m. (0000 and 1200 GMT[6])—were studied. Figures C-57 and C-71 in appendix C show the diurnal differences in the cumulative distribution of initial gradients from 0 to 100 m for these two stations for the 4 months studied.

Superrefractive conditions normally accompany nocturnal inversions. At Nicosia this

[6] GMT (Greenwich Mean Time) is the same as UT (Universal Time).

proves to be the case for all seasons, with a very definite maximum in August, when anticyclonic upper air circulation intensifies the humidity decrease aloft and radiational cooling lowers the surface temperature 15°C below that found during the day.

Aden, a coastal station with less change in its diurnal temperature cycle than Nicosia (an interior valley station on a fairly large island), exhibits superrefraction day and night for all seasons. During August and November initial gradients have a wide range of values, with the largest variation occurring at 0000 GMT, but in February and May the nocturnal stability apparently is seldom destroyed by convective mixing, and the 1200 GMT (1500 LST) initial refractivity gradient may exceed the 0000 GMT (0300 LST) gradient. However, the early morning inversion is usually more significant from a radio-meteorological viewpoint because

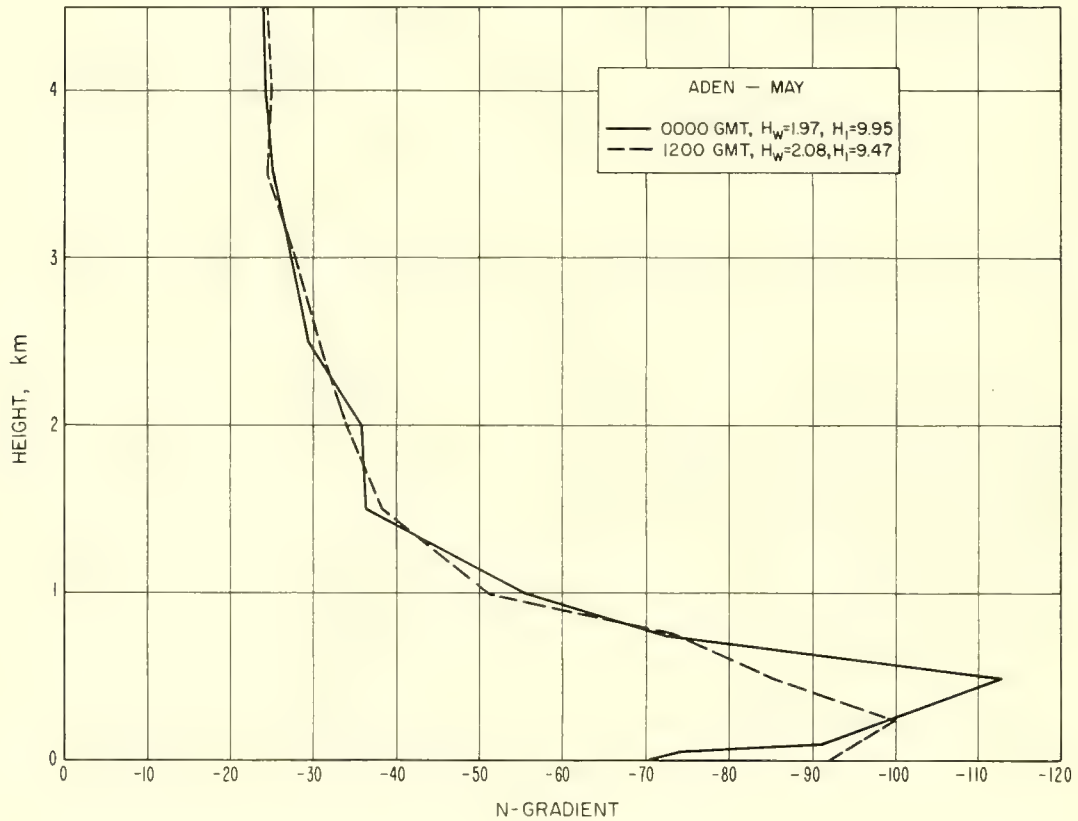

FIGURE 5. *Five-year mean vertical refractive gradient profile: Aden.*

the refractivity gradient is much more intense from 250 m to 750 m, thus affecting more radio frequencies. This can be noted in figure 5, representing a 5-year mean of the vertical gradient observed from 0 to 4.5 km during May.

Figure 6 presents the same data for Nicosia during a 5-year August period. Because scale heights are also a measure of stability and stratification, figures 5 and 6 not only give the differences in the mean total N-gradient values in the lower atmosphere, but also the wet (H_w) and dry (H_1) scale heights. Five-year mean values of N_s at Aden in May were found to be 382 (surface wet term of 123) at 0000 GMT and 374 (surface wet term of 119) at 1200 GMT. The corresponding values at Nicosia in August were 341 (wet term of 83) and 310 (wet term of 62).

The percentage of occurrence of subrefraction (N/km$>$0) is larger at night (0000 GMT) in February and November at both locations. However, this diurnal trend is much more pronounced at Nicosia, particularly in November when the percentage of night subrefraction is over 30 percent larger than the daytime percentage of occurrence.

5.5. Reliability and Limitations of Ground-Based Refractivity Gradient Data

Because ground-based gradients are so sensitive to local effects, such as terrain and land-water relationships, it was impossible to contour figures C-1 through C-56 for individual small areas. For instance, although Madrid (on the high interior plateau of Spain) experiences little ducting during the year, it is surrounded by areas of high ducting incidence, and no attempt was made to delineate this small region of nonducting. Also, refractivity gradients calculated from radiosonde observation levels separated by less than 20 m may be seriously affected by instrumental errors, so ground-based layers less than 20 m thick were not included in the analysis. Consequently, very shallow ducting (such as that found at certain times over oceans, under dense jungle canopies, and in

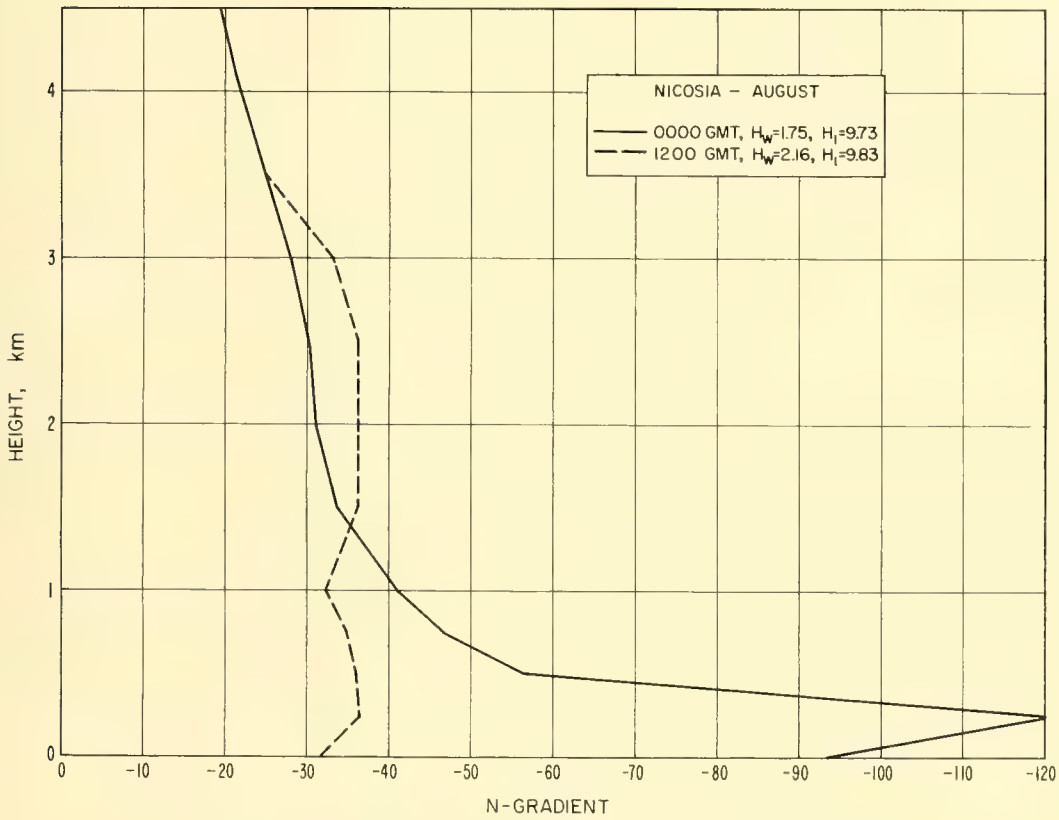

FIGURE 6. *Five-year mean vertical refractive gradient profile: Nicosia.*

mountain valleys) is not included in the contoured data; however, such layers may be intense enough to create trapping conditions for frequencies down to 600 Mc/s [Jeske, 1964; Baynton et al., 1965; Behn and Duffee, 1965].

The time of day represented by the available observational data must also be considered for any variable which has a definite diurnal trend. Therefore, for a true comparison of worldwide gradient behavior, it would be desirable to use comparable data recorded at least twice a day at standard local or sun-referenced time. However, because simultaneous data are needed for the preparation of synoptic maps, all stations in the U.S.A. and many in the European countries schedule radiosonde observations at 0000 GMT and 1200 GMT. Many stations in other parts of the world take only one observation per day (usually at either 0000 GMT or 1200 GMT, but there are exceptions, e.g., 0600 GMT at Abidjan, Dakar, and Niamey). Even if all stations had a common GMT hour for taking observations, the diurnal problem would still exist because the *local* time for any designated *GMT*

time would be distributed throughout the day as one traversed the globe. For instance, the following stations (in tropical areas where the occurrence of either subrefractive or superrefractive layers is especially dependent upon the time of day) were used in this report:

Station	*Local time*	*GMT*
*Aden, Federation of South Arabia	0300	0000
*Curacao, Netherlands Antilles	2000	0000
Fort Lamy, Republic of Chad	0100	0000
*Hilo, Hawaii	1400	0000
Lae, Territory of New Guinea	1000	0000
Majuro Island, Marshall Islands	1200	0000
Singapore	0700	0000

Those stations marked with an asterisk also take observations at 1200 GMT. However, when evaluating the apparently low level of duct occurrence at some locations (e.g., Majuro) and high occurrence at others (e.g., Fort Lamy), and when checking the subrefraction occurrence at warm, dry continental locations, such as Niamey (where no midday observation is taken), the local time of the radiosonde ascent should be considered.

In addition to the spatial and temporal limitations imposed by the use of available radiosonde data, there are instrument recording limitations (see sec. 2) which must be considered when evaluating N-gradients. Although the alternating sequence system of observing the humidity and temperature can put a lower limit on the thickness and thus mask the true gradient of atmospheric layers which can be detected by radiosonde, the response of the radiosonde temperature and humidity elements is a more serious problem in the measurement of the intensity and number of superrefractive gradients at or near the surface. For example, in typical ducting situations during May in a tropical (Saigon) and in a temperate climate (Bordeaux), correction of both humidity and temperature sensor time lags as suggested by Bean and Dutton [1961] would intensify gradients of —293 N/km (Saigon) and —212 N/km (Bordeaux) to —377 N/km and —362 N/km, respectively. This type of correction also would have increased the percentage occurrence of superrefractive and ducting gradients in the majority of cases. Such extensive recalculations were not possible in this study, but the possibility that more intensive gradients may occur in larger percentages at some locations (particularly in temperate, humid climates) should be kept in mind when applying values obtained from any of the figures in appendix C.

Another limitation which applies primarily to the detection of subrefractive layers (figs. C-1 through C-12) in hot, dry regions is the high electrical resistance of the lithium chloride humidity element at very low humidities which causes open-circuit signals ("motorboating"). At stations such as Aoulef, Algeria, where the daytime surface temperature often exceeds 30°C, the relative humidity may be below the motorboating boundary at *all* levels from surface upward, and all relative humidity values (except the surface) are estimated, usually in values which are equal to, or less than, the surface value. However, it is quite probable in these highly convective conditions that the *absolute* humidity remains constant with height, instead of rapidly decreasing (as the estimated relative humidity values would indicate). If it did remain constant, fairly persistent subrefractive gradients would be found in such areas during the hours of most intense solar heating.

6. World Maps of Mean Tropopause Altitudes

Maps have been prepared of the mean tropopause altitudes which were calculated in the course of obtaining the mean N-profiles for the 112 station sample, as discussed previously. The maps, for the 4 "seasonal" months, are shown in appendix D. The zone of maximum tropopause altitudes for each month seems to correspond quite well with the mean position of the Intertropical Convergence Zone.

As stated earlier, the criterion for determining the tropopause altitude for each radiosonde ascent was the altitude of the base of the first layer or layers which had a total thickness of at least 2 km and a temperature lapse rate of less than 2°C/km. The mean tropopause altitude for each station and for each month was determined by a simple average of all of the individual values for the profiles in the sample (usually of 5 years' length). The reliability or consistency of these maps is difficult to assess, since the results of determining tropopause altitudes depend to a great extent on the criteria used for selection of the first stratospheric layer. The criterion used here is the one in most common usage [U.S. Weather Bureau, 1964], but other criteria may be applicable where the results are intended for use in specific atmospheric problems. These maps supplement tropopause data presented in other reports and atlases [For example, Willett, 1944; U.S. Navy, 1955-59; Smith, 1963; Smith et al., 1963; Kantor and Cole, 1965].

7. Appraisal of Results

7.1. Accuracy of $N(z)$ Maps

The general accuracy of the 5-year mean values used in the $N(z)$ study was checked by computing the standard deviation of the year-to-year monthly means and dividing by the square root of 5. This should be a good estimate of the rms (standard) error of the 5-year mean values as compared to the true long-term mean (assuming there are no trends in the data). Table 1 shows the estimated standard error of the 5-year mean N_s values for 40 stations, arranged by climatic classification. The percentage errors should be similar for the $N(z)$ parameters (with the possible exception of scale heights) at various altitudes. The combined (rms) standard error of 5-year mean N_s for the 40 stations for February and August was 2.37 N-units, or about 0.7 percent of the mean N_s. It is significant that even the standard 30-year period recommended (e.g., by the WMO) for standard climatological normals would have a nominal standard error of about $\pm$ 1.0 N-unit (2.37 divided by $\sqrt{6}$), or about 0.3 percent of mean N_s values.[7] The 30-year means would thus have an advantage of only about 50 percent in rms error, as opposed to the 5-year means actually used.

TABLE 1. *Standard errors of 5-year mean values of monthly mean* N_S *for 40 stations.*

Climatic type	Number of stations	February* (N-units)	August* (N-units)	12-month estimate (rms of Feb. and Aug.) (N-units)	12-month rms as percentage of mean N_S
Arctic	2	1.6	0.6	1.2	0.4
Subarctic	2	1.2	2.8	2.1	0.7
Marine west coast	4	1.5	1.9	1.7	0.5
Marine (ships)	4	2.2	1.5	1.9	0.6
Continental (cool)	2	1.0	2.9	2.2	0.7
Continental (warm) and subtropical	3	2.2	1.6	1.9	0.6
Semiarid cool, high altitude	2	1.4	3.5	2.7	1.0
Arid and semi-arid tropical	8	2.4	3.8	3.2	0.9
Monsoon	3	3.2	1.3	2.5	0.7
Equatorial	6	(seasons not applicable)		2.7	0.7
All (rms of above)	40	—	—	2.37	0.7

**For stations in the Southern Hemisphere, months were reversed (February was combined with August for northern stations, etc.).*

[7] Thirty-year means are used because there are long-term trends in most climatological series; thus a standard period is desirable for comparison between stations.

The overall accuracy of the three-part exponential model was checked in two ways. First, a check was made of the accuracy of recovering the $\overline{\Delta N}$ values using the three-part exponential. Here the value of $\overline{\Delta N}$ was calculated, using the wet- and dry-term tropospheric exponentials, and the value obtained was compared with the actual $\overline{\Delta N}$ from the mean N-profile. Figure 7 shows the results of such a comparison for 95 of the 112 stations in the original sample for which coincident data of several types were available. The true value of $\overline{\Delta N}$ from the mean N-profile is the dependent variable, and the value recovered from the wet and dry exponentials is the independent variable. The rms error in recovering $\overline{\Delta N}$ was 9.2 N-units; however, if those stations (points shown as crosses on fig. 7) which are in areas where the three-part exponential model is of questionable validity (as shown in fig. A-30) are eliminated from the sample, the rms error is reduced to 6.4 N-units. The regression line shown in figure 7 is for this reduced sample. The deviation of the regression line from the 45° line (labeled "perfect agreement" in fig. 7: zero intercept and unity slope) is significant at the 5-percent level; thus it would appear that this is not the best usage for the three-part exponential model. Use of the $\overline{\Delta N}$ maps in appendix B is recommended rather than the $N(z)$ maps, for this purpose.

The second check was to use the $N(z)$ maps to recover the values of $N(z)$ for some of the actual station locations, at different heights above the surface, and compare these with the actual values of mean $N(z)$. This would be a check not only on the three-part exponential model but also upon the contouring process. Table 2 shows the results of such an error analysis.

Thirty-two of the original 112 stations were selected on an areal basis, and the corresponding three-part exponential model was constructed for each of these stations, for all 4 months, using the maps in appendix A. These exponential models were then used to calculate $N(z)$ for three heights (3, 8, 16 km) for each month, and the results were compared with the actual mean N-profiles. The mean and maximum values of the absolute errors thus derived are shown in table 2. Stations and seasons in this sample

which are characterized by a high (tropical-type) tropopause showed larger errors at 16 km than at 8 km, the reverse of the usual trend in table 2. It is apparent from inspection of table 2 that errors in recovering $N(z)$ at altitudes of 3 km or more are likely to be small.

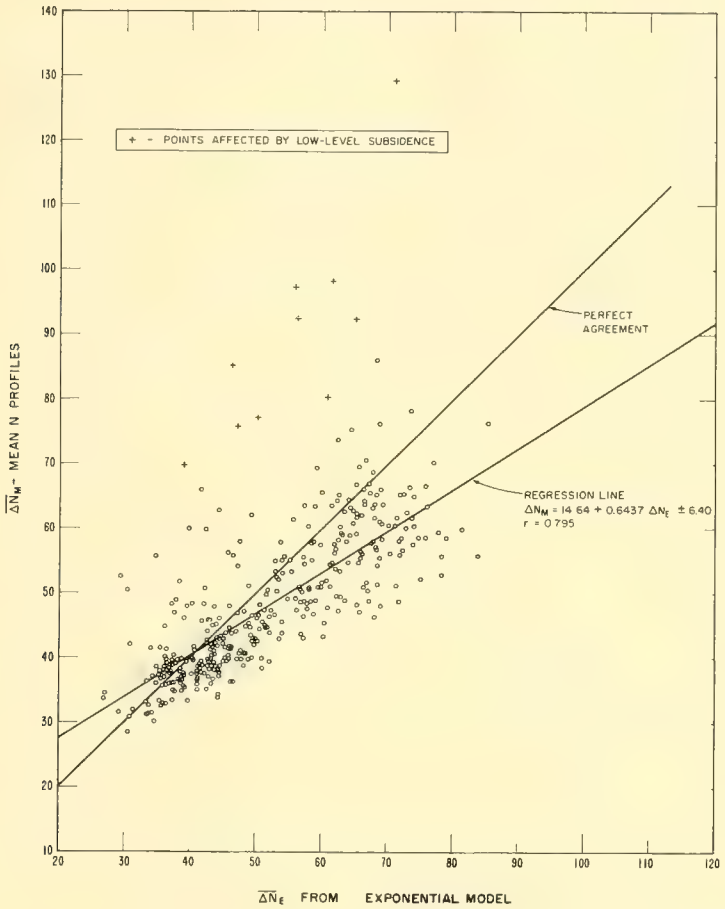

FIGURE 7. *Correlation of* $\overline{\Delta N}$*: monthly mean N-profiles versus monthly mean exponential model.*

TABLE 2. *Absolute errors in recovering mean* N *from map contours for 32 stations (in* N*-units).*

Month	3 km		8 km		16 km	
	Mean	Max	Mean	Max	Mean	Max
Feb.	1.0	2.1	1.6	3.6	0.6	1.7
May	1.3	3.2	1.4	3.3	0.9	2.3
Aug.	1.4	2.1	1.9	3.7	0.8	1.6
Nov.	2.0	4.0	1.3	3.0	1.2	3.0
Year	1.4	4.0	1.6	3.7	0.9	3.0

The total variance, σ_T^2, in using the maps of $N(z)$ given in appendix A can be estimated in terms of the following error model:

$$\sigma_T^2 \cong \sigma_5^2 + \sigma_M^2, \qquad (7)$$

where σ_5^2 is the variance of 5-year mean values (as compared to long-term means), σ_M^2 is the variance of errors in mapping $N(z)$. Random instrumental errors are included in σ_5^2. The value of σ_5 can be estimated at about 2.5 N-units (table 1), while σ_M may be estimated at 1.5$\times$ P.E., where the probable error, P.E., is given approximately by the mean absolute errors in table 2. These would yield 2.1 N at 3 km, 2.4 N at 8 km, and 1.4 N at 16 km, for σ_M. A reasonable estimate for σ_M at the surface (0 km) would be 1.0 N-unit. These estimates may be combined to yield approximate σ_T values, as shown in table 3. Minimum and maximum values were obtained by permutations of the values in tables 1 and 2. The standard errors of the 5-year means have been assumed to be a constant percent of mean $N(z)$, independent of altitude.

TABLE 3. *Approximate total standard errors, σ_T, for* N(z) *maps in appendix A.*

	0	3 km	8 km	16 km
In terms of N-units				
Average	2.6	1.9	1.8	1.0
Minimum	1.4	1.3	1.3	0.6
Maximum	4.3	2.8	2.2	1.3
As percent of mean $N(z)$				
Average	0.8	1.1	1.5	2.5
Minimum	0.4	0.7	1.1	1.6
Maximum	1.3	1.6	1.9	3.3
Mean $N(z)$	320	175	117	38

It is probable that the percent errors given in table 3 do not increase materially above 16 km; asymptotic values of 3, 2, and 4 percent for average, minimum, and maximum relative standard errors are probably good estimates for altitudes from 20 to 30 km, while above 35 km the standard errors are probably no more than 0.2 N-units.

There are also undoubtedly some bias errors involved in the $N(z)$ maps, although they are probably quite small. Sources of these bias errors would include the equation for N itself (Smith-Weintraub formula), the radiosonde in-

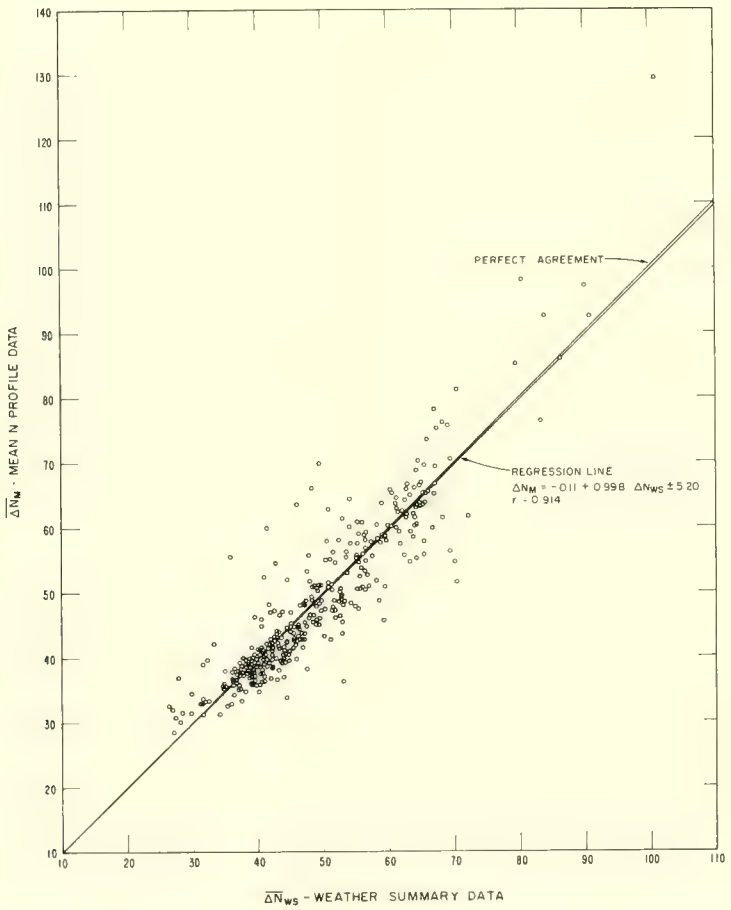

FIGURE 8. *Correlation of* $\overline{\Delta N}$*: monthly mean* N*-profiles versus monthly mean weather summary data.*

strument (where the sensor lag would seem to assure a slight positive bias for all upper-air N values, even over long-term means), and certain peculiarities in the mapping and curve-fitting procedures which might produce bias for some values of z and not others (e.g., the bias due to the sharp "knee" of the D_1 and D_2 exponential terms at the N-tropopause as compared with the smooth transition of real mean N-profiles; note example in fig. 2). It should be noted that this last type of bias error was (automatically) included in the mean absolute errors given in table 2, since there was no easy way of separating this type of error from the others. Hence table 3 includes an allowance for this particular source of bias error.

7.2 Accuracy of $\overline{\Delta N}$ Maps

As a check on the method used to calculate the $\overline{\Delta N}$ values from which the maps in appendix B were derived, the $\overline{\Delta N}$ values from the weather summary data were obtained for all 90 of the stations which were also contained in the mean N-profile sample; the $\overline{\Delta N}$ values for the months of February, May, August, and November were then compared with the corresponding values from the actual mean N-profiles. However, the period of record involved in the mean N-profile study was not, in general, even partially coincident with the 1960-64 period used for the $\overline{\Delta N}$ study. Thus it was expected that the variance, σ_D^2, of the differences between the weather summary $\overline{\Delta N}$ values (from which the maps given in appendix B were obtained) and the $\overline{\Delta N}$ values from the mean N-profiles would have two components,

$$\sigma_D^2 = \sigma_R^2 + \sigma_E^2, \tag{8}$$

where σ_R^2 is the variance of the real difference in the two 5-year mean values of ΔN (because they are obtained from different time periods), and σ_E^2 is the variance of the differences which are caused by the interpolation errors inherent in the method used to obtain the $\overline{\Delta N}$ from the weather summary data. Since the real differences (represented by σ_R) would be expected to have a near-zero mean for a worldwide data sample, a regression analysis of the two types of $\overline{\Delta N}$ values should reveal any bias which had been produced by the interpolation method used in the $\overline{\Delta N}$ study. Figure 8 shows the results of such a comparison, with $\overline{\Delta N}$ from the mean N-profiles as the dependent variable, and $\overline{\Delta N}$ from the weather summary data as the independent variable. There is no statistically significant bias shown, since the regression line is almost identical with the "perfect agreement" line (zero intercept and slope of unity).

An evaluation of the relative sizes of σ_R and σ_E was made by calculating the rms difference between the two types of $\overline{\Delta N}$ values for a restricted sample containing only those stations where the mandatory pressure level used to calculate the $\overline{\Delta N}$ values from the weather summary data was within $\pm$ 100 m of 1 km above the surface; the rms difference thus calculated was 3.9 N-units. Since any interpolation errors would be expected to be quite small for this restricted sample, it was concluded that the 3.9 N-unit rms represented essentially the value of σ_R as given in (8).

The value of σ_D as given in figure 8 is 5.2 N-units; thus by (8) the value of σ_E is probably on the order of 3.5 N-units. This should be a good approximation to that part of the overall rms error in the $\overline{\Delta N}$ maps which is assignable to the interpolation method used on the weather summary data.

The overall accuracy of the $\overline{\Delta N}$ maps given in figures B-2 through B-13 depends on several factors: the accuracy of the interpolation method, the variability of the 5-year mean period as compared with a standard WMO 30-year mean period, and the heterogeneous nature of the local observation times included in the data sample. The weather summary data were mostly derived from observations taken at 0000 GMT, although many stations in different parts of the world supplied data taken at 1100 or 1200 GMT, while others supplied data averaged at two, or in a few cases four, times per day. In this study no attempt was made to correct for diurnal variations imposed by the fixed observation times of the various stations; hence diurnal variability must be added to the sources of possible error in the maps. It is reasonable to assume that the actual (unknown) standard error of the maps is not independent of the true value of monthly mean ΔN desired, but that it is more likely a certain percentage of the true value. Since the overall correlation between the contoured and true values is probably quite high, it is plausible to estimate the standard error of the maps as a percentage of the contoured values. On figure 8 it is found that an allowance of $\pm$ 10 percent from the perfect-agreement line (in the vertical) will exclude only 23 percent of the 360 data points (40 above the limits, and 44 below the limits); for a normal distribution, 32.5 percent of the points should be excluded by the standard error limits. Therefore, allowing for some added error from diurnal variability, it seems reasonable to estimate the overall standard error of the maps of $\overline{\Delta N}$ as approximately 10 percent of the contoured values.

This is equivalent to assuming an error model,

$$\sigma_T^2 = \sigma_5^2 + \sigma_E^2 + \sigma_t^2, \tag{9}$$

where the terms have the same meaning as those in (7) and (8), with $\sigma_5^2 \cong \sigma_R^2$ (possibly as low as $\frac{1}{2}\ \sigma_R^2$) in (8), and where σ_t^2 is the variance assignable to diurnal variations in $\overline{\Delta N}$. The value of σ_t should be on the order of 2 to 4 N-units, which is an estimate based on inspection of the CCIR maps [CCIR, 1965].

There is doubtless some bias error in the $\overline{\Delta N}$ maps; the discussion given for bias errors in the $N(z)$ maps is mostly applicable to the $\overline{\Delta N}$ maps. Here the bias due to the radiosonde is relatively larger, because of the differencing used to obtain $\overline{\Delta N}$ values. This mean bias error may be as high as 1 percent of the $\overline{\Delta N}$ values, but data adequate for checking on this possibility are not available.

7.3. Accuracy of Gradient Maps

It is very difficult to assess the probable errors in the maps of the different kinds of initial gradients given in appendix C. The primary reason for this is that no data are available except those used to prepare the maps. It is likely that the most serious source of discrepancies will arise because of the admixture of data taken at widely differing local times. In line with the results of the $\overline{\Delta N}$ error analysis, an overall error of about 15 percent of the contoured values seems reasonable, but may be higher or lower, depending on the area being considered. The maps in appendix C are probably best suited for the depiction of climatic tendencies of subrefraction and superrefraction.

8. Conclusions

It seems clear that the most significant conclusion which can be drawn from this study (pertaining to future requirements) is that careful selection of data by local time of observation, and the segregation of these data into types, e.g., nighttime and midafternoon, prior to analysis or mapping, is probably equally as important as obtaining larger samples. The effects of such an analysis on the results given in this atlas would probably be slight in the case of the $N(z)$ maps, somewhat larger in the case of the $\overline{\Delta N}$ maps, and might well have a profound effect on the ground-based gradient maps of appendix C.

9. References

Air Ministry, Meteorological Office (1961), Tables of Temperature, Relative Humidity and Precipitation for the World, vols. I-VI (Her Majesty's Stationery Office, London).

Baynton, H. W., H. L. Hamilton, Jr., P. E. Sherr, and J. J. B. Worth (1965), Radio climatology of a tropical rain forest, J. Geophys. Res. **70**, No. 2, 504–508.

Bean, B. R. (1954), Prolonged space-wave fadeouts in 1046 Mc observed in Cheyenne Mountain propagation program, Proc. IRE **42**, No. 5, 848–853.

Bean, B. R. (1959), Climatology of ground-based radio ducts, J. Res. NBS **63D** (Radio Prop.), No. 1, 29–34.

Bean, B. R. (1961), Concerning the bi-exponential nature of tropospheric radio refractive index, Beitr. Physik Atmosphäre **34**, Nos. 1/2, 81–91.

Bean, B. R. (1962), The radio refractive index of air, Proc. IRE **50**, No. 3, 260–273.

Bean, B. R., and B. A. Cahoon (1957), A note on the climatic variation of absolute humidity, Bull. Am. Meteorol. Soc. **38**, No. 7, 395–398.

Bean, B. R., and B. A. Cahoon (1961a), Limitations of radiosonde punch-card records for radio-meteorological studies, J. Geophys. Res. **66**, No. 1, 328–331.

Bean, B. R., and B. A. Cahoon (1961b), Correlation of monthly median transmission loss and refractive index profile characteristics, J. Res. NBS **65D** (Radio Prop.), No. 1, 67–74.

Bean, B. R., and E. J. Dutton (1961), Concerning radiosondes, lag constants, and refractive index profiles, J. Geophys. Res. **66**, No. 11, 3717–3722.

Bean, B. R., and F. M. Meaney (1955), Some applications of the monthly median refractivity gradient in tropospheric propagation, Proc. IRE **43**, No. 10, 1419–1431.

Bean, B. R., and G. D. Thayer (1959), On models of the atmospheric refractive index, Proc. IRE **47**, No. 5, 740–755.

Bean, B. R., G. D. Thayer, and B. A. Cahoon (1960a), Methods of predicting the atmospheric bending of radio rays, J. Res. NBS **64D** (Radio Prop.), No. 5, 487–492.

Bean, B. R., J. D. Horn, and A. M. Ozanich, Jr. (1960b), Climatic charts and data of the radio refractive index for the United States and the world, NBS Monograph No. 22.

Behn, R. C., and R. A. Duffee (1965), The structure of the atmosphere in and above tropical forests, Rept. No. BAT-171-8, Battelle Memorial Institute, Columbus, Ohio.

Bunker, A. F. (1953), On the determination of moisture gradients from radiosonde records, Bull. Am. Meteorol. Soc. **34**, 406–409.

CCIR (International Radio Consultative Committee) (1963), Influence of the atmosphere on wave propagation, Rept. 233, Documents of the 10th Plenary Assembly, vol. 2 (Geneva).

CCIR (International Radio Consultative Committee) (1965), Propagation over the surface of the earth and through the non-ionized regions of the atmosphere, Rept. G.l.d(V), Conclusions of the interim meetings of Study Group V (Geneva).

Dodd, A. V. (1965), Dew point distribution in the contiguous United States, Monthly Weather Rev. **93**, No. 2, 113–122.

Dutton, E. J., and B. R. Bean (1965), The bi-exponential nature of tropospheric gaseous absorption of radio waves, Radio Sci. J. Res. NBS **69D**, No. 6, 885–892.

du Castel, F. (1961), Propagation Tropospherique et Faisceaux Hertziens Transhorizon, 140–141. (Editions Chiron, Paris.)

Hutchings, J. W. (1961), Water vapor transfer over the Australian continent, J. Meteorol. **18**, 615–634.

Jeske, H. (1964), Transhorizon-transmission and height gain measurements above the sea with waves in the range of 1.8 cm to 187 cm under special consideration of meteorological influences, Proc. 1964 World Conf. on Radio Meteorology, Am. Meteorol. Soc., Boston, Mass. 458–463.

Kantor, A. J., and A. E. Cole (1965), Monthly atmospheric structure, surface to 80 km, J. Appl. Meteorol. **4**, No. 2, 228–237.

Kerr, D. E. (1951), Propagation of Short Radio Waves, MIT Radiation Lab. Series, vol. 13. (McGraw-Hill Book Co., Inc., New York, N. Y.).

Knoll, D. W. (1941), Climatology Asiatic Station, Hydrographic Office, U. S. Navy, Washington, D. C.

List, R. J. (1958), Smithsonian Meterological Tables, 204. (Smithsonian Inst., Washington, D. C.).

Michaelis, J., and E. Gossard (1958), Distribution of refractive layers over the North Pacific and Arctic, NEL Rept. No. 841, U. S. Navy Electronics Lab., San Diego, Calif.

Misme, P., B. R. Bean, and G. D. Thayer (1960), Models of the atmospheric radio refractive index, Proc. IRE **48**, No. 8, 1498–1501.

Misme, P. (1964), A meteorological parameter for radioclimatological purposes, Radio Sci. J. Res. NBS **68D**, No. 7, 851–855.

Reitan, C. H. (1963), Surface dew point and water vapor aloft, J. Appl. Meteorol. **2**, No. 6, 776–779.

Rydgren, B. (1963), Proposal for a Swedish radio standard atmosphere, Rapport A518, Forsvarets, Forskningsanstalt, Stockholm.

Saxton, J. A. (1951), Propagation of metre waves beyond the normal horizon, Proc. Inst. Elec. Engrs. (London) **98**, Pt. III, 360–369.

Serra, A. (1955), Atlas Climatologico do Brasil, vol. 1. (Conselho Nacional de Geografia e Service de Meteorologia, Rio de Janeiro.)

Smith, E. K., and S. Weintraub (1953), The constants in the equation for atmospheric refractive index at radio frequencies, Proc. IRE **41**, 1035–1037.

Smith, J. W. (1963), The vertical temperature distribution and the layer of minimum temperature, J. Appl. Meteorol. **2**, No. 5, 655–667.

Smith, O. E., W. M. McMurray, and H. L. Crutcher (1963), Cross sections of temperature, pressure, and density near the 80th meridian west, National Aeronautics and Space Administration, Washington, D. C.

Thompson, B. W. (1965), The Climate of Africa (Oxford University Press, Nairobi).

Trewartha, G. T. (1961), The Earth's Problem Climates (Univ. of Wisconsin Press, Madison, Wisc.).

Tunnell, G. A. (1964), Periodic and random fluctuations of the wind at Aden, Meteorol. Mag. **93**, No. 1100, 70–82.

UNESCO (1958), Arid Zone Research X, Climatology, Reviews of Research, 159 (Imprimerie Firmin-Didot, Paris).

U. S. Navy, Chief of Naval Operations (1955-1959), Marine Climatic Atlas of the World, vols. 1-5, NAVAER 50-1C-528 through 50-1C-532, U. S. Govt. Printing Office, Washington, D. C.

U. S. Weather Bureau (1964), Manual of Radiosonde Observations, Circular P, 7th ed., U. S. Govt. Printing Office, Washington, D. C.

Wagner, N. K. (1960), An analysis of radiosonde effects on the measured frequency of occurrence of ducting layers, J. Geophys. Res. **65**, 2077–2085.

Wagner, N. K. (1961), The effect of the time constant of radiosonde sensors on the measurement of temperature and humidity discontinuities in the atmosphere, Bull. Am. Meteorol. Soc. **42**, No. 5, 317–321.

Willett, H. C. (1944), Descriptive Meteorology (Academic Press, Inc., New York, N. Y.).

10. Appendix A. World Maps of $N(z)$ Parameters

Data from the weather stations listed alphabetically in table A–1 were used to prepare the maps in this appendix. Each station is preceded by a number to identify its location on figure A–1 and followed by a listing of surface refractivity values at the 1, 5, 50, 95, and 99 percent cumulative distribution levels for the 4 months of February, May, August, and November.

The $N(z)$ parameters (all referenced to sea level) which are necessary to calculate N at any altitude, z, in kilometers, are D_0, W_0, H_1, H_2, H_w, and z_t. These are given in figures A–2 through A–25. The z_t chart for any particular month will determine which of the dry-term curves will be used. If the desired altitude (above sea level) of $N(z)$ is *below* the z_t value at the specified location, use the tropospheric equation

$$N(z) = D_0 \exp\left\{-\frac{z}{H_1}\right\} + W_0 \exp\left\{-\frac{z}{H_w}\right\} . \tag{A–1}$$

If the desired altitude is *above* the z_t value, use

$$N(z) = D_0 \exp\left\{-\frac{z_t}{H_1} - \frac{(z - z_t)}{H_2}\right\} + W_0 \exp\left\{-\frac{z}{H_w}\right\} . \tag{A–2}$$

All three scale heights are required for equation (A–2), whereas only two, H_1 and H_w, appear in the tropospheric equation. If the surface altitude of the location is greater than 1 km, it is suggested that the "standard atmosphere" value of *3 km* be substituted for H_w (see sec. 3.3).

To illustrate the step-by-step procedure for determining refractivity from the $N(z)$ parameters, the following example (assuming heights of 2 km and 20 km above the surface at a location 200 m above sea level, at latitude 15°N and longitude 0°, in August) is given:

(a) Refractivity at 2 km above the surface:

(1) At the assumed location, interpolate linearly between contours on figures A–19 to obtain z_t (13.8 km) to see whether the altitude above sea level, z (2.2 km), is above or below the z_t value. It is below, so equation (A–1) should be used.

(2) The map values at 15°N and 0° of the parameters needed to calculate (A–1) are:

$D_0 = 267.5$ N-units	(fig. A–14)
$W_0 = 105.0$ N-units	(fig. A–15)
$H_1 = 9.35$ km	(fig. A–16)
$H_w = 2.19$ km	(fig. A–18)

(3) If these values are substituted in (A–1), $N(z)$ is found to be 249.9 N-units at 2 km above the surface. (Probable errors due to contouring and data restrictions would suggest the use of only three significant figures, i.e., 250 N-units.)

(b) Refractivity at 20 km above surface:

(1) Check to see whether the assumed altitude ($z = 20.2$ km above sea level) is above or below the z_t value. Since it is above, (A–2) should be used.

(2) All the parameters are needed for this calculation. In addition to the four values listed in calculation (a) above, these are required:

$H_2 = 5.90$ km	(fig. A–17)
$z_t = 13.8$ km	(fig. A–19)

TABLE A-1. *Cumulative distribution levels (in percent) of surface refractivity*

Ident. No.	Station	Elevation (meters)	Latitude	Longitude	February					May					August					November				
					1	5	50	95	99	1	5	50	95	99	1	5	50	95	99	1	5	50	95	99
1.	Abidjan, Ivory Coast	15	05 15N	03 56W	405.0	401.2	390.3	373.0	356.7	397.5	396.2	387.5	377.0	365.1	384.2	381.5	375.2	366.2	361.0	399.2	396.7	385.4	377.9	358.5
2.	Adelaide, Australia	11	34 56S	138 35E	365.9	343.0	314.0	285.7	282.2	349.3	340.2	324.7	307.2	299.6	334.4	330.8	317.8	303.5	295.3	346.1	340.3	310.2	284.9	281.6
3.	Aden, Arabia	4	12 50N	45 01E	391.3	377.9	357.1	336.5	315.5	411.3	397.8	381.9	342.9	308.7	400.6	393.1	366.6	338.5	323.7	381.2	376.3	360.2	335.8	314.1
4.	Amundsen-Scott, Antarctica*	2800	90 00S	00 00	239.6	234.6	226.5	216.8	211.9	262.3	257.0	244.2	233.8	227.3	259.2	256.7	246.0	236.1	231.8	234.6	233.5	227.2	216.9	214.3
5.	Anchorage, Alaska	40	61 10N	149 59W	322.0	317.5	307.2	299.8	293.5	322.5	318.9	308.9	296.2	292.8	339.6	336.3	324.3	308.5	297.3	315.3	314.2	306.6	298.7	295.6
6.	Antofagasta, Chile	137	23 25S	70 28W	357.6	352.8	344.9	334.0	325.2	339.5	338.7	331.8	324.4	322.6	340.2	335.9	328.6	319.8	310.2	342.6	341.5	334.8	325.9	321.4
7.	Aoulef, Algeria	290	26 58N	01 05E	326.4	303.7	284.4	269.2	266.1	296.2	290.2	275.8	268.4	267.4	313.2	302.3	275.9	270.9	270.1	332.2	309.3	288.8	269.8	268.3
8.	Argentia, Newfoundland	17	47 18N	54 00W	329.2	323.8	309.4	300.4	297.7	338.8	329.1	315.8	305.2	299.8	367.1	357.2	337.5	322.6	316.3	343.7	334.7	316.7	305.4	302.2
9.	Ascension Island	79	07 58S	14 24W	378.2	371.6	360.0	347.0	339.1	375.8	370.3	358.4	344.1	335.4	362.5	357.9	346.6	331.0	327.5	368.2	360.9	350.4	336.4	331.2
10.	Athinai, Greece	9	37 54N	23 44E	335.8	330.6	317.6	306.8	299.1	349.6	343.9	331.9	317.7	311.3	364.5	357.5	332.1	313.2	305.5	357.2	351.1	333.4	317.6	313.4
11.	Atlanta, Ga.	309	33 39N	84 25W	348.1	337.3	308.3	294.3	289.4	367.1	360.9	340.1	296.8	289.3	378.3	372.3	357.0	328.3	315.7	349.0	341.5	307.2	292.1	281.1
12.	Bahrain Island	2	26 16N	50 38E	366.1	361.5	338.0	315.3	308.6	409.2	396.7	373.5	341.6	329.6	429.6	423.6	392.5	361.2	359.3	388.7	382.4	357.4	332.1	317.7
13.	Balboa (Albrook), Panama C.Z.	9	08 58N	79 33W	382.3	378.0	367.8	353.7	345.1	393.5	390.2	381.7	369.7	364.3	394.1	391.0	383.0	371.7	365.0	394.5	389.3	381.1	370.1	351.6
14.	Bangui, Central African Republic	385	04 23N	18 34E	371.8	366.3	352.8	319.7	299.1	375.1	369.3	359.6	341.3	338.5	369.3	366.4	359.6	344.6	340.7	374.1	366.0	357.9	339.2	321.0
15.	Barrow, Alaska	4	71 18N	156 47W	351.4	343.0	328.9	314.6	310.7	321.0	318.5	314.5	310.4	308.7	334.0	329.7	318.1	312.0	308.8	334.8	332.2	315.4	307.4	305.6
16.	Beograd, Yugoslavia	243	44 47N	20 32E	325.0	319.2	308.8	297.8	290.1	343.5	337.2	322.7	304.0	295.0	357.4	347.4	328.8	311.1	300.4	329.0	324.9	312.6	303.9	284.1
17.	Bitburg, Germany	366	49 57N	06 34E	308.4	305.2	299.0	288.9	285.3	319.7	318.4	300.9	289.4	286.6	339.0	332.4	318.1	304.8	298.9	362.2	316.0	303.6	296.4	292.2
18.	Bordeaux, France	48	44 51N	00 42W	337.7	332.0	320.9	308.4	304.5	353.7	345.5	332.5	320.0	312.5	366.8	359.8	344.4	332.9	324.8	343.1	336.4	323.6	316.1	313.8
19.	Brownsville, Tex.	6	25 55N	97 28W	375.5	371.6	351.9	314.0	304.4	393.7	389.5	372.4	338.2	325.2	396.4	391.9	381.2	367.6	354.4	382.9	376.8	348.8	312.0	305.6
20.	Calcutta, India	6	22 39N	88 27E	376.8	372.4	343.9	322.3	313.9	420.9	414.0	395.4	366.8	354.4	412.0	406.6	396.3	385.0	378.1	387.9	381.1	357.3	341.4	334.4
21.	Canton Island	3	02 46S	171 43W	385.4	382.2	371.0	361.8	355.9	395.2	391.8	379.5	366.8	363.1	398.1	390.3	375.6	363.7	360.2	388.2	383.9	369.1	358.3	353.8
22.	Caribou, Maine	191	46 52N	68 01W	319.2	313.3	305.7	297.8	294.7	338.1	327.8	307.7	294.8	290.0	364.4	354.0	327.3	310.6	304.6	334.2	319.8	307.7	298.7	296.1
23.	Charleston, S. C.	14	32 54N	80 02W	358.3	352.3	326.4	304.7	299.3	384.5	378.4	356.1	320.6	309.7	397.3	389.7	376.6	351.2	337.2	367.7	359.6	325.9	304.8	298.9
24.	Chatham Island	49	45 58S	176 33W	357.6	356.2	339.6	320.0	317.5	339.8	337.8	324.5	307.1	297.2	335.5	334.6	322.3	310.5	304.0	348.1	345.1	331.9	315.2	313.2
25.	Chita, U.S.S.R.	671	52 05N	113 29E	310.4	307.8	297.3	287.0	282.6	299.4	295.6	281.4	268.2	259.0	335.2	327.9	309.9	289.9	277.8	308.2	304.1	291.6	282.4	279.1
26.	Clark Field, the Philippines	149	15 01N	120 33E	375.3	368.3	348.8	329.7	318.0	391.9	382.1	365.4	343.3	333.1	395.1	387.3	372.8	358.8	347.5	384.1	377.2	360.7	338.2	328.0
27.	Cocoa Beach, Fla.	5	28 14N	80 36W	372.7	367.4	344.2	317.2	309.4	391.2	385.5	367.0	334.1	321.8	402.5	395.7	383.8	367.8	356.7	380.3	373.9	351.7	317.8	311.0
28.	Columbia, Mo.	239	38 58N	92 22W	331.8	319.0	303.8	294.8	290.1	363.2	351.5	325.2	300.4	293.4	375.2	368.3	344.4	317.4	310.6	336.9	327.0	303.4	292.3	285.5
29.	Coppermine, Northwest Territories	9	67 49N	115 15W	345.9	341.8	328.6	319.6	312.9	316.4	316.3	313.5	308.9	306.3	363.8	354.7	327.4	308.6	279.5	338.7	331.3	313.1	306.6	305.4
30.	Coral Harbour, Northwest Territories	59	64 12N	83 22W	341.2	339.8	329.0	311.8	306.6	321.8	317.1	311.1	306.8	304.9	337.2	327.8	316.2	306.8	300.3	326.9	323.8	312.6	304.3	300.1
31.	Curacao Island	8	12 11N	68 58W	381.0	378.8	368.3	359.8	352.5	394.1	390.0	378.0	366.0	361.7	397.7	393.0	382.4	372.4	365.1	391.6	386.8	378.2	368.9	362.9
32.	Dakar, Senegal	22	14 44N	17 30W	367.6	363.5	346.0	319.7	290.0	378.6	373.4	358.4	343.3	335.8	398.2	393.9	381.7	364.8	358.2	388.0	381.8	365.5	339.2	327.5
33.	Darwin, Australia	27	12 26S	130 52E	410.8	402.2	377.6	355.1	329.3	396.9	390.8	359.5	327.0	324.7	380.3	366.3	341.7	285.5	280.8	391.8	388.0	364.8	337.9	333.5
34.	Denver, Colo.	1625	39 46N	104 53W	262.5	259.2	251.8	241.4	235.9	282.4	277.5	260.7	238.8	232.0	304.2	296.9	273.8	250.0	244.1	268.2	262.2	253.1	242.2	240.3
35.	El Paso, Tex.	1194	31 48N	106 24W	290.4	281.8	263.4	250.0	243.4	296.7	288.6	256.2	238.2	232.9	324.7	318.2	294.5	264.8	255.0	289.4	282.6	264.8	253.9	247.4
36.	Ezeiza, Argentina*	20	34 50S	58 32W	379.6	370.4	346.8	325.4	320.4	364.4	354.8	328.7	318.3	284.3	340.2	338.7	323.2	312.7	311.5	364.9	357.4	342.2	320.6	309.7
37.	Fairbanks, Alaska*	138	64 49N	147 52W	342.8	335.3	311.0	294.1	290.9	323.3	318.3	302.2	284.9	280.5	336.5	332.7	319.3	302.1	293.7	314.3	310.8	301.2	294.2	291.7
38.	Ft. Lamy, Chad	300	12 08N	15 02E	332.5	326.3	297.8	280.0	274.8	365.3	361.2	344.9	296.5	281.2	378.2	377.7	369.3	358.8	355.6	368.1	361.4	312.7	285.7	274.3
39.	Ft. Smith, Northwest Territories	203	60 01N	112 00W	352.4	336.4	316.5	301.9	299.3	320.3	315.2	302.9	289.6	285.1	352.0	338.3	320.6	305.3	295.3	322.9	320.5	307.0	300.3	295.9
40.	Ft. Trinquet, Mauritania	359	25 14N	11 37W	324.0	318.8	291.7	270.9	265.8	327.5	317.7	300.2	267.1	265.7	357.4	338.6	296.8	265.8	260.8	332.9	326.3	306.4	272.9	267.5
41.	Gough Island*	40	40 21S	09 53W	357.0	354.5	332.1	320.2	319.0	346.4	346.1	325.8	312.8	310.6	342.6	340.1	324.7	310.1	308.1	349.6	338.5	322.6	311.7	304.3
42.	Guryev, U.S.S.R.	−21	47 07N	51 55E	—	327.4	317.2	297.4	—	350.0	340.9	320.1	298.8	292.2	380.2	365.3	330.5	300.0	299.1	335.9	326.6	318.2	300.2	289.8
43.	Hilo, Hawaii	11	19 44N	155 04W	368.4	365.1	351.6	333.4	329.0	373.2	370.5	358.4	345.0	336.8	383.4	378.9	364.1	348.5	342.3	378.2	374.2	359.0	339.2	332.9
44.	Hong Kong	66	22 18N	114 10E	371.7	367.3	332.7	308.4	295.9	400.7	394.8	378.9	349.8	333.6	402.7	395.1	385.8	370.1	361.1	379.8	369.2	340.5	305.9	298.0
45.	Invercargill, New Zealand	1	46 25S	168 19E	351.7	345.4	327.3	312.4	307.3	337.9	334.0	322.0	310.7	307.4	333.7	329.3	317.9	306.3	301.8	342.0	335.7	322.2	308.9	304.3
46.	Isachsen, N.W.Territories	31	78 47N	103 32W	355.8	348.7	333.3	317.3	310.3	322.4	319.8	313.6	307.9	306.2	326.6	321.9	314.4	307.1	286.0	341.4	336.5	321.5	310.5	306.5
47.	Joliet, Ill.	179	41 30N	88 10W	319.7	316.3	308.4	301.7	299.4	351.5	346.4	319.9	304.4	294.0	391.1	369.6	342.5	319.7	306.5	333.8	322.1	306.8	299.8	297.0
48.	Karaganda, U.S.S.R.	555	49 48N	73 08E	310.1	305.9	296.3	291.5	287.6	315.7	309.8	298.0	276.0	270.8	329.7	324.3	307.7	286.5	277.6	305.7	303.0	297.6	291.4	288.5
49.	Key West, Fla.	3	24 34N	81 47W	382.3	376.5	359.2	324.2	315.7	391.8	387.5	373.9	348.6	335.7	404.9	394.2	382.9	367.4	358.7	391.0	384.7	365.8	337.0	328.7
50.	Khartoum, Sudan	385	15 36N	32 33E	307.2	295.3	284.8	273.4	268.8	345.7	336.9	284.1	264.1	259.3	374.1	369.7	355.6	334.3	298.4	322.4	315.9	299.4	283.8	280.2
51.	Koror, Palau Islands	29	07 20N	134 29E	394.6	392.6	384.6	374.4	368.2	398.1	395.2	388.0	379.4	378.0	396.8	393.7	386.2	378.0	372.8	399.0	395.4	388.3	380.9	377.3
52.	Lae, New Guinea*	12	06 45S	146 59E	408.6	388.3	377.0	355.9	345.4	394.0	392.9	382.3	363.3	359.1	394.1	384.7	376.4	360.8	355.3	416.7	396.2	379.8	364.1	355.5
53.	Lihue, Hawaii	36	21 59N	159 21W	368.0	363.4	351.1	330.8	324.3	368.5	365.5	355.1	337.8	331.8	379.3	375.6	362.6	351.3	347.1	378.8	373.0	360.5	348.1	338.9
54.	Lima, Peru	135	12 06S	77 02W	377.7	368.9	357.7	346.3	341.6	354.6	351.9	344.5	337.5	334.7	342.8	341.3	337.9	331.4	328.2	351.3	348.5	343.0	335.8	330.2
55.	Long Beach, Calif.	20	33 49N	118 09W	342.2	334.4	316.6	296.8	292.3	344.6	340.6	331.0	310.6	295.9	361.3	353.5	343.4	330.7	313.2	349.6	344.7	329.2	304.3	291.8

56.	Lourenco Marques, Portuguese East Africa.	44	25	55S	32	34E	391.9	386.1	370.6	352.2	346.4	370.3	363.3	347.0	321.1	318.7	358.4	353.9	336.4	303.6	280.1	386.4	378.4	359.1	342.1	319.7
57.	Luanda, Portuguese West Africa	70	08	49S	13	13E	386.5	381.9	368.3	352.2	342.3	387.6	383.7	364.7	349.1	343.3	361.2	357.6	349.7	335.9	330.8	386.7	383.8	371.6	359.0	351.9
58.	Lvov, U.S.S.R.	329	49	49N	23	57E	315.9	312.0	303.7	296.0	289.6	334.3	331.0	314.0	300.4	297.6	346.9	343.6	329.3	316.0	305.0	325.3	321.4	310.5	302.0	298.4
59.	Macquarie Island	6	54	30S	158	57E	329.0	326.8	315.1	301.3	298.6	328.3	324.7	312.4	298.2	297.2	324.4	322.2	314.3	300.2	294.9	323.3	321.0	310.0	298.5	293.9
60.	Madrid, Spain	601	40	28N	03	34W	315.3	311.2	299.4	284.5	283.0	319.4	316.4	302.7	282.8	282.6	326.5	324.4	291.5	272.5	261.7	309.4	308.1	299.2	290.6	287.1
61.	Majuro Island	3	07	05N	171	23E	390.3	389.0	381.2	367.1	363.3	398.4	394.3	386.6	377.3	371.6	398.1	396.2	385.7	375.3	369.8	400.6	394.9	387.2	376.3	372.7
62.	Marion Island	26	46	53S	37	52E	336.4	332.1	318.5	307.5	305.3	328.0	324.8	313.6	303.3	299.3	329.7	326.8	312.9	303.9	302.1	329.1	324.8	313.3	304.7	300.2
63.	Mazatlan, Mexico	78	23	11N	106	26W	370.1	365.9	351.4	328.2	315.1	384.7	378.3	365.7	352.6	344.3	405.9	400.2	384.7	371.0	367.3	386.2	381.9	364.2	341.6	334.9
64.	Miami, Fla.	4	25	49N	80	17W	376.4	371.1	350.3	319.8	310.2	386.5	383.8	367.0	341.2	330.6	394.2	389.5	377.6	361.1	357.4	378.5	375.0	351.6	322.3	309.1
65.	Midway Island	13	28	13N	177	23W	365.0	361.4	339.9	317.8	313.7	376.9	372.2	351.0	328.0	322.7	389.0	384.3	372.2	357.2	352.6	383.6	379.8	358.8	332.0	324.9
66.	Moosonee, Ontario	10	51	16N	80	39W	335.2	330.5	317.2	306.4	304.5	328.3	320.8	314.6	303.2	298.3	360.8	352.7	331.8	320.4	316.3	331.0	318.9	313.2	306.5	304.8
67.	Moscow, U.S.S.R.	156	55	49N	37	37E	323.2	319.1	306.3	295.5	280.5	336.3	332.6	312.8	295.0	292.3	347.6	342.3	326.8	306.0	297.8	322.9	318.9	309.3	286.4	277.8
68.	Mount Clemens, Mich.*	176	42	36N	86	56W	315.7	311.1	304.2	298.9	297.5	339.0	333.6	311.0	295.6	292.9	371.0	361.6	333.8	311.2	302.8	326.8	323.0	306.7	297.9	293.7
69.	Nairobi, Kenya	1798	01	18S	36	45E	302.2	297.9	285.2	249.1	246.6	310.3	306.7	296.9	271.8	259.5	298.0	294.7	283.8	263.8	254.2	308.1	302.9	293.4	263.5	251.3
70.	Nandi, Fiji Islands	16	17	45S	177	27E	402.7	394.7	383.6	374.0	365.2	383.0	380.4	367.7	349.3	338.7	381.2	376.9	358.9	337.4	329.1	389.2	384.4	371.7	349.3	343.4
71.	Nantucket, Mass.	14	41	15N	70	04W	329.3	326.3	314.9	303.6	300.5	347.9	341.9	326.8	308.2	302.5	382.4	376.0	356.8	329.2	319.4	347.6	342.2	321.0	305.0	300.4
72.	New Delhi, India	216	28	35N	77	12E	329.4	327.3	314.9	301.6	297.2	345.6	342.2	319.1	295.2	280.1	398.7	396.7	385.6	370.8	363.8	354.6	340.4	324.3	310.2	300.0
73.	New York, N.Y.	5	40	39N	73	47W	332.3	324.1	308.8	300.1	295.6	358.9	352.4	323.4	299.8	294.5	385.0	379.8	348.9	316.5	309.9	359.6	339.3	313.5	300.9	295.3
74.	Niamey, Niger*	226	13	29N	02	10E	302.6	301.0	287.4	279.7	279.2	374.8	371.7	352.8	304.5	296.5	384.1	382.4	371.8	362.8	319.8	361.8	356.9	322.3	294.9	290.1
75.	Nicosia, Cyprus	218	35	09N	33	17E	330.2	326.5	312.3	294.4	287.6	348.0	341.9	313.7	280.4	270.4	374.2	365.7	326.9	281.2	267.4	349.1	337.7	314.5	293.9	287.6
76.	Nouvelle Amsterdam Island	28	37	50S	77	34E	374.9	365.6	343.7	317.5	312.8	355.9	353.6	332.6	314.5	306.0	345.0	340.4	327.8	312.7	308.8	351.3	348.8	333.8	313.0	307.0
77.	Odessa, U.S.S.R.	64	46	29N	30	38E	323.4	320.9	314.5	307.1	304.0	354.3	346.9	329.1	312.0	305.3	372.4	367.4	337.2	313.7	307.4	344.4	336.4	321.8	309.9	306.5
78.	Okhotsk, U.S.S.R.	7	59	22N	143	12E	329.6	326.9	315.3	306.4	298.8	322.4	320.6	313.7	298.5	295.4	347.9	345.6	336.1	314.3	298.9	322.2	319.5	311.6	302.3	296.6
79.	Ostersund, Sweden	309	63	11N	14	37E	310.8	308.8	299.7	291.7	288.3	322.1	314.2	303.7	293.8	289.5	335.2	328.3	316.7	304.3	299.9	312.1	310.0	303.9	296.7	293.7
80.	Perth, Australia	60	31	57S	115	49E	362.0	344.8	316.4	284.7	281.5	360.3	345.5	321.1	298.5	290.4	345.6	338.9	320.5	301.6	294.6	350.4	337.3	315.8	289.2	283.4
81.	Pittsburgh, Pa.*	351	40	30N	80	13W	314.4	311.8	295.7	284.8	279.5	339.8	335.8	309.2	286.7	281.2	358.4	354.6	333.4	306.2	302.7	—	317.0	300.0	292.2	—
82.	Port Lyautey, Morocco	12	34	18N	06	36W	349.6	343.6	328.5	306.7	295.4	363.1	357.0	338.9	315.8	290.7	376.4	372.4	356.3	329.9	318.8	356.4	353.5	337.9	313.2	300.5
83.	Puerto Montt, Chile	6	41	29S	72	51W	354.7	349.5	335.6	321.8	315.6	345.5	339.2	326.5	317.4	311.6	335.6	331.9	323.6	315.6	310.9	343.6	340.5	330.2	319.7	315.0
84.	Raoul Island	49	29	15S	177	55W	382.7	377.9	352.0	335.2	324.1	372.1	367.3	343.2	323.3	319.8	360.5	355.1	331.5	313.2	309.4	365.2	362.0	342.0	323.9	317.8
85.	Recife, Brazil	10	08	07S	34	55W	396.8	389.4	373.1	350.6	345.4	398.3	392.2	376.8	358.7	343.9	392.5	383.5	366.8	349.1	343.6	394.1	384.2	365.4	342.7	329.5
86.	Sable Island, Nova Scotia	3	46	56N	60	02W	325.3	321.3	312.0	305.6	301.9	336.6	333.2	324.5	315.9	311.8	371.4	365.8	351.1	336.2	327.1	345.5	339.9	319.8	309.0	304.9
87.	Saigon, Viet Nam	10	10	49N	106	40E	385.5	383.2	367.6	343.6	330.7	403.6	399.1	390.8	380.4	375.1	399.1	396.5	387.9	378.1	371.8	395.7	391.1	379.8	356.3	342.1
88.	San Diego, Calif.	9	32	44N	117	10W	343.5	339.5	326.9	307.2	293.5	346.1	342.3	332.7	315.8	295.4	364.0	359.1	349.3	335.4	330.0	350.0	346.2	327.5	288.6	282.7
89.	San Juan, P. R.	19	18	26N	66	00W	373.6	371.0	359.0	340.7	334.1	387.5	384.1	374.2	357.4	347.9	394.1	390.0	379.0	366.7	359.8	390.4	385.0	372.6	355.2	348.8
90.	Seattle, Wash.	15	47	41N	122	16W	330.2	327.1	317.9	306.2	300.7	341.1	333.2	322.2	306.3	299.8	348.1	343.9	333.9	320.0	314.4	336.2	332.4	323.6	312.9	305.2
91.	Shemya, Alaska	37	52	43N	174	06E	320.7	316.2	306.2	298.4	296.9	322.2	319.2	311.4	302.9	299.8	343.5	336.9	326.3	315.8	307.6	322.7	318.0	306.2	297.4	294.2
92.	Singapore	18	01	21N	103	54E	388.0	385.4	378.5	369.0	367.0	401.0	396.5	388.4	376.8	338.0	394.5	392.9	386.0	376.2	330.6	391.7	388.8	382.4	374.2	364.5
93.	Stanley, Falkland Islands	53	51	42S	57	52W	334.7	331.8	318.0	303.8	299.3	328.1	324.6	314.9	306.8	302.6	321.5	320.5	314.0	305.3	303.0	331.5	324.8	315.8	301.6	295.5
94.	Swan Island	10	17	24N	83	56W	380.4	378.0	368.4	341.8	333.4	396.3	390.8	380.0	353.4	340.7	394.9	393.0	386.7	379.4	377.4	395.2	391.0	379.5	351.0	342.0
95.	Syktyvkar, U.S.S.R.*	96	61	40N	50	51E	328.5	318.6	308.0	300.6	298.0	328.0	321.4	309.5	295.9	292.4	358.3	348.9	324.0	308.6	305.2	328.7	320.7	313.3	303.6	301.5
96.	Tananarive, Malagasy Republic*	1310	18	54S	47	32E	362.3	325.0	318.3	300.4	259.7	326.1	312.8	302.5	294.4	290.6	311.8	307.9	298.2	292.1	276.2	320.2	317.9	311.0	302.0	289.6
97.	Tashkent, U.S.S.R.	428	41	16N	69	16E	310.9	306.5	296.9	280.0	276.4	331.8	321.6	306.4	289.8	283.9	327.4	315.9	300.9	288.0	280.1	312.7	309.7	299.9	279.6	276.0
98.	Tateno, Japan	27	36	03N	140	08E	326.9	322.8	313.0	300.0	295.2	371.4	364.2	341.7	313.7	306.6	397.4	394.2	380.7	356.2	351.8	350.1	344.0	326.1	310.9	303.5
99.	Tatoosh Island, Wash.	26	48	23N	124	44W	331.9	328.2	318.9	304.3	299.8	336.0	333.9	326.4	317.0	311.1	348.2	344.5	337.9	331.2	329.2	340.9	335.5	322.7	307.9	303.0
100.	Townsville, Australia	4	19	16S	146	45E	400.2	391.3	365.5	338.2	329.4	378.6	370.0	343.2	313.6	295.4	362.6	356.9	333.0	306.7	285.6	383.0	376.4	354.6	318.3	281.7
101.	Tripoli, Libya	10	32	54N	13	17E	339.5	335.3	321.0	295.7	285.1	367.9	361.3	342.3	307.4	284.4	395.8	387.1	364.2	330.9	311.0	364.2	351.6	329.2	306.0	290.8
102.	Tura, U.S.S.R.*	147	64	16N	100	14E	358.2	348.5	324.9	305.2	301.4	316.2	310.6	300.8	290.3	284.5	343.4	336.7	318.4	298.6	292.8	343.3	338.7	319.2	304.6	301.6
103.	Verkhoyansk, U.S.S.R.*	135	67	33N	133	23E	366.2	359.2	342.4	322.5	314.9	311.8	309.8	300.2	289.8	287.3	340.8	335.0	313.5	303.0	297.8	352.9	351.7	336.2	314.8	307.9
104.	Vladivostok, U.S.S.R.	138	43	07N	131	54E	317.2	313.8	309.1	303.4	294.4	334.3	330.1	316.8	298.1	291.3	376.9	371.3	353.4	330.8	314.4	322.9	321.1	308.0	300.1	295.2
105.	Wake Island	4	19	17N	166	39E	383.0	377.2	360.9	338.9	330.0	387.5	384.0	373.6	354.1	344.2	395.3	391.6	382.1	370.8	364.0	393.3	388.9	376.5	361.1	355.3
A.	Ship A*	‡	62	00N	33	00W	328.8	325.9	307.0	293.9	292.1	330.0	327.0	318.6	309.7	282.7	335.8	333.4	324.9	313.5	276.7	330.0	326.8	309.8	297.9	294.5
C.	Ship C	‡	52	45N	35	30W	332.3	329.9	312.9	302.9	298.8	339.7	335.3	320.8	308.6	305.9	355.2	348.9	332.0	318.6	316.3	338.3	335.7	318.5	304.8	302.1
D.	Ship D	‡	44	00N	41	00W	349.8	344.9	318.9	306.5	303.7	358.2	355.4	329.8	312.1	308.3	383.2	378.0	358.5	331.8	323.7	362.1	355.4	327.6	311.3	308.6
J.	Ship J	‡	52	30N	20	00W	337.2	332.9	317.5	301.7	297.6	340.8	339.3	321.5	312.7	308.8	359.5	357.7	345.3	324.1	318.6	346.1	344.2	331.2	315.6	293.9
K.	Ship K	‡	45	00N	16	00W	343.4	340.6	325.1	311.1	308.8	352.8	350.3	336.5	319.2	314.5	371.5	366.7	349.5	330.1	325.3	351.9	347.0	331.3	315.9	310.4
M.	Ship M	‡	66	00N	02	00E	323.6	321.1	311.7	304.9	302.8	333.8	330.9	319.8	307.7	304.5	341.9	338.4	327.6	313.6	310.4	330.0	327.0	315.8	303.7	297.9
V.	Ship V	‡	34	00N	164	00E	356.4	350.8	323.6	311.0	308.5	374.5	370.3	351.7	322.9	317.0	393.0	390.9	378.4	351.3	338.5	379.0	375.1	344.8	323.1	318.5

**Less than 3 years of data.*
‡ No elevation given.

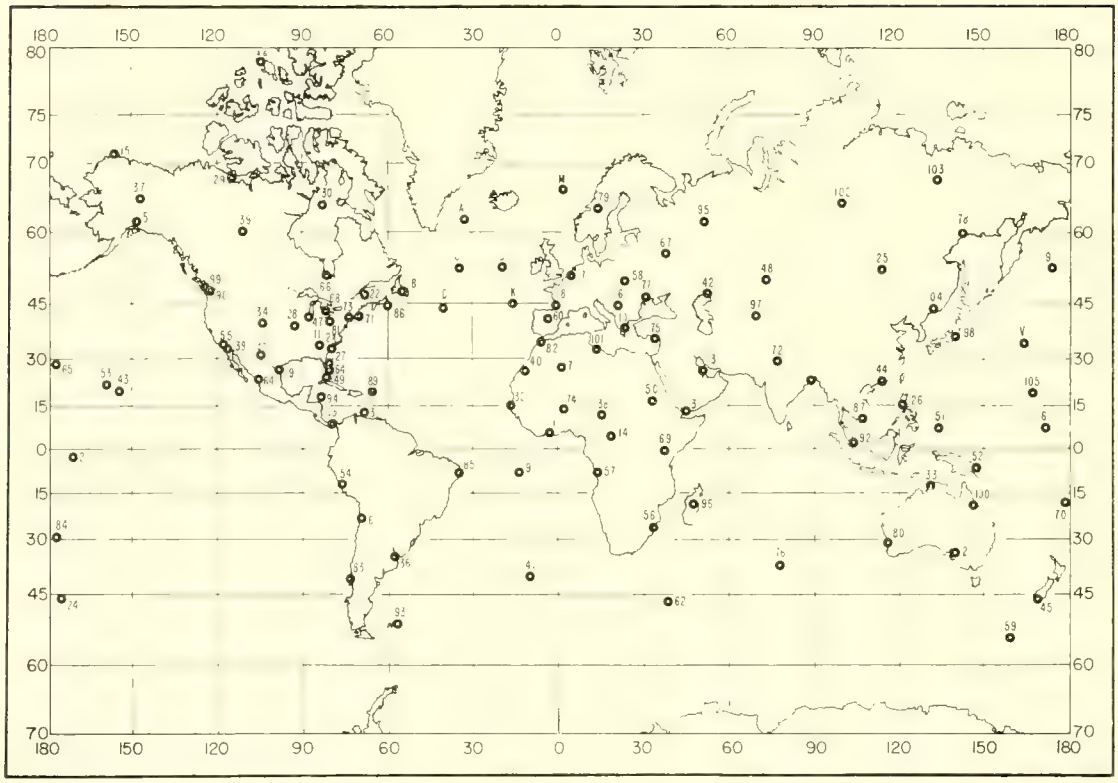

FIGURE A-1. *Location of* N(z) *data stations.*

(3) If these values are substituted in (A–2), $N(z)$ is found to be 20.7 N-units at 20 km above the surface.

Figures A–26 through A–29 are seasonal maps of the standard prediction error of the exponential fits to the mean wet-term profiles used in the $N(z)$ parameter maps. An rms error in the wet term of more than 5 N-units was considered to be a reasonable limiting criterion for locations where the $N(z)$ model should be used with caution, if at all. Figure A–30 delineates these areas; the cross-hatched areas indicate that the error was in excess of 5 N-units for 2 or more of the seasonal months (February, May, August, and November) and the single-hatching depicts areas where only 1 of the 4 months showed such large errors. Further discussion of the uncertainty in these areas can be found in section 3.4.

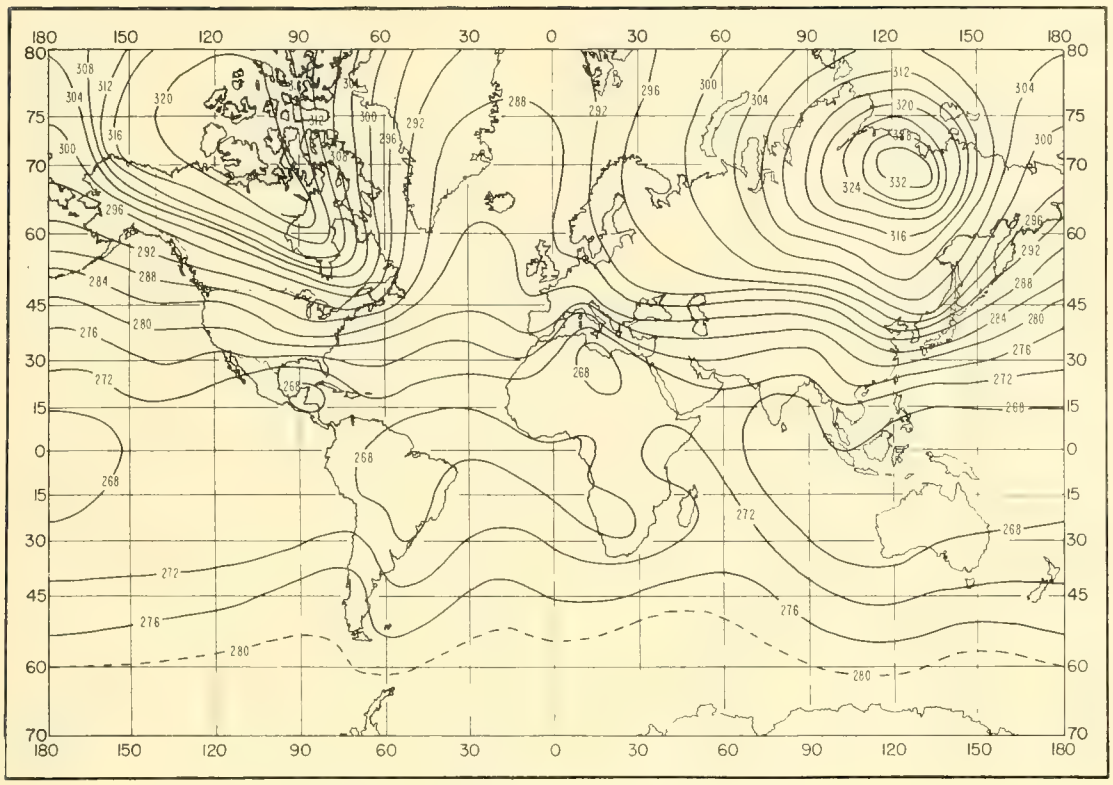

FIGURE A-2. *Mean sea-level dry term,* D_o: *February.*

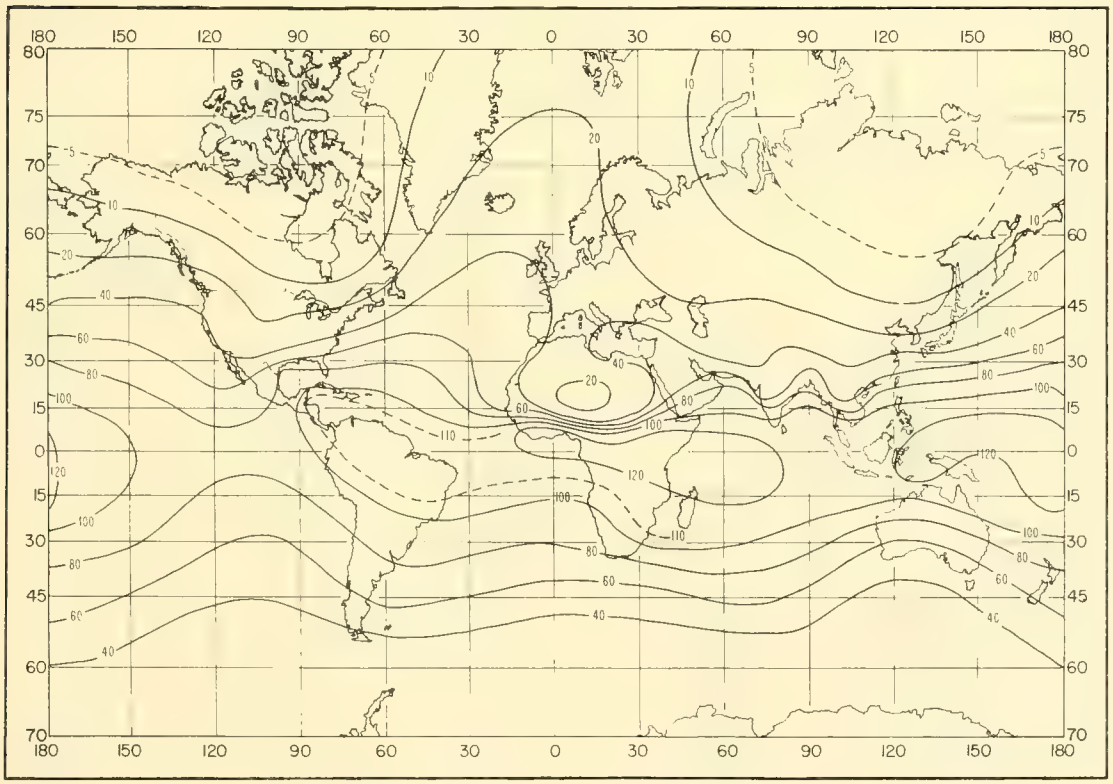

FIGURE A-3. *Mean sea-level wet term,* W_o: *February.*

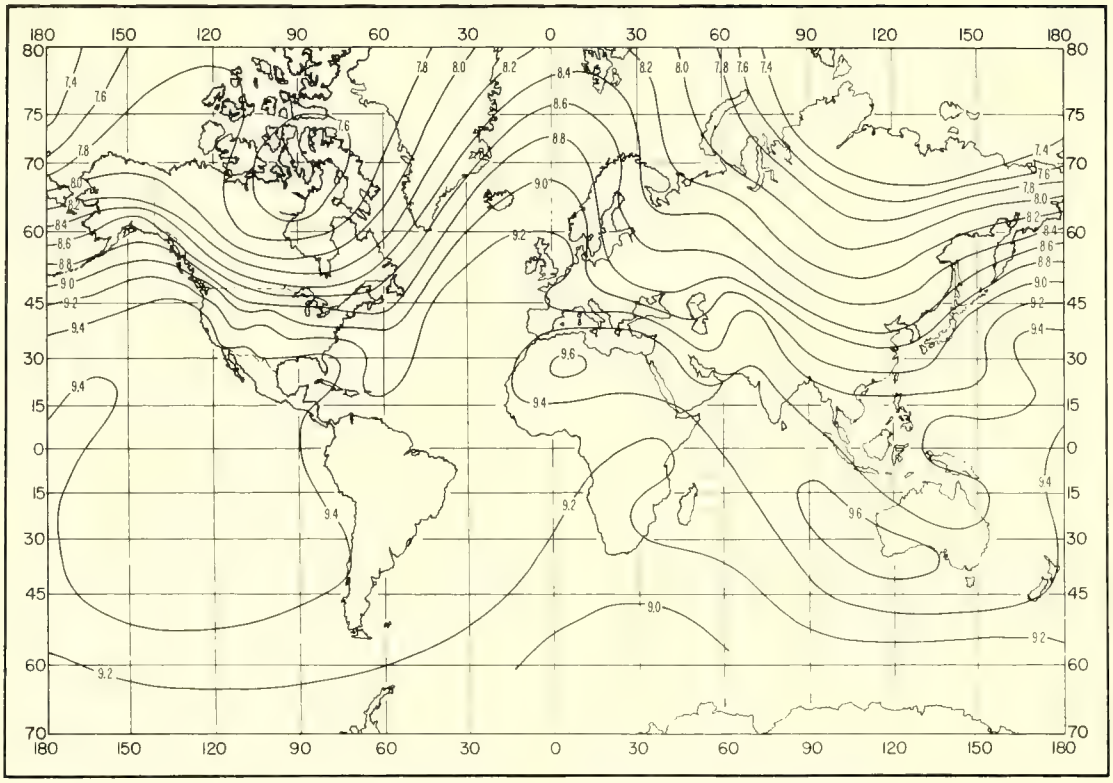

FIGURE A-4. *Dry-term tropospheric scale height in km,* H_1: *February.*

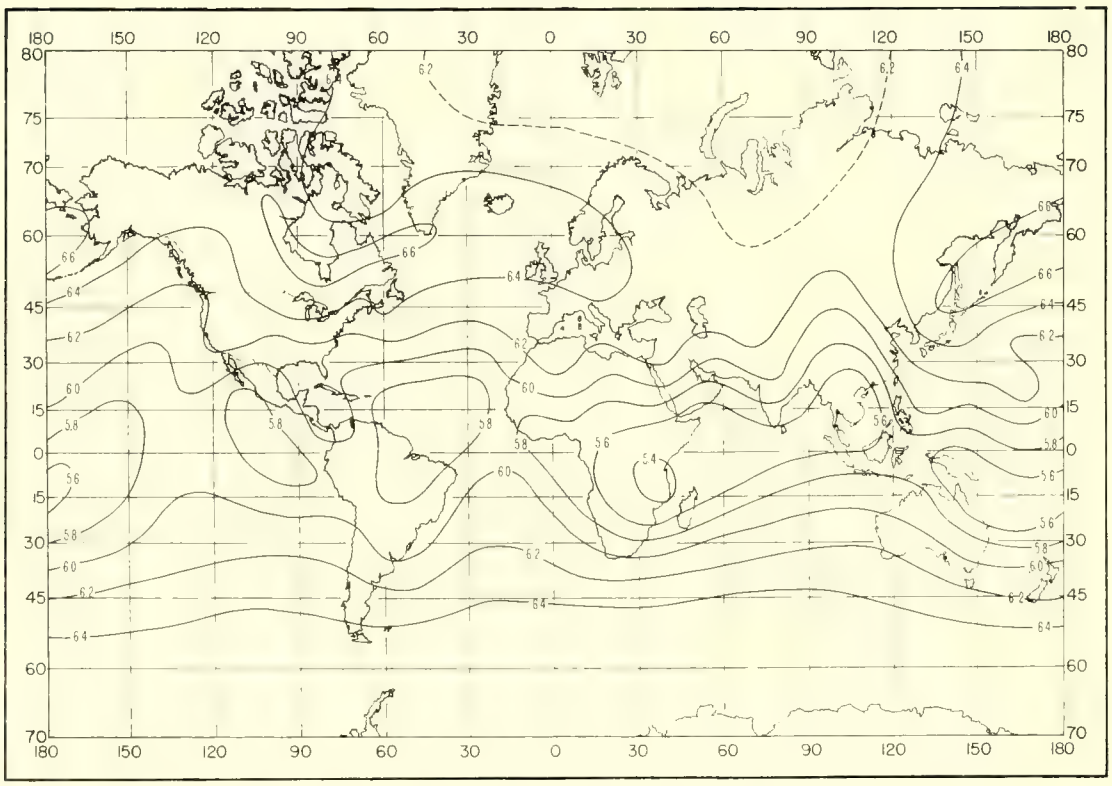

FIGURE A-5. *Dry-term stratospheric scale height in km,* H_2: *February.*

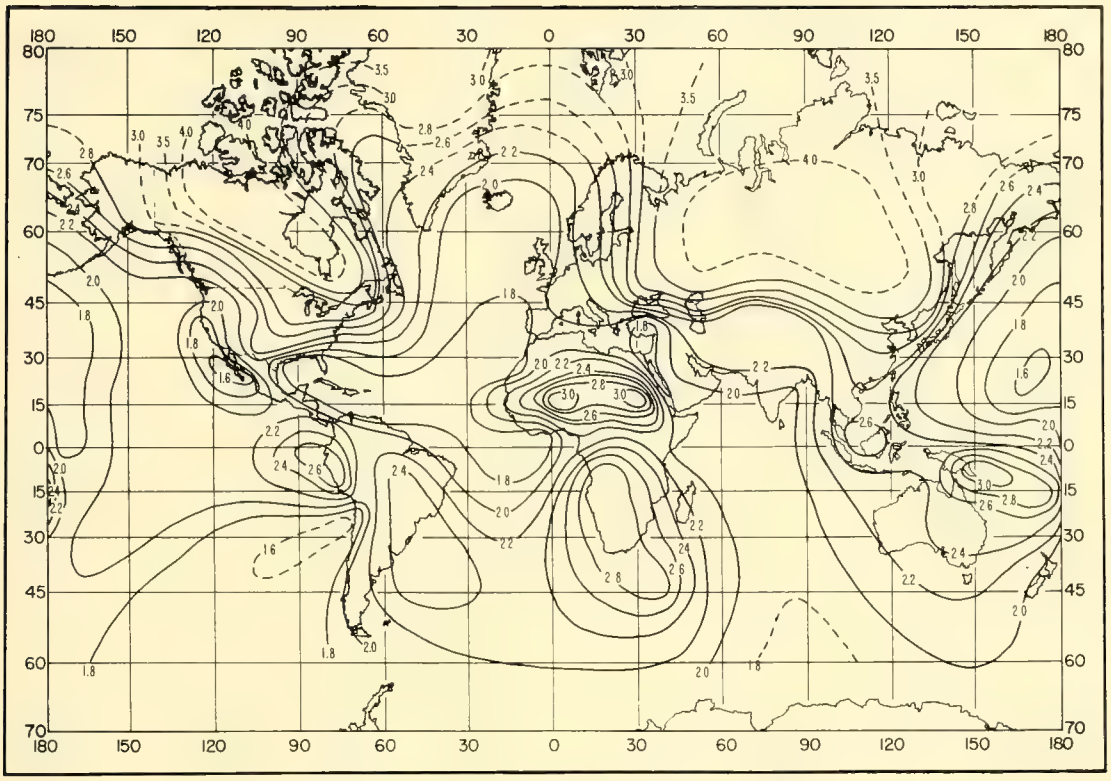

FIGURE A-6. *Wet-term scale height in km,* H_w: *February.*

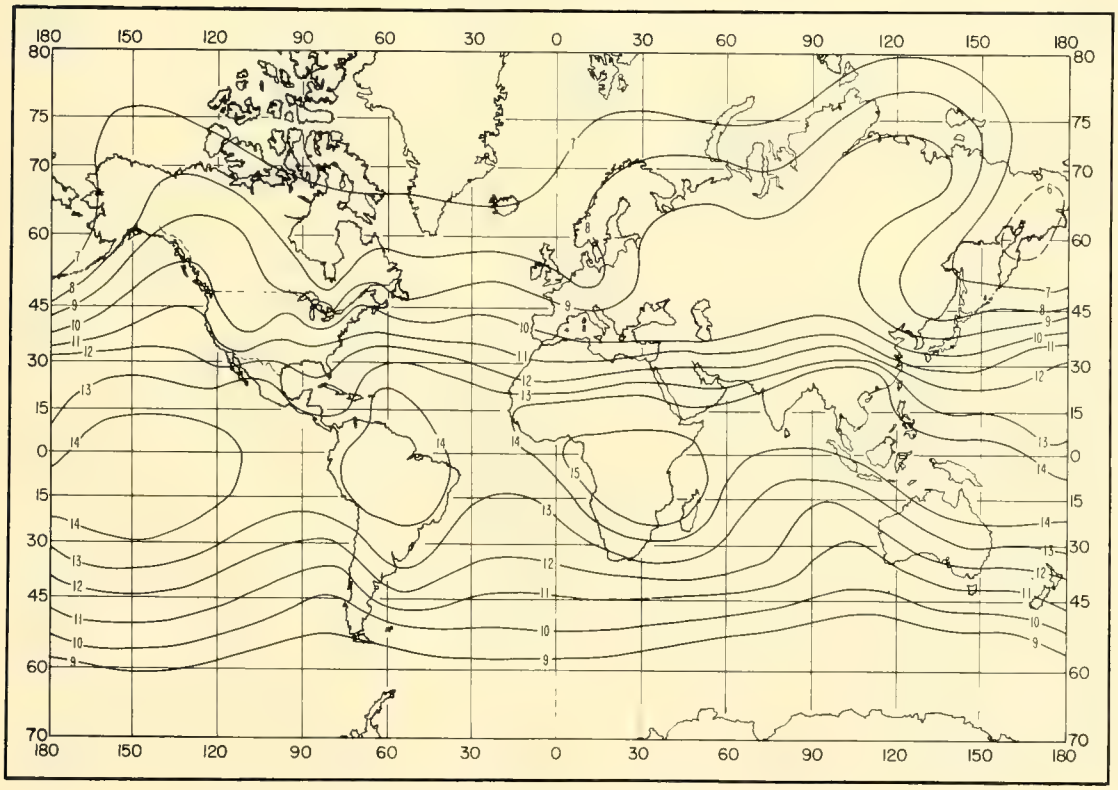

FIGURE A-7. *Mean density tropopause altitude in km,* z_t: *February.*

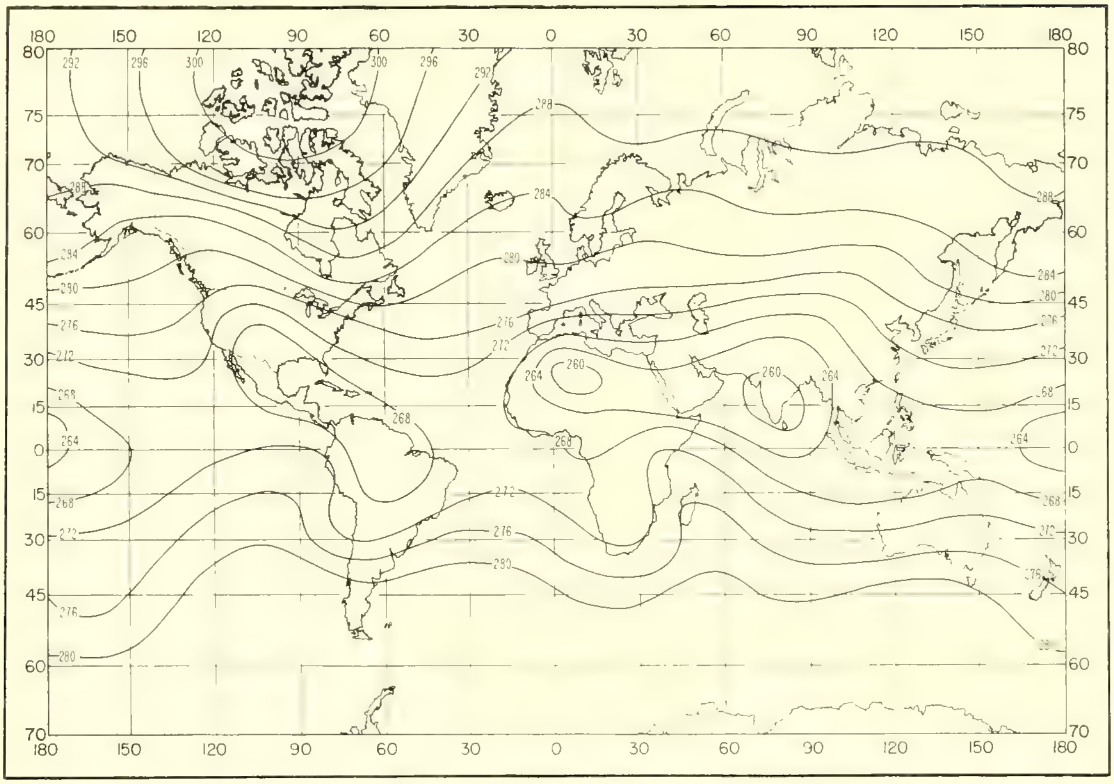

FIGURE A-8. *Mean sea-level dry term,* D_o: *May.*

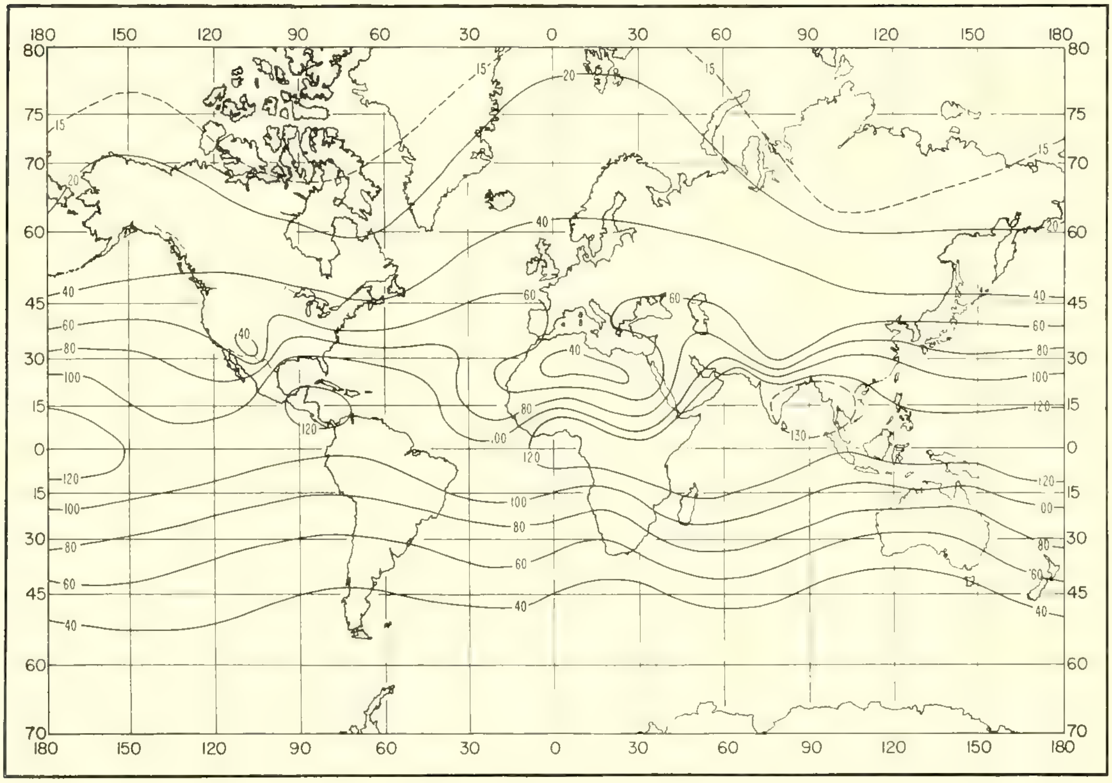

FIGURE A-9. *Mean sea-level wet term,* W_o: *May.*

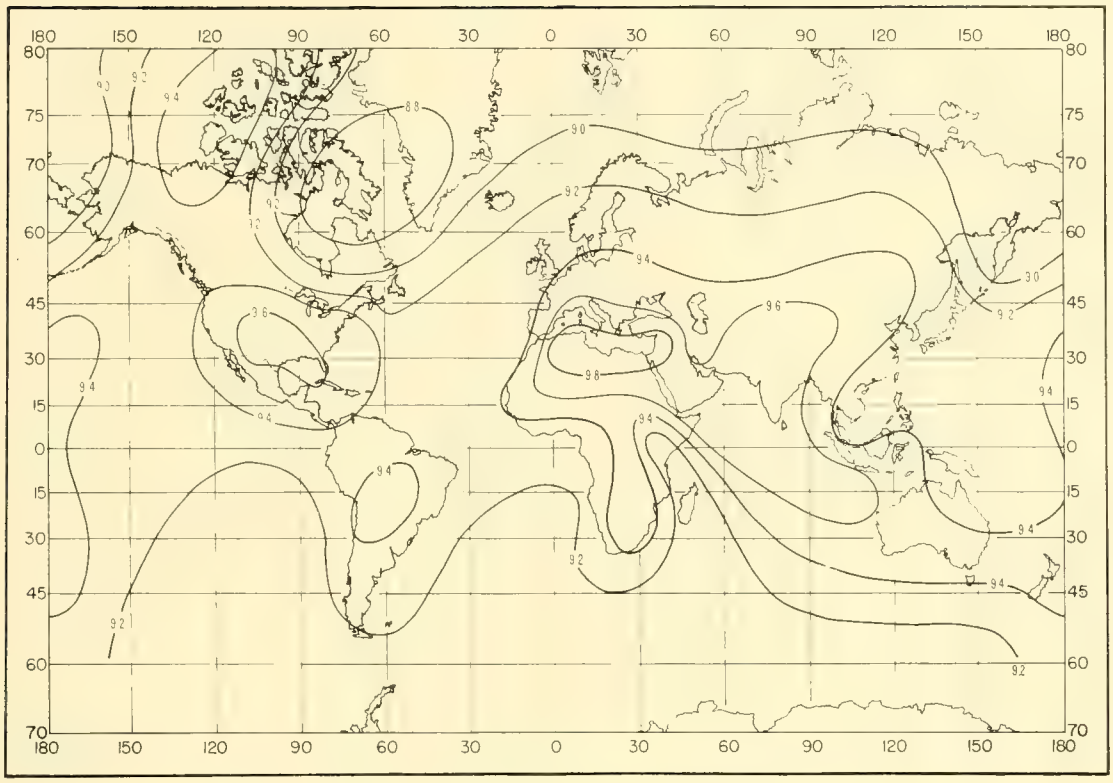

FIGURE A-10. *Dry-term tropospheric scale height in km,* H_1: *May.*

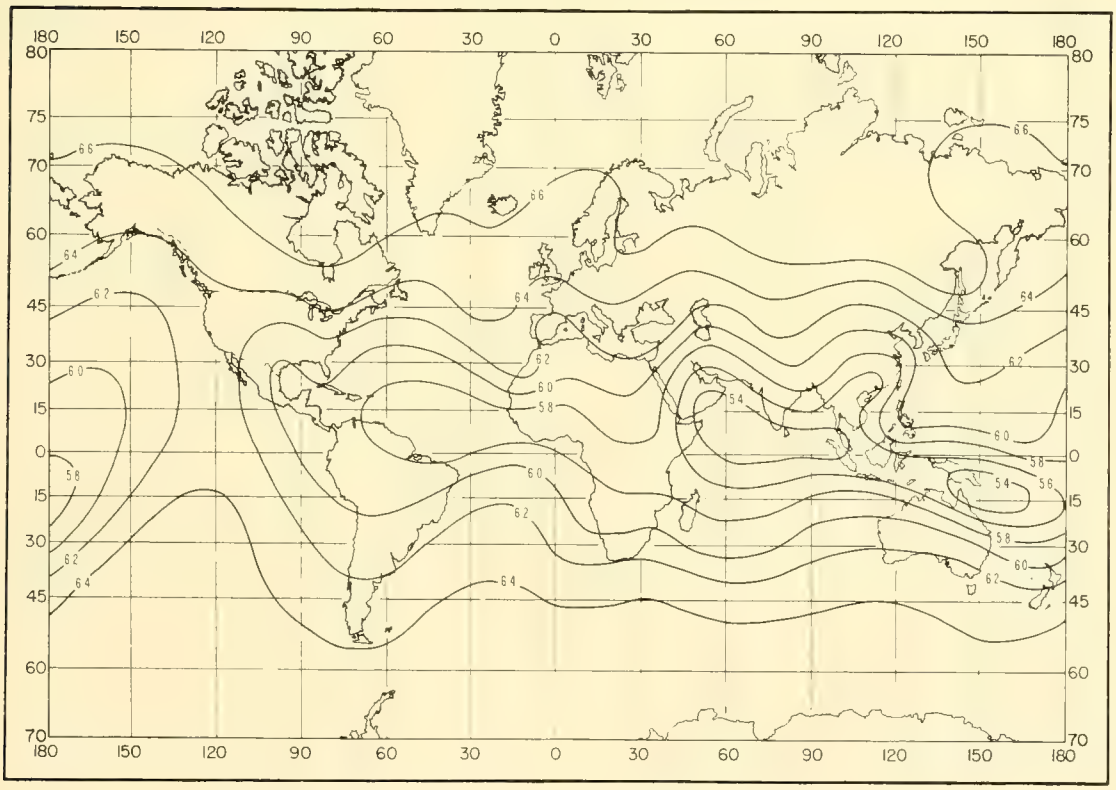

FIGURE A-11. *Dry-term stratospheric scale height in km,* H_2: *May.*

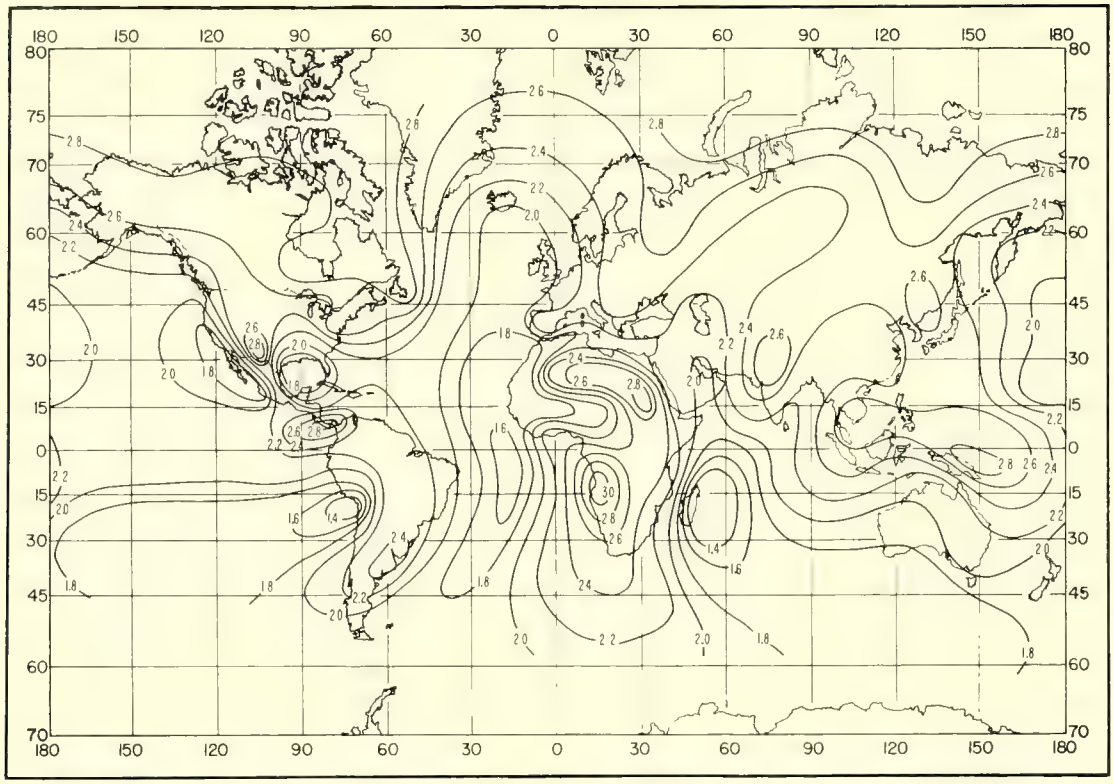

FIGURE A-12. *Wet-term scale height in km,* H_w: *May.*

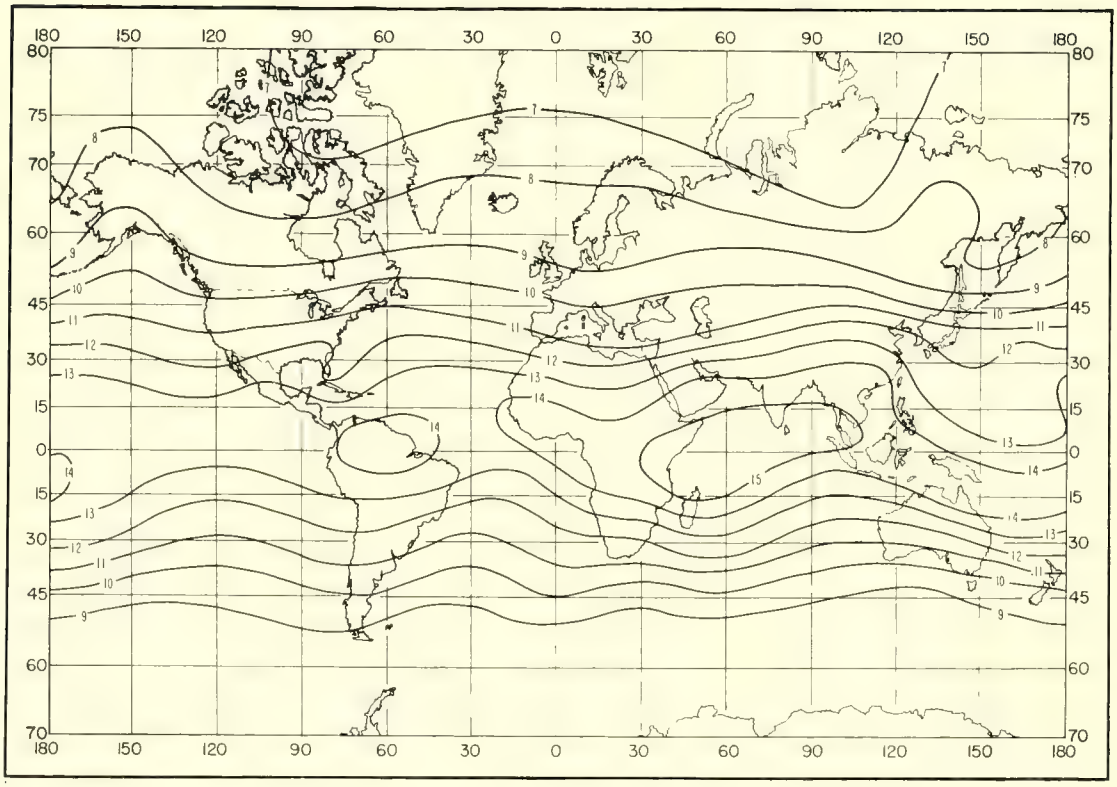

FIGURE A-13. *Mean density tropopause altitude in km,* z_t: *May.*

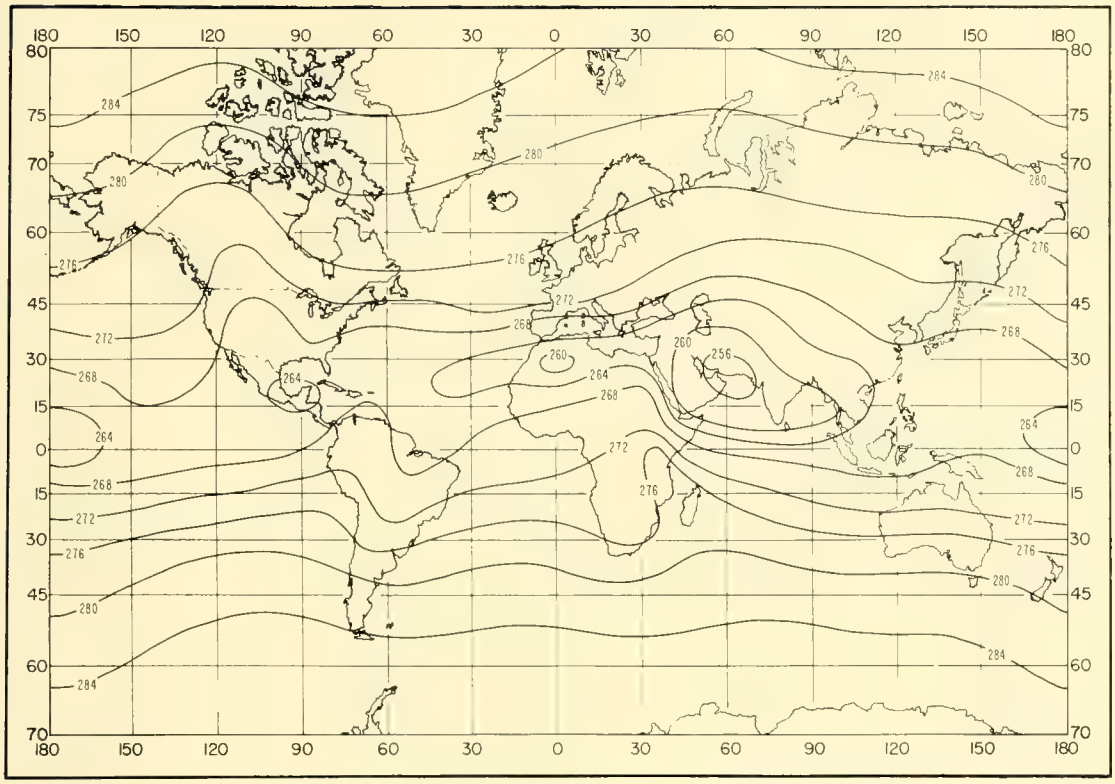

FIGURE A-14. *Mean sea-level dry term,* D_o: *August.*

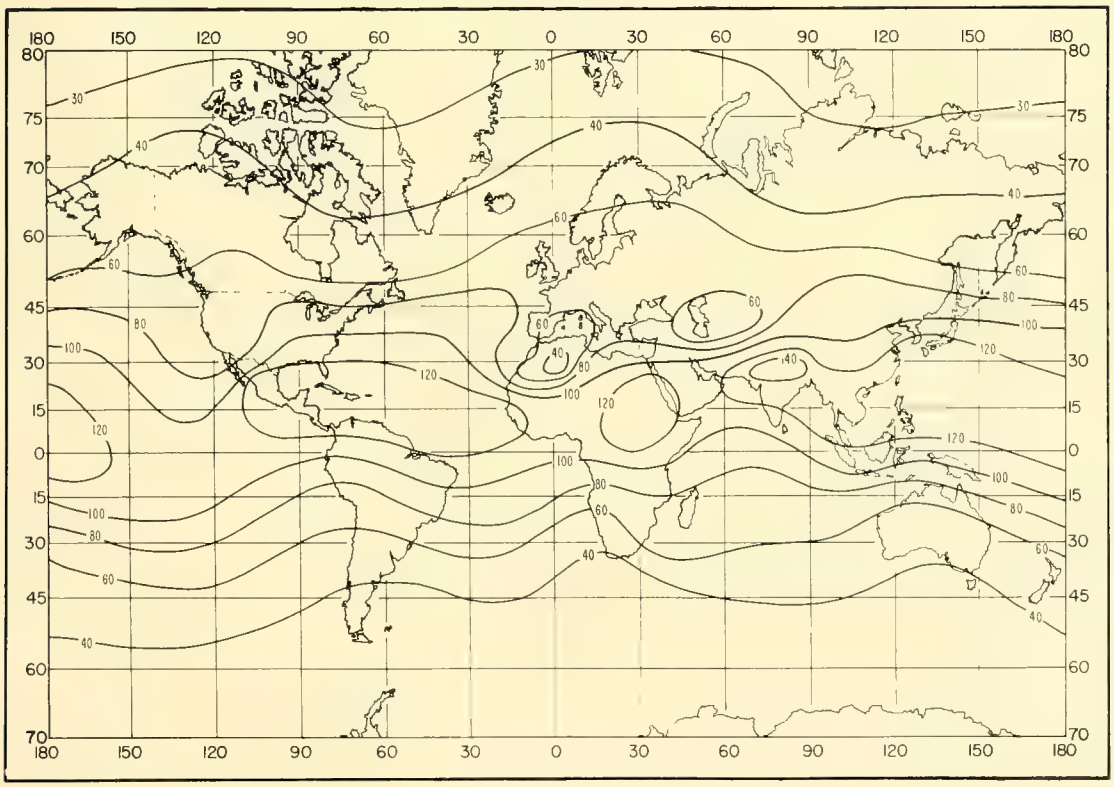

FIGURE A-15. *Mean sea-level wet term,* W_o: *August.*

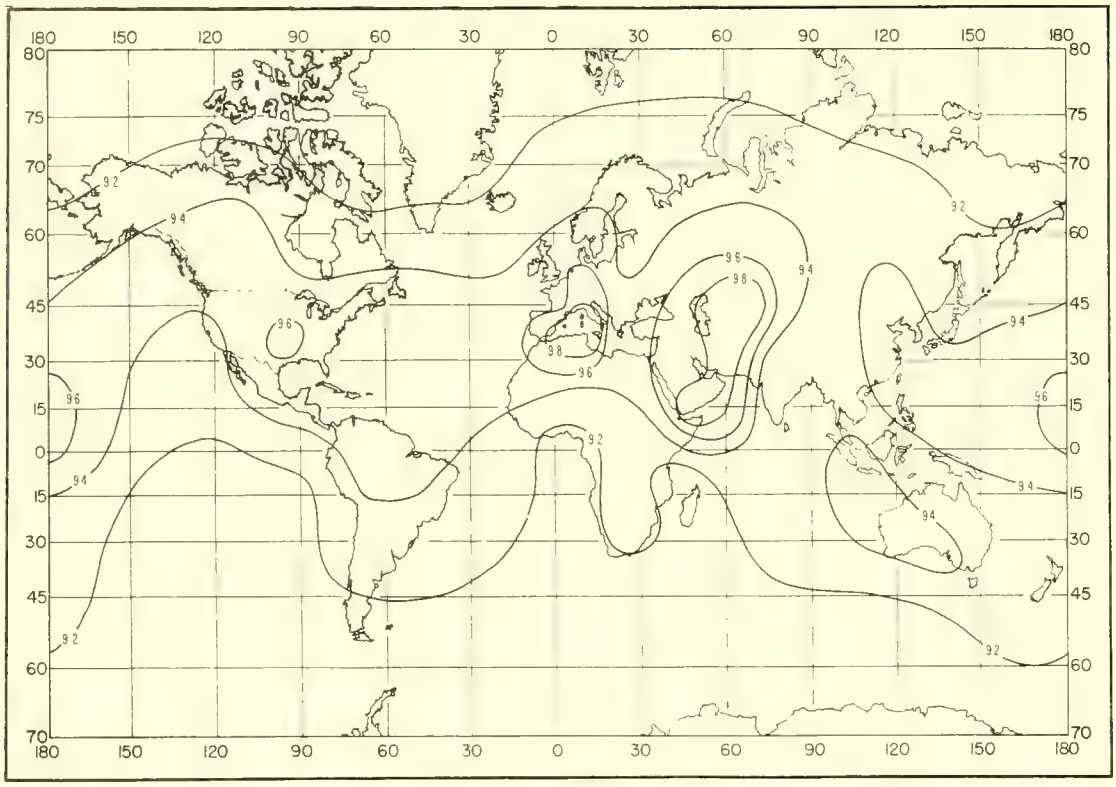

FIGURE A-16. *Dry-term tropospheric scale height in km,* H_1: *August.*

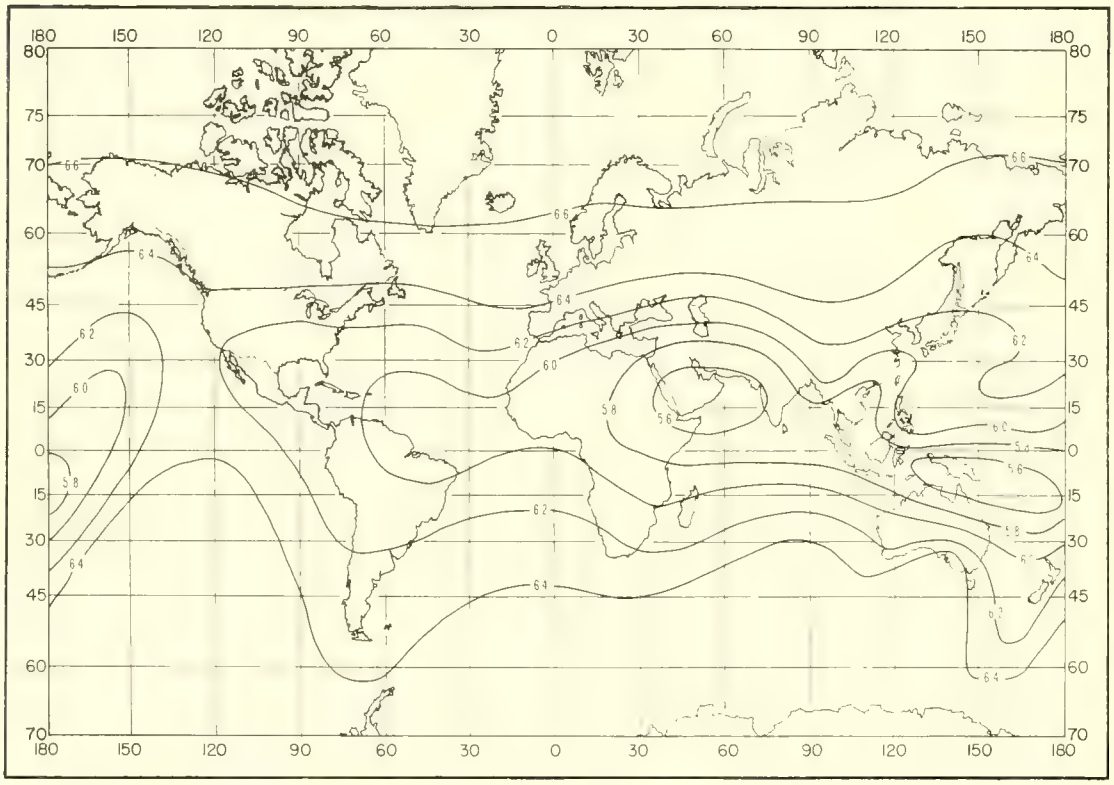

FIGURE A-17. *Dry-term stratospheric scale height in km,* H_2: *August.*

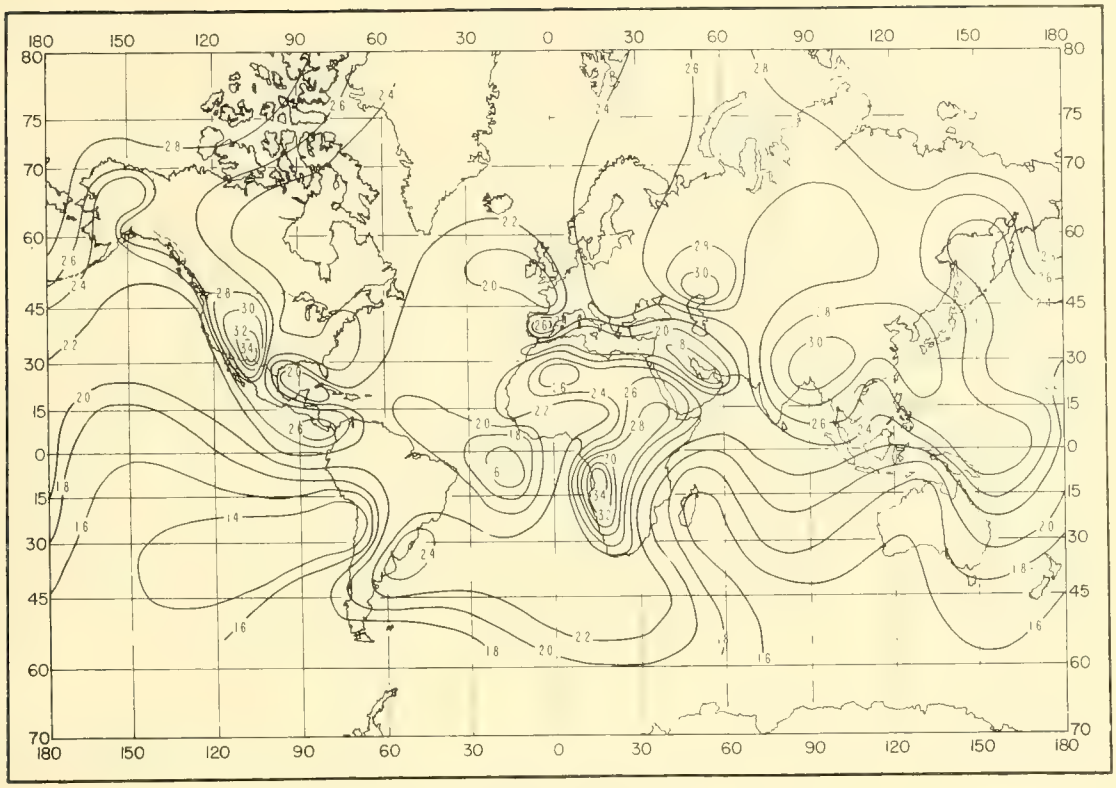

FIGURE A-18. *Wet-term scale height in km,* H_w: *August.*

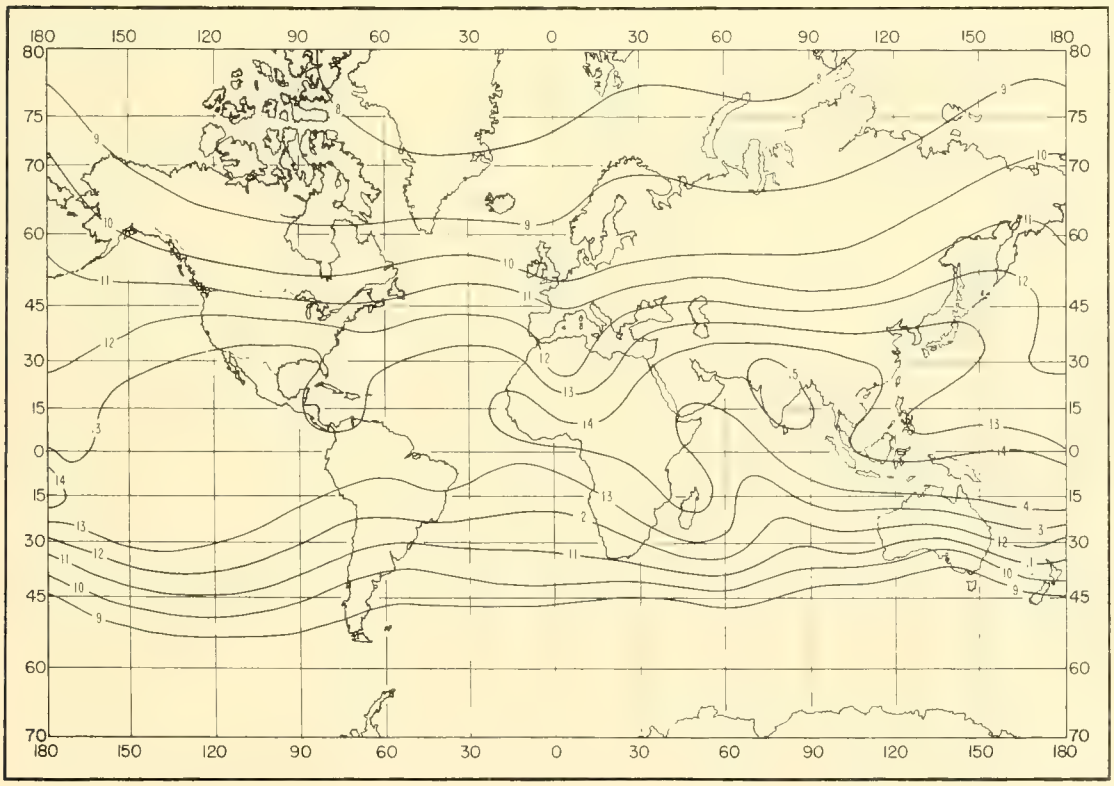

FIGURE A-19. *Mean density tropopause altitude in km,* z_t: *August.*

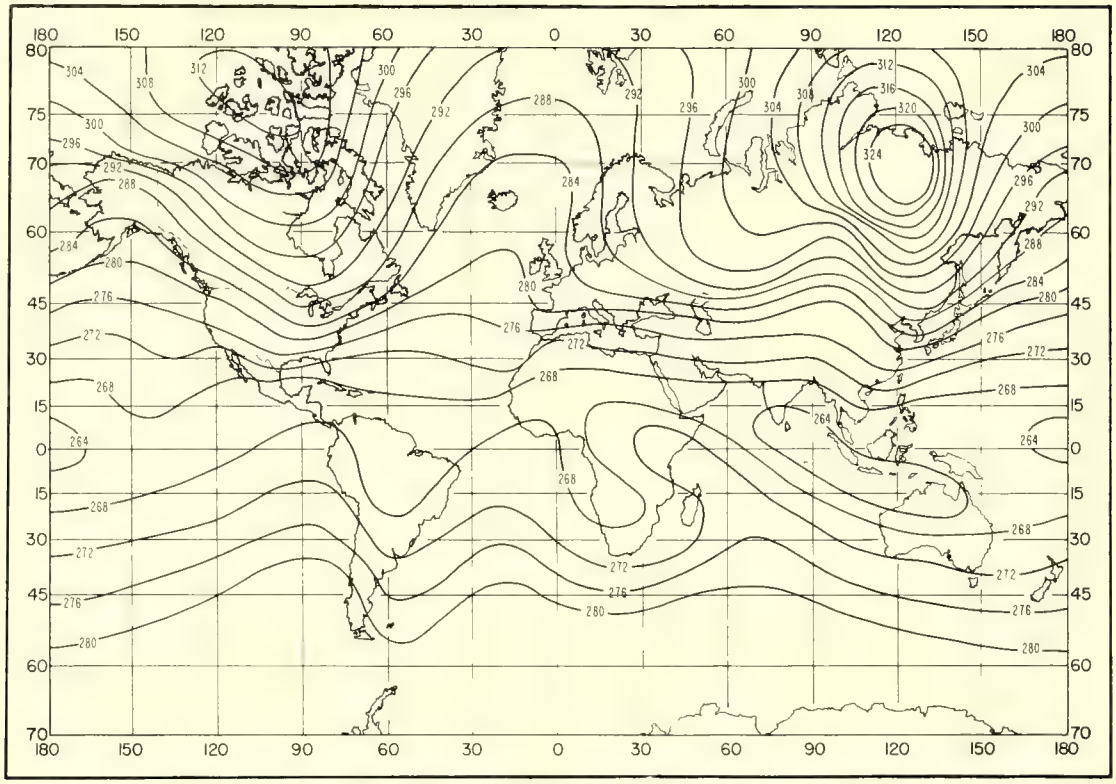

FIGURE A-20. *Mean sea-level dry term,* D_o: *November.*

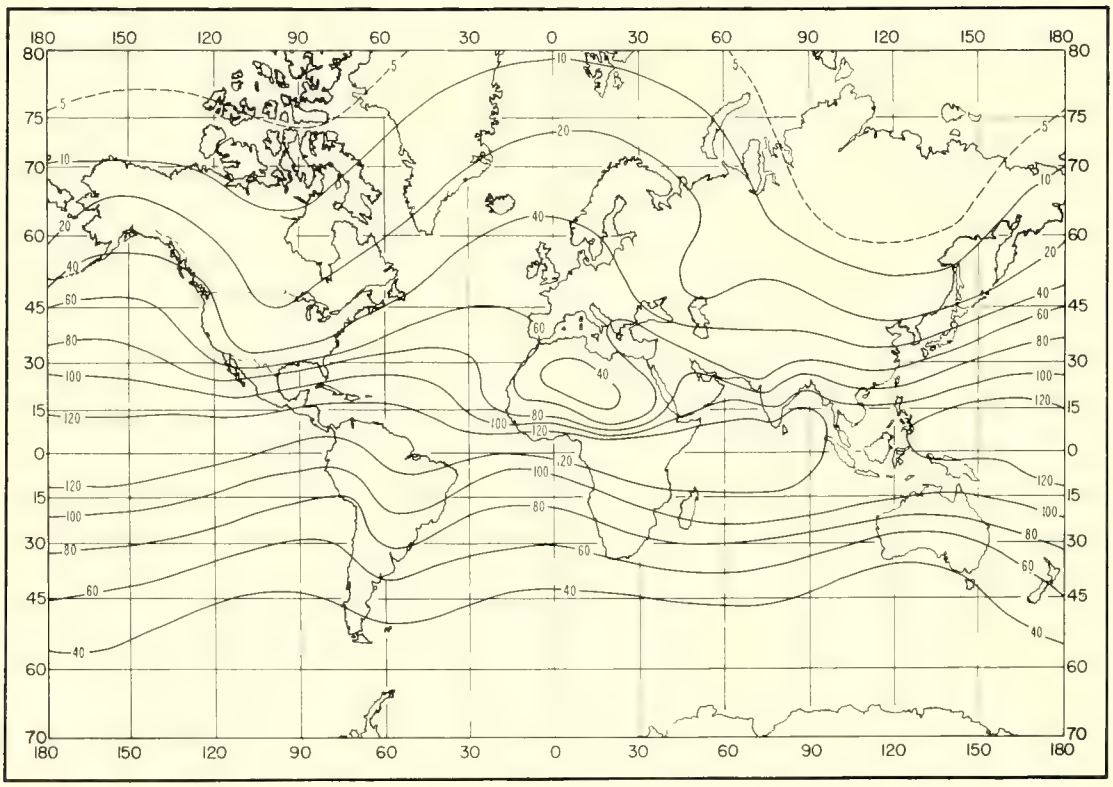

FIGURE A-21. *Mean sea-level wet term,* W_o: *November.*

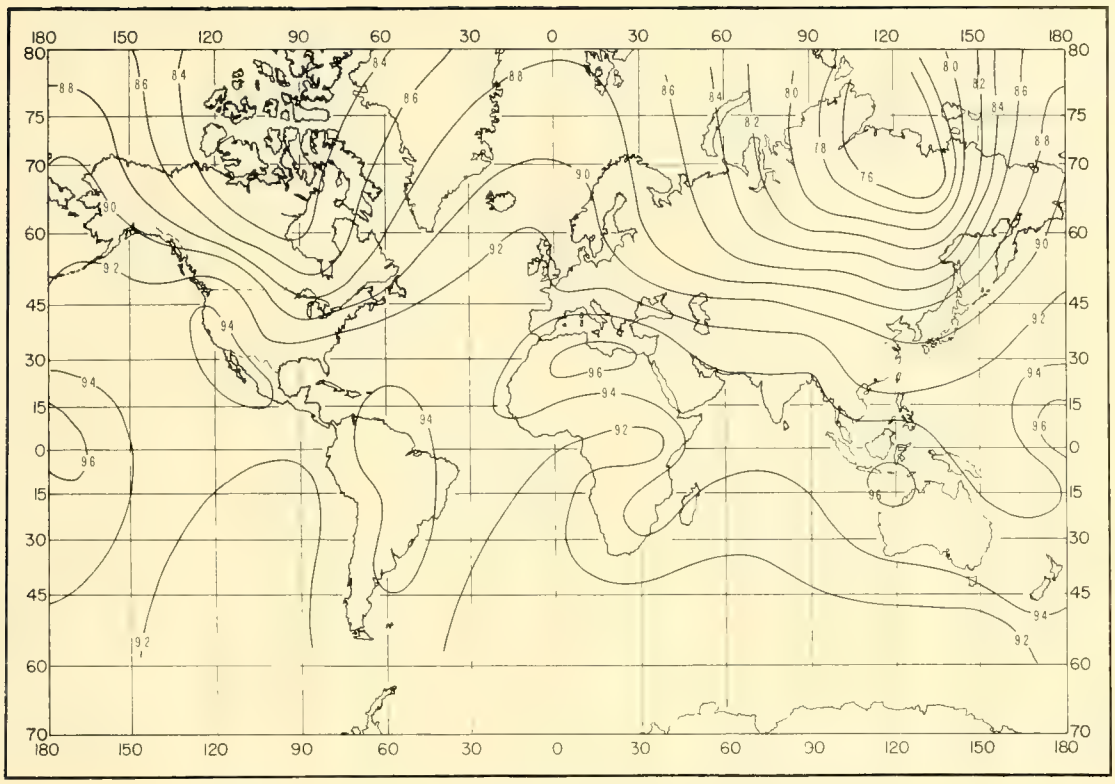

FIGURE A-22. *Dry-term tropospheric scale height in km,* H_1: *November.*

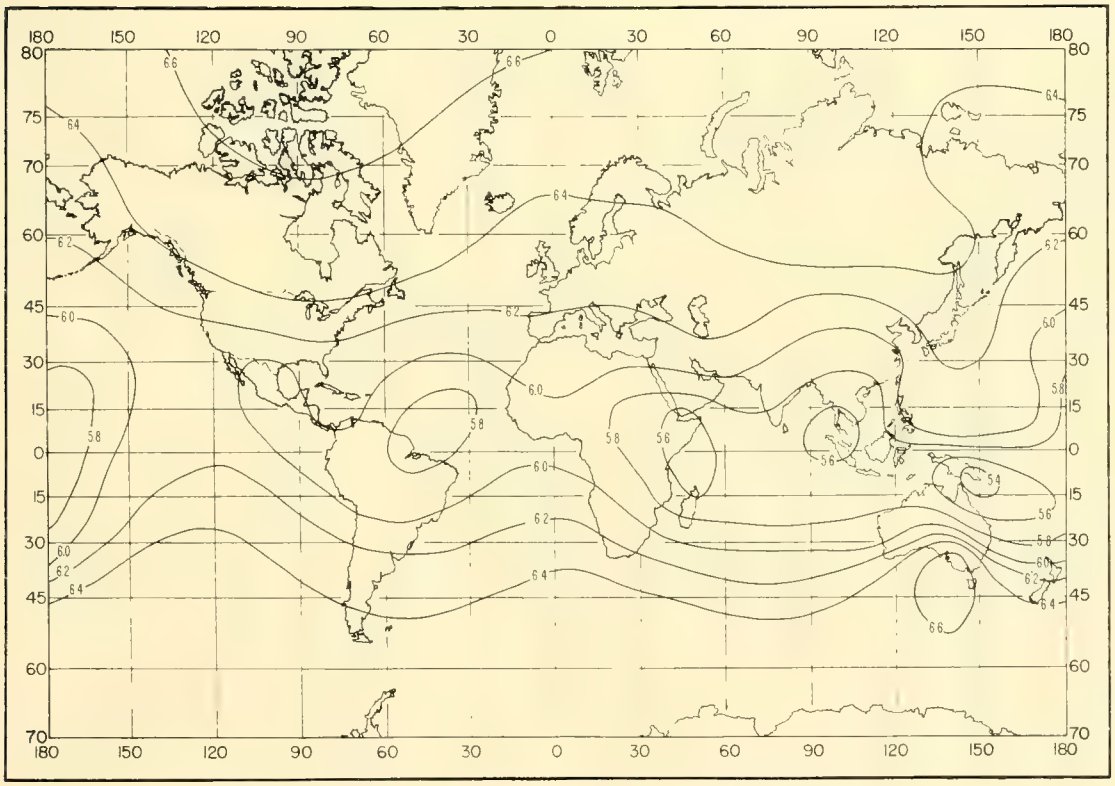

FIGURE A-23. *Dry-term stratospheric scale height in km,* H_2: *November.*

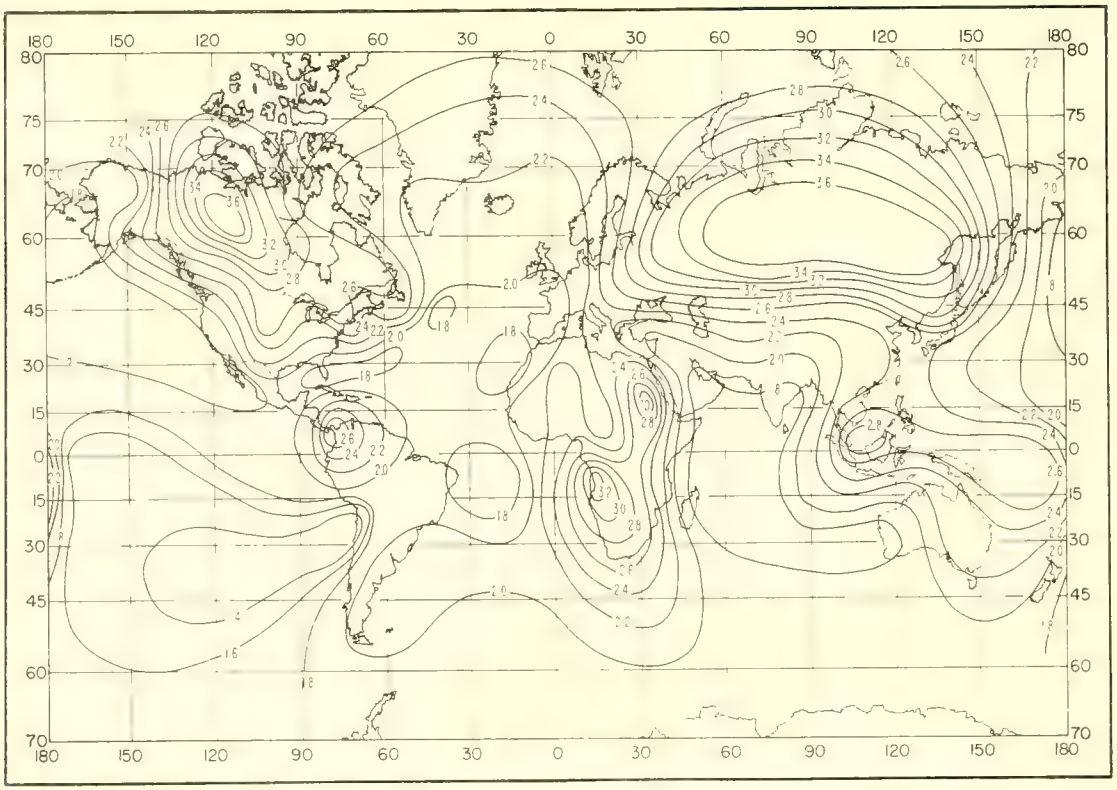

FIGURE A-24. *Wet-term scale height in km,* H_w: *November.*

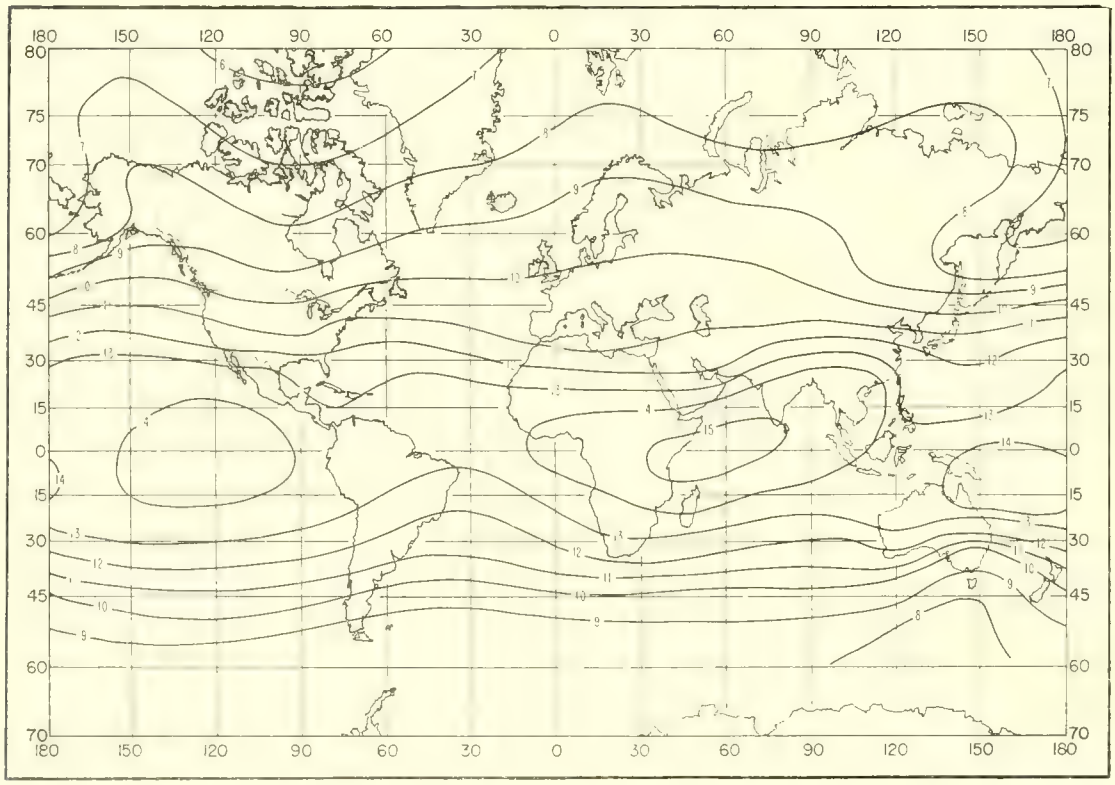

FIGURE A-25. *Mean density tropopause altitude in km,* z_t: *November.*

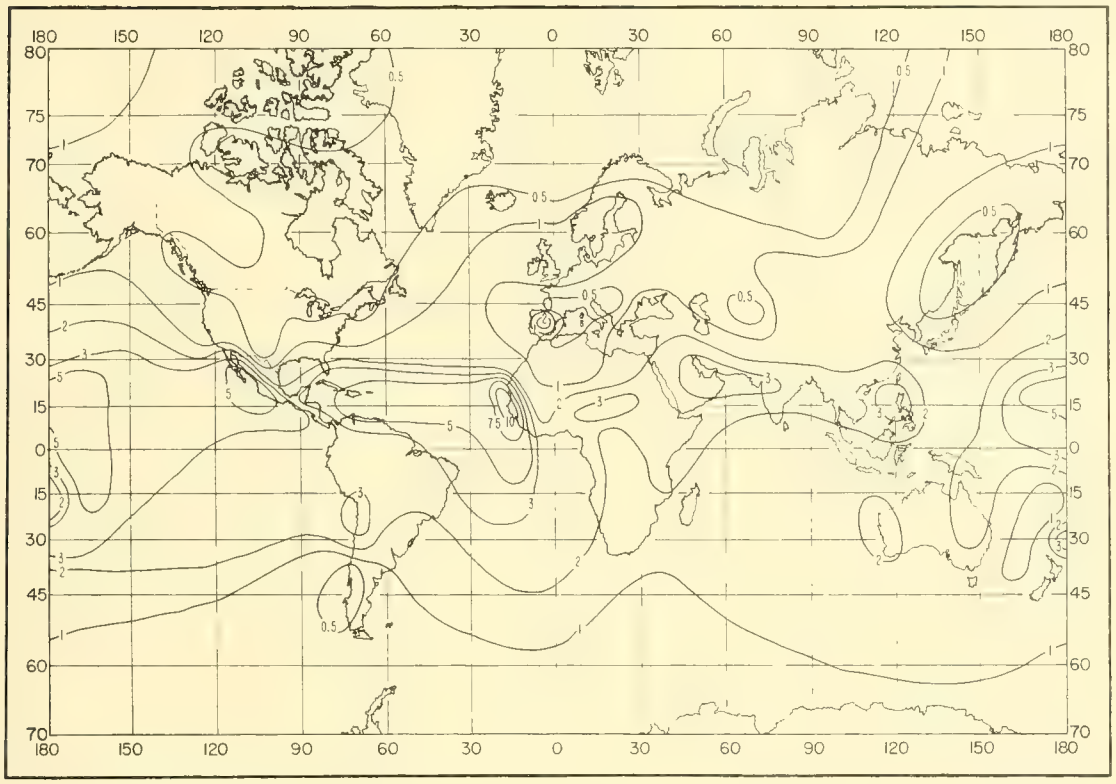

FIGURE A-26. *Standard prediction error of the exponential fit to the mean wet-term profile: February.*

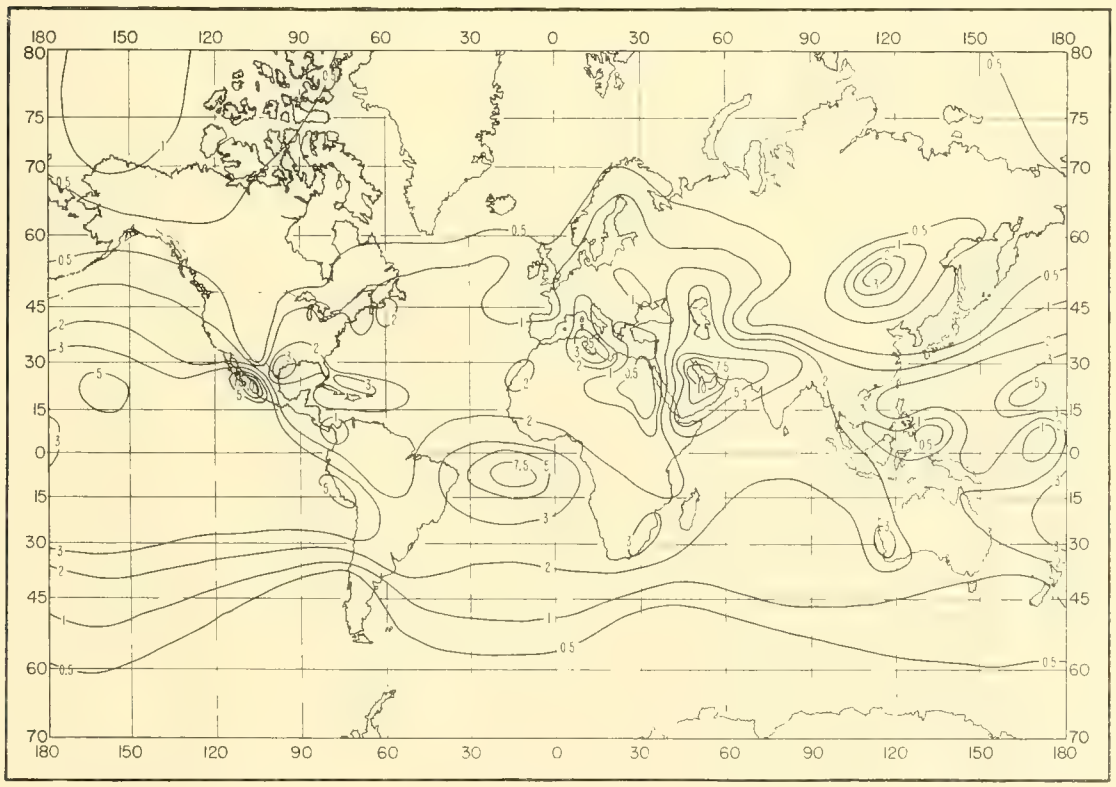

FIGURE A-27. *Standard prediction error of the exponential fit to the mean wet-term profile: May.*

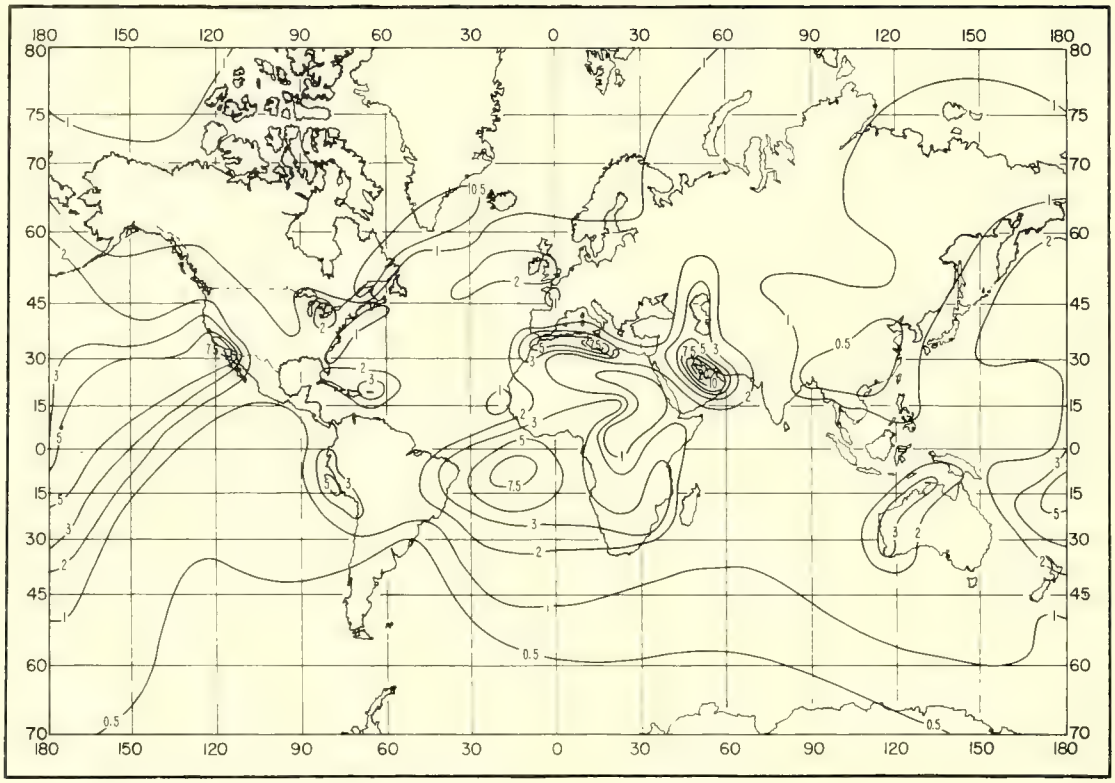

FIGURE A-28. *Standard prediction error of the exponential fit to the mean wet-term profile: August.*

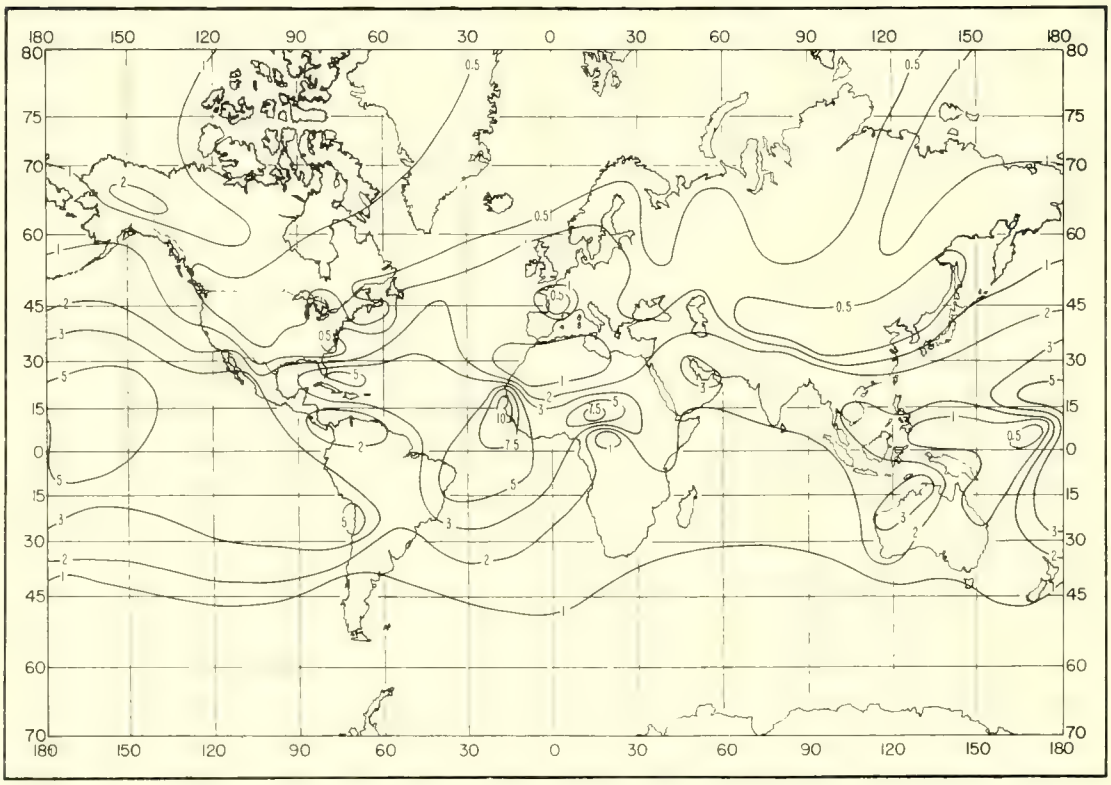

FIGURE A-29. *Standard prediction error of the exponential fit to the mean wet-term profile: November.*

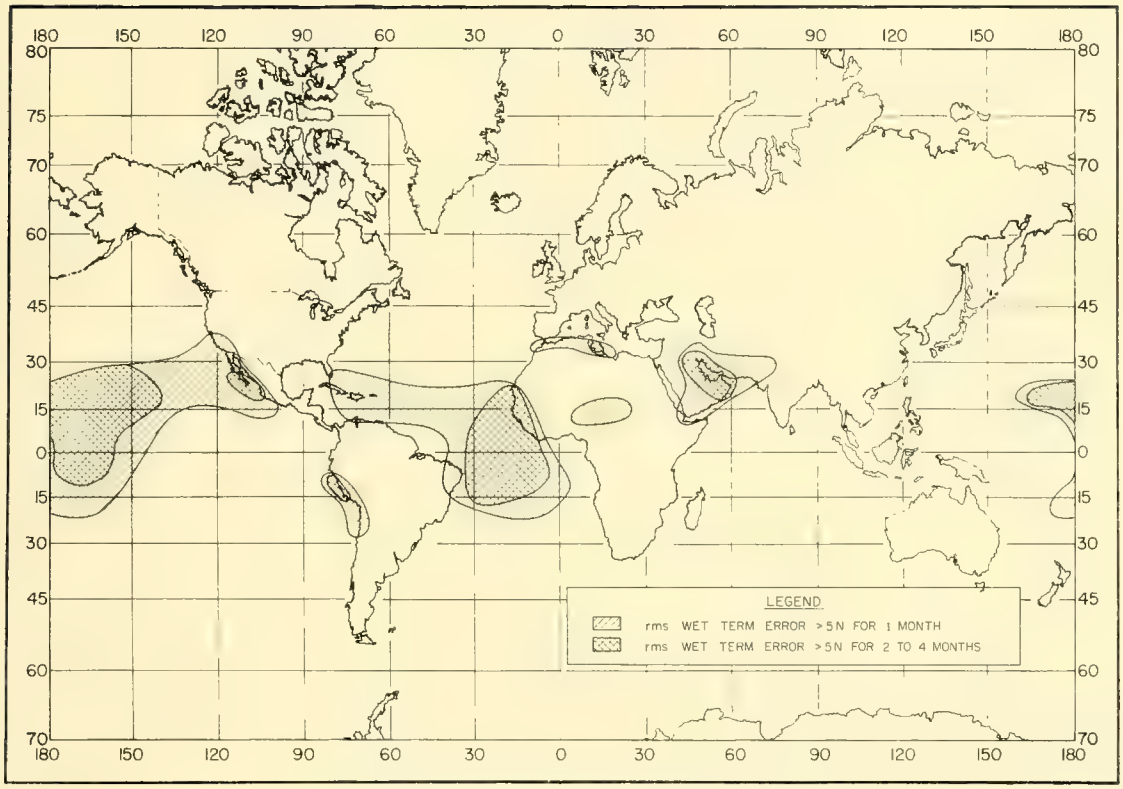

FIGURE A-30. *Areas of doubtful applicability of three-part exponential model of* $N(z)$ *for* $z < 6$ *km.*

11. Appendix B. World Maps of $\overline{\Delta N}$.

The weather stations from which data were obtained for this study are shown in figure B–1. Their locations, elevations and the 5-year mean surface refractivity for each month of the year are alphabetically listed in table B–1.

The monthly $\overline{\Delta N}$ values between the surface and 1 km above the surface are presented in figures B–2 through B–13. If the $\overline{\Delta N}$ at a specific location is desired for a certain month and year for which a monthly mean surface refractivity value, $\overline{N_s}$, is available, the following relationships may be used:

$$\overline{\Delta N} = b\ (\overline{N_s} - \overline{\overline{N_s}})\ +\ \overline{\overline{\Delta N}}, \tag{B–1}$$

where

$$\overline{\overline{N_s}} = \overline{\overline{N_o}} \exp^{-0.1(z)}; \qquad z = \text{elevation above sea level in km.}$$

World maps of $\overline{\overline{N_o}}$ (the yearly sea-level value of refractivity), b (the slope of the regression line (B–1)), and $\overline{\overline{\Delta N}}$ (the mean annual value of the refractivity difference between surface and 1 km) are presented in figures B–14 through B–16.

If the $\overline{\Delta N}$ value were required at a station with an elevation of 300 m and a location of 30°N and 30°E, here is the procedure which would be used. Available surface weather reports indicate that the mean N_s was 314 for a recent month for which a value of $\overline{\Delta N}$ is needed. Therefore, at the assumed location, these values are interpolated linearly from the figures:

$\overline{\overline{N_o}} = 320$ (fig. B–14)

$\overline{\overline{\Delta N}} = 48$ N-units (fig. B–15)

$b = 0.60$ (fig. B–16)

$\overline{\overline{N_s}} = 320 \exp^{-0.1(0.3)} = 311$

Using the value of 314 for $\overline{N_s}$, $\overline{\Delta N}$ is found to be 50 N-units.

In some areas of the world (e.g., where the assumption of an exponential distribution of the wet term is largely invalid; see sec. 3.4), the use of the regression method to predict $\overline{\Delta N}$ has definite limitations. To delineate these locations, figures B–17, B–18, B–19, and B–20 are presented. The first two figures are world maps of the correlation coefficient and the standard error of estimate of the regression line of $\overline{\Delta N}$ versus $\overline{N_s}$ for the 60 months of station data, and figure B–19 gives the percentage of this standard error to the $\overline{\overline{\Delta N}}$ value. Areas with correlation coefficients < 0.5 (fig. B–17), standard errors > 5 N-units (fig. B–18), and standard errors > 12 percent of $\overline{\overline{\Delta N}}$ (fig. B–19) are shaded, but the use of equation (B–1) for any location in these shaded areas may still be valid if:

(a) a low correlation coefficient occurs with a small standard error (typical of stations with a small seasonal range of variability in both N_s and ΔN), or

(b) a large error is found with a good correlation (typical of stations with distinct wet-dry seasons).

However, if the coefficient is less than 0.7 (reducing the variance of $\overline{\Delta N}$ to ~ 50 percent) *and* the standard error is greater than 10 percent of $\overline{\overline{\Delta N}}$ (as discussed in sec. 7), it would be reasonable to assume that the yearly dependence of $\overline{\Delta N}$ upon N_s is not sufficient to justify the regression prediction method. Areas represented by these criteria are shaded in figure B–20.

TABLE B-1. *Mean surface refractivity.*

Station	Elevation (meters)	Latitude	Longitude	Jan.	Feb.	Mar.	Apr.	May	June	July	Aug.	Sept.	Oct.	Nov.	Dec.
Abidjan, Ivory Coast	15	05 15N	03 56W	383	389	389	387	387	382	377	373	380	384	387	383
Adelaide, Australia	11	34 56S	138 35E	316	321	321	321	322	323	322	319	318	313	313	314
Aden, Arabia	4	12 50N	45 01E	365	364	371	380	385	386	379	378	376	372	366	369
Albrook (Balboa), Panama C.Z.	9	08 58N	79 33W	366	360	365	368	375	375	372	381	382	379	378	375
Albuquerque, N. Mex.	1620	35 03N	106 37W	254	251	248	245	253	251	267	274	259	256	251	251
Aldan, U.S.S.R.	680	58 37N	125 22E	297	296	289	284	283	292	305	304	293	287	291	297
Alert, Northwest Territories	62	82 30N	62 20W	326	327	330	321	312	313	313	315	310	313	320	324
Alexander Bay, South Africa	22	28 34S	16 32E	342	341	340	336	330	327	326	325	328	329	334	338
Alger/Maison, Algeria	28	36 43N	03 14E	326	323	327	329	337	346	354	355	354	344	333	328
Alice Springs, Australia	546	23 48S	133 53E	283	287	288	290	290	287	289	281	282	284	285	284
Allahabad, India	98	25 27N	81 44E	327	312	303	291	299	338	385	391	379	353	325	324
Alma Ata, U.S.S.R.	851	43 14N	76 56E	284	283	285	287	293	294	299	295	286	285	285	284
Amundsen-Scott, Antarctica	2800	90 00S	00 00	221	229	243	246	246	245	246	247	244	236	226	220
Anadyr, U.S.S.R.	62	64 47N	177 34E	314	317	319	321	310	312	325	321	313	308	311	314
Anchorage, Alaska	40	61 10N	149 59W	307	307	305	306	308	318	324	324	316	306	307	307
Ankara, Turkey	902	39 57N	32 53E	284	283	283	284	290	292	290	286	287	288	286	287
Antofagasta, Chile	122	23 28S	70 26W	338	341	337	333	330	327	325	327	326	328	333	334
Aoulef, Algeria	290	26 58N	01 05E	294	288	283	280	279	277	274	278	287	291	294	299
Argentia, Newfoundland	17	47 18N	54 00W	311	310	310	313	320	323	335	339	331	320	318	312
Arkhangelsk, U.S.S.R.	13	64 35N	40 30E	312	312	311	311	315	324	331	333	324	316	314	312
Ashkabad, U.S.S.R.	230	37 58N	58 20E	307	305	305	311	305	305	303	306	300	305	305	309
Aswan, United Arab Republic	196	23 58N	32 47E	299	287	280	280	278	276	285	288	291	294	299	305
Athens, Ga.	246	33 57N	83 19W	308	308	312	321	335	352	360	361	347	325	316	308
Athinai, Greece	107	37 58N	23 43E	316	314	316	317	325	325	326	323	326	327	329	322
Auckland, New Zealand	49	36 51S	174 46E	339	345	341	339	339	331	327	329	328	326	329	334
Bahia Blanca, Argentina	72	38 44S	62 11W	320	323	328	320	319	315	316	312	317	321	320	319
Bahrain Island	2	26 16N	50 37E	338	339	342	348	361	365	381	386	382	370	353	341
Baker Lake, Northwest Territories	9	64 18N	96 00W	329	333	326	316	312	314	318	320	314	312	317	325
Bangkok, Thailand	16	13 44N	100 30E	366	377	385	393	393	391	390	391	393	390	374	363
Bangui, Central African Republic	385	04 23N	18 34E	348	347	359	362	361	363	361	362	361	363	362	354
Barrow, Alaska	4	71 18N	156 47W	323	325	325	315	313	316	318	319	315	311	318	324
Beer Ya Aqov, Israel	49	32 00N	34 54E	324	322	323	327	332	339	351	355	347	337	324	323
B-Elan, U.S.S.R.	23	46 57N	142 43E	312	312	311	311	314	326	339	341	331	317	312	311
Beni Abbes/Colomb, Algeria	498	30 08N	02 10W	294	289	283	275	274	276	269	273	284	291	294	296
Benina, Libya	125	32 06N	20 16E	323	322	319	324	324	338	350	349	343	339	331	326
Beograd, Yugoslavia	139	44 48N	20 28E	310	311	308	312	324	331	335	331	320	318	317	312
Bismarck, N. Dak.	506	46 46N	100 45W	296	296	294	289	296	306	313	308	299	293	294	295
Bjornoya Island	14	74 31N	19 01E	310	310	310	312	315	316	320	320	317	312	311	310
Blagoveshchensk, U.S.S.R.	137	50 16N	127 30E	318	311	304	299	304	325	336	339	318	305	307	314
Bloemfontein, South Africa	1422	29 07S	26 11E	283	284	288	277	270	264	265	259	264	267	279	285
Boise, Idaho	871	43 34N	116 13W	284	284	279	280	286	285	283	281	278	283	285	285
Bombay, India	11	18 54N	72 49E	347	352	362	371	380	386	389	388	384	375	364	355
Bordeaux, France	48	44 51N	00 42W	320	323	322	323	330	337	343	342	343	332	324	321
Brest, France	103	48 27N	04 25W	319	316	318	321	326	332	338	337	336	331	323	324
Brisbane, Australia	41	27 28S	153 02E	351	357	351	343	328	323	319	320	325	326	337	347
Broken Hill, Zambia	1206	14 27S	28 28E	319	322	315	309	293	285	282	278	279	282	305	317
Brownsville, Tex.	6	25 55N	97 28W	337	344	346	359	366	377	375	377	370	357	345	339
Bruxelles, Belgium	100	50 48N	04 21E	314	313	315	317	324	333	338	337	334	328	321	318
Bukhta Tikhaya, U.S.S.R.	6	80 19N	52 48E	326	320	321	316	313	312	314	315	313	311	314	319
Bukhta Tiksi, U.S.S.R.	8	71 35N	128 55E	332	327	324	317	312	316	319*	320	314	311	322	327
Byrd Station, Antarctica	1500	80 00S	120 00W	253	257	259	261	267	266	263	267	262	259	254	253
Cairo, United Arab Republic	68	30 08N	31 24E	314	312	313	313	318	329	341	347	338	334	331	322
Calcutta, India	6	22 39N	88 27E	337	338	346	366	381	389	394	395	394	379	346	341
Camaguey, Cuba	122	21 25N	77 52W	351	353	357	363	370	377	378	379	379	376	365	360
Canton Island	3	02 46S	171 43W	374	372	377	381	377	377	379	376	373	373	373	372
Cape Hatteras, N. C.	3	35 16N	75 33W	319	323	324	337	349	364	376	374	366	347	332	326
Caribou, Maine	191	46 52N	68 01W	307	305	303	305	310	325	332	330	323	313	308	306
Charleville, Australia	299	26 25S	146 17E	325	335	329	324	316	314	309	302	303	304	303	310
Chatham Island	49	45 58S	176 33W	330	339	336	330	327	323	322	324	322	327	329	332
Chiangmai, Thailand	313	18 47N	98 59E	338	332	336	349	368	371	375	377	376	369	358	345
Chita, U.S.S.R.	671	52 05N	113 29E	300	294	287	281	279	297	310	308	293	288	291	295
Christchurch, New Zealand	8	43 32S	172 37E	334	335	337	334	326	324	323	323	324	320	321	327
Clark Field, the Philippines	170	15 08N	120 35E	345	344	345	351	362	367	366	369	366	363	357	349
Cloncurry, Australia	188	20 40S	140 30E	338	339	333	311	310	305	307	299	295	300	308	321
Cocos Island	5	12 05S	96 53E	373	380	372	378	379	376	374	372	372	370	369	369
Columbia, Mo.	239	38 58N	92 22W	305	305	306	312	327	343	353	352	330	316	306	306
Coppermine, Northwest Territories	9	67 49N	115 15W	327	329	328	318	313	318	318	322	316	312	318	323
Coral Harbour, Northwest Territories	59	64 12N	83 22W	324	324	322	312	310	313	317	319	314	309	313	317
Cordoba, Argentina	479	31 19S	64 13W	328	331	332*	321*	318	305	303	298	300	314	318	327
Curacao Island	16	12 11N	68 59W	372	368	372	376	380	380	382	384	384	382	379	376
Dakar, Senegal	22	14 44N	17 30W	342	342	348	351	358	367	371	377	381	379	360	342
Dar Es Salaam, Tanzania	58	06 52S	39 16E	376	376	382	379	370	362	359	357	361	366	372	375
Darwin, Australia	27	12 26S	130 52E	380	382	387	372	359	338	344	338	360	373	374	385
Denver, Colo.	1625	39 46N	104 53W	251	249	250	249	257	259	264	269	256	252	252	251
D.F. Malan (Capetown), South Africa	49	33 55S	18 36E	337	341	337	333	333	330	329	327	328	330	330	334
Dijarbakir, Turkey	652	37 55N	40 12E	293*	292	293	297	298	289	289	282	276	284	297	294
Djakarta, Indonesia	8	06 11S	106 50E	382	383	382*	383	382	376	367*	366	368	375	380	380
Dodge City, Kans.	791	37 46N	99 58W	285	286	287	291	306	316	322	318	308	294	285	284
Douala, Cameroon	13	04 01N	09 43E	382	382	383	382	382	380	379	379	380	379	381	382
Durban, South Africa	14	29 58S	30 57E	365	367	365	356	345	333	338	336	343	349	357	360

TABLE B-1. (*Continued*)

Station	Elevation (meters)	Latitude	Longitude	Jan.	Feb.	Mar.	Apr.	May	June	July	Aug.	Sept.	Oct.	Nov.	Dec.
Edmonton, Alberta	676	53 34N	113 31W	290	287	287	286	287	298	307	308	296	288	288	287
Egedesminde, Greenland	48	68 42N	52 52W	311	311	310	309	310	314	318	318	311	309	307	306
El Adem, Libya	157	31 51N	23 55E	314	312	312	314	322	330	337	343	336	329	322	317
El Paso, Tex.	1194	31 48N	106 24W	266	261	258	255	260	266	284	289	272	271	263	262
Ely, Nev.	1908	39 17N	114 51W	249	249	248	247	251	249	248	249	248	249	249	249
Entebbe, Uganda	1146	00 03N	32 27E	320	321	323	325	326	323	321	320	322	320	318	319
Eureka, Northwest Territories	2	80 00N	85 56W	332	335	338	325	313	315	316	316	314	317	327	333
Ezeiza, Argentina	20	34 50S	58 32W	340	349	344	338	331	326	325	326	328	333	335	338
Fairbanks, Alaska	138	64 49N	147 52W	314	309	304	301	304	315	322	322	311	305	308	314
Forrest, Australia	160	30 51S	128 06E	311	319	319	313	315	313	313	316	317	309	300	310
Ft. Lamy, Chad	300	12 08N	15 02E	288	279	282	298	316	337	353	360	358	336	297	294
Ft. Nelson, British Columbia	375	58 50N	122 35W	306	302	296	294	295	307	314	313	305	298	299	303
Ft. Smith, Northwest Territories	203	60 01N	111 58W	315	311	306	302	301	307	316	317	310	305	305	311
Ft. Trinquet, Mauritania	359	25 14N	11 37W	302	301	300	304	305	311	308	313	312	310	309	303
Funchal, Madeira	110	32 38N	16 54W	329	329	324	329	336	345	352	352	349	344	335	330
Gauhati, India	54	26 11N	91 45E	336	332	333	348	368	385	392	394	388	377	356	344
Giles, Australia	514	25 02S	128 18E	292	293	287	283	294	288	287	284	279	286	281	289
Goose Bay, Labrador	44	53 19N	60 25W	310	310	309	308	309	315	324	324	315	310	308	309
Gough Island	40	40 19S	09 54W	334	334	332	328	328	324	324	324	322	324	326	332
Great Falls, Mont.	1115	47 30N	111 21W	272	271	270	269	271	277	278	273	271	270	270	269
Green Bay, Wisc.	210	42 29N	88 08W	306	305	306	308	316	329	338	342	327	316	306	306
Guryev, U.S.S.R.	−21	47 07N	51 55E	315	314	315	314*	315	331*	325	326	320	320*	317	316*
Habbaniya, Iraq	45	33 22N	43 34E	320	318	317	317	311	302	303	306	310	309	321	322
Helsinki, Finland	58	60 19N	24 58E	309	311	311	312	316	325	333	334	327	319	314	311
Hilo, Hawaii	11	19 44N	155 04W	350	349	349	353	358	359	361	367	362	361	358	356
Hobart, Tasmania, Australia	54	42 53S	147 20E	319	323	323	317	315	313	314	314	314	312	312	319
Hong Kong	66	22 18N	114 10E	331	334	348	363	378	385	391	391	383	360	348	334
International Falls, Minn.	360	48 34N	93 23W	301	300	297	296	300	313	323	323	311	303	298	299
Istanbul, Turkey	40	40 58N	29 05E	317	317	318	323	333	342	352	354	342	333	329	321
Izmir, Turkey	25	38 24N	27 10E	317	316	314	319	326	332	334	332	324	328	325	322
Jodhpur, India	224	26 18N	73 01E	301	290	292	284	297	339	355	368	359	310	297	303
Johnston Island	5	16 44N	169 31W	363	361	365	371	366	376	375	375	378	376	371	366
Karachi, West Pakistan	4	24 48N	66 59E	324	341	355	370	384	394	391	391	387	368	350	330
Karaganda, U.S.S.R.	555	49 48N	73 08E	296	297	295	295	296	304	312*	311	296	294	296	297
Kaunas, U.S.S.R.	75	54 53N	23 53E	310	311	310	313	322	327	337	336	327	320	316	312
Keflavik, Iceland	50	63 59N	22 37W	309	310	311	313	317	321	325	323	322	316	313	306
Khabarovsk, U.S.S.R.	72	48 31N	135 10E	316	311	306	306	310	329	346	346	328	310	307	313
Kharkov, U.S.S.R.	153	49 56N	36 17E	309	308	308	308	311	321	325	325	317	317	314	309
Khartoum, Sudan	385	15 36N	32 33E	287	284	283	285	286	305	328	341	329	302	296	293
Khatanga, U.S.S.R.	24	71 59N	102 28E	331	328	320*	316	312	314*	321	317	313	313	325	328
Kirensk, U.S.S.R.	258	57 46N	108 07E	318	312	306	299	301	314	324	324	311	304	306	314
Kobenhavn, Denmark	6	55 38N	12 40E	314	314	315	316	319	325	333	333	329	324	321	316
Kolpashev, U.S.S.R.	76	58 18N	82 54E	316	313	311	309	308	317	333	330	320	311	312	314
Koror, Palau Islands	29	07 20N	134 29E	385	383	383	387	391	385	388	387	388	386	388	387
Krasnoiarsk, U.S.S.R.	194	56 00N	92 53E	309	305	304	301	300	310	327	327	315	305	304	310
Kustanay, U.S.S.R.	171	53 13N	63 37E	310	309	308	305	304	321*	328	320	311	307	307	310
Kyev, U.S.S.R.	182	50 27N	30 30E	308	307	306	307	313	320	324	328	319	314	314	308
La Coruna, Spain	57	42 23N	08 22W	320	321	323	324	331	334	340	342	341	334	324	320*
Lae, New Guinea	8	06 44S	147 00E	378	377	379	381	382	377	377	377	377	376	380	379
Lagos, Nigeria	40	06 35N	03 20E	377	382	382	384	385	378	373	372	379	382	381	379
Lake Charles, La.	5	30 13N	93 09W	325	328	330	346	362	375	382	380	369	350	333	329
Las Vegas, Nev.	664	36 05N	115 09W	283	279	274	269	267	264	279	284	271	275	278	280
Leningrad, U.S.S.R.	4	59 58N	30 18E	312	312	312	312	318	327	334	334	327	320	315	313
Leopoldville (Kinshasa), Democratic Republic of the Congo	290	04 19S	15 19E	369	368	368	367	368	355	345	346	352	360	364	367
Lerwick, United Kingdom	82	60 08N	01 11W	314	315	315	316	320	324	329	330	329	324	318	313
Lima, Peru	135	12 06S	77 02W	354	357	356	350	343	339	336	338	336	340	342	349
Lindenberg, East Germany	105	52 13N	14 07E	311	313	312	213	319	325	336	332	326	322	317	313
Lisboa, Portugal	103	38 46N	09 08W	325	328	328	324	329	330	335	336	341	330	326	327
Lourenco Marques, Portuguese East Africa	44	25 55S	32 34E	371	370	366	361	348	341	339	341	345	356	357	362
Luanda, Portuguese West Africa	70	08 49S	13 13E	375	374	377	380	369	356	351	352	359	367	375	374
Lvov, U.S.S.R.	329	49 49N	23 57E	302	306	301	307	315	322	330	327	318	312	309	304
Macquarie Island	6	54 30S	158 57E	320	319	319	317	316	314	315	316	315	314	312	320
Madras, India	16	13 00N	80 11E	364	363	368	379	379	367	369	376	380	384	379	366
Madrid, Spain	657	40 24N	03 41W	296	296	296	291	300	304	298	299	305	304	300	301
Majuro Island	3	07 05N	171 23E	383	378	381	385	387	381	383	383	383	383	384	383
Malakal, Sudan	389	09 33N	31 39E	298	292	299	320	337	353	358	362	363	358	329	304
Malye-Karmakuly, U.S.S.R.	16	72 23N	52 44E	311*	315	312	312	311	316	322*	321*	—	312*	314*	314*
Maracay, Venezuela	442	10 15N	67 39W	339	335	336	345	354	352	353	353	354	355	350	344
Marion Island	26	46 53S	37 52E	317	317	319	316	313	313	313	314	313	314	314	313
Maun, South Africa	945	19 59S	23 25E	323	324	319	301	284	279	275	271	274	282	308	321
Mawson, Antarctica	14	67 36S	62 53E	299	298	300	303	305	306	306	306	303	300	298	299
Mazatlan, Mexico	78	23 11N	106 26W	346	339	342	351	360	374	379	380	384	377	354	340
McMurdo Sound, Antarctica	45	77 51S	166 40E	302	301	310	307	310	311	312	315	308	304	299	299
Medford, Oreg.	405	42 23N	122 52W	305	303	301	300	304	307	306	305	306	307	307	307
Melbourne, Australia	44	37 49S	144 58E	328	328	330	326	321	324	322	319	320	319	324	322
Merida, Mexico	22	20 58N	89 31W	350	349	354	363	369	376	379	378	381	370	357	353
Mersa Matruh, United Arab Republic	25	31 20N	27 13E	319	319	321	323	336	348	361	361	345	340	334	323
Miami, Fla.	4	25 49N	80 17W	341	343	347	357	367	375	379	379	380	362	352	346
Milano, Italy	120	45 28N	09 17E	313	315	315	319	330	340	346	348	340	329	319	316
Moscow, U.S.S.R.	156	55 49N	37 37E	307	306	305	306	314	322	332	327	318	313	310	307

TABLE B-1. (*Continued*)

Station	Elevation (meters)	Latitude	Longitude	Jan.	Feb.	Mar.	Apr.	May	June	July	Aug.	Sept.	Oct.	Nov.	Dec.
Mould Bay, Northwest Territories	15	76 14N	119 20W	331	330	332	322	314	314	316	317	312	313	323	328
Murmansk, U.S.S.R.	50	68 58N	33 03E	309	309	308	308	310	315	324	325	317	313	311	309
Mys Cheliuskin, U.S.S.R.	13	77 43N	104 17E	328	326	326	318	314	315	317	316	314	312	320	321
Mys Kamenny, U.S.S.R.	7	68 28N	73 36E	319	321	318	314	313	316	321	327	314*	314	315	322
Mys Schmidt, U.S.S.R.	7	68 55N	179 29W	322	326	325	318	313	317	318	318	316	312	315	320*
Nagphur, India	310	21 06N	79 07E	319	300	297	305	308	343	370	369	361	341	321	317
Nairobi, Kenya	1798	01 18S	36 45E	277	278	277	289	289	282	281	280	277	276	284	286
Nandi, Fiji Islands	16	17 45S	177 27E	380	382	381	379	373	367	364	362	367	367	371	373
Nantucket, Mass.	14	41 15N	70 04W	311	312	312	318	327	340	355	354	347	330	320	313
Naryan-Mar, U.S.S.R.	7	67 39N	53 01E	313	313	313	312	313	315	325	325	318	313	313	315
Nashville, Tenn.	184	36 07N	86 41W	309	311	311	324	338	351	363	361	340	326	313	312
Naval Orcades Island	4	60 45S	44 43W	309	308	307	308	307	307	309	306	307	307	307	307
Neuquen, Argentina	270	38 57S	68 07W	296	303	305*	310*	304	300	304	302	299	300	297	296
New Delhi, India	216	28 35N	77 12E	313	311	308	299	306	334	373	379	362	332	318	313
Niamey, Niger	226	13 29N	02 10E	286	281	285	308	331	351	362	369	369	343	308	294
Nicosia, Cyprus	218	35 09N	33 17E	317	315	313	314	315	325	326	331	325	318	320	319
Nitchequon, Quebec	515	53 12N	70 35W	298	296	293	291	293	299	311	307	301	296	293	295
Nome, Alaska	14	64 30N	165 26W	313	315	315	313	313	320	326	326	318	311	312	315
Norfolk Island	110	29 03S	167 56E	352	357	349	348	336	336	331	334	335	337	340	348
Norman Wells, Northwest Territories	64	65 18N	126 51W	322	321	317	310	308	314	327	325	315	309	315	318
North Platte, Nebr.	850	41 08N	100 42W	282	281	281	282	295	307	317	314	294	289	283	281
Norway Base, Antarctica	50	70 20S	02 00W	302	303	303	309	309	311	313	313	309	305	301	302
Nouvelle Amsterdam Island	28	37 50S	77 34E	340	339	336	335	332	324	327	328	325	328	330	339
Oakland, Calif.	6	37 44N	122 12W	323	324	324	326	329	334	337	337	335	330	323	321
Odessa, U.S.S.R.	64	46 29N	30 38E	312	313	312	315	327	334	337	336	326	323	321	315
Okhotsk, U.S.S.R.	7	59 22N	143 12E	316	314	311	309	312	320	332	337	321	307	310	314
Omsk, U.S.S.R.	94	54 56N	73 24E	315	312	311	309	305	316	331	328	316	307	311	313
Onslow, Australia	4	21 40S	115 07E	344	350	355	332	327	330	321	317	322	316	325	337
Ostersund, Sweden	309	63 11N	14 37E	299	299	299	299	301	310	313	314	310	304	303	298
Ostrov Chetyrekhstolbovoy, U.S.S.R.	6	70 38N	162 24E	325	327	325	317	312	315	316	317	316	313	319	324
Ostrov Dikson, U.S.S.R.	20	73 30N	80 14E	324	323	318	315	313	315*	320	320	314	311	316	320
Papeete, Tahiti Island	2	17 33S	149 37W	375	376	378	377	375	368	366	362	363	368	373	375
Perth, Australia	60	31 57S	115 49E	330	330	333	330	327	326	325	323	323	324	320	324
Peshawar, West Pakistan	359	34 01N	71 35E	303	301	309*	312	304	305	347*	365*	373*	318	311	304
Petropavlovsk Kamcatskij, U.S.S.R.	7	52 58N	158 45E	303	304	305	305	309	320	326	331	320	311	306*	303
Ponape, Caroline Islands	37	06 58N	158 13E	379	380	380	384	385	386	384	384	384	384	384	378
Port Blair, India	79	11 40N	92 43E	364	365	369	371	385	384	382	386	384	382	378	367
Port Elizabeth, South Africa	61	33 59S	25 36E	351	350	350	339	331	328	329	328	332	335	339	346
Port Harrison, Quebec	20	58 27N	78 08W	319	318	317	312	313	315	321	322	317	313	310	314
Pretoria, South Africa	1368	25 45S	28 14E	301	300	298	287	275	270	270	266	276	282	294	299
Puerto Montt, Chile	3	41 28S	72 56W	336	337	331	328	326	328	326	324	325	326	326	331
Quetta/Samungli, West Pakistan	1601	30 15N	66 53E	263	258	267	269	262	276	282	276	270	261	256	259
Raizet, Guadaloupe Island	8	16 16N	61 31W	368	361	363	369	370	374	377	379	380	377	374	369
Raoul Island	49	29 15S	177 55W	349	352	353	346	342	334	331	331	333	335	338	346
Resistencia, Argentina	52	27 28S	58 59W	356	362	362	353	346	332	329	332	337	345	342	354
Resolute Bay, Northwest Territories	64	74 43N	94 59W	325	328	330	319	311	313	315	315	310	310	319	320
Roma, Italy	131	41 48N	12 36E	314	317	316	319	328	334	338	339	335	326	321	318
Saigon, Viet Nam	10	10 49N	106 40E	363	362	369	375	384	386	384	386	384	383	373	370
Saint Paul, Alaska	6	57 09N	170 13W	313	311	311	312	314	320	326	326	322	315	311	312
Salisbury, Rhodesia	1480	17 56S	31 05E	302	305	295	288	279	277	271	270	274	275	288	300
Salt Lake City, Utah	1288	40 46N	111 58W	270	268	265	264	268	267	270	272	265	268	270	271
Samarovo, U.S.S.R.	37	60 58N	69 04E	316	312	311	309	310	321	330	329	318	311	314	315
Samsun, Turkey	44	41 17N	36 20E	311	313	316	320	330	343	346	347	337	329	322	313
San Diego, Calif.	9	32 44N	117 10W	320	325	325	328	332	339	346	350	346	337	323	317
San Juan, P. R.	19	18 26N	66 00W	358	358	359	363	371	376	378	378	378	374	370	365
Sapporo, Japan	18	43 03N	141 20E	309	309	310	310	318	332	349	353	337	323	313	309
Saratov, U.S.S.R.	135	51 34N	46 00E	304	306	303	305	307	315	322	318	314	307	305	305
Sault Ste. Marie, Mich.	221	46 28N	84 22W	307	306	304	305	309	325	333	332	323	315	307	306
Shemya, Alaska	37	52 43N	174 06E	308	308	311	315	318	321	327	327	324	316	310	307
Singapore	18	01 21N	103 54E	375	377	382	385	387	384	383	382	382	382	380	381
Sodankyla, Finland	179	67 22N	26 39E	306	306	306	304	305	309	319	320	313	307	307	306
Stanley, Falkland Islands	53	51 42S	57 52W	317	316	318	316	313	312	313	311	312	312	314	314
Stockholm, Sweden	52	59 21N	18 04E	311	310	310	311	311	318	328	329	324	321	315	312
Stuttgart, Germany	315	48 50N	09 12E	303	303	304	306	313	319	322	325	319	312	306	302
Sverdlovsk, U.S.S.R.	284	56 50N	60 38E	306	303	302	300	302	314	324	319	309	303	305	304
Swan Island	10	17 24N	83 56W	368	364	371	377	382	386	387	387	388	383	375	371
Syktyvkar, U.S.S.R.	96	61 40N	50 51E	311	309	308	308	310	317	325	324	318	312	311	311
Tacubaya, Mexico	2306	19 24N	99 12W	249	247	242	247	252	263	265	266	265	258	254	251
Taipei, Taiwan	8	25 02N	121 31E	338	342	349	357	372	381	384	384	380	364	357	343
Tamanrasset, Algeria	1378	22 48N	05 32E	246	248	244	243	243	252	251	252	255	251	252	250
Tananarive, Malagasy Republic	1310	18 54S	47 32E	312	311	312	307	299	295	291	289	290	294	305	311
Tashkent, U.S.S.R.	478	41 20N	69 18E	296	295	298	304	308	301	302	304	297	297	300	300
Tatoosh Island, Wash.	26	48 23N	124 44W	318	321	317	321	328	332	336	340	336	328	324	321
Tbilisi, U.S.S.R.	404	41 43N	44 48E	299	297	298	305	314	320	331	330	321	311*	308	303
The Pas, Manitoba	272	53 58N	101 06W	310	305	302	301	304	316	326	326	312	305	303	305
Tourane, Viet Nam	7	16 02N	108 11E	365*	366	372*	382*	385*	383*	385*	390*	389*	386*	376*	363*
Townsville, Australia	4	19 15S	146 46E	376	378	371	363	351	339	333	336	339	356	361	366
Trivandrum, India	64	08 29N	76 57E	362	364	370	380	385	382	382	380	379	380	378	368
Tromso, Norway	9	69 42N	19 01E	307	309	311	310	316	321	328	328	321	313	312	308
Tura, U.S.S.R.	147	64 16N	100 14E	334	324	307*	304	301*	313	324	318	310	306	316*	329

TABLE B-1. *(Continued)*

Station	Elevation (meters)	Latitude	Longitude	Jan.	Feb.	Mar.	Apr.	May	June	July	Aug.	Sept.	Oct.	Nov.	Dec.
Turukhansk, U.S.S.R.	37	65 47N	87 57E	324	318	312	308	305	311	323	324	316	310	316	324
Ushuaia, Argentina	6	54 48S	68 19W	311	312	307	308	308	310	310	308	309	305	305	303
Valentia, United Kingdom	14	51 56N	10 15W	320	319	321	322	325	332	337	336	335	329	324	320
Valparaiso, Chile	41	33 01S	71 39W	345	346	343	334	332	333	331	332	332	334	335	338
Vera Cruz, Mexico	16	19 12N	96 08W	361	367	370	380	382	386	386	387	383	379	368	361
Verkhoyansk, U.S.S.R.	135	67 33N	133 23E	345	341	320	307	301	308	316	314	307	310	331	345
Vishakhapatnam, India	3	17 43N	83 14E	357	356	369	391	392	391	384	386	389	380	358	353
Vladivostok U.S.S.R.	138	43 07N	131 54E	308	305	304	307	314	329	347	350	332	311	304	306
Vologda, U.S.S.R.	118	59 17N	39 52E	309	308	307	308	312	325	335	330	319	314	311	309
Wajima, Japan	7	37 23N	136 54E	314	314	316	322	332	348	369	371	355	336	324	318
Wake Island	4	19 17N	166 39E	356	359	363	367	371	378	380	384	383	380	373	368
Washington, D. C.	20	38 51N	77 02W	310	311	309	320	328	342	354	352	343	328	316	313
Whitehorse, Yukon	698	60 43N	135 04W	291	287	284	282	282	287	292	293	289	284	284	289
Wien/Hohe-Warte, Austria	203	48 15N	16 22E	306	307	307	309	316	325	332	333	322	317	312	308
Wilkes Stn., Antarctica	12	66 15S	110 35E	301	302	300	303	303	306	307	303	303	301	299	302
Windhoek, South-West Africa	1728	22 34S	17 06E	263	269	267	265	248	247	245	241	237	240	256	250
Ship A	‡	62 00N	33 00W	307	312	312	315	317	323	326	324	320	314	311	306
Ship B	‡	56 30N	51 00W	310	310	312	312	318	321	326	325	320	315	311	309
Ship C	‡	52 45N	35 30W	317	315	315	321	322	328	332	333	330	323	319	315
Ship D	‡	44 00N	41 00W	327	323	324	328	334	340	356	360	348	336	330	330
Ship E	‡	35 00N	48 00W	339	336	337	341	351	366	374	374	368	357	349	346
Ship I	‡	59 00N	19 00W	315	315	316	319	321	327	330	328	324	320	318	315
Ship J	‡	52 30N	20 00W	322	319	321	323	324	333	337	337	333	327	326	319
Ship K	‡	45 00N	16 00W	329	322	327	329	335	342	348	348	345	338	330	332
Ship M	‡	66 00N	02 00E	312	314	315	316	319	321	327	327	326	318	318	312
Ship N	‡	30 00N	140 00W	340	339	335	338	340	344	349	351	350	348	345	342
Ship P	‡	50 00N	145 00W	316	318	318	317	324	328	333	336	335	325	319	317
Ship V	‡	34 00N	164 00E	328	331	335	340	350	359	379	381	369	366	355	337

* *Less than 3 years of data.*
‡ *No elevation given.*

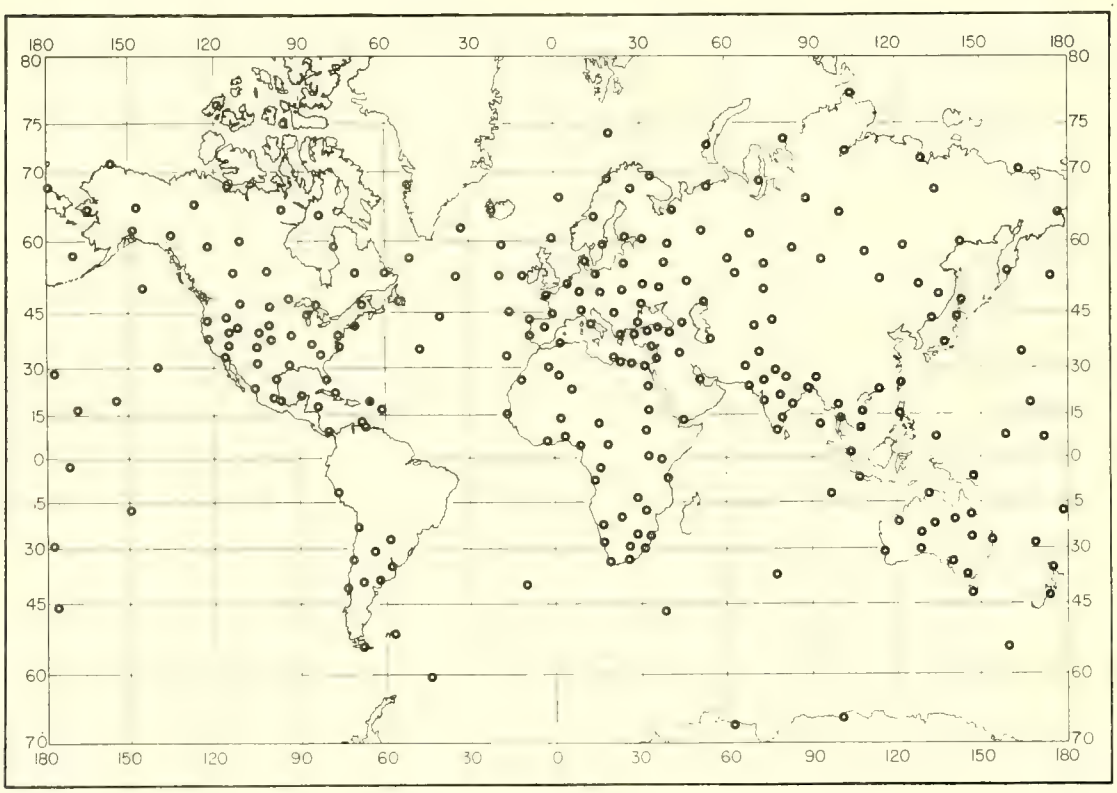

FIGURE B-1. *Location of* ΔN *data stations.*

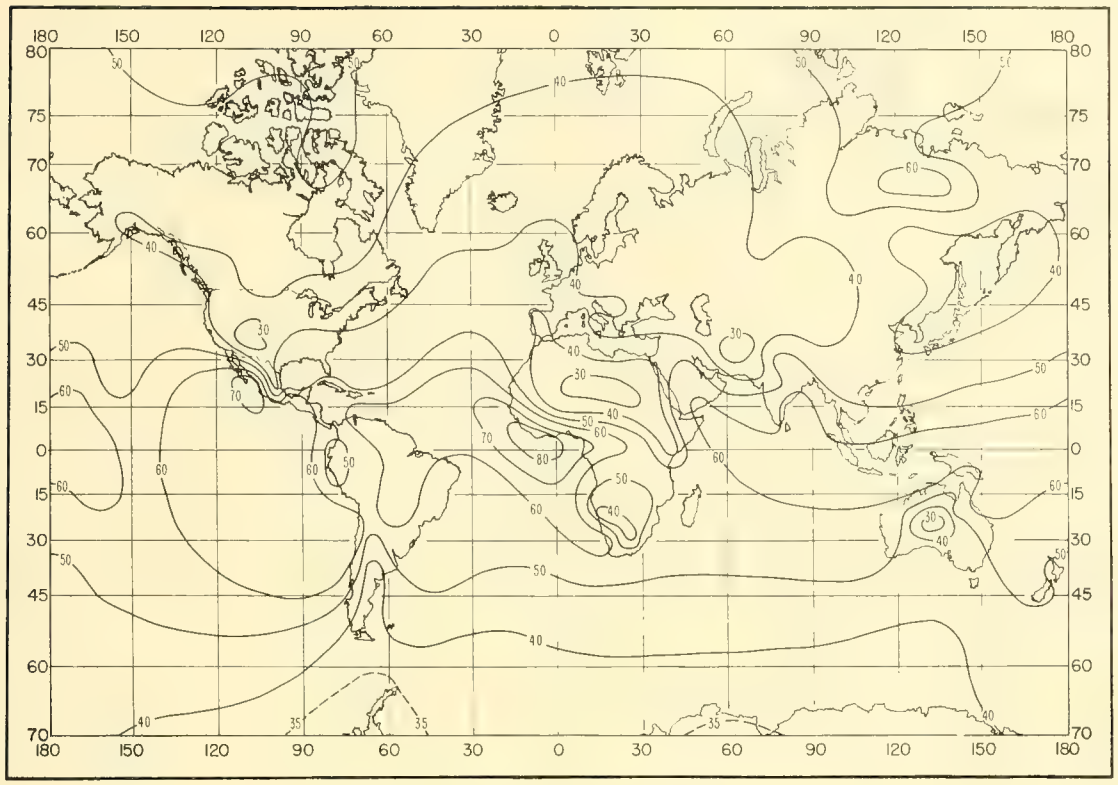

FIGURE B-2. *Monthly mean* ΔN: *January.*

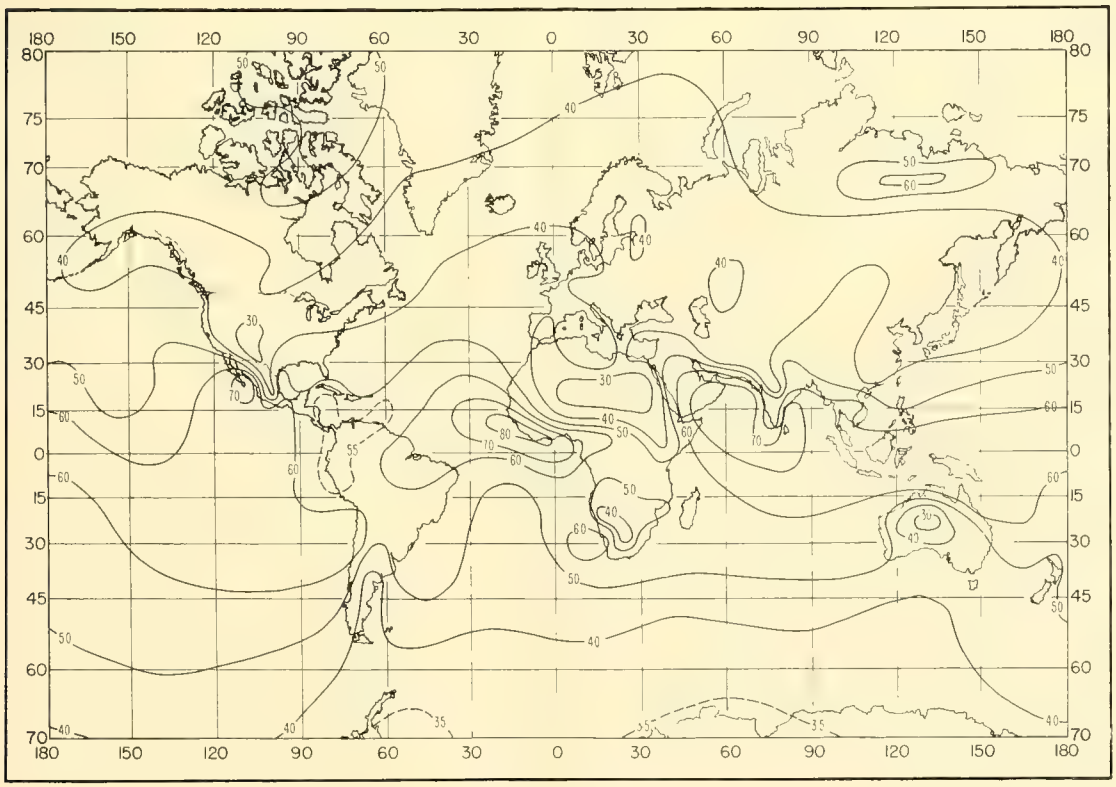

FIGURE B-3. *Monthly mean* ΔN: *February.*

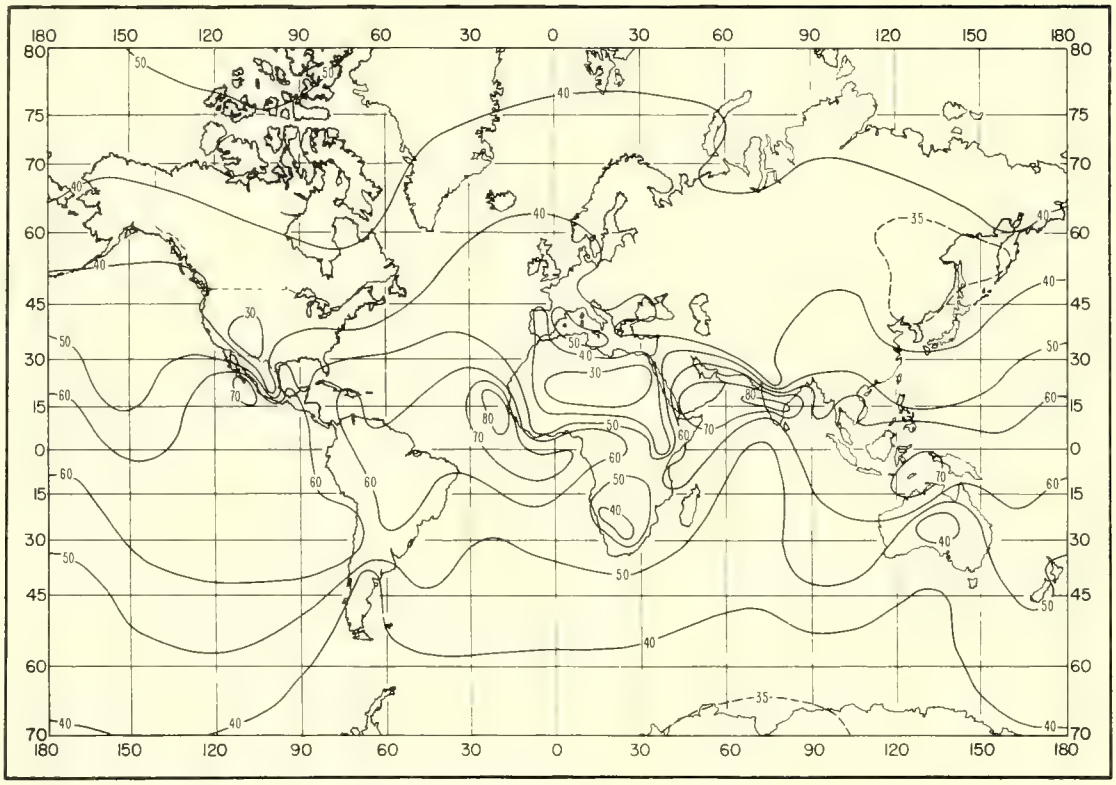

FIGURE B-4. *Monthly mean* ΔN: *March.*

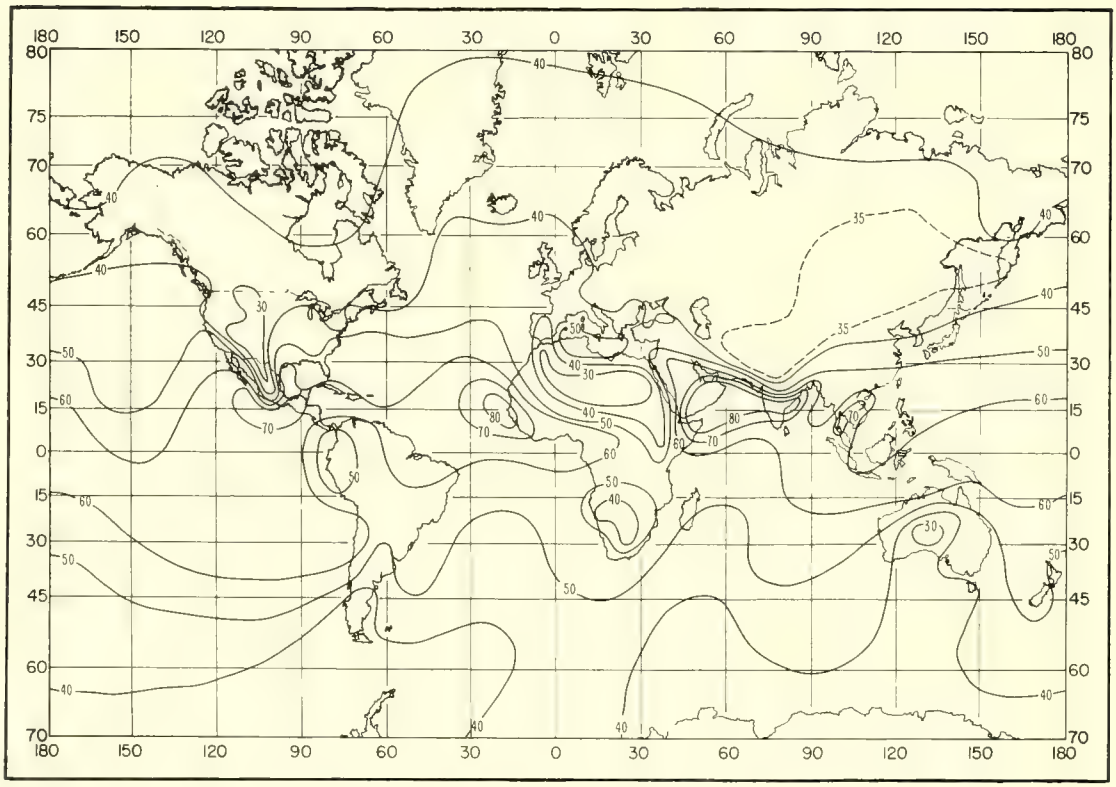

FIGURE B-5. *Monthly mean* ΔN: *April.*

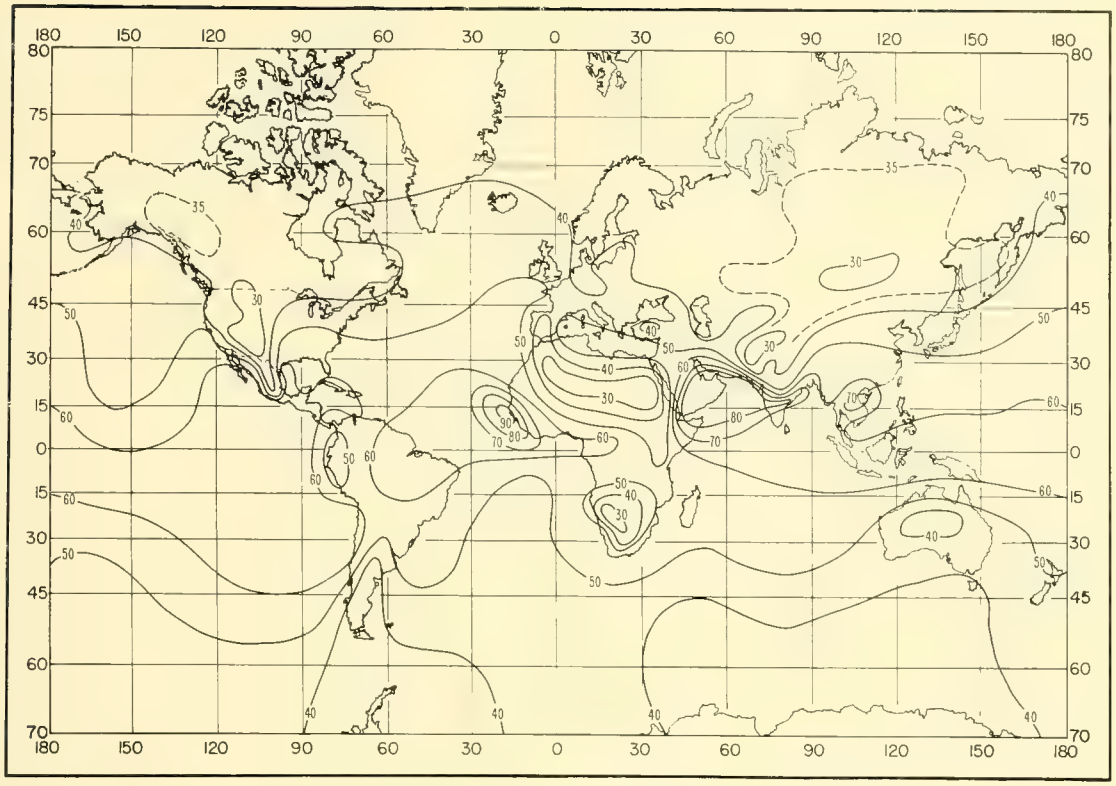

FIGURE B-6. *Monthly mean* ΔN: *May.*

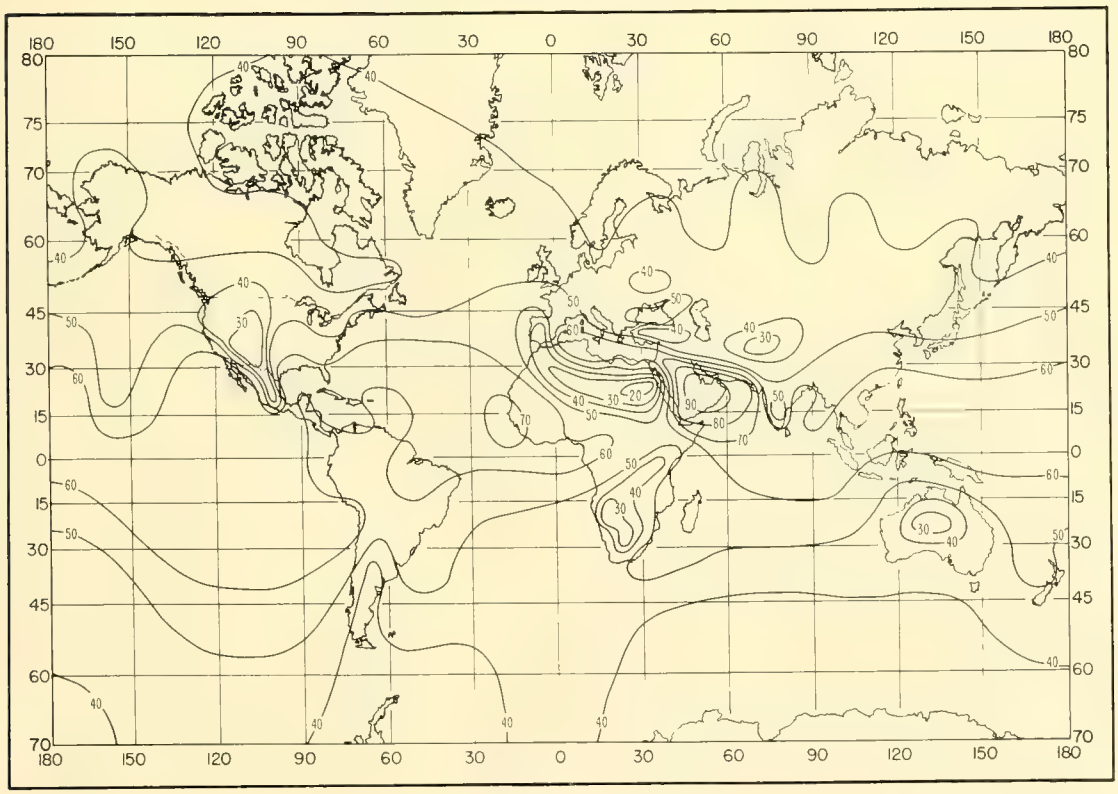

FIGURE B-7. *Monthly mean* ΔN: *June.*

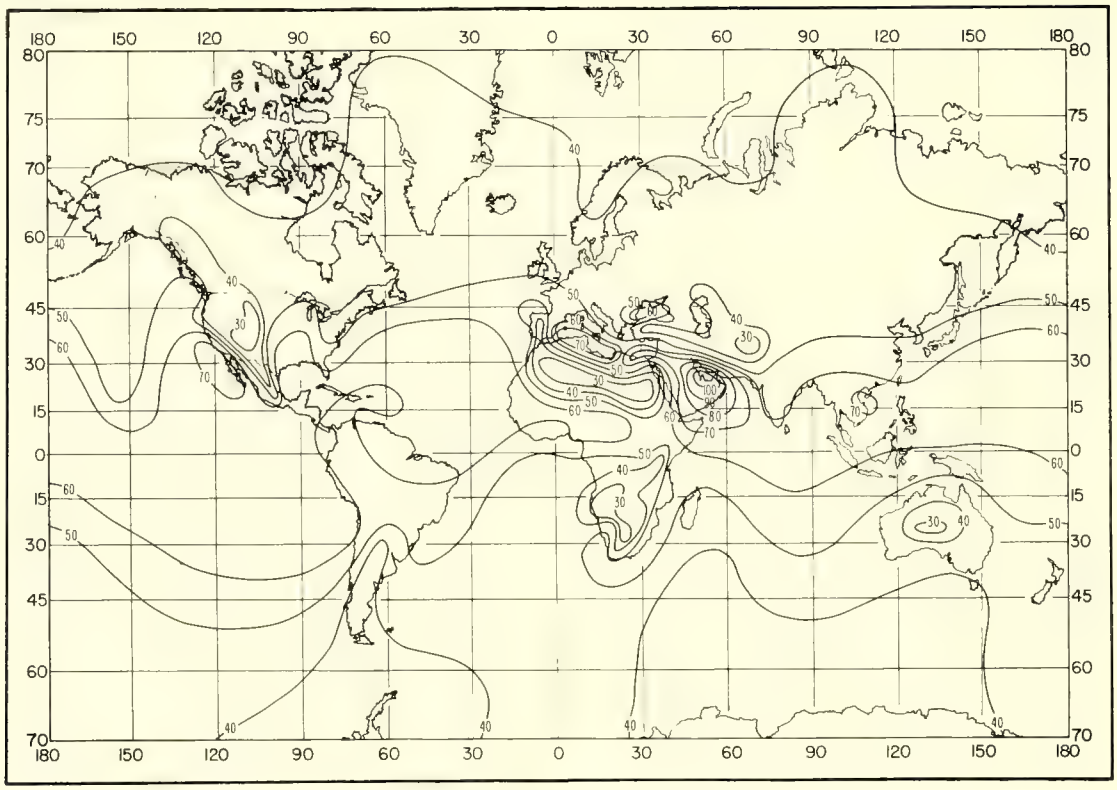

FIGURE B-8. *Monthly mean* ΔN: *July.*

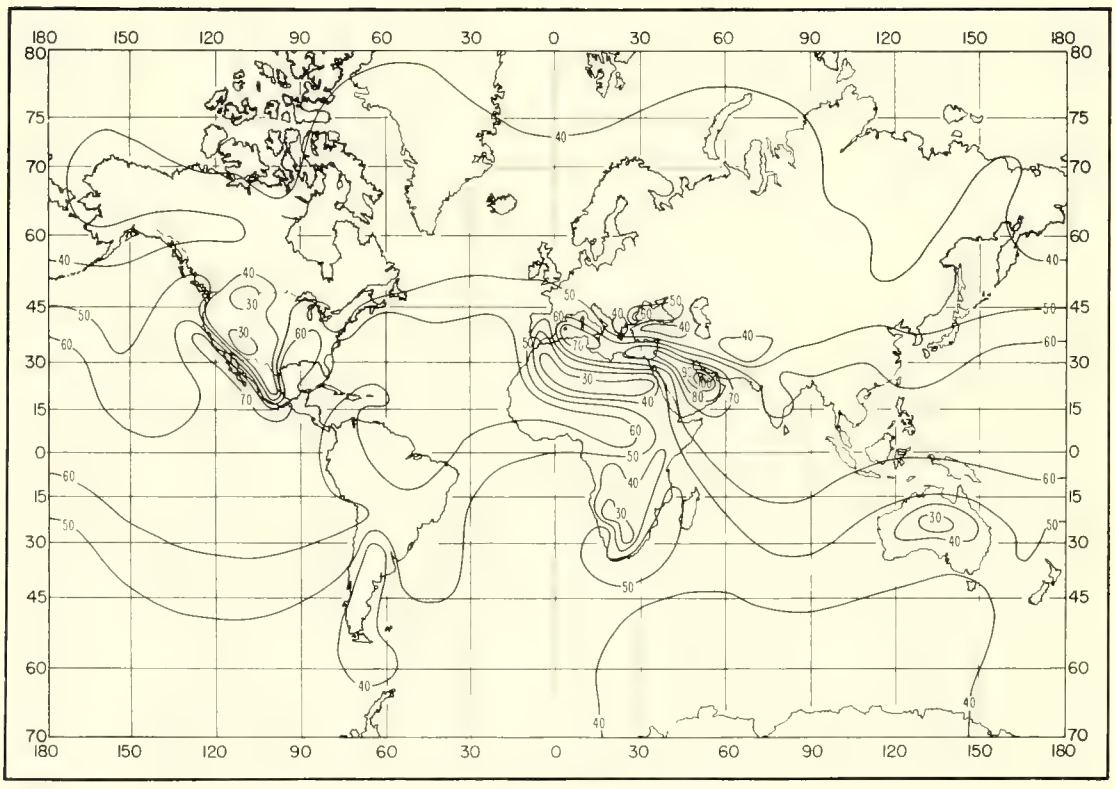

FIGURE B-9. *Monthly mean* ΔN: *August.*

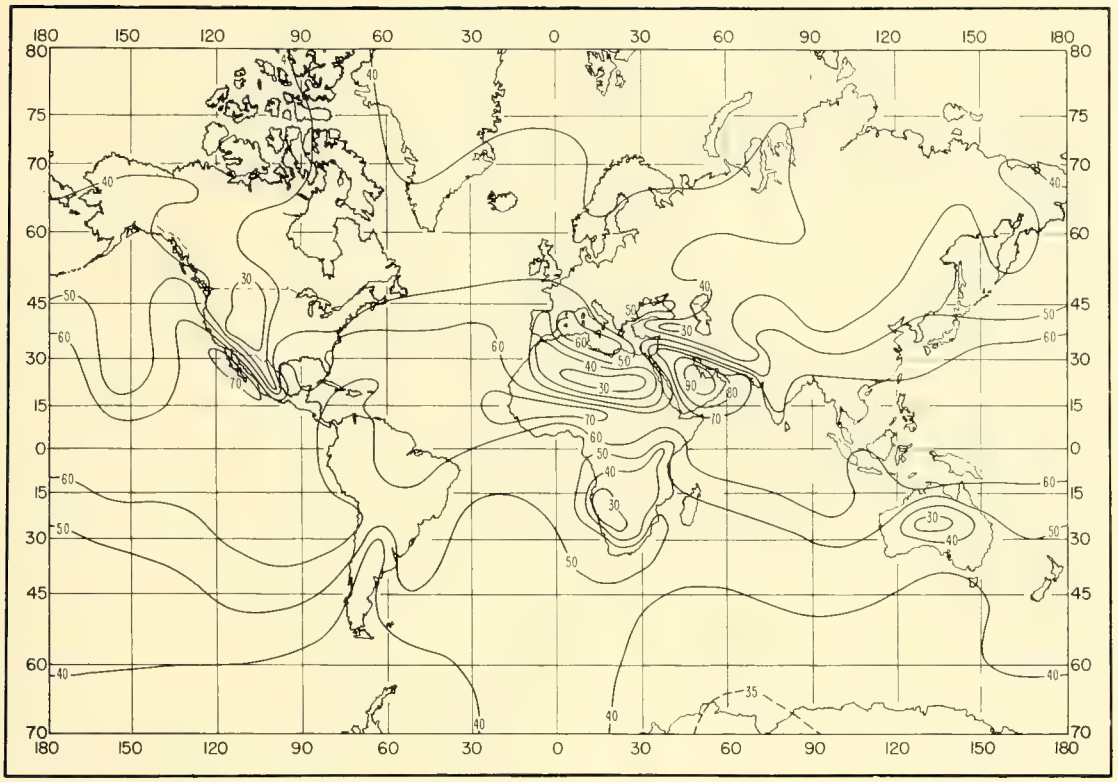

FIGURE B-10. *Monthly mean* ΔN: *September.*

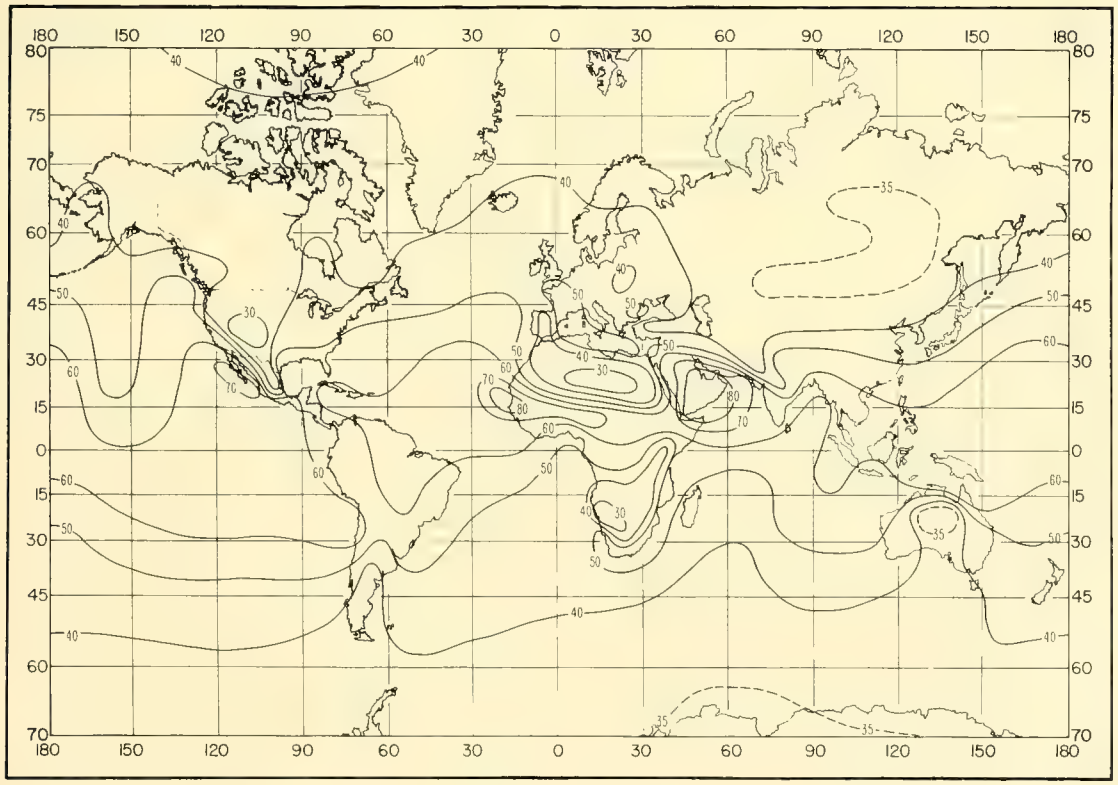

FIGURE B-11. *Monthly mean* ΔN: *October.*

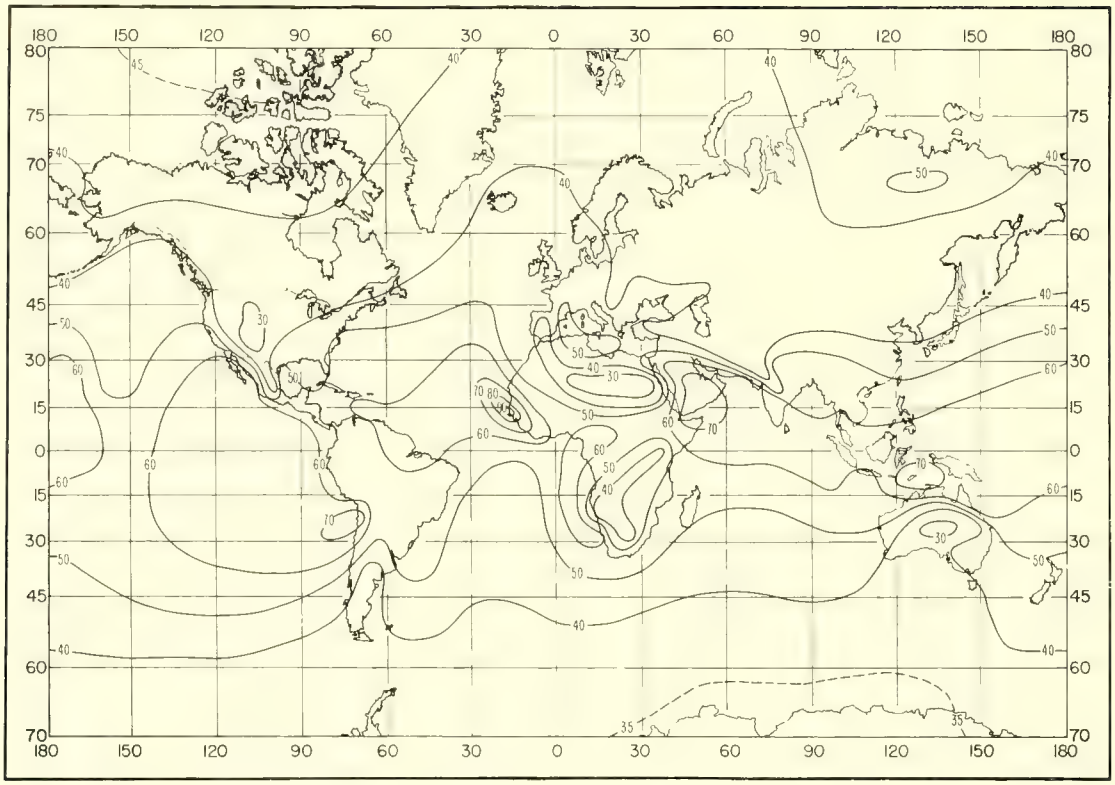

FIGURE B-12. *Monthly mean* ΔN: *November.*

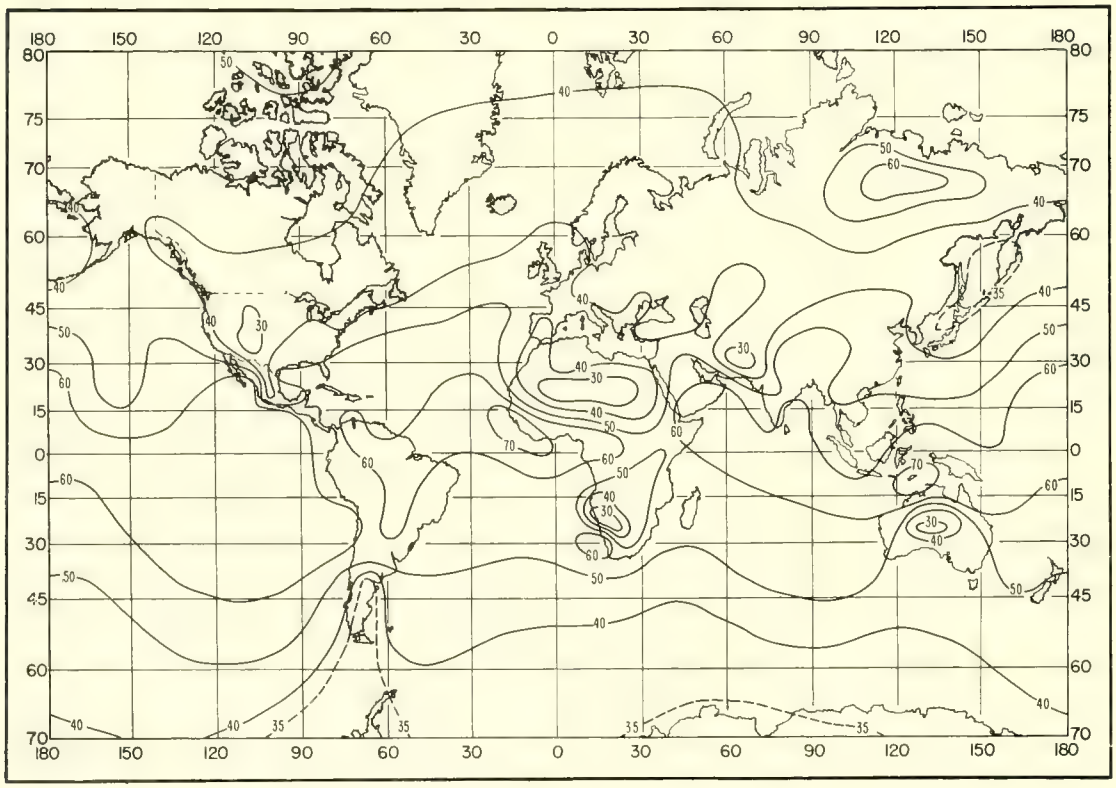

FIGURE B-13. *Monthly mean* ΔN: *December.*

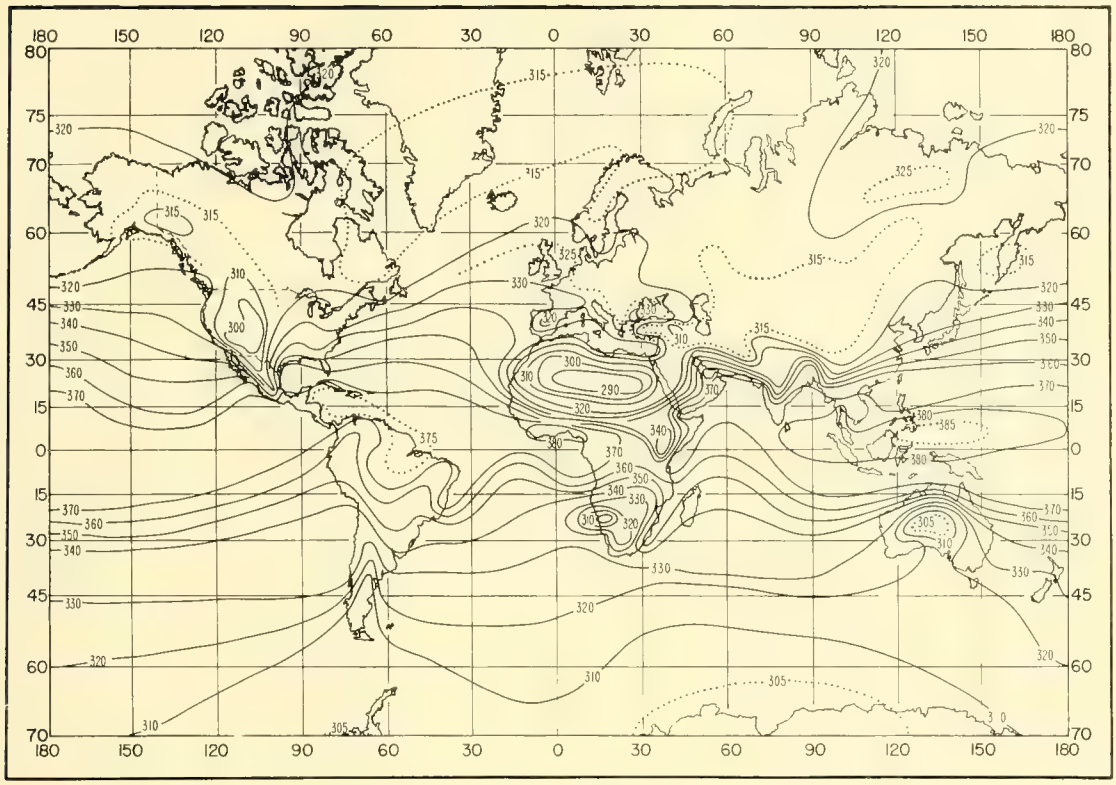

FIGURE B-14. *Annual mean of sea-level refractivity,* $\overline{\overline{N}}_o$.

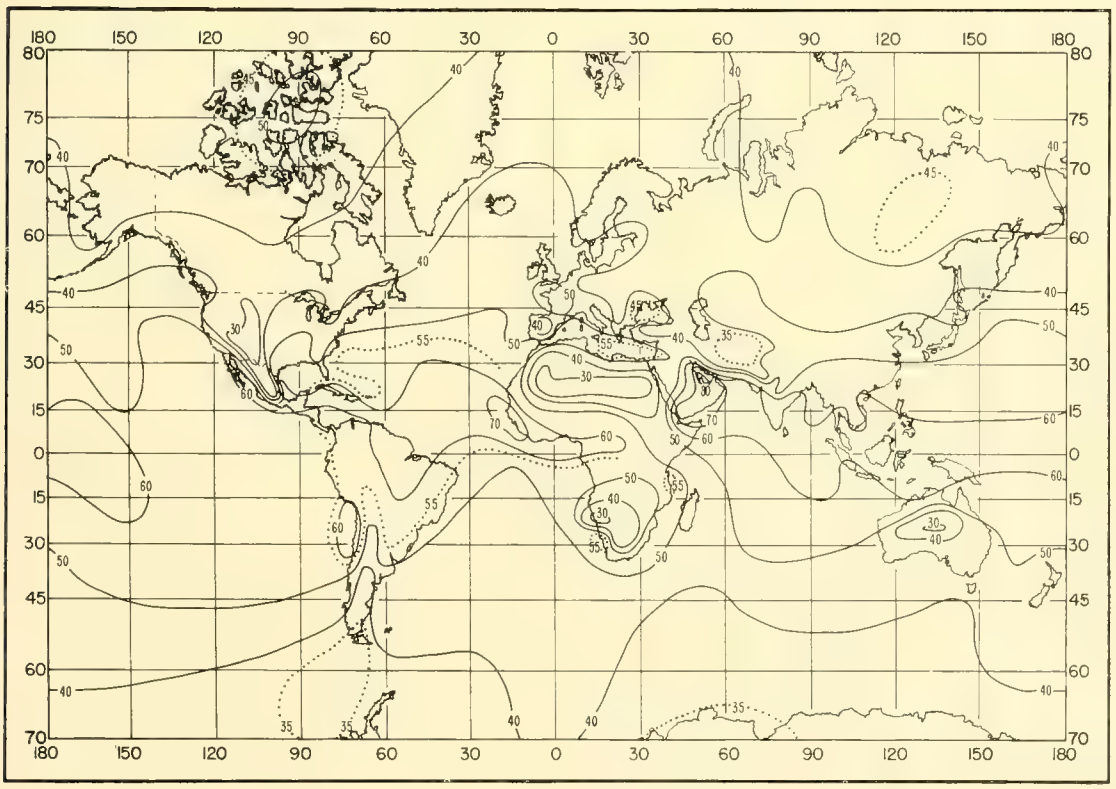

FIGURE B-15. *Annual mean of refractivity gradient between surface and 1 km,* $\overline{\overline{\Delta N}}$.

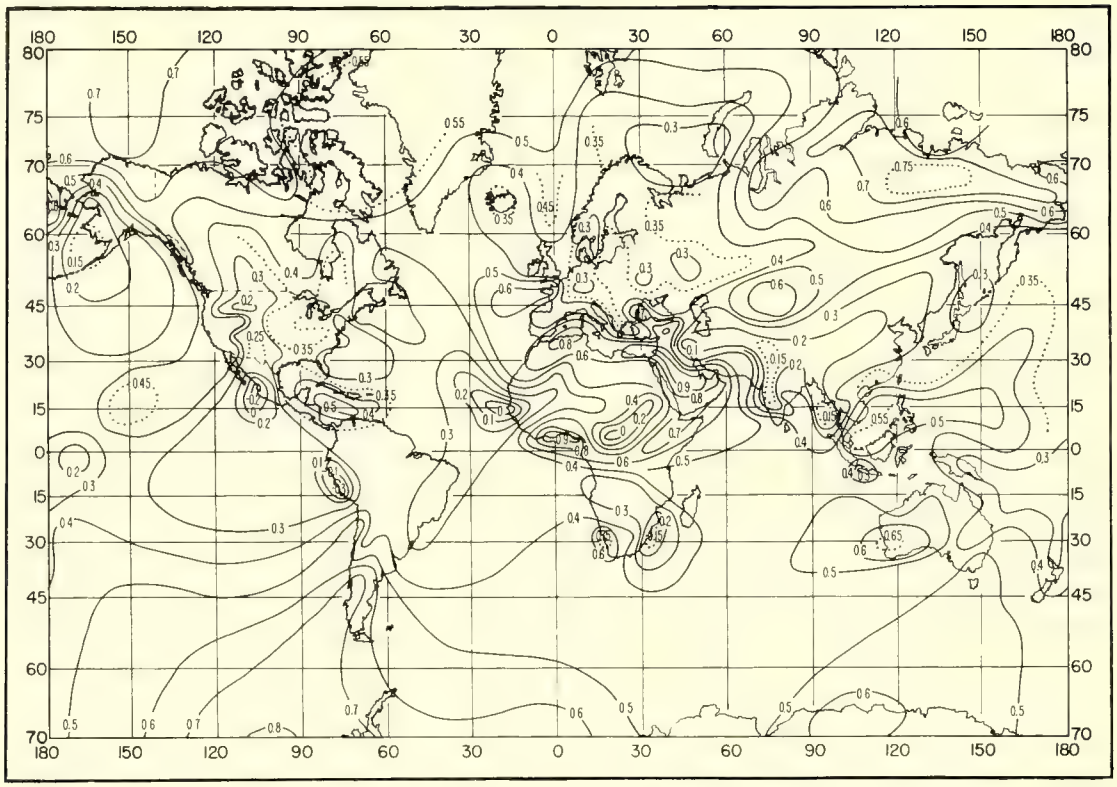

FIGURE B-16. *Slope of regression line of* $\overline{\Delta N}$ *versus* $\overline{N}_s$, b.

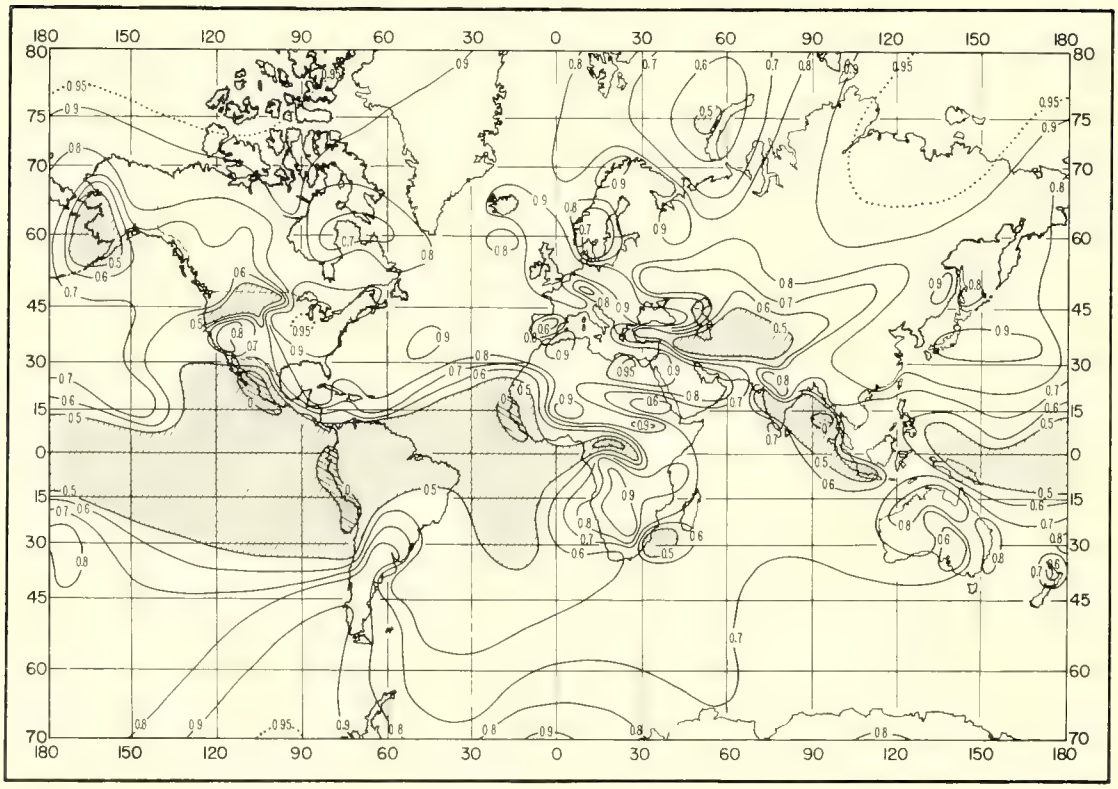

FIGURE B-17. *Correlation coefficient of* $\overline{\Delta N}$ *versus* $\overline{N}_s$.

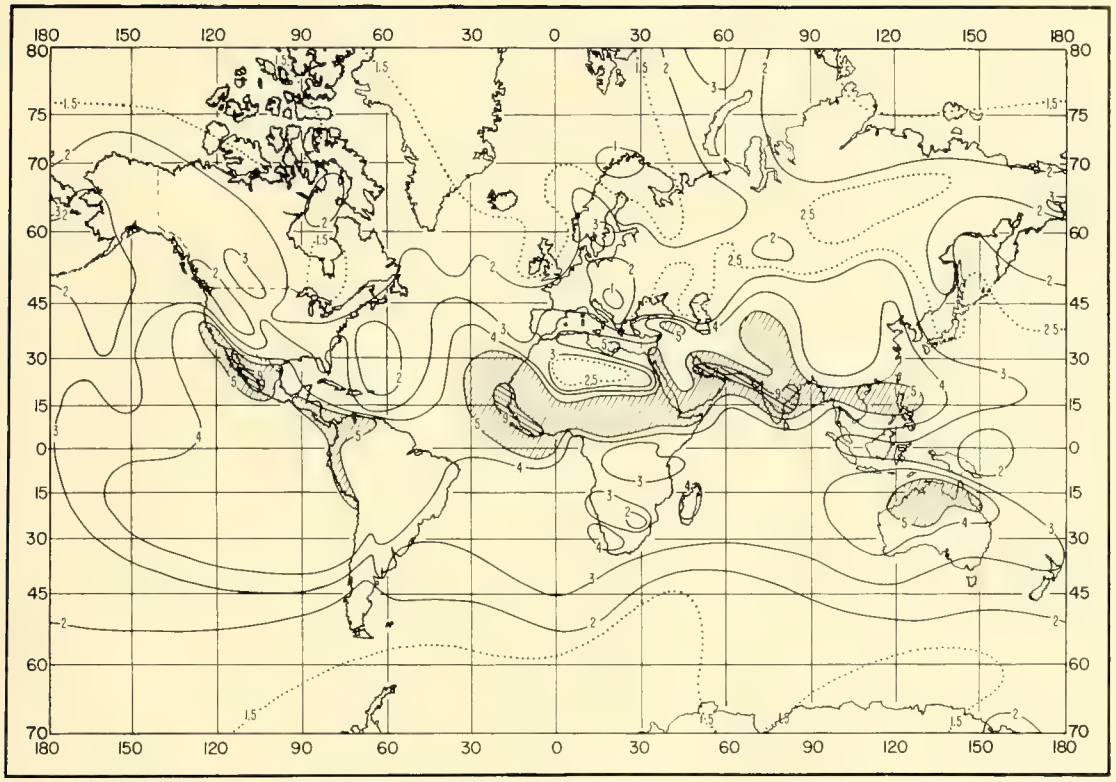

FIGURE B-18. *Standard prediction error of the regression line of* $\overline{\Delta N}$ *versus* $\overline{N}_s$.

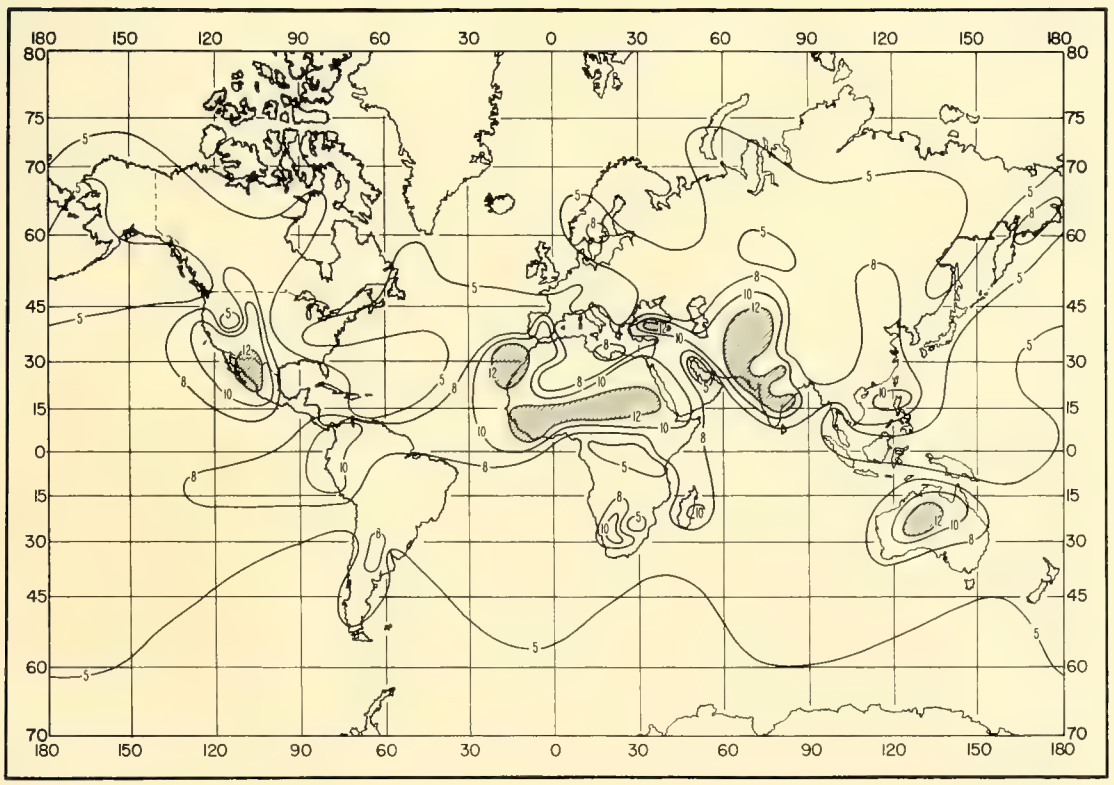

FIGURE B-19. *Standard prediction error of the regression line of* $\overline{\Delta N}$ *versus* $\overline{N}_s$ *as a percent of* $\overline{\overline{\Delta N}}$.

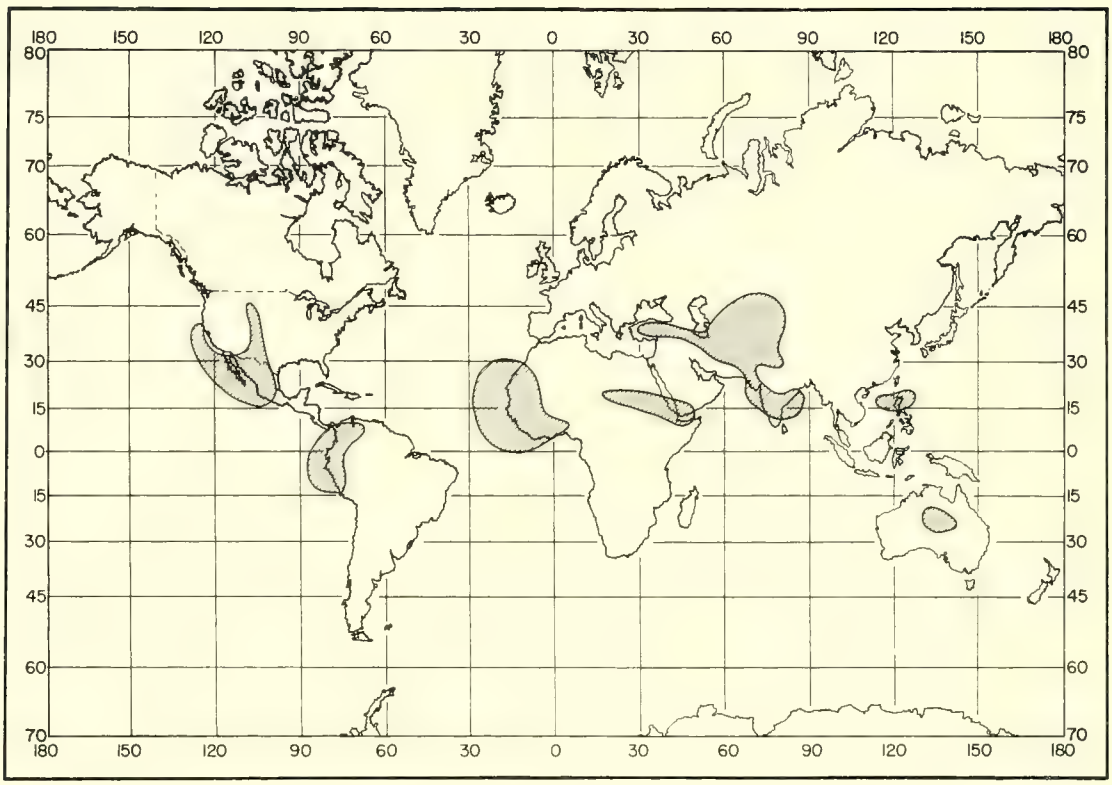

FIGURE B-20. *Areas of doubtful applicability of using* $\overline{N}_s$ *to predict* $\overline{\Delta N}$.

12. Appendix C. World Maps and Cumulative Distribution Charts of Gradients of Ground-Based Atmospheric Layers

Initial gradient data, obtained (see sec. 5) for 99 of the 112 stations listed in table A–1, are presented in groups of seasonal world maps which illustrate various aspects of the percentage distribution of gradients in ground-based layers. The specific map groups are given below.

Figures C-1 through C-4: Percent of time gradient $\geqq 0$ (N/km).

Figures C-5 through C-12: Gradient exceeded 10 and 2 percent of the time for 100-m layer.

Figures C-13 through C-20: Percent of time gradient $\leqq -100$ (N/km) and percent of superrefractive layers $>$ 100 m thick.

Figures C-21 through C-28: Percent of time gradient $\leqq -157$ (N/km) and percent of ducting layers $>$ 100 m thick.

Figures C-29 through C-40: Percentage of time trapping frequency is below 3000 Mc/s, below 1000 Mc/s, and below 300 Mc/s.

Figures C-41 through C-56: Lapse rate of refractivity (N/km) exceeded 25, 10, 5, and 2 percent of the time for 100-m layer.

Cumulative probability distribution charts were prepared for 22 climatically diverse locations for the months of February, May, August, and November (figs. C-57 through C-78). The alphabetical listing of these stations in table C-1 includes seasonal median and minimum trapping frequency values when these were available. Distribution data for two separate times of day at Aden and Nicosia are shown in figures C-57 and C-71. The negative gradient of 50 N-units/km, which is generally considered to be a good normal value for ground-based layers, has been indicated on each of the distributions by a dashed line to provide a common reference for the vertical scale. The circled value on the distribution line represents the *mean* ground-based gradient (of any layer thickness greater than 20 m) for each month.

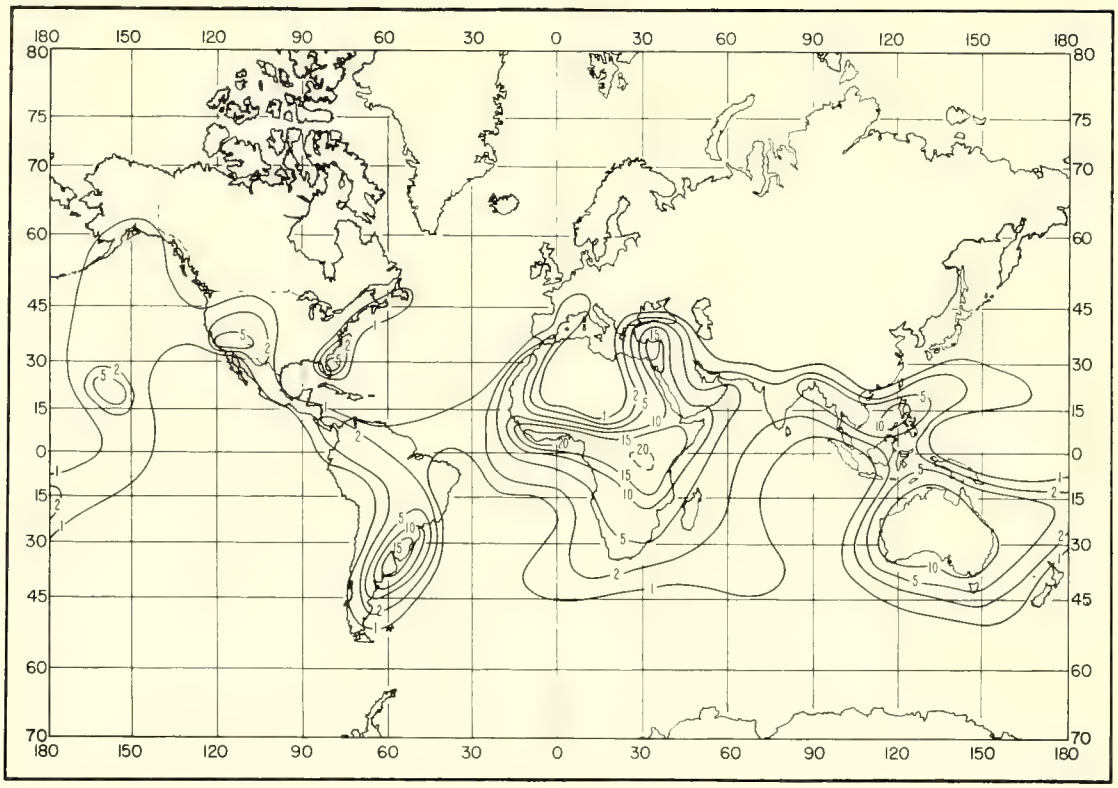

FIGURE C-1. *Percent of time gradient ≥ 0 (N/km): February.*

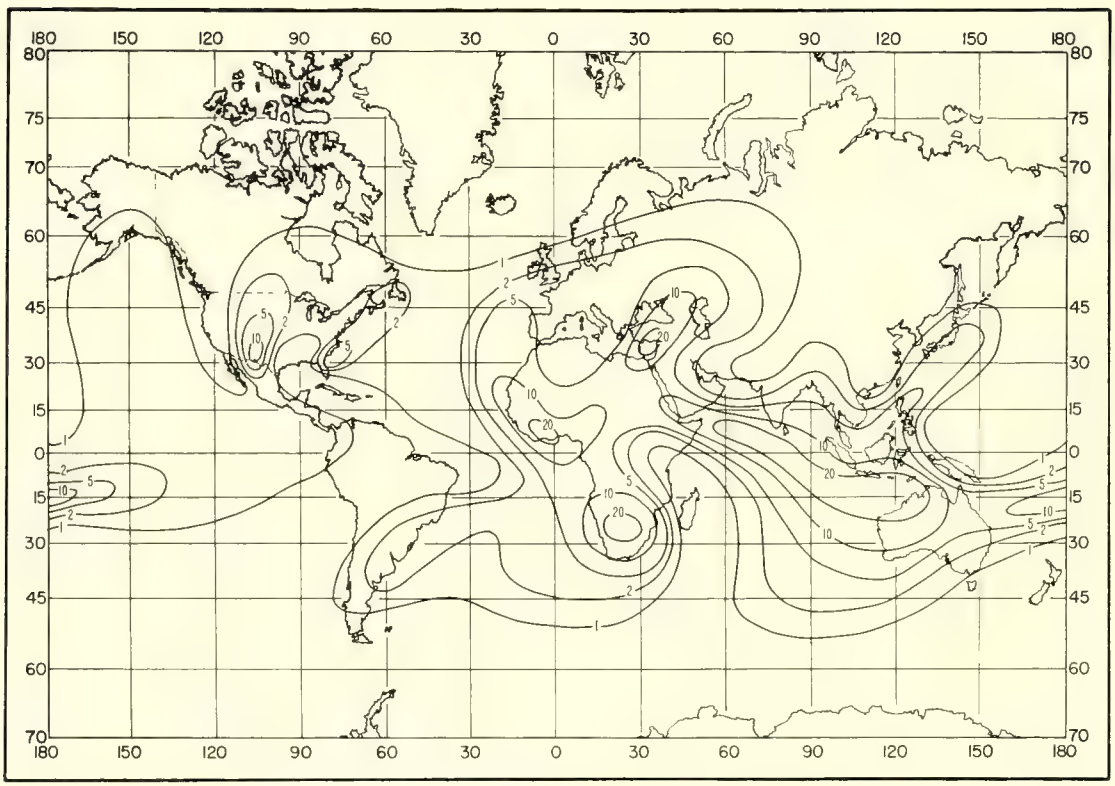

FIGURE C-2. *Percent of time gradient ≥ 0 (N/km): May.*

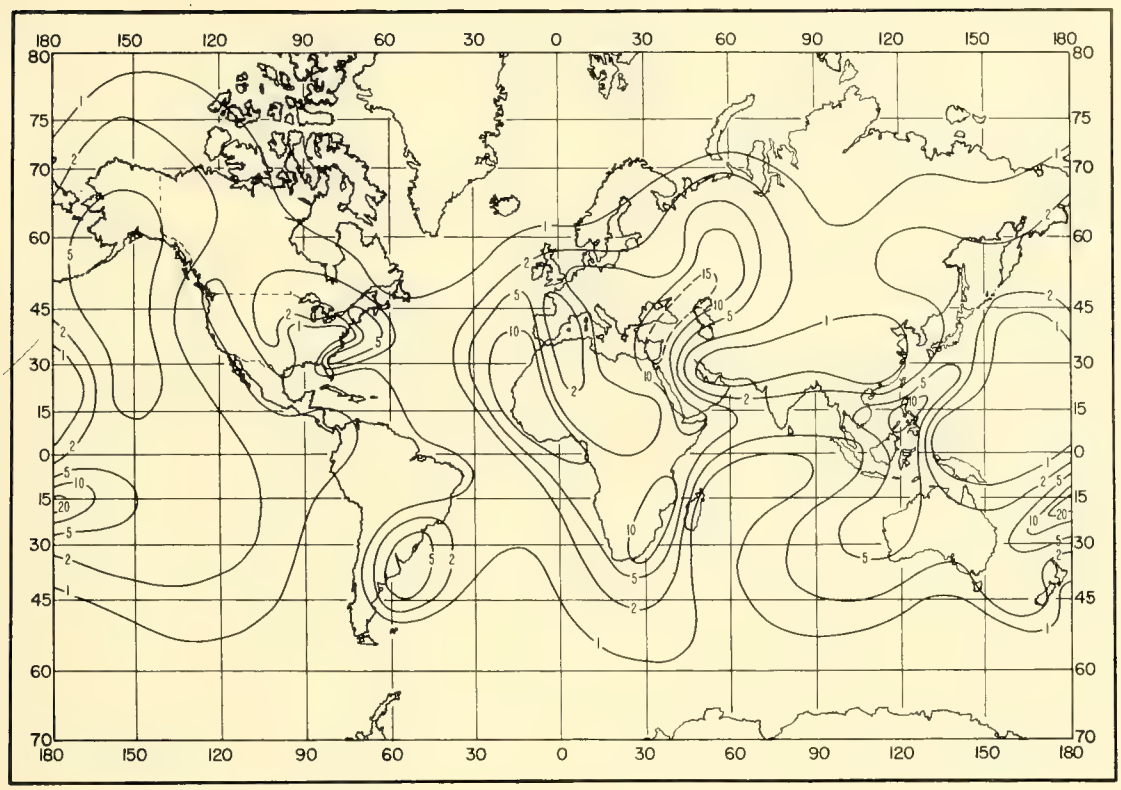

FIGURE C-3. *Percent of time gradient ≥ 0* (N/*km*): *August.*

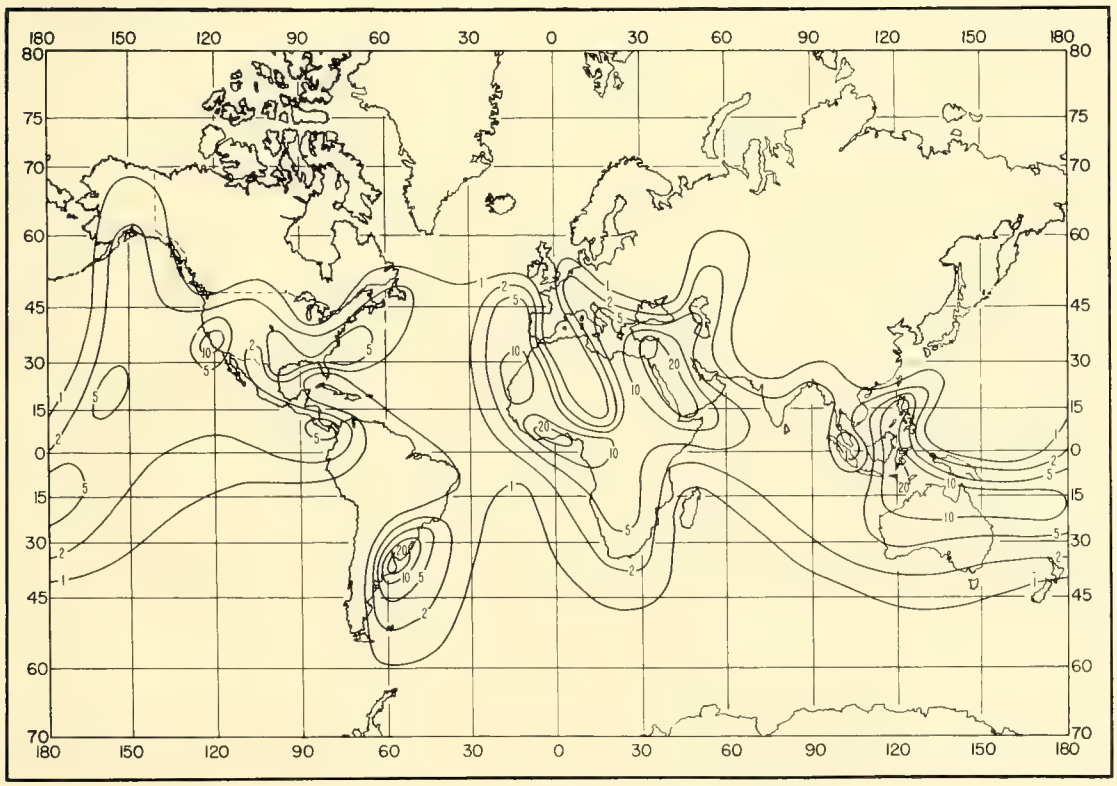

FIGURE C-4. *Percent of time gradient ≥ 0* (N/*km*): *November.*

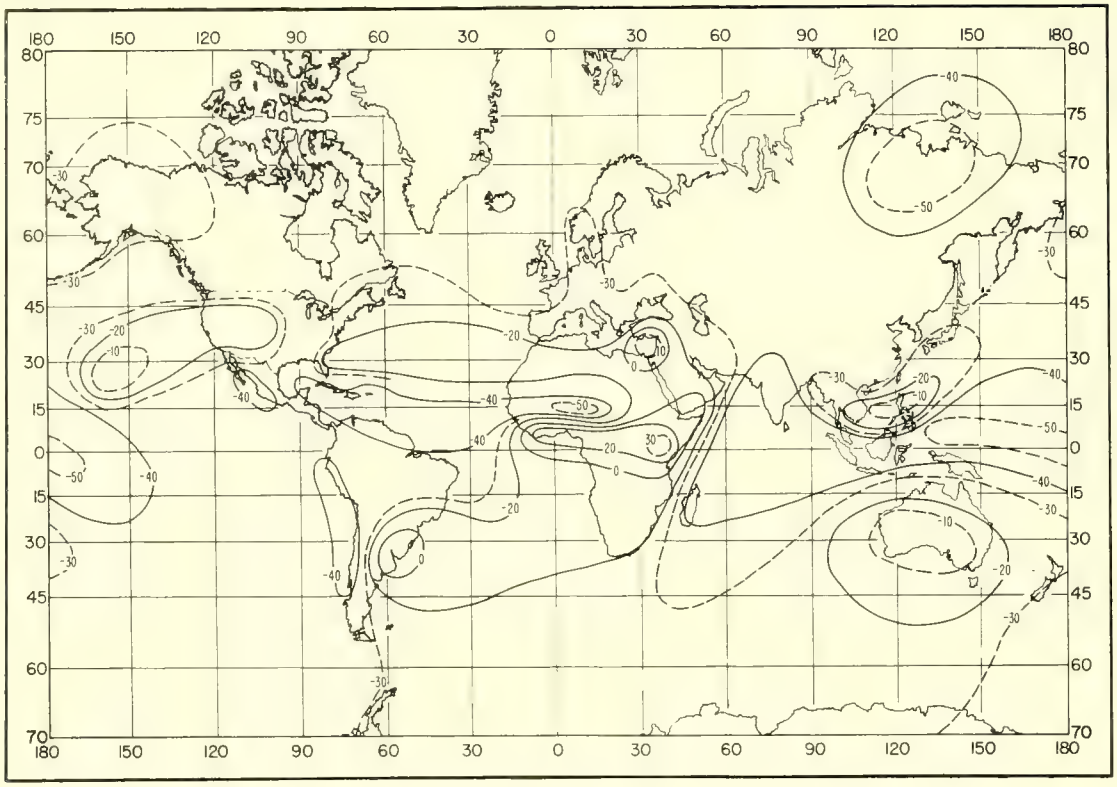

FIGURE C-5. *Gradient (N/km) exceeded 10 percent of the time for 100-m layer: February.*

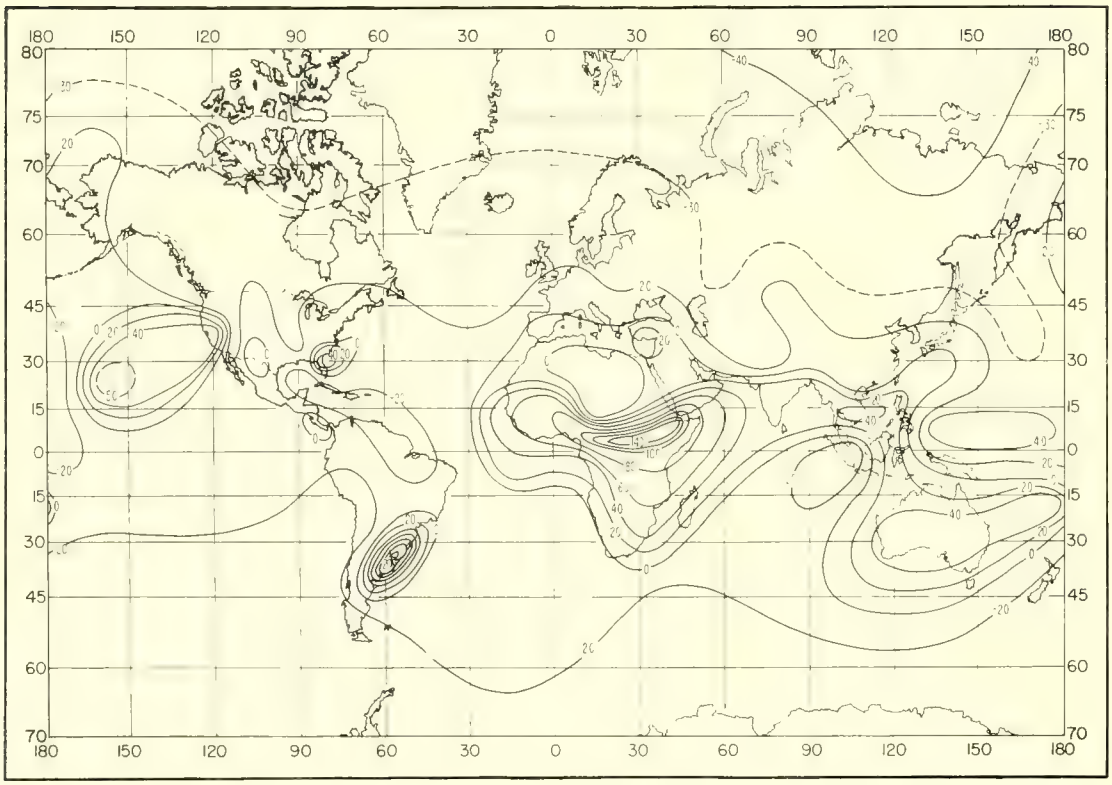

FIGURE C-6. *Gradient (N/km) exceeded 2 percent of the time for 100-m layer: February.*

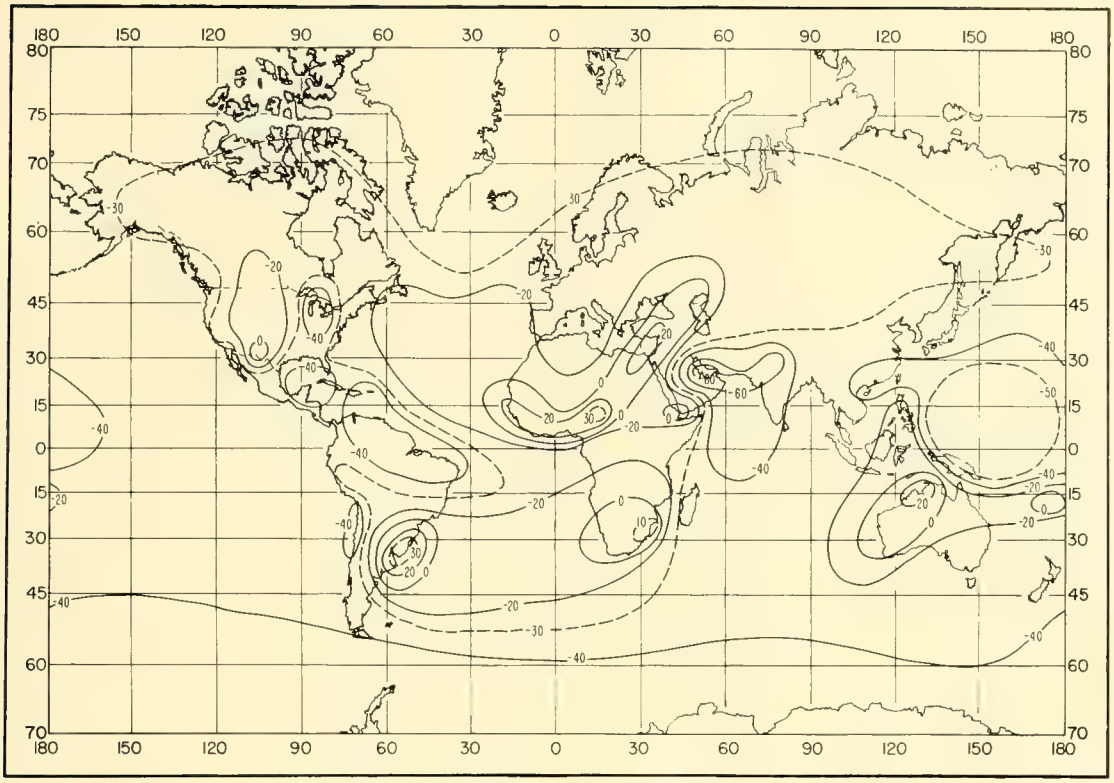

FIGURE C-7. *Gradient (N/km) exceeded 10 percent of the time for 100-m layer: May.*

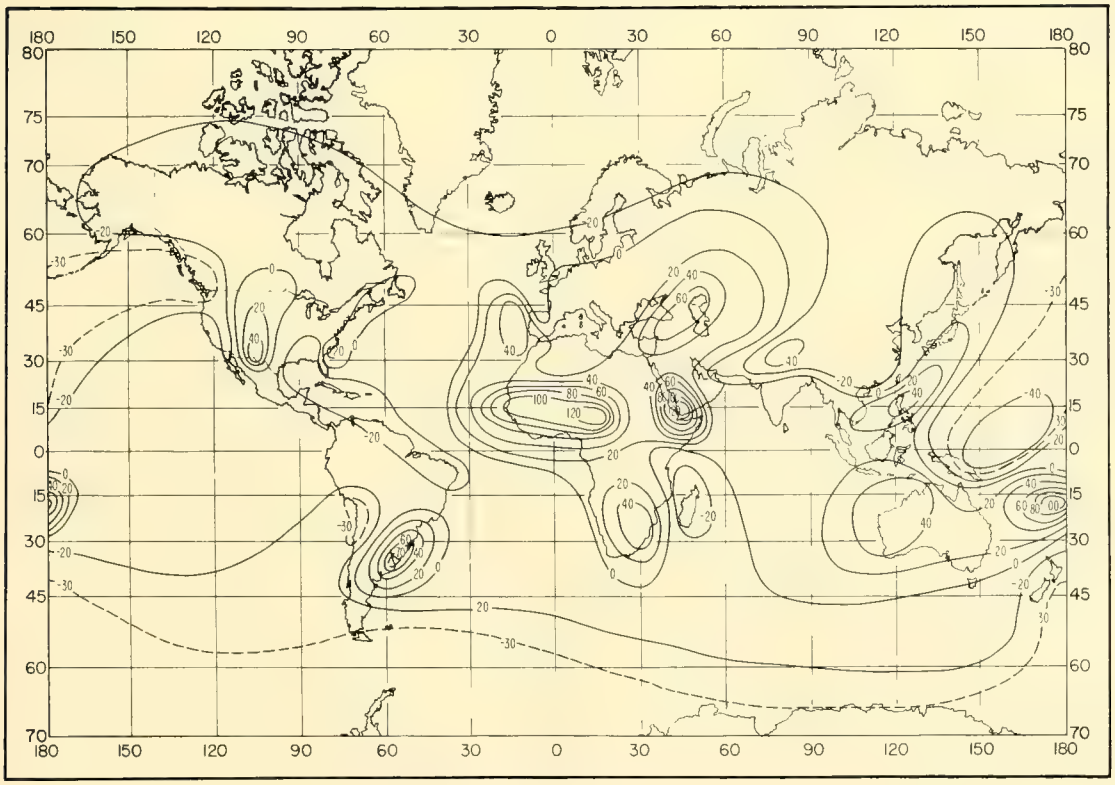

FIGURE C-8. *Gradient (N/km) exceeded 2 percent of the time for 100-m layer: May.*

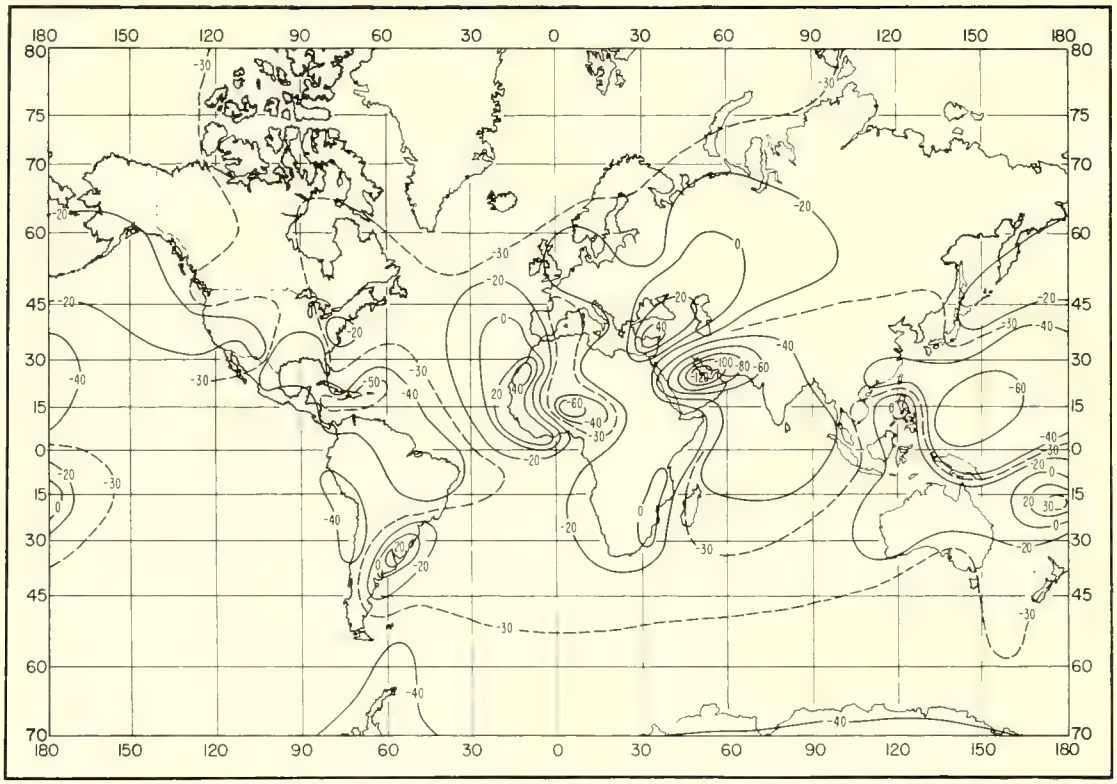

FIGURE C-9. *Gradient* (N/*km*) *exceeded 10 percent of the time for 100-m layer: August.*

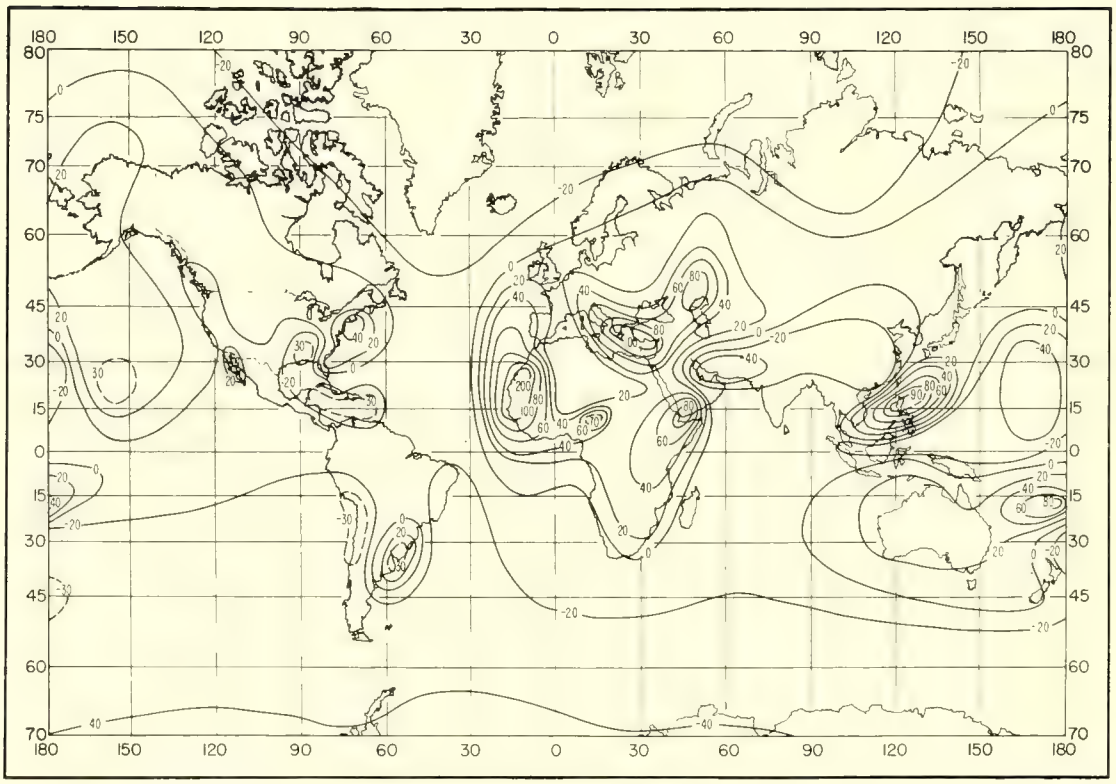

FIGURE C-10. *Gradient* (N/*km*) *exceeded 2 percent of the time for 100-m layer: August.*

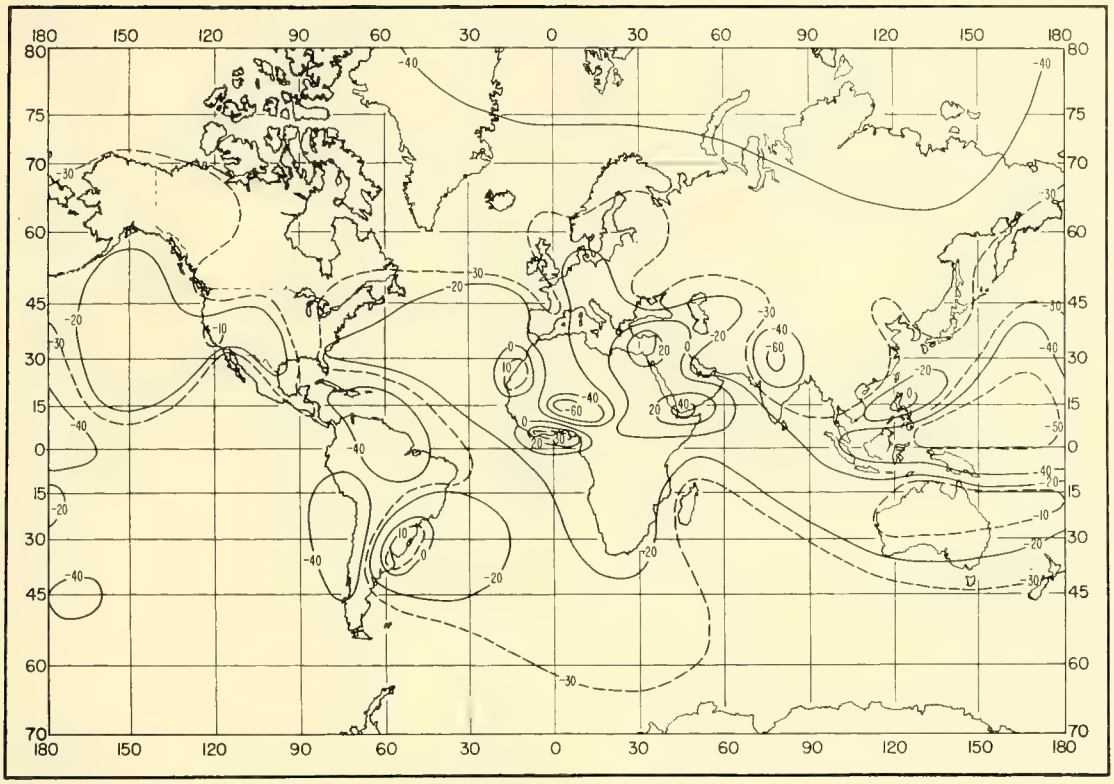

FIGURE C-11. *Gradient* (N/*km*) *exceeded 10 percent of the time for 100-m layer: November.*

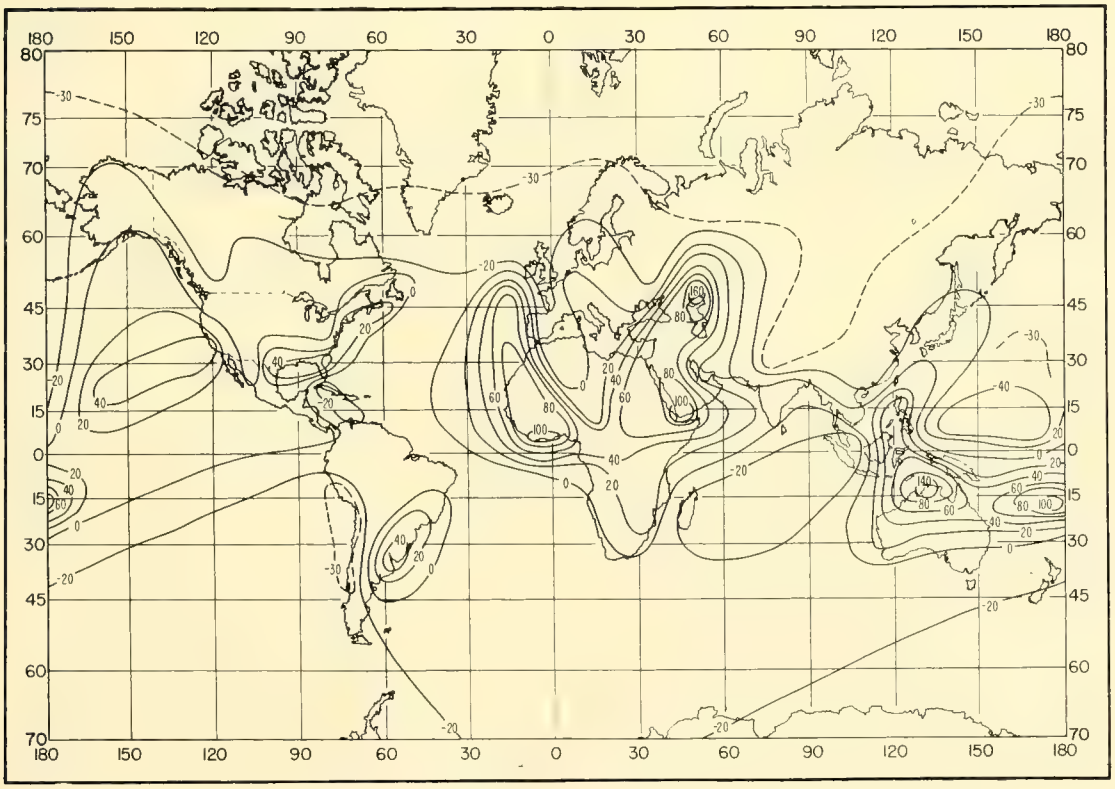

FIGURE C-12. *Gradient* (N/*km*) *exceeded 2 percent of the time for 100-m layer: November.*

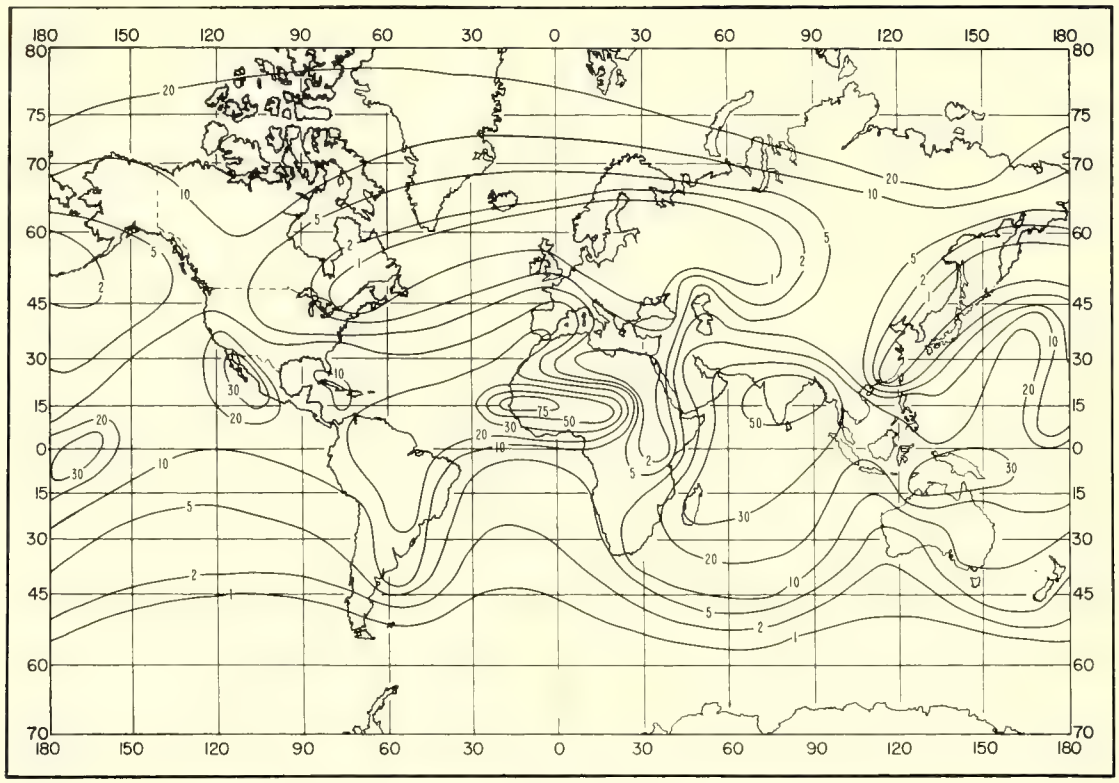

FIGURE C-13. *Percent of time gradient ≤ −100 (N/km): February.*

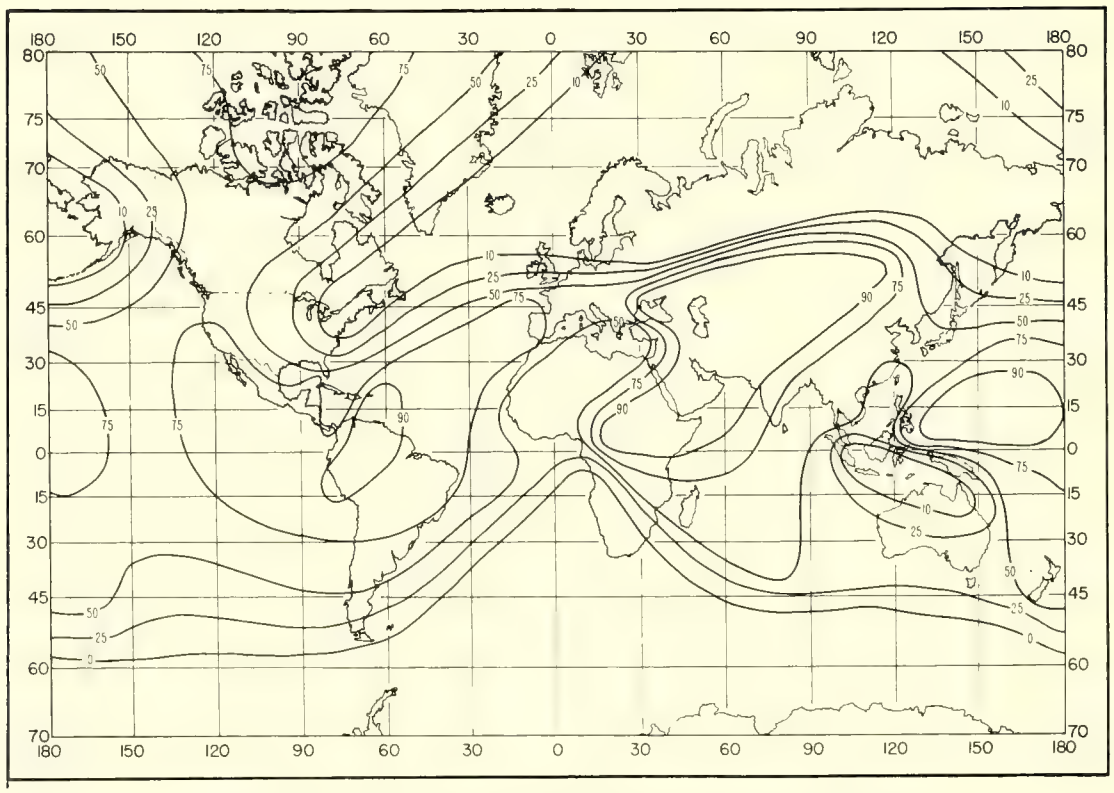

FIGURE C-14. *Percent of superrefractive layers thicker than 100 m: February.*

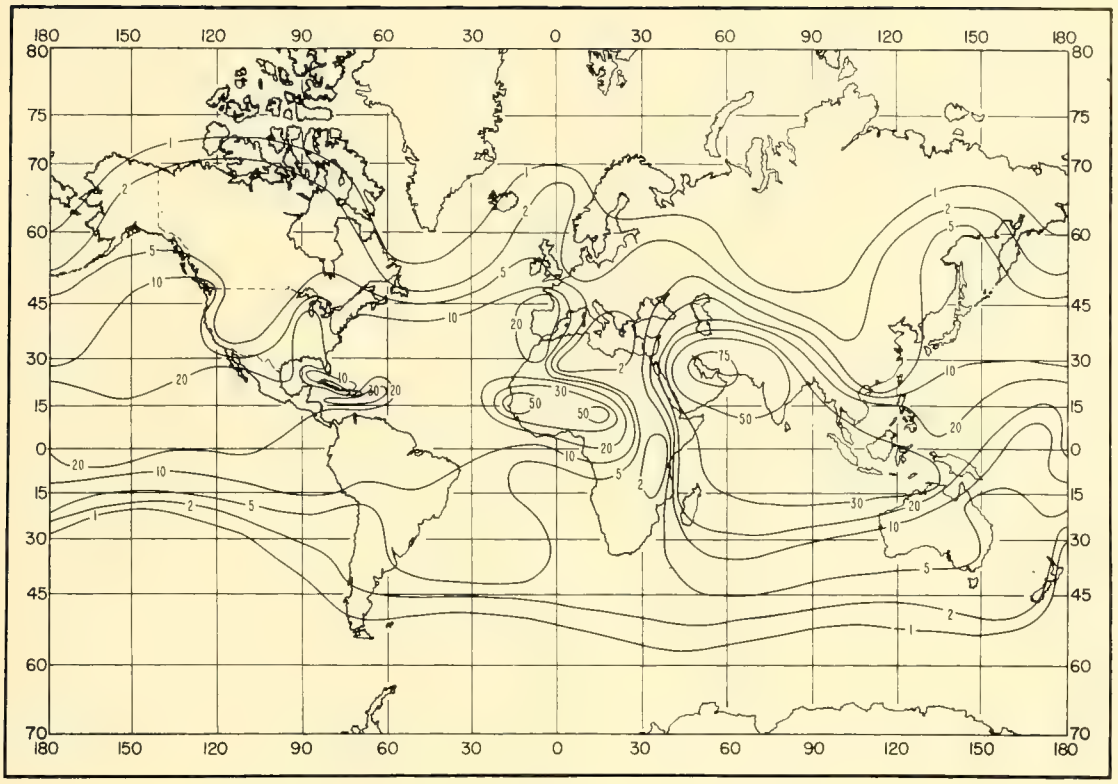

FIGURE C-15. *Percent of time gradient* ≤ -100 (N/*km*): *May.*

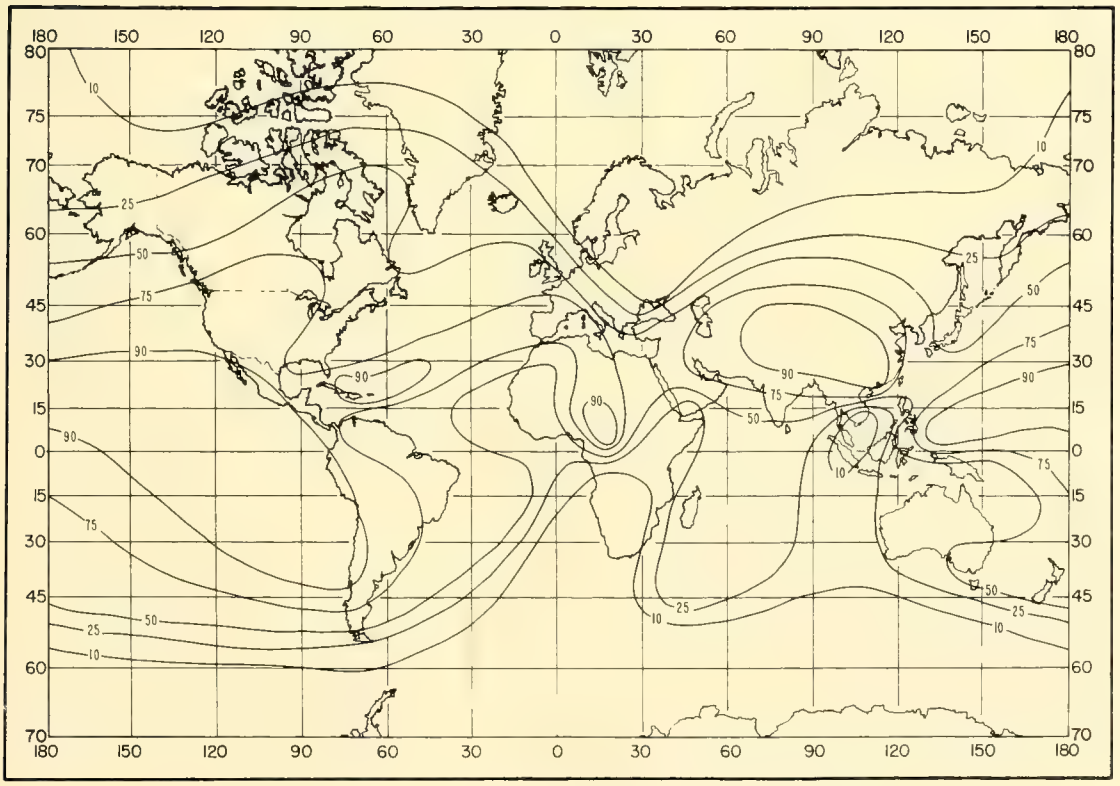

FIGURE C-16. *Percent of superrefractive layers thicker than 100 m: May.*

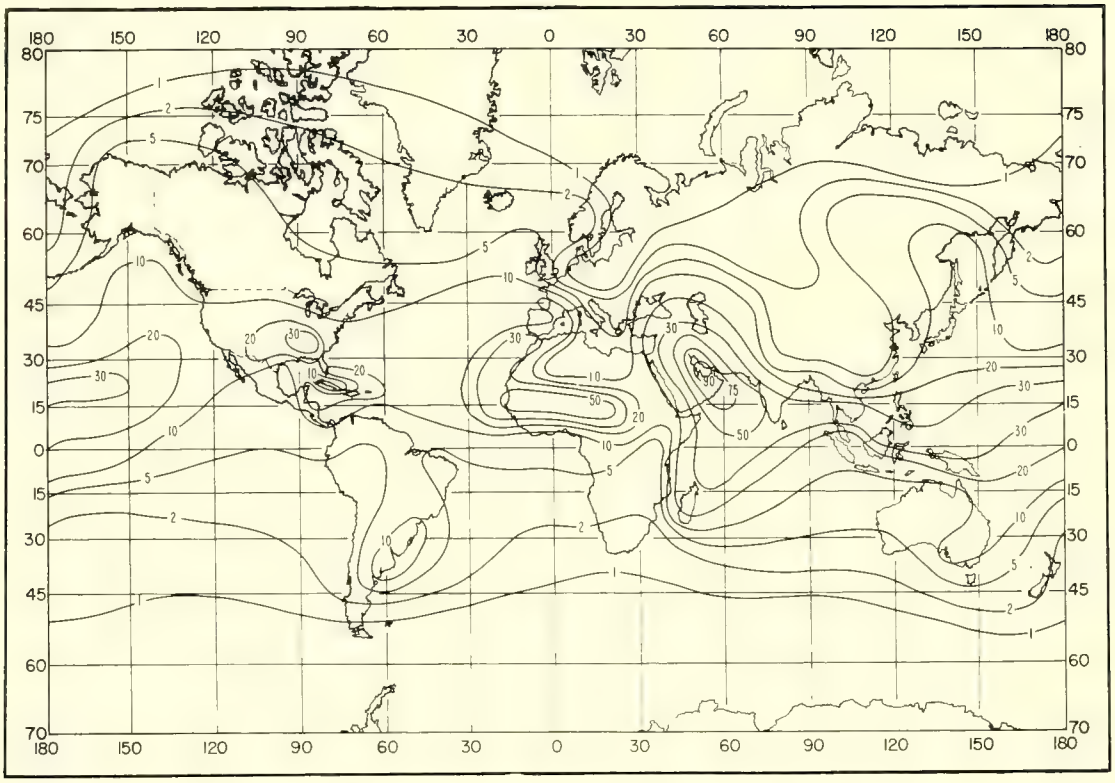

FIGURE C-17. *Percent of time gradient ≤ −100 (N/km): August.*

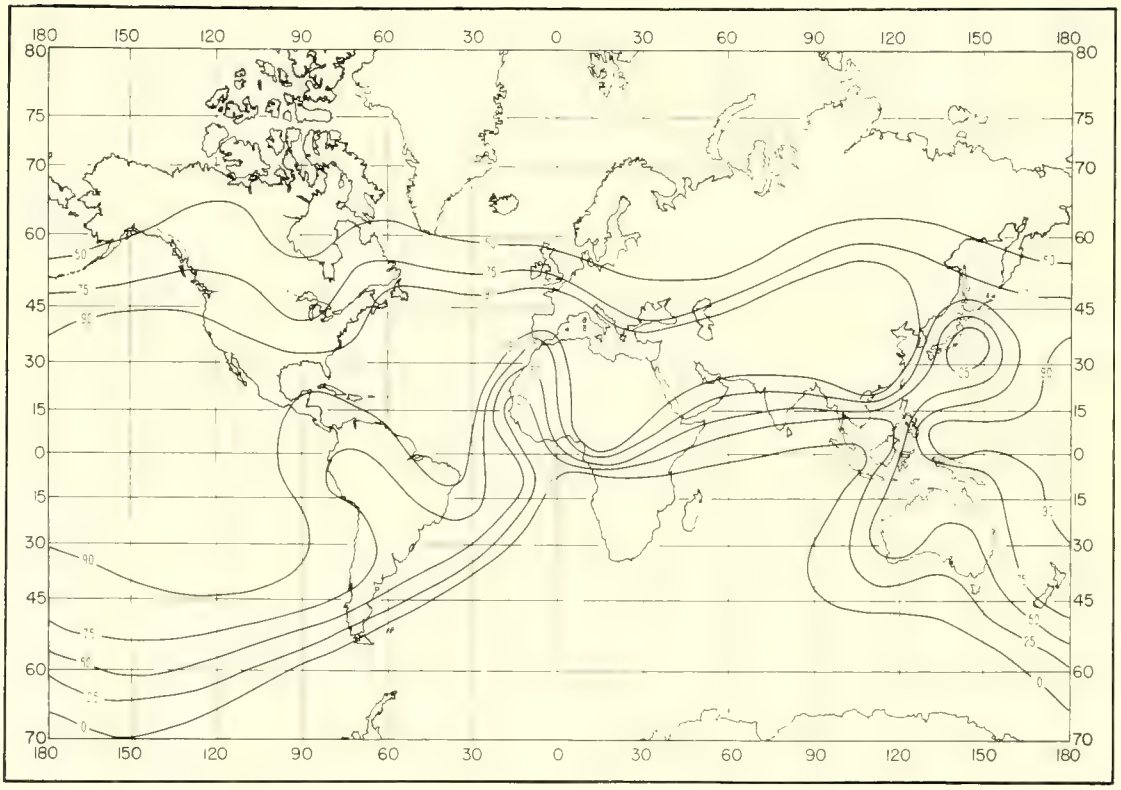

FIGURE C-18. *Percent of superrefractive layers thicker than 100 m: August.*

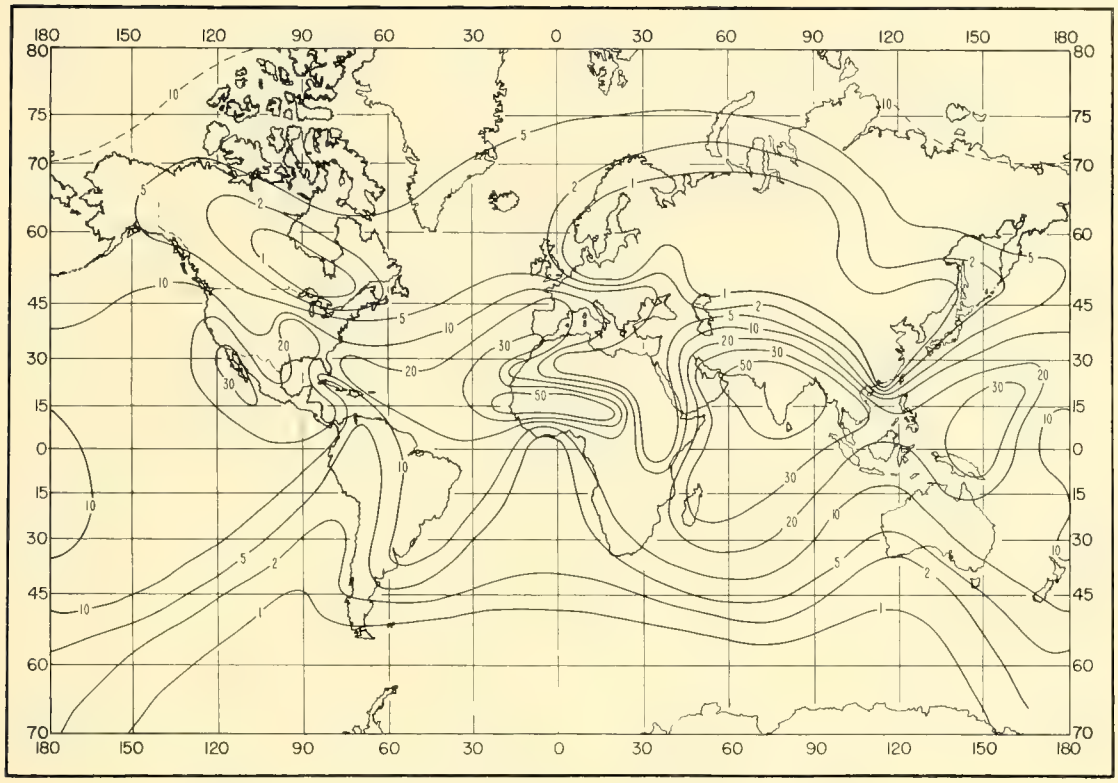

FIGURE C-19. *Percent of time gradient ≤ −100 (N/km): November.*

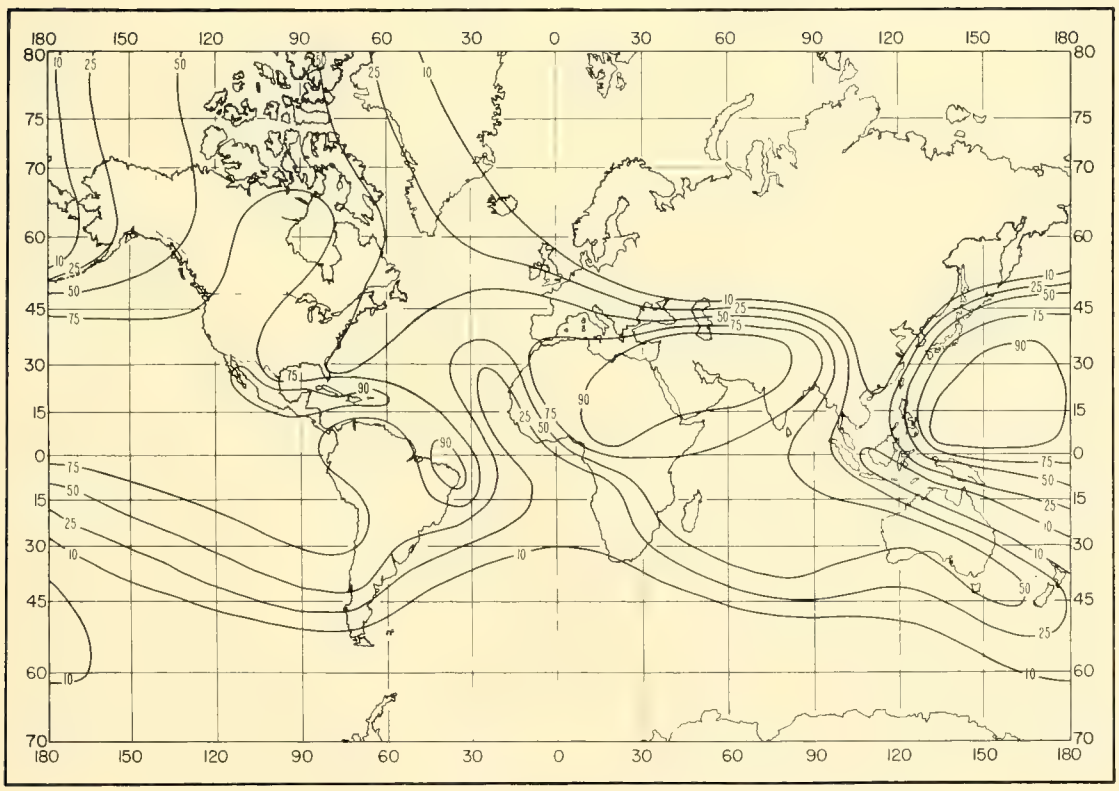

FIGURE C-20. *Percent of superrefractive layers thicker than 100 m: November.*

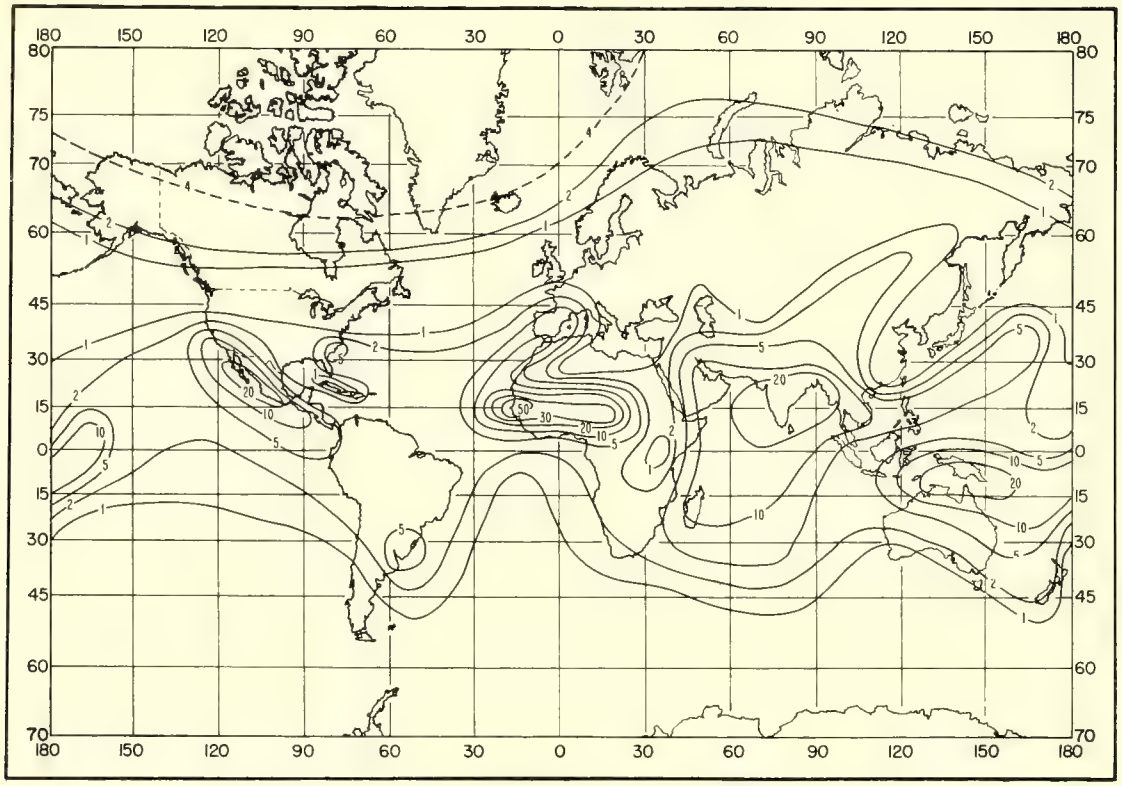

FIGURE C-21. *Percent of time gradient ≤ −157 (N/km): February.*

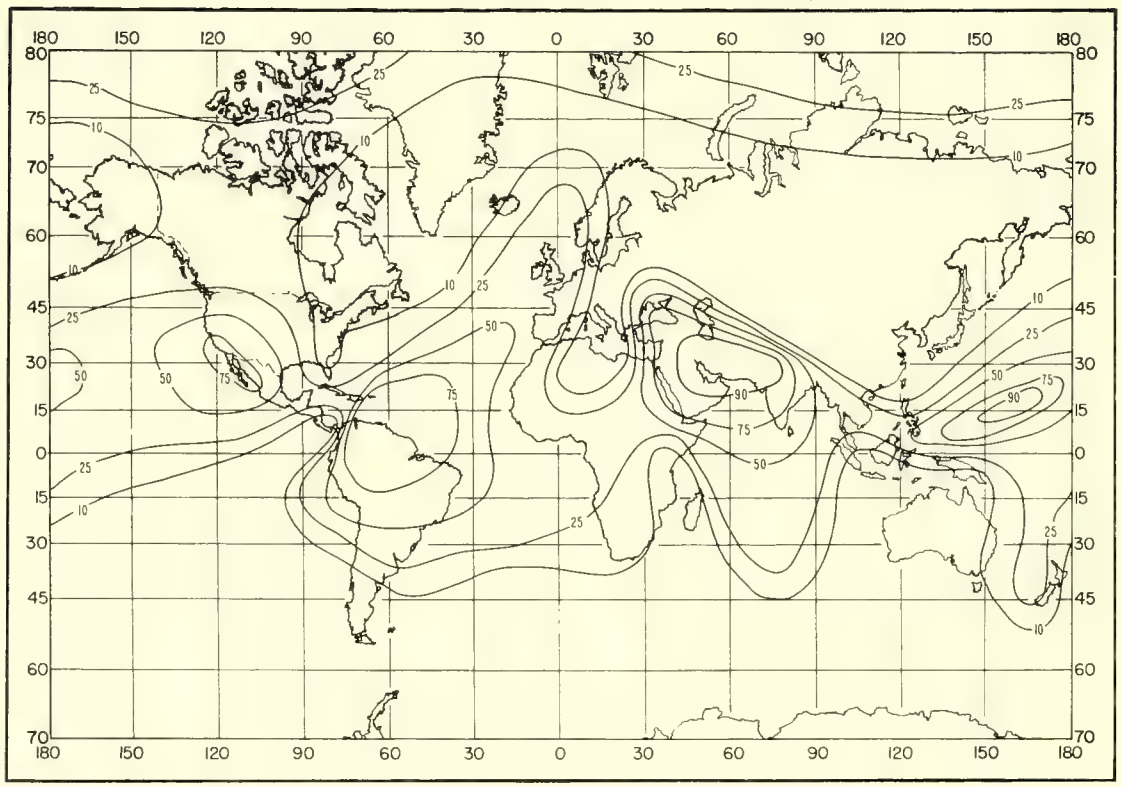

FIGURE C-22. *Percent of ducting layers thicker than 100 m: February.*

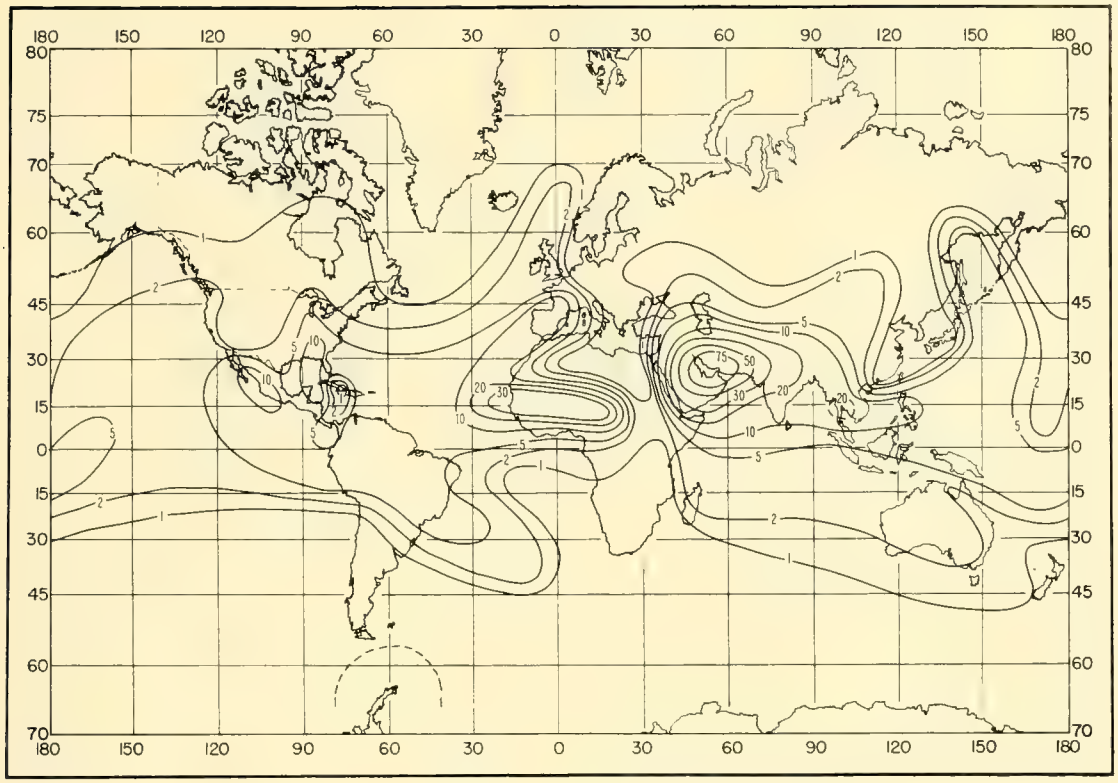

FIGURE C-23. *Percent of time gradient ≤ −157 (N/km): May.*

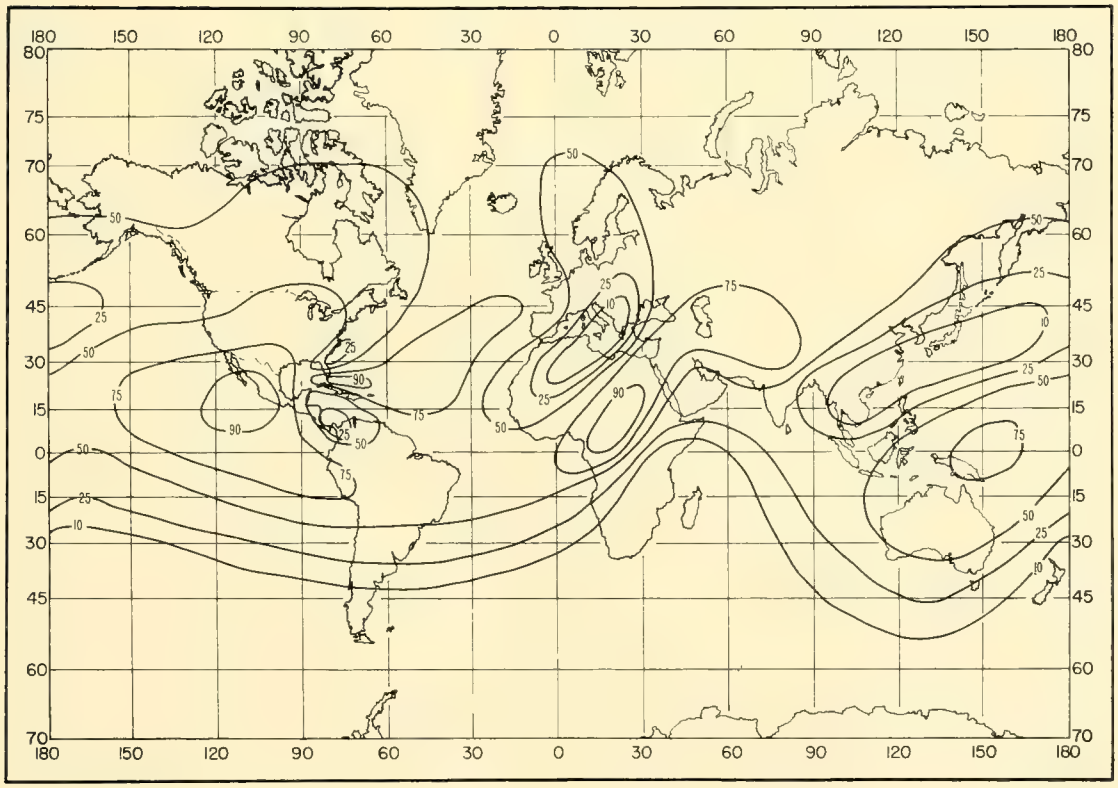

FIGURE C-24. *Percent of ducting layers thicker than 100 m: May.*

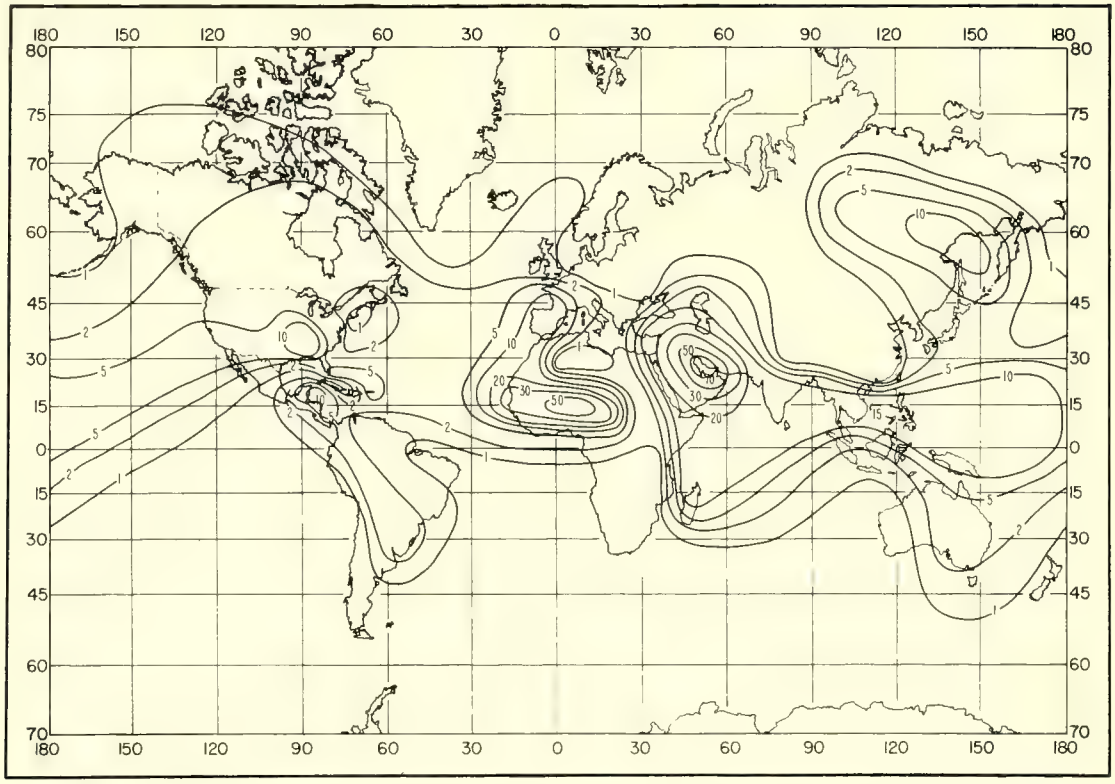

FIGURE C-25. *Percent of time gradient* ≤ -157 (N/*km*): *August.*

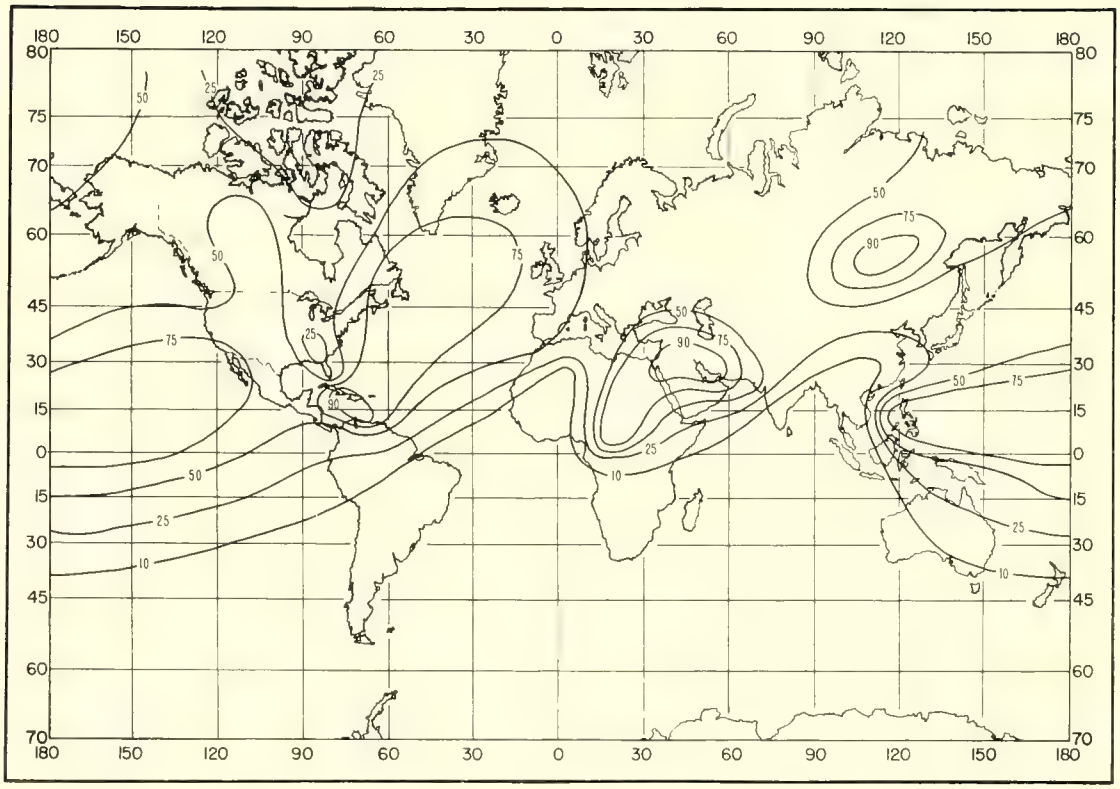

FIGURE C-26. *Percent of ducting layers thicker than 100 m: August.*

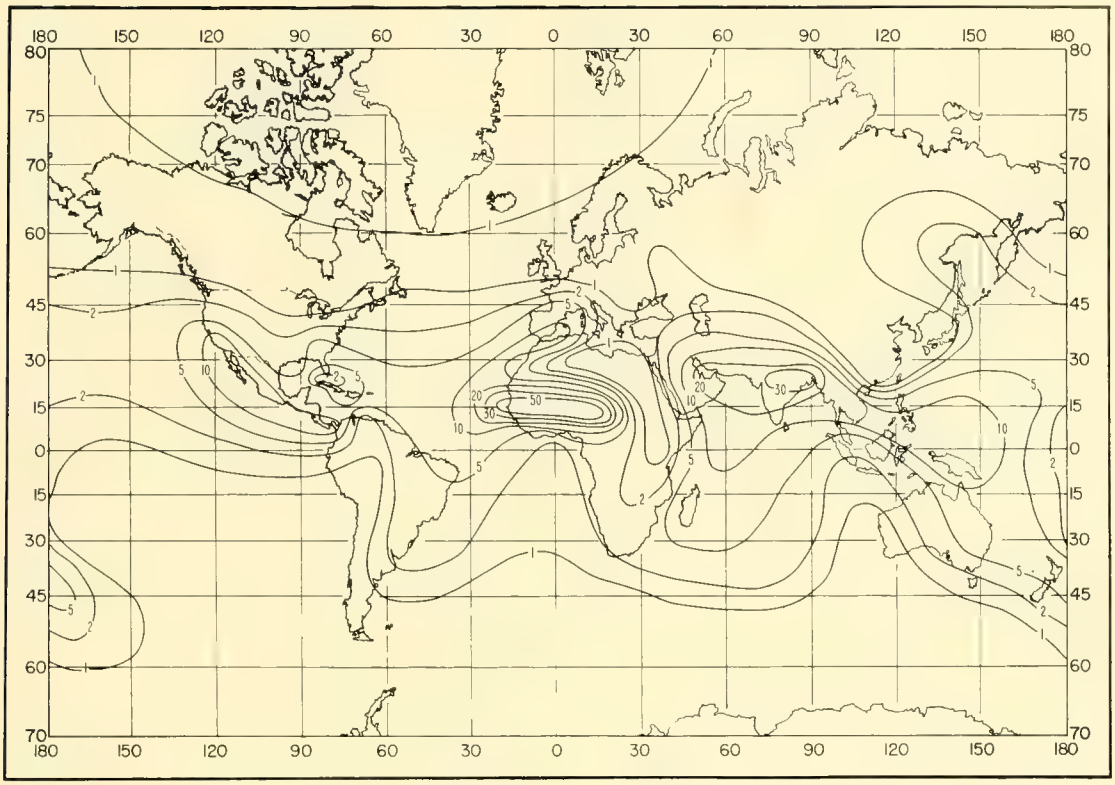

FIGURE C-27. *Percent of time gradient* ≤ -157 (N/*km*): *November.*

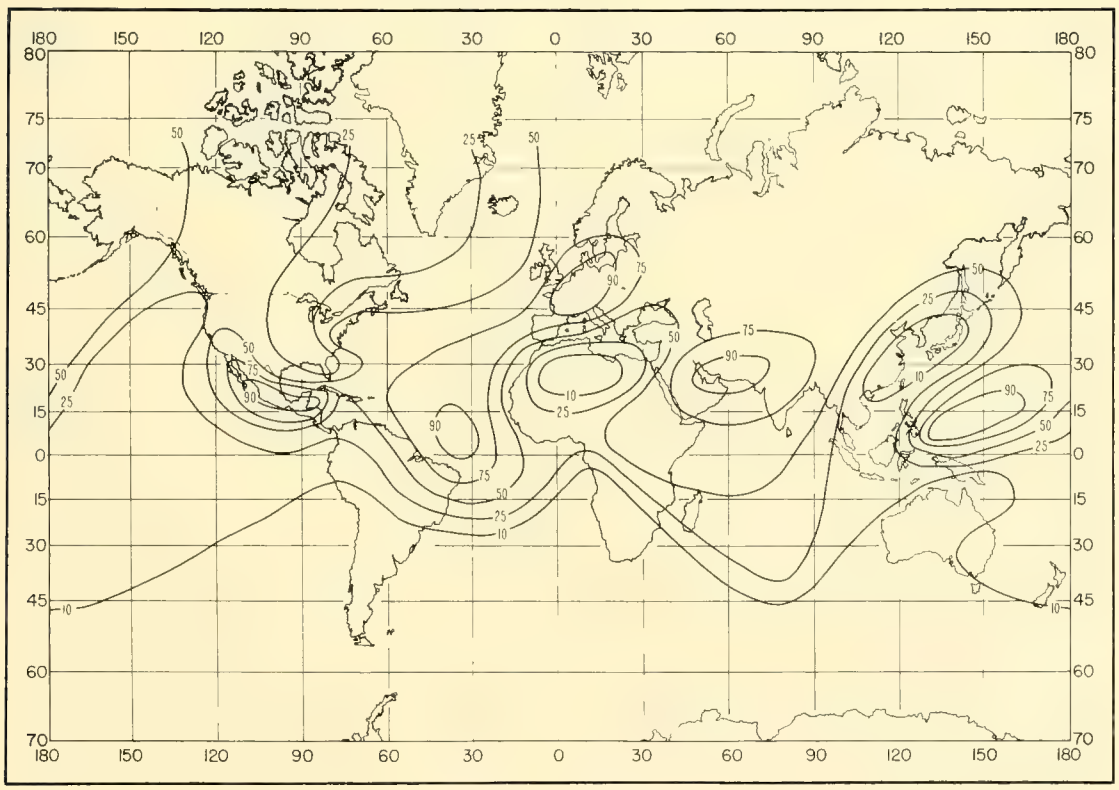

FIGURE C-28. *Percent of ducting layers thicker than 100 m: November.*

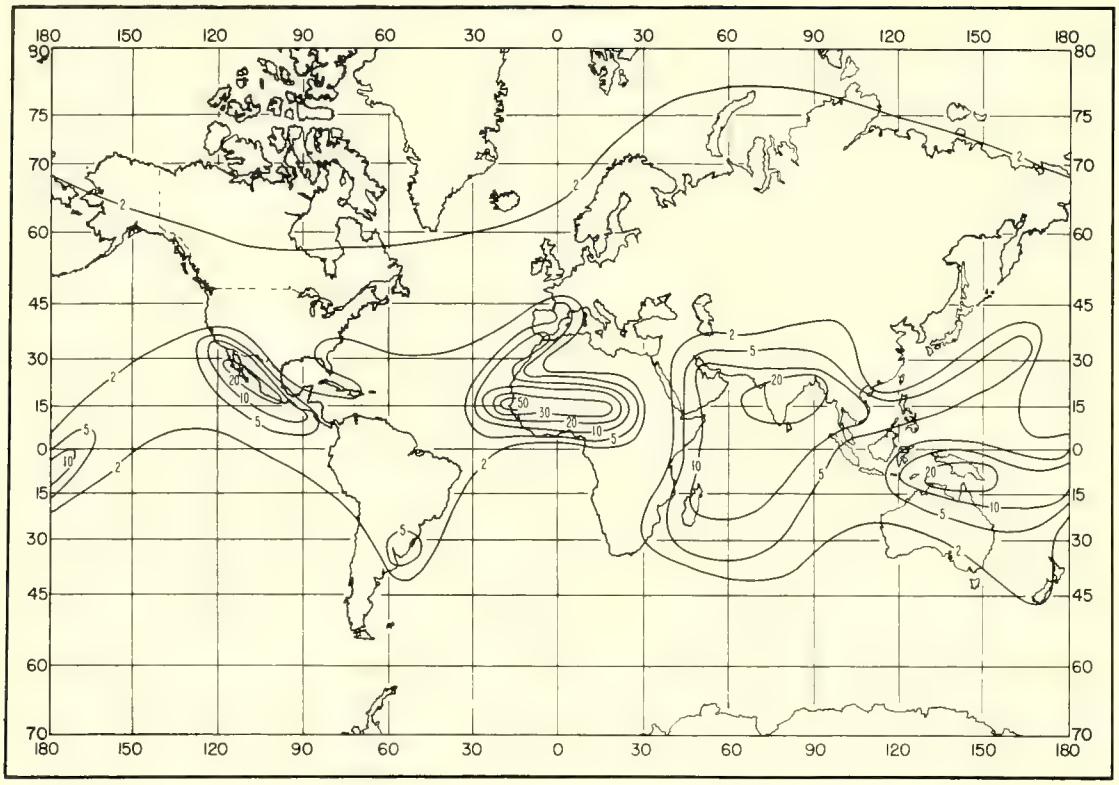

FIGURE C-29. *Percent of time trapping frequency < 3000 Mc/s: February.*

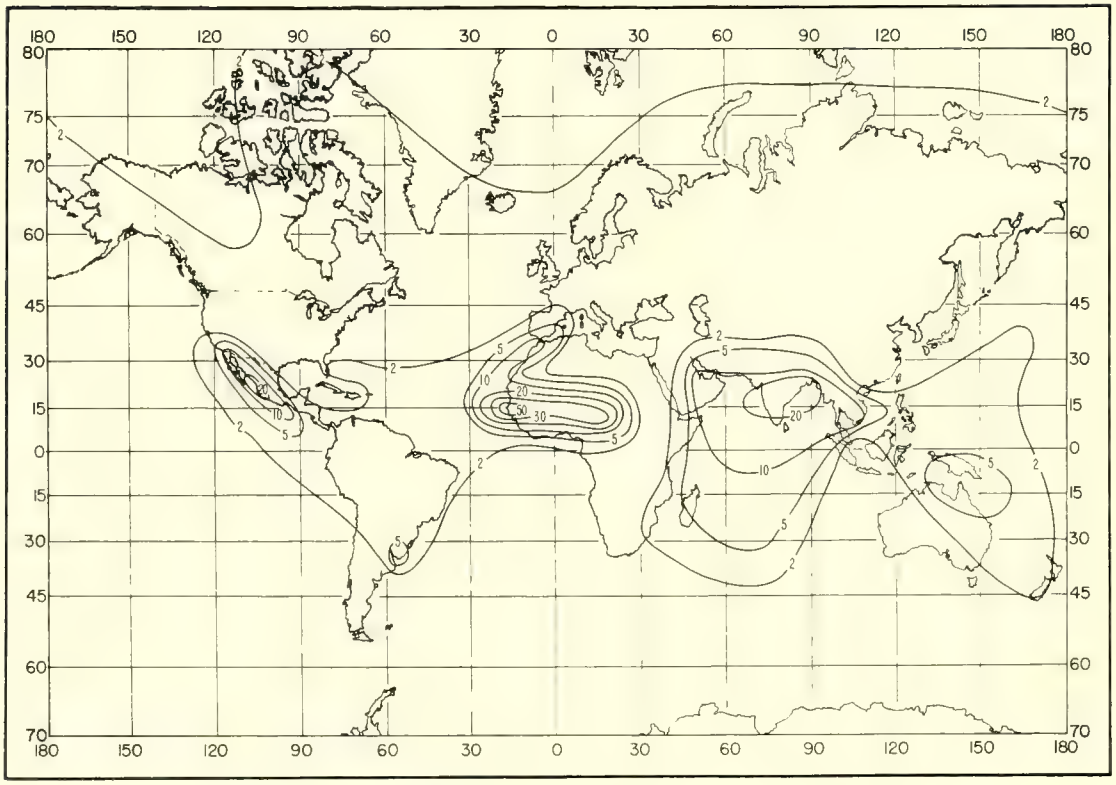

FIGURE C-30. *Percent of time trapping frequency < 1000 Mc/s: February.*

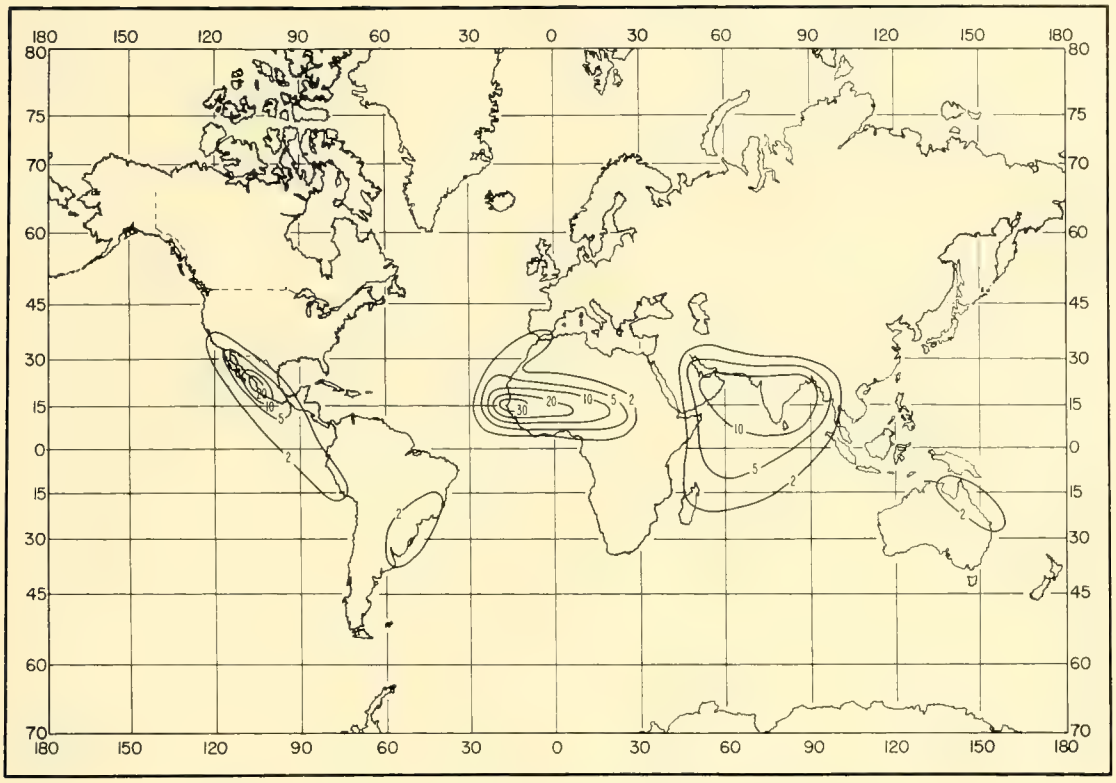

FIGURE C-31. *Percent of time trapping frequency < 300 Mc/s: February.*

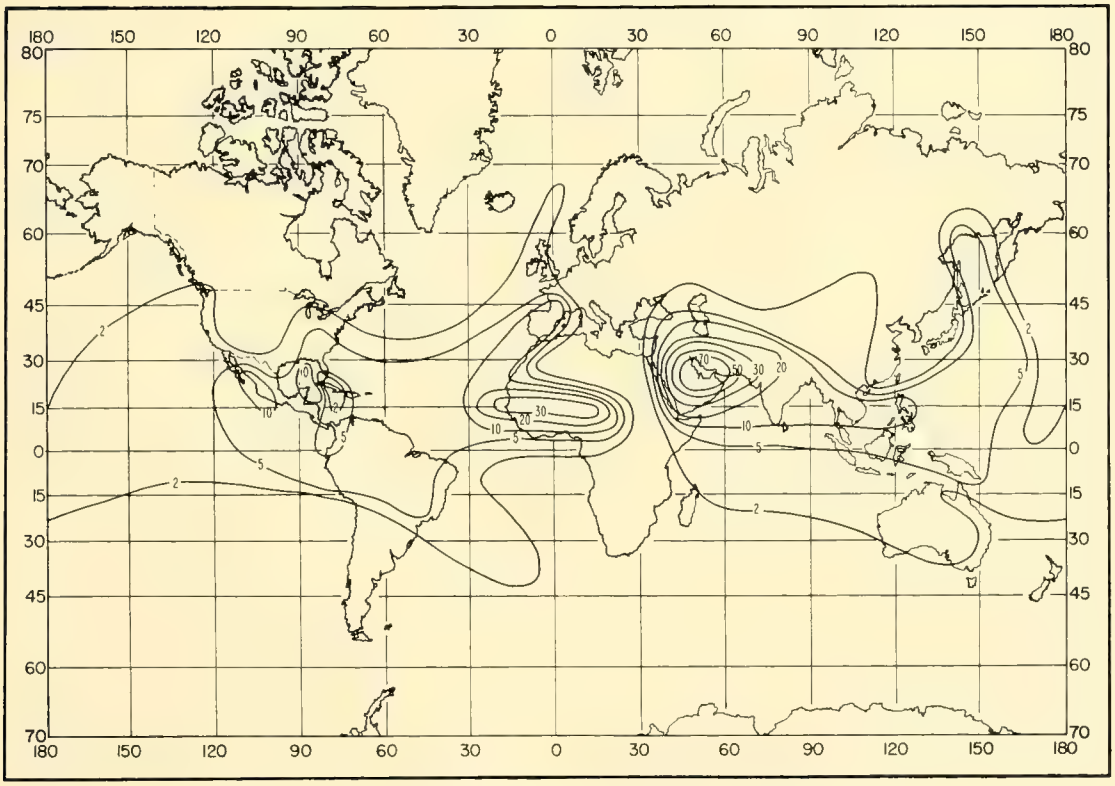

FIGURE C-32. *Percent of time trapping frequency < 3000 Mc/s: May.*

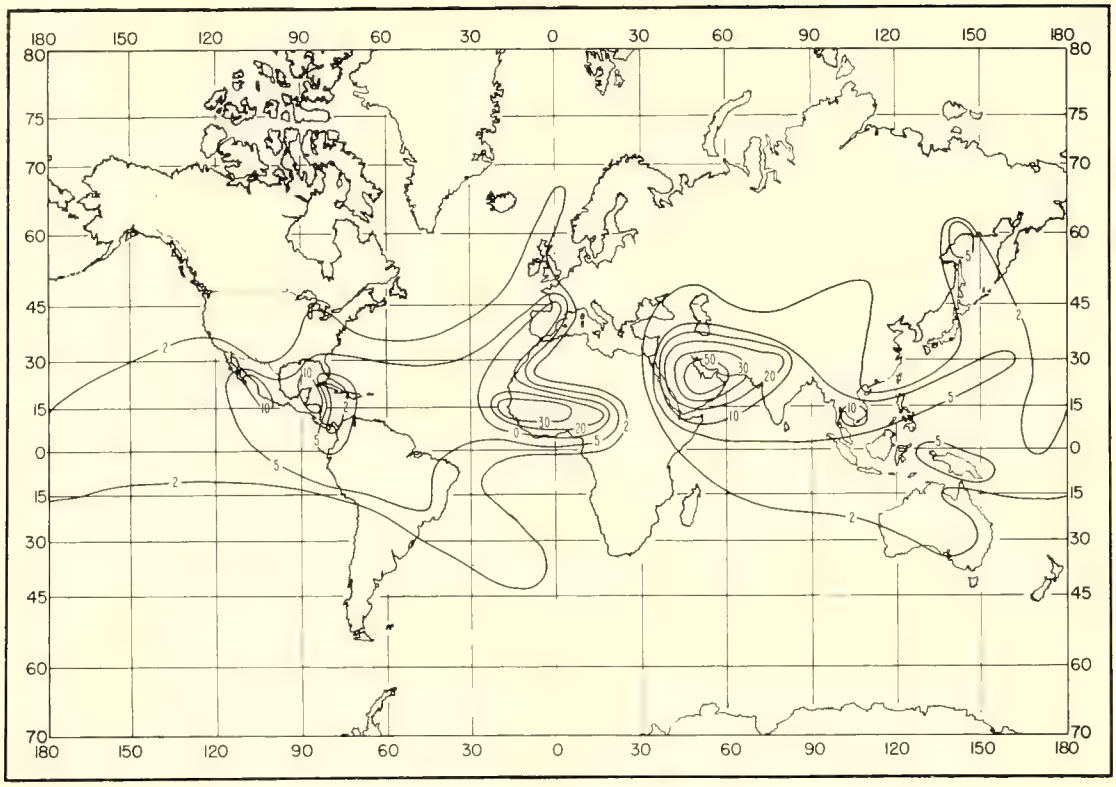

FIGURE C-33. *Percent of time trapping frequency < 1000 Mc/s: May.*

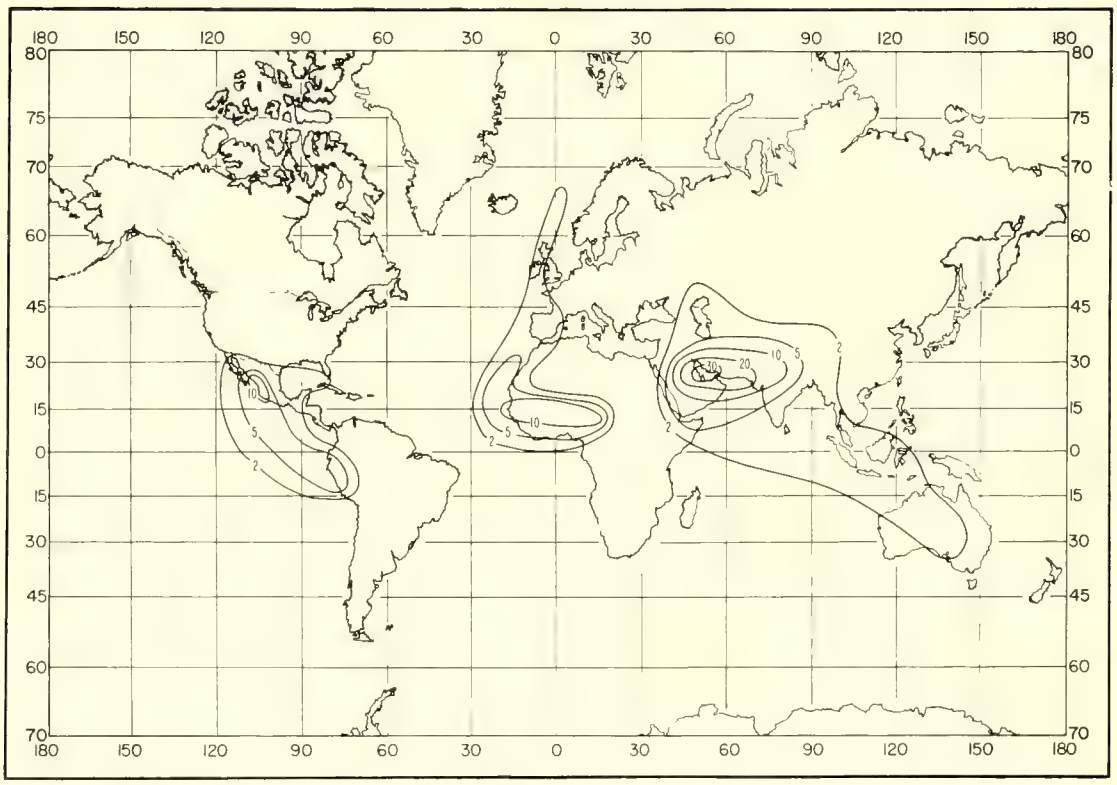

FIGURE C-34. *Percent of time trapping frequency < 300 Mc/s: May.*

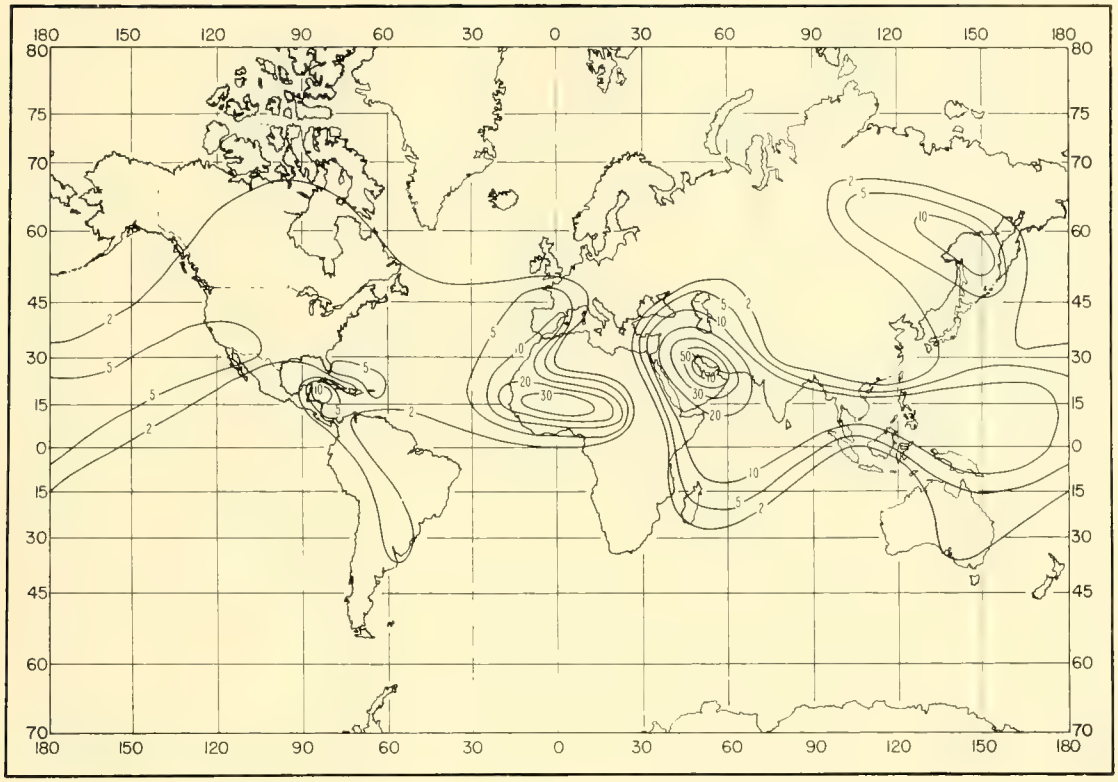

FIGURE C-35. *Percent of time trapping frequency < 3000 Mc/s: August.*

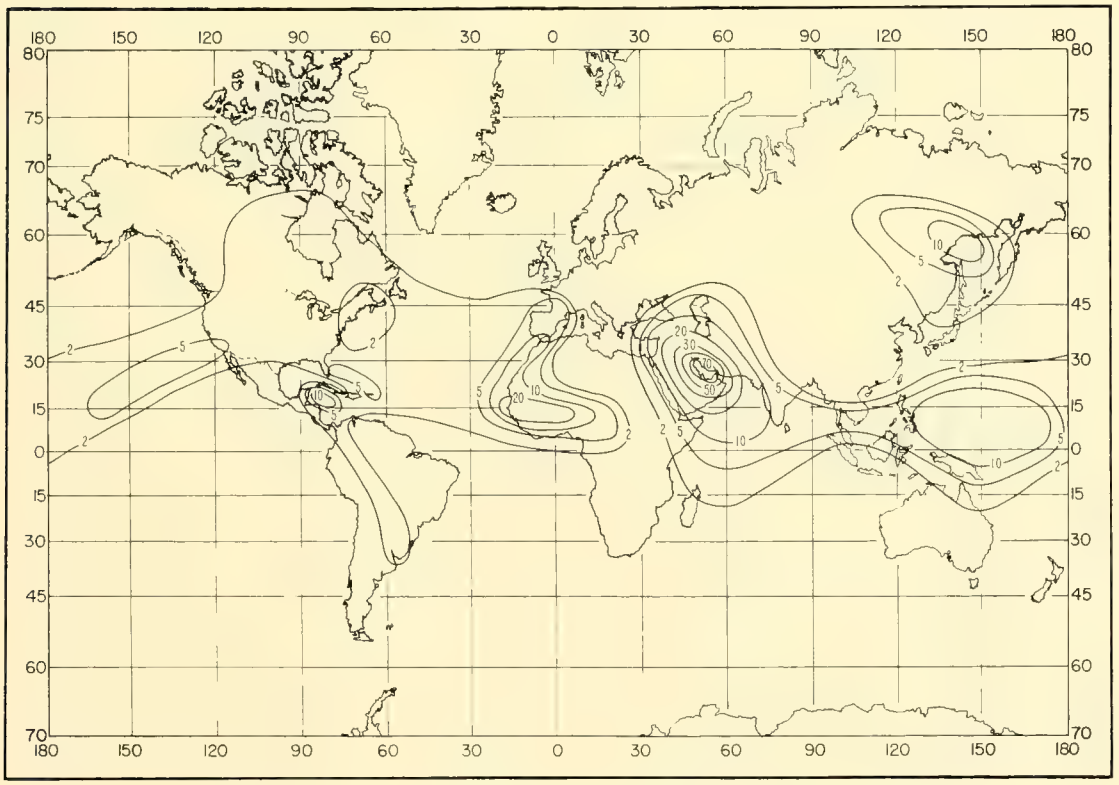

FIGURE C-36. *Percent of time trapping frequency < 1000 Mc/s: August.*

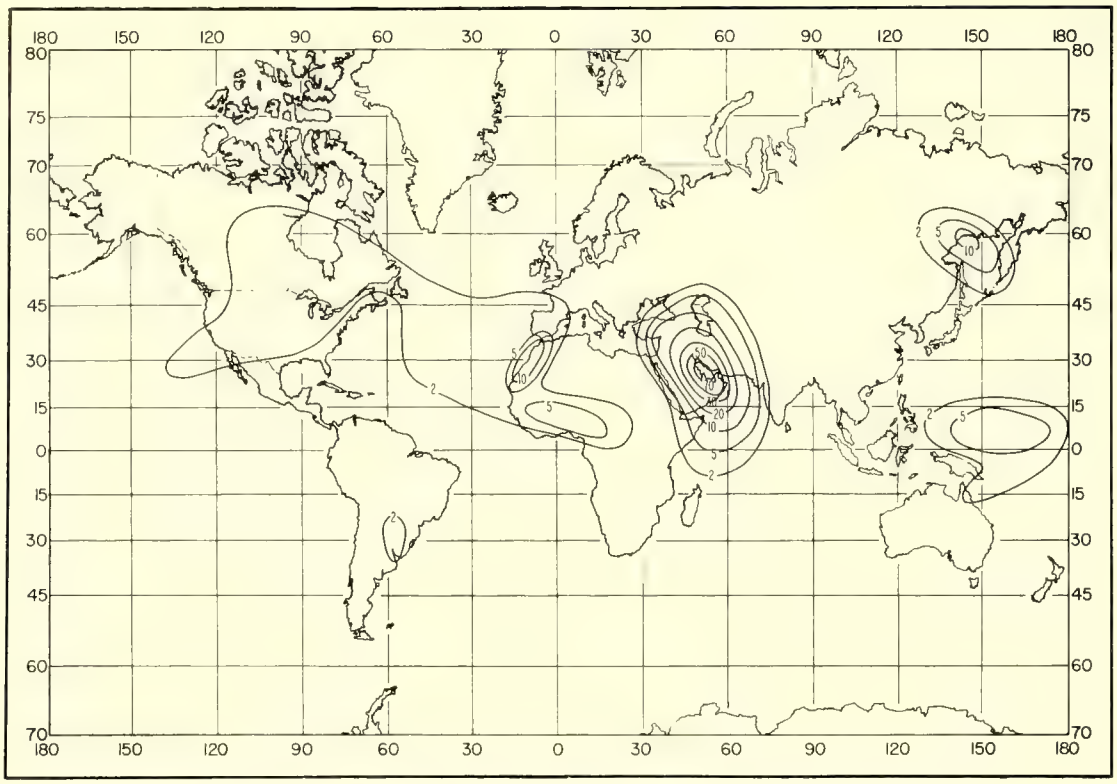

FIGURE C-37. *Percent of time trapping frequency < 300 Mc/s: August.*

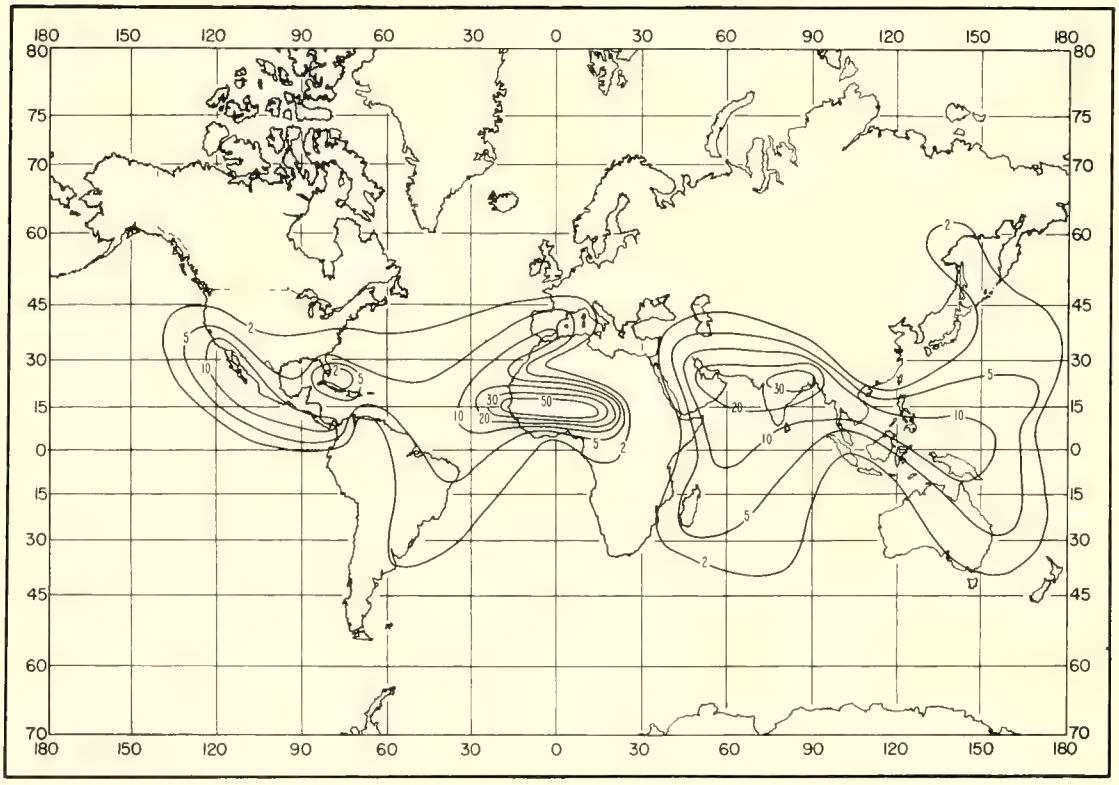

FIGURE C-38. *Percent of time trapping frequency < 3000 Mc/s: November.*

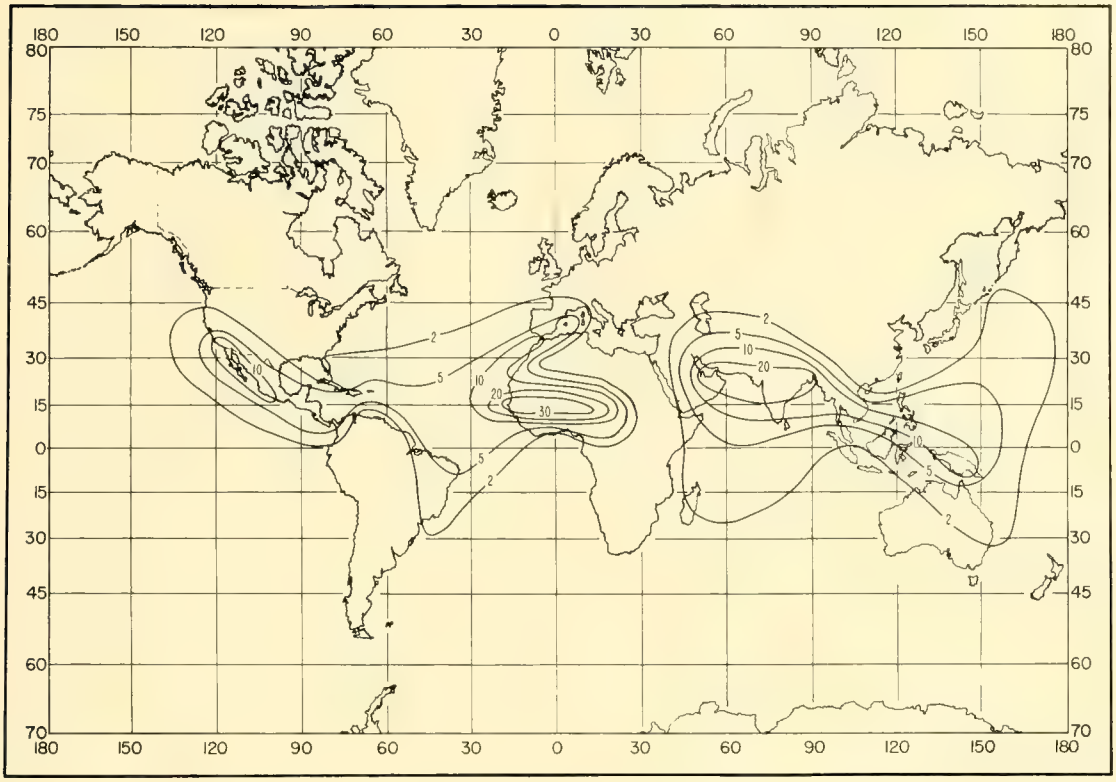

FIGURE C-39. *Percent of time trapping frequency < 1000 Mc/s: November.*

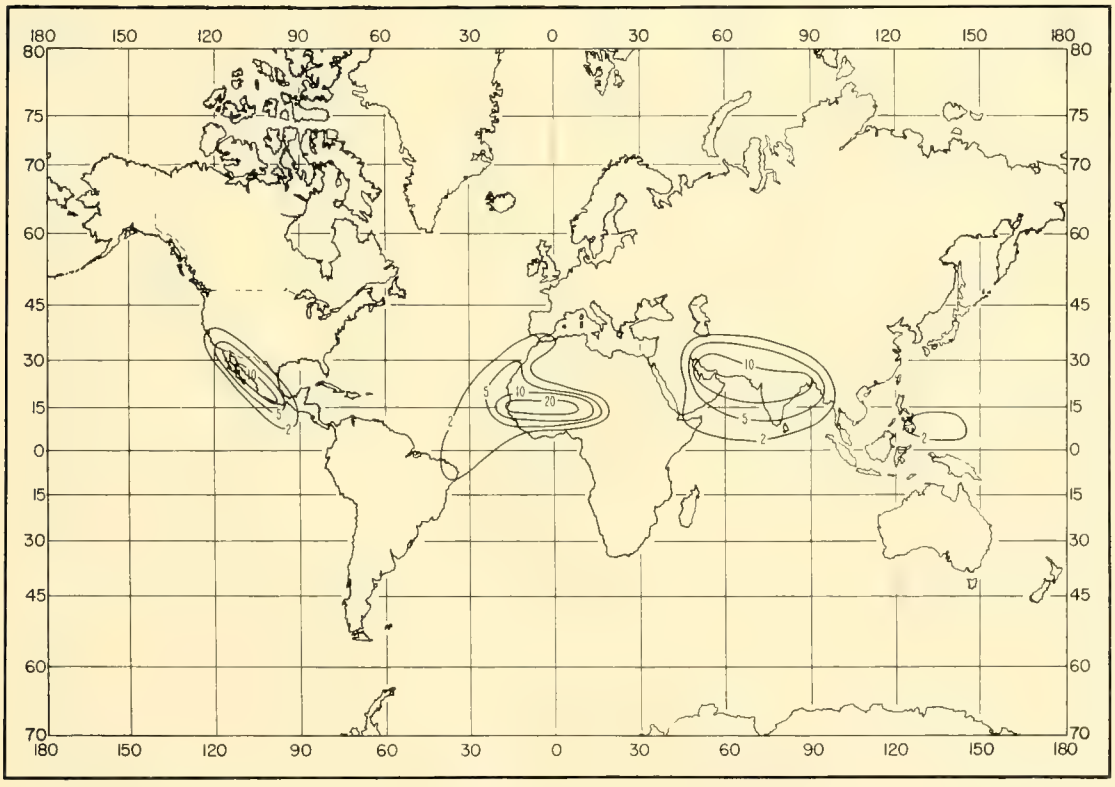

FIGURE C-40. *Percent of time trapping frequency < 300 Mc/s: November.*

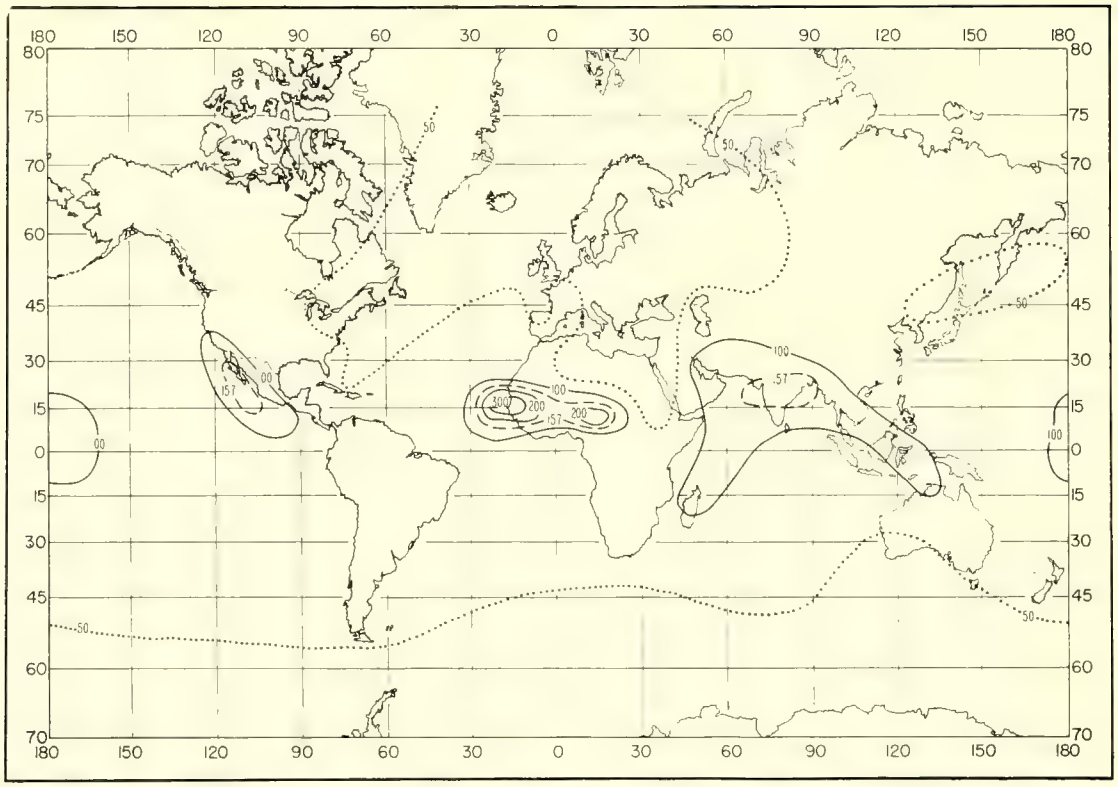

FIGURE C-41. *Lapse rate of refractivity* (N/*km*) *exceeded 25 percent of time for 100-m layer: February.*

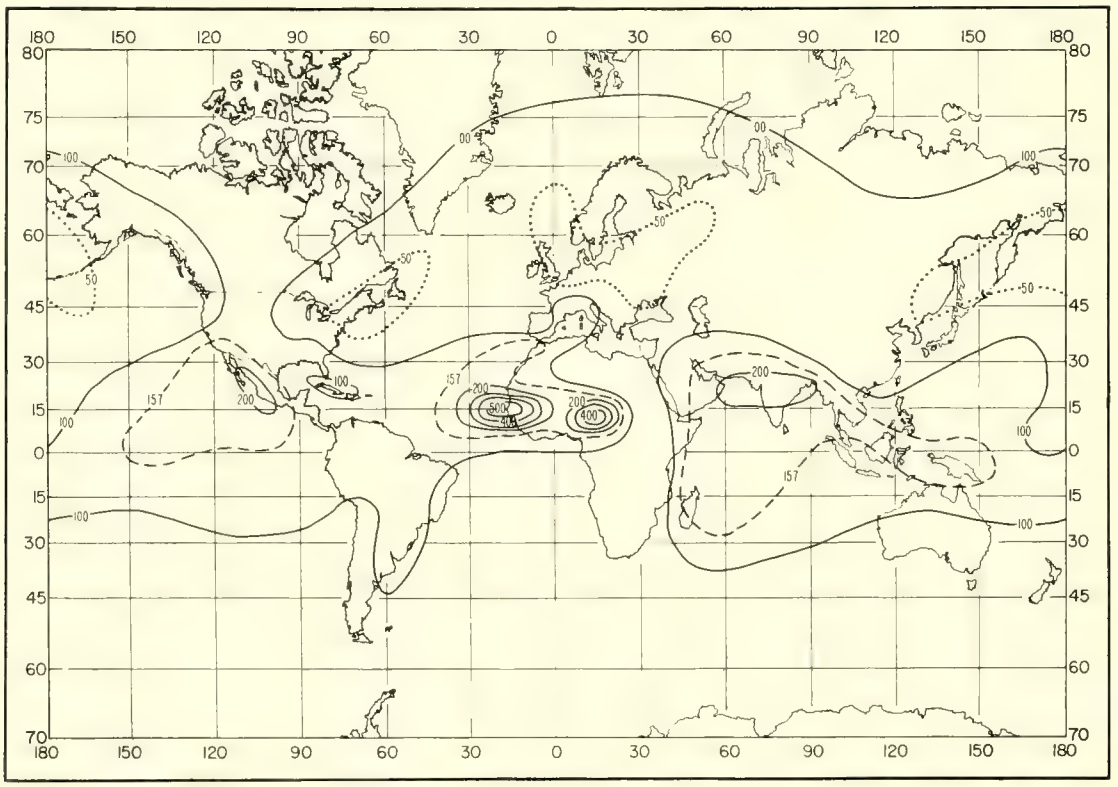

FIGURE C-42. *Lapse rate of refractivity* (N/*km*) *exceeded 10 percent of time for 100-m layer: February.*

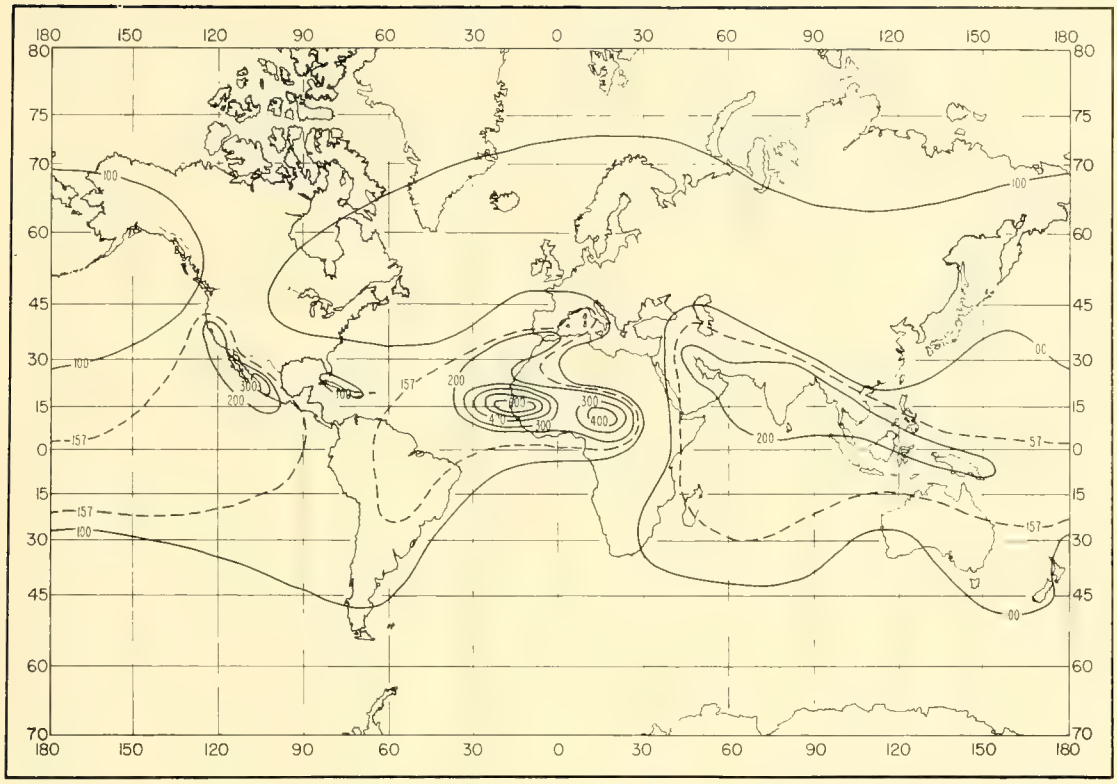

FIGURE C-43. *Lapse rate of refractivity (N/km) exceeded 5 percent of time for 100-m layer: February.*

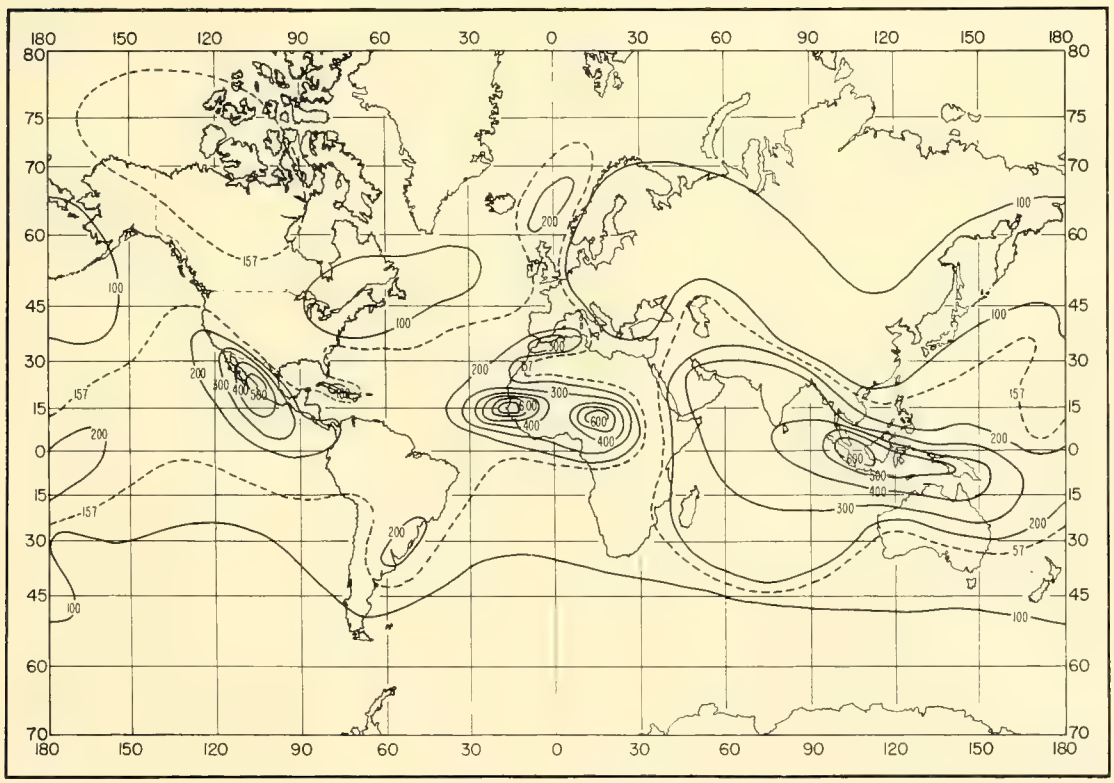

FIGURE C-44. *Lapse rate of refractivity (N/km) exceeded 2 percent of time for 100-m layer: February.*

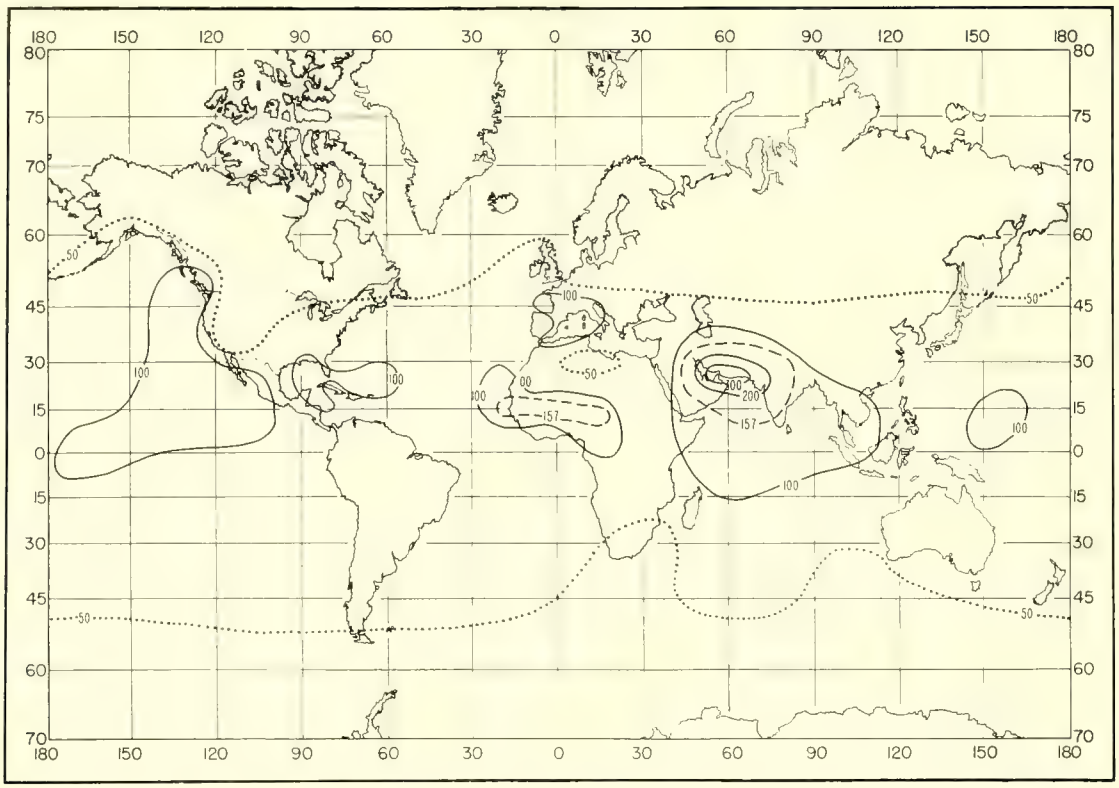

FIGURE C-45. *Lapse rate of refractivity* (N/*km*) *exceeded 25 percent of time for 100-m layer: May.*

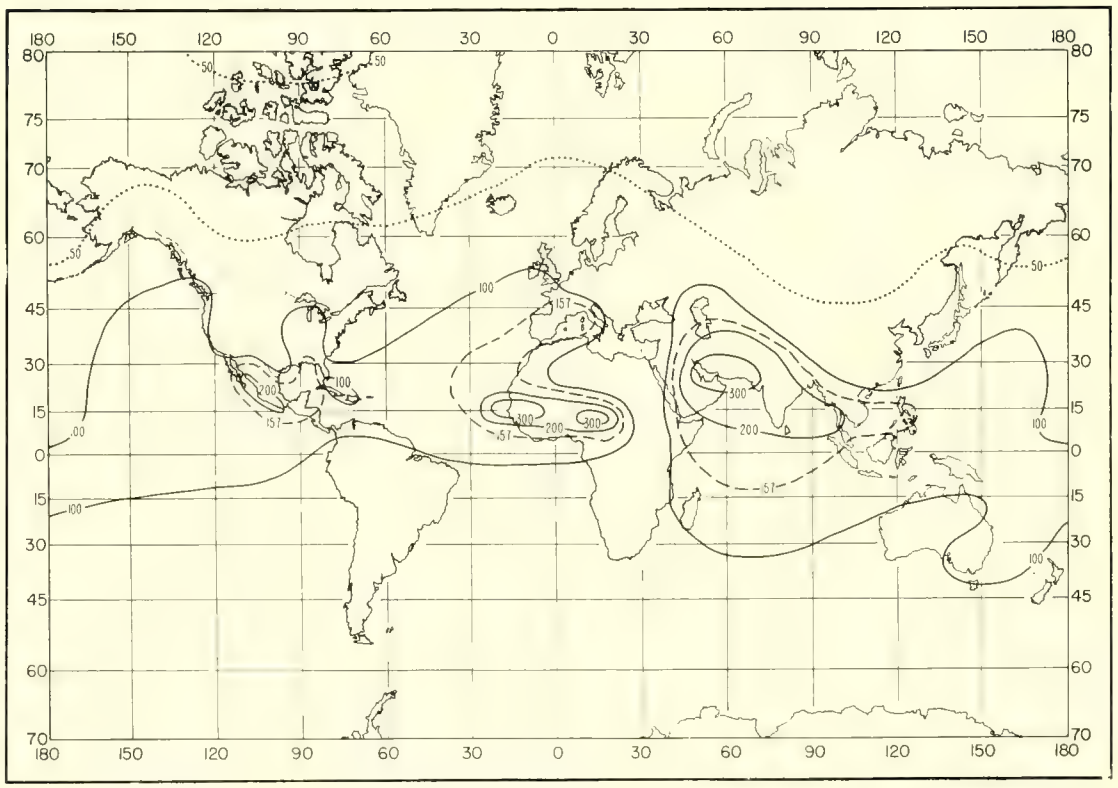

FIGURE C-46. *Lapse rate of refractivity* (N/*km*) *exceeded 10 percent of time for 100-m layer: May.*

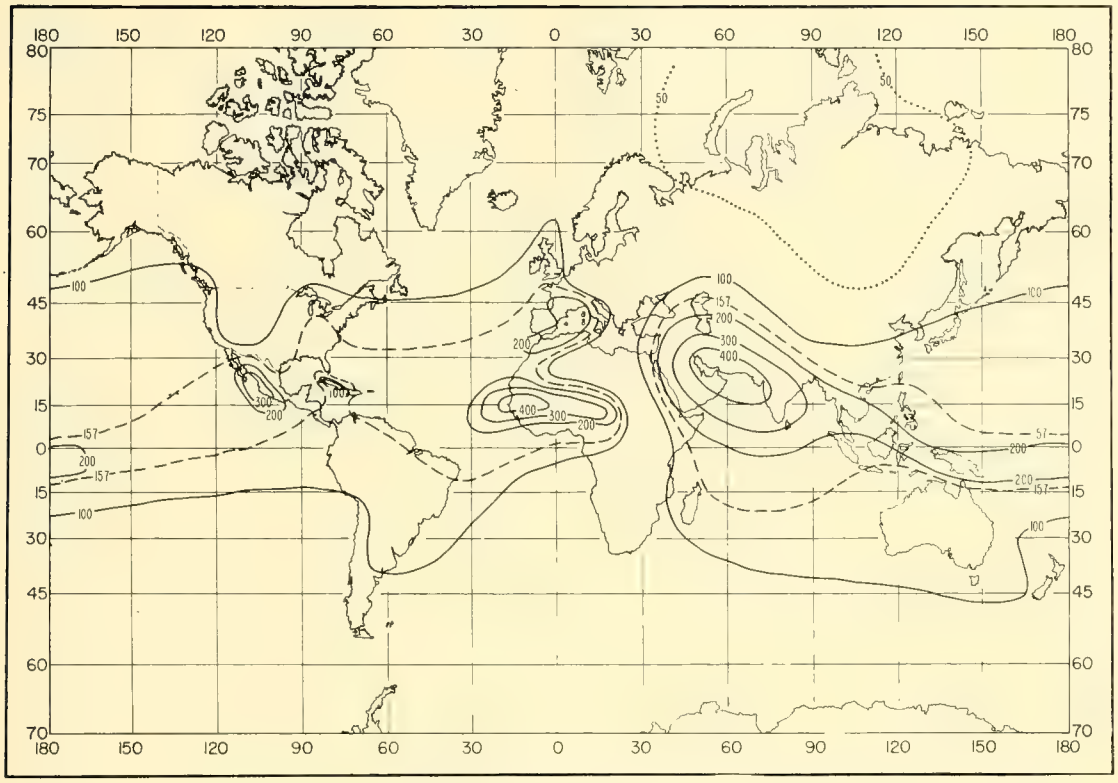

FIGURE C-47. *Lapse rate of refractivity* (N/*km*) *exceeded 5 percent of time for 100-m layer: May.*

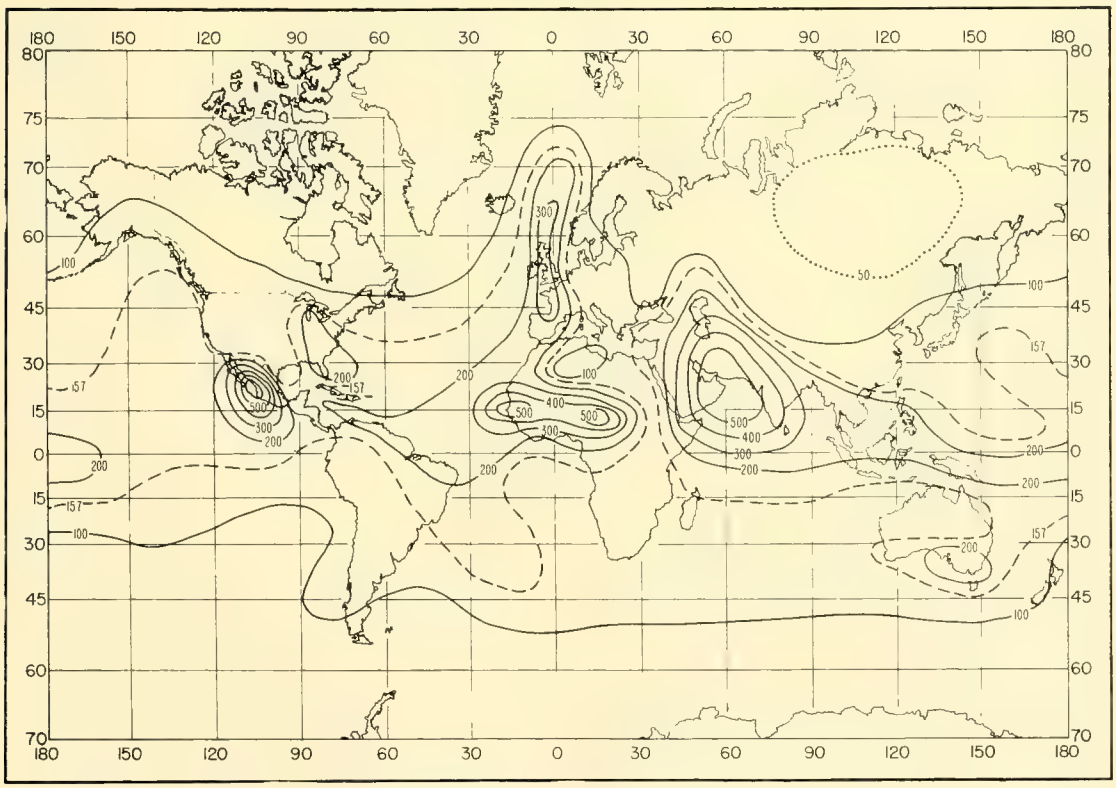

FIGURE C-48. *Lapse rate of refractivity* (N/*km*) *exceeded 2 percent of time for 100-m layer: May.*

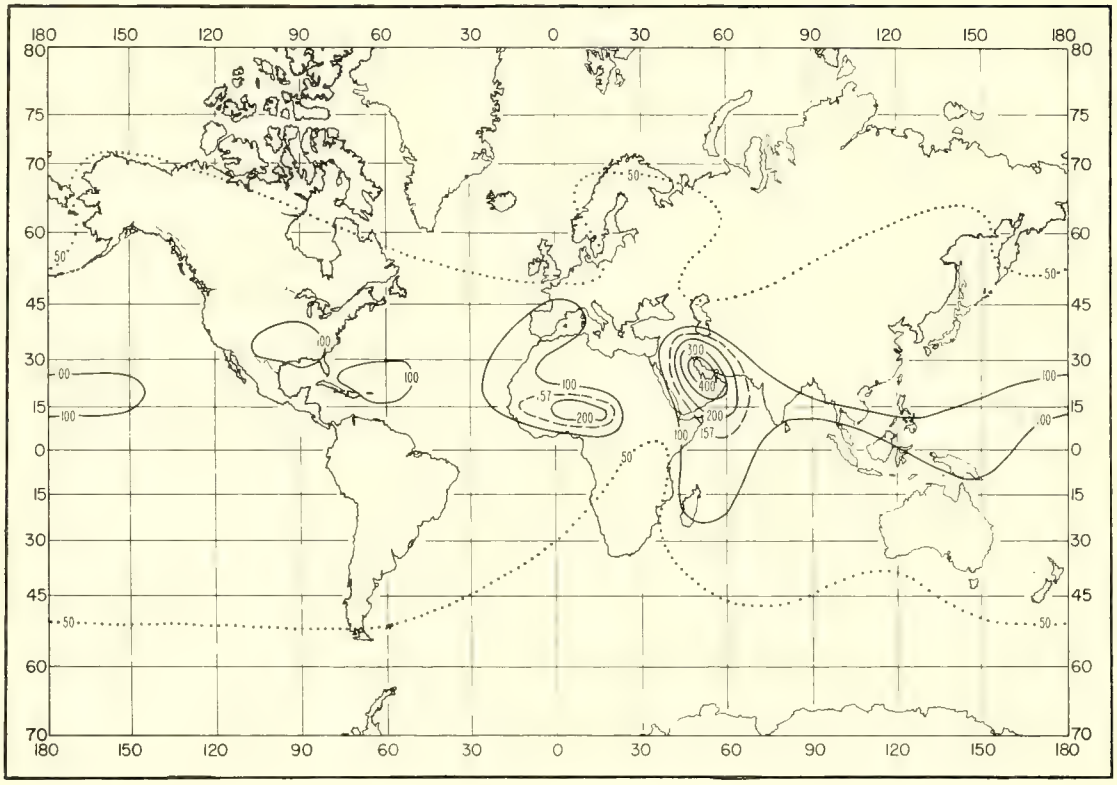

FIGURE C-49. *Lapse rate of refractivity* (N/*km*) *exceeded 25 percent of time for 100-m layer: August.*

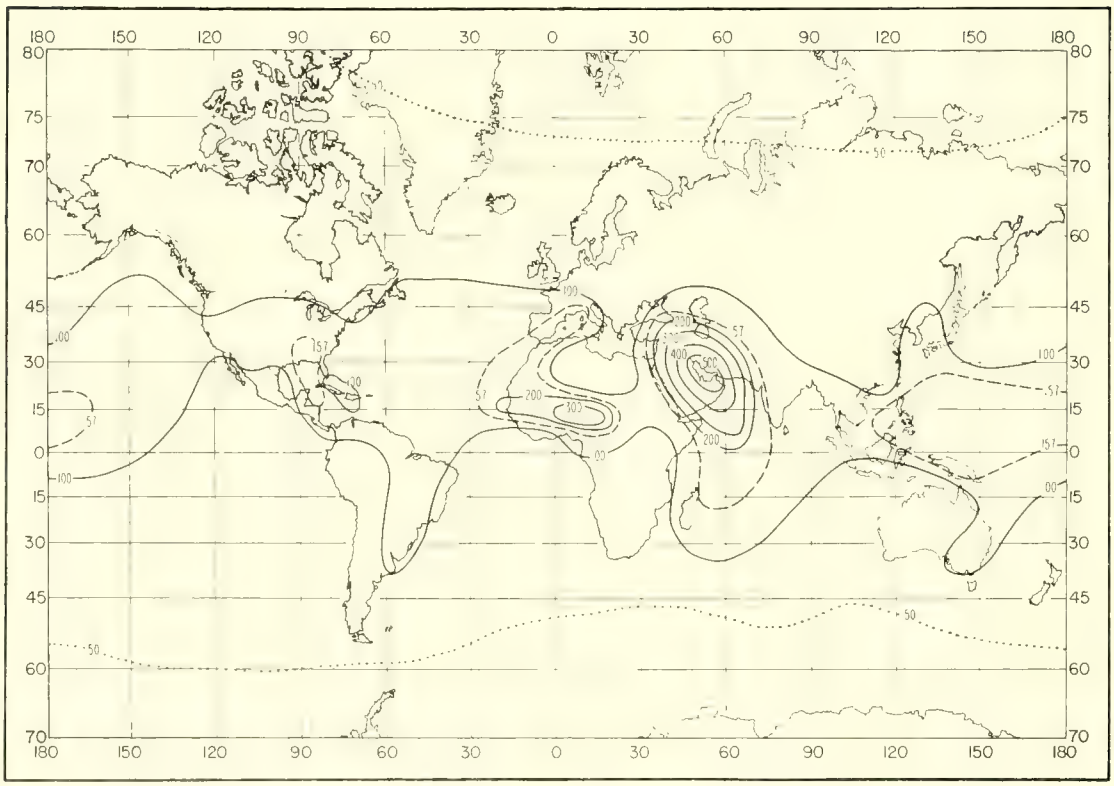

FIGURE C-50. *Lapse rate of refractivity* (N/*km*) *exceeded 10 percent of time for 100-m layer: August.*

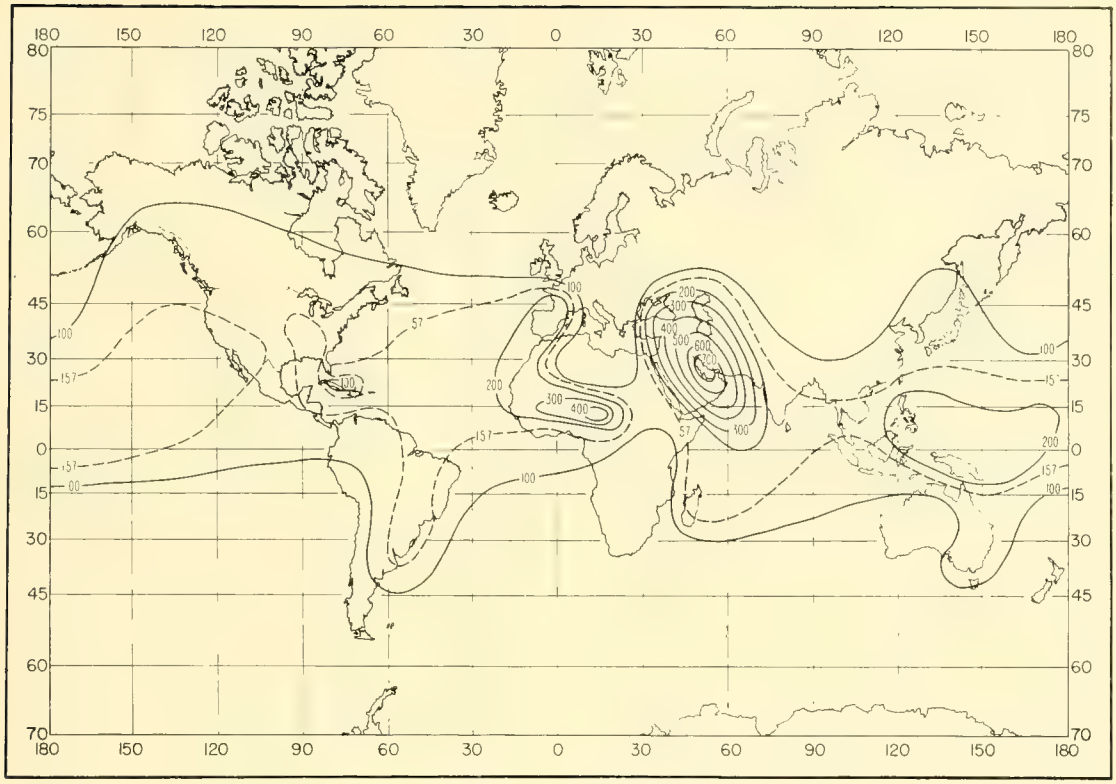

FIGURE C-51. *Lapse rate of refractivity* (N/*km*) *exceeded 5 percent of time for 100-m layer: August.*

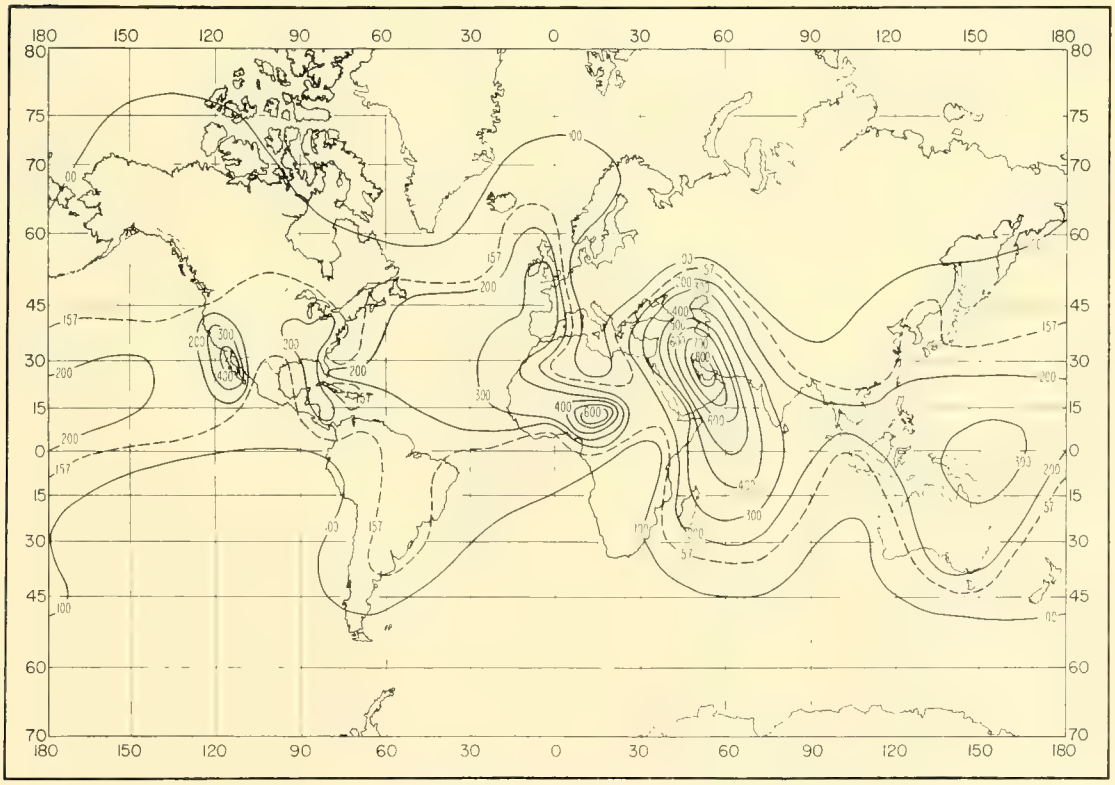

FIGURE C-52. *Lapse rate of refractivity* (N/*km*) *exceeded 2 percent of time for 100-m layer: August.*

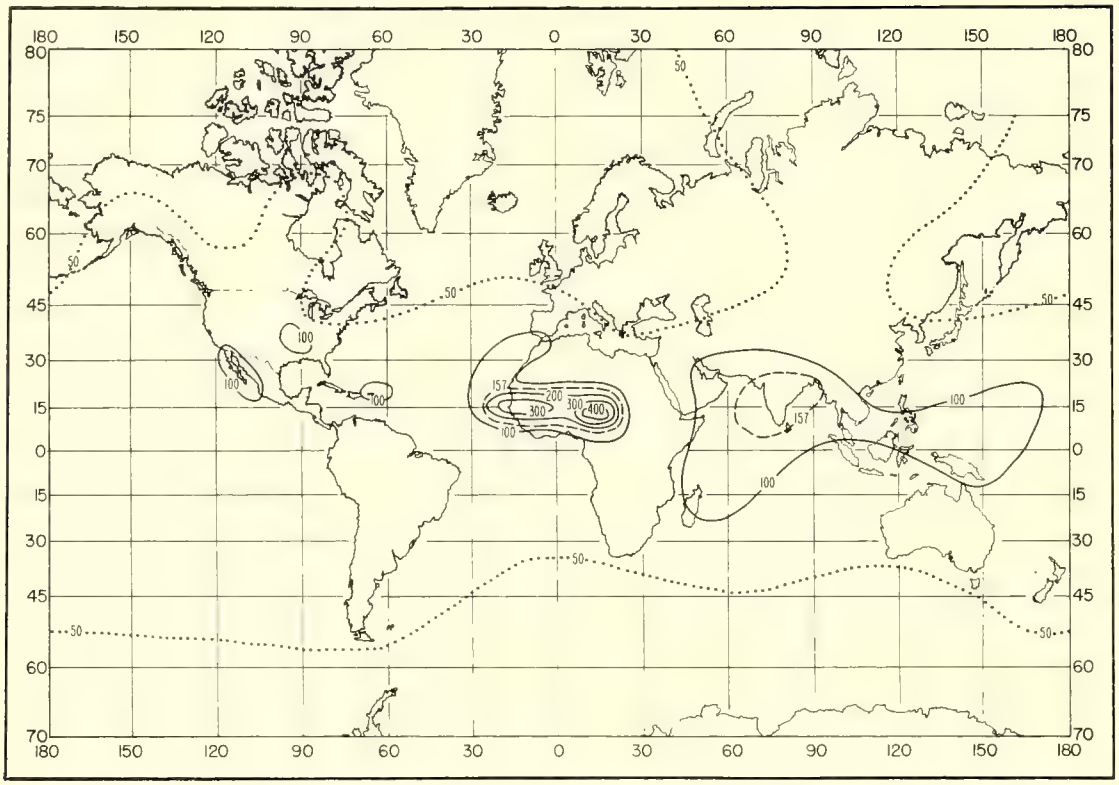

FIGURE C-53. *Lapse rate of refractivity* (N/km) *exceeded 25 percent of time for 100-m layer: November.*

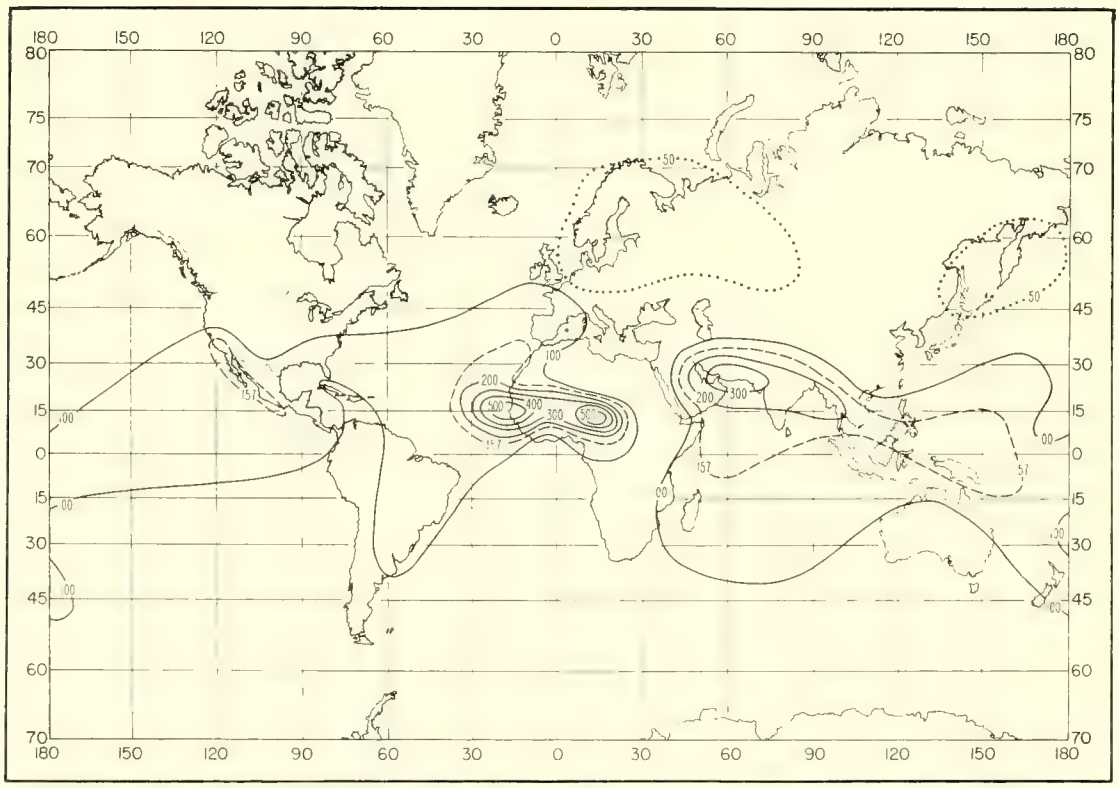

FIGURE C-54. *Lapse rate of refractivity* (N/km) *exceeded 10 percent of time for 100-m layer: November.*

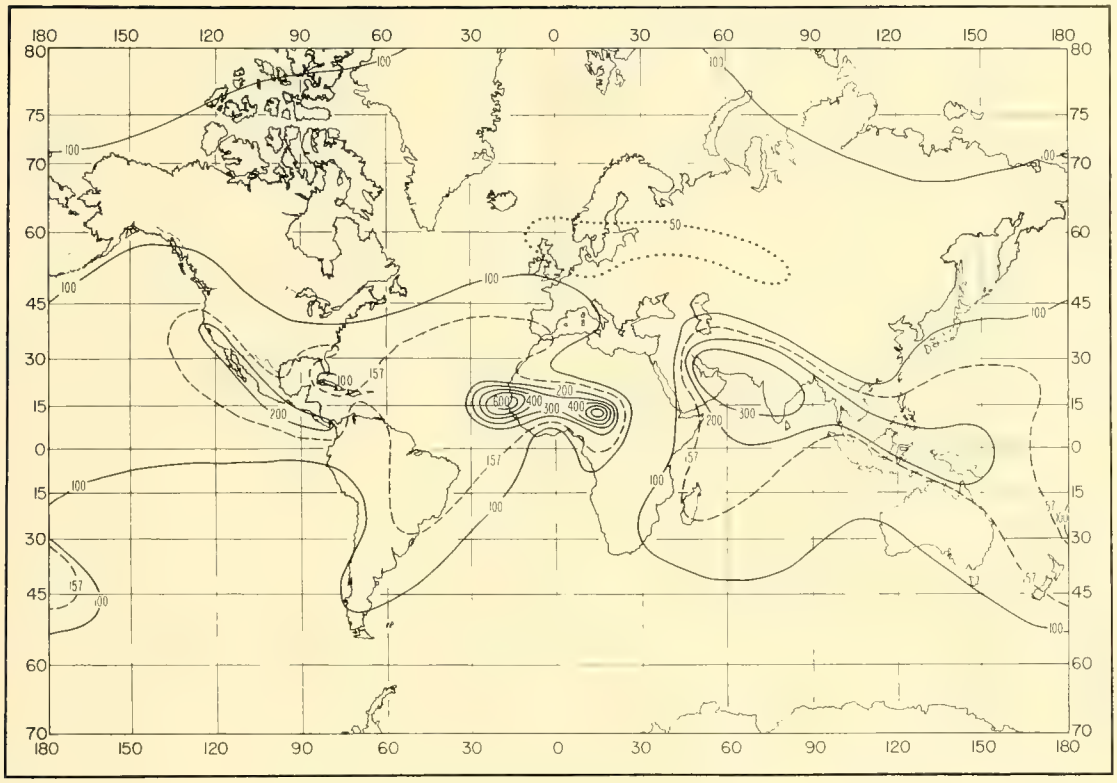

FIGURE C-55. *Lapse rate of refractivity* (N/*km*) *exceeded 5 percent of time for 100-m layer: November.*

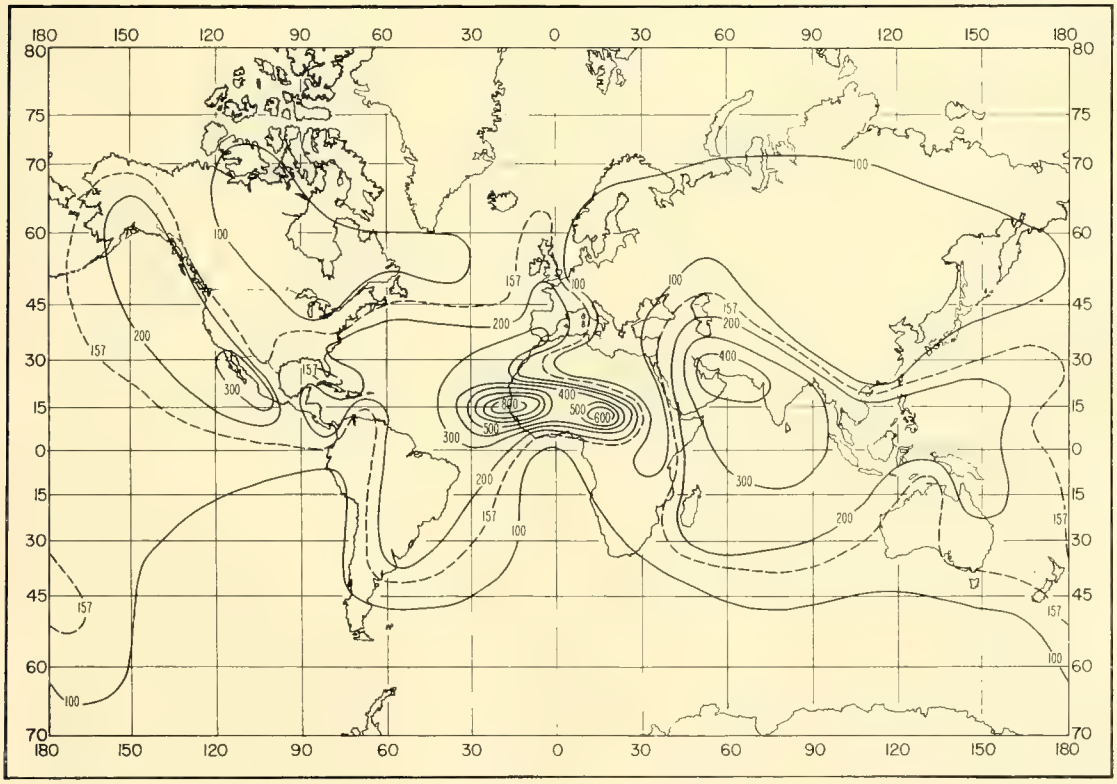

FIGURE C-56. *Lapse rate of refractivity* (N/*km*) *exceeded 2 percent of time for 100-m layer: November.*

TABLE C-1. *Median and minimum trapping frequency (Mc/s) of ducting layers.*

Station	Feb.		May		Aug.		Nov.	
	Med	Min	Med	Min	Med	Min	Med	Min
Aden, Arabia 0000 GMT	478	82	865	40	898	41	485	114
1200 GMT	475	82	767	51	582	41	522	122
Amundsen-Scott, Antarctica	2503	*	531	266	495	272	†	
Balboa (Albrook), Panama C. Z.	743	311	676	270	663	242	657	314
Bangui, Central African Republic	280	66	569	247	265	176	369	294
Bordeaux, France	1300	190	565	99	402	89	442	186
Dakar, Senegal	328	56	409	43	848	162	378	35
Denver, Colo.	‡	*	‡	*	‡		‡	
Ezeiza, Argentina	681	123	181	*	383	*	1403	*
Fort Smith, Northwest Territories	872	9	430	*	145	43	1345	*
Hilo, Hawaii	862	482	801	346	467	253	1035	496
Long Beach, Calif	‡		‡		‡		‡	
Lourenco Marques, Portuguese East Africa	554	245	†		2334	*	2404	430
Nandi, Fiji Islands	‡		‡		‡	*	‡	*
New York, N.Y.	‡	*	‡		‡	*	‡	*
Nicosia, Cyprus 0000 GMT	1143	*	307	125	137	44	398	*
1200 GMT	†		290	*	680	122	1223	*
Ostersund, Sweden	†		‡		†		†	
Perth, Australia	4864	*	709	*	799	*	649	*
Saigon, Viet Nam	532	155	610	326	904	403	539	264
San Juan, P. R.	671	51	631	41	595	227	535	53
Ship Station "C"	320	*	843	*	1028	*	308	*
Tashkent, U.S.S.R.	†		†		334	*	774	*
Vladivostok, U.S.S.R.	†		499	*	584	50	1253	*

* *Less than 5 ducting layers during month.*
† *No ducting.*
‡ *Trapping frequencies not computed.*

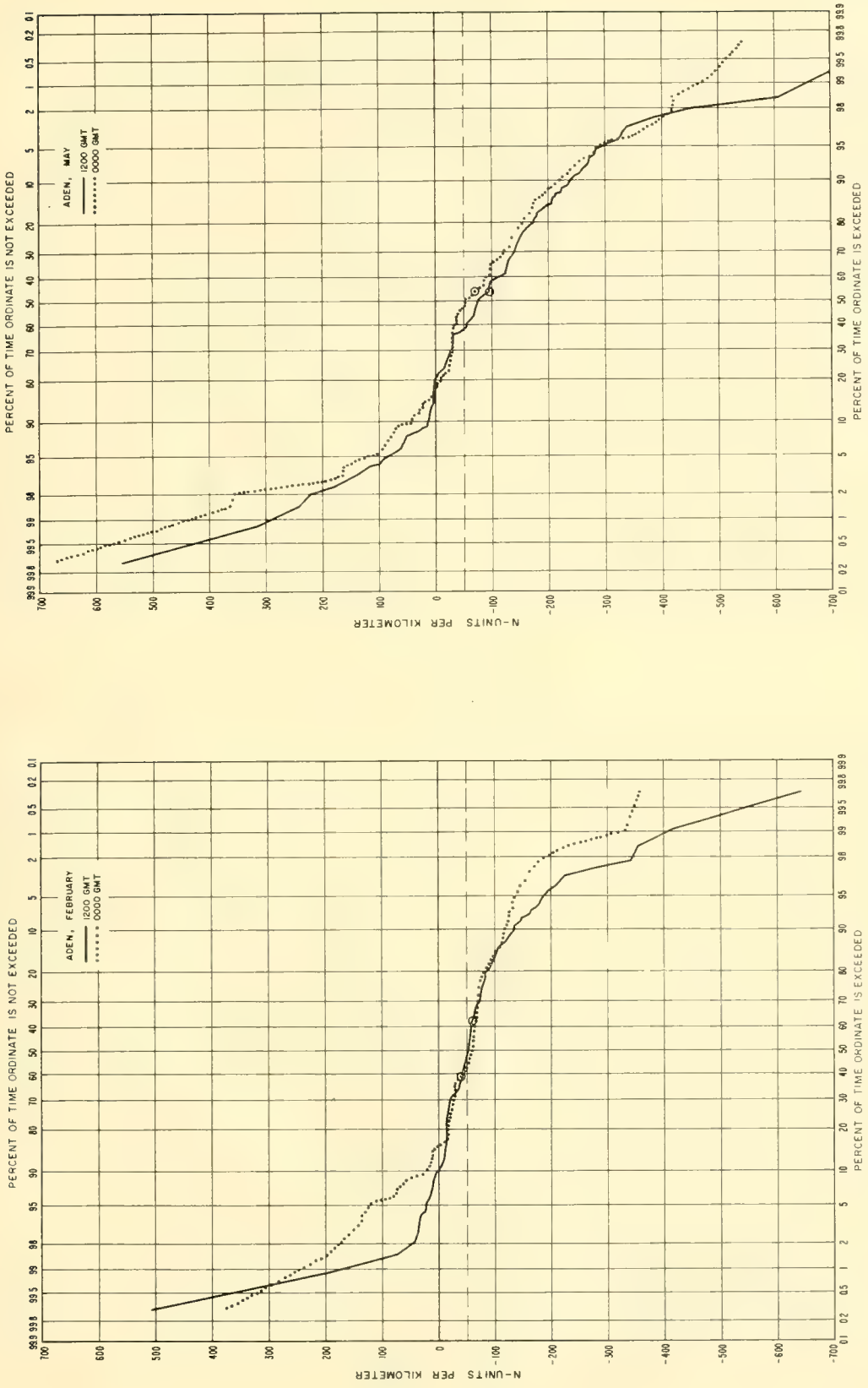

FIGURE C-57. (*a*) *Cumulative probability distributions of* dN/dh *for ground-based 100-m layer: Aden, Arabia (February, May).*

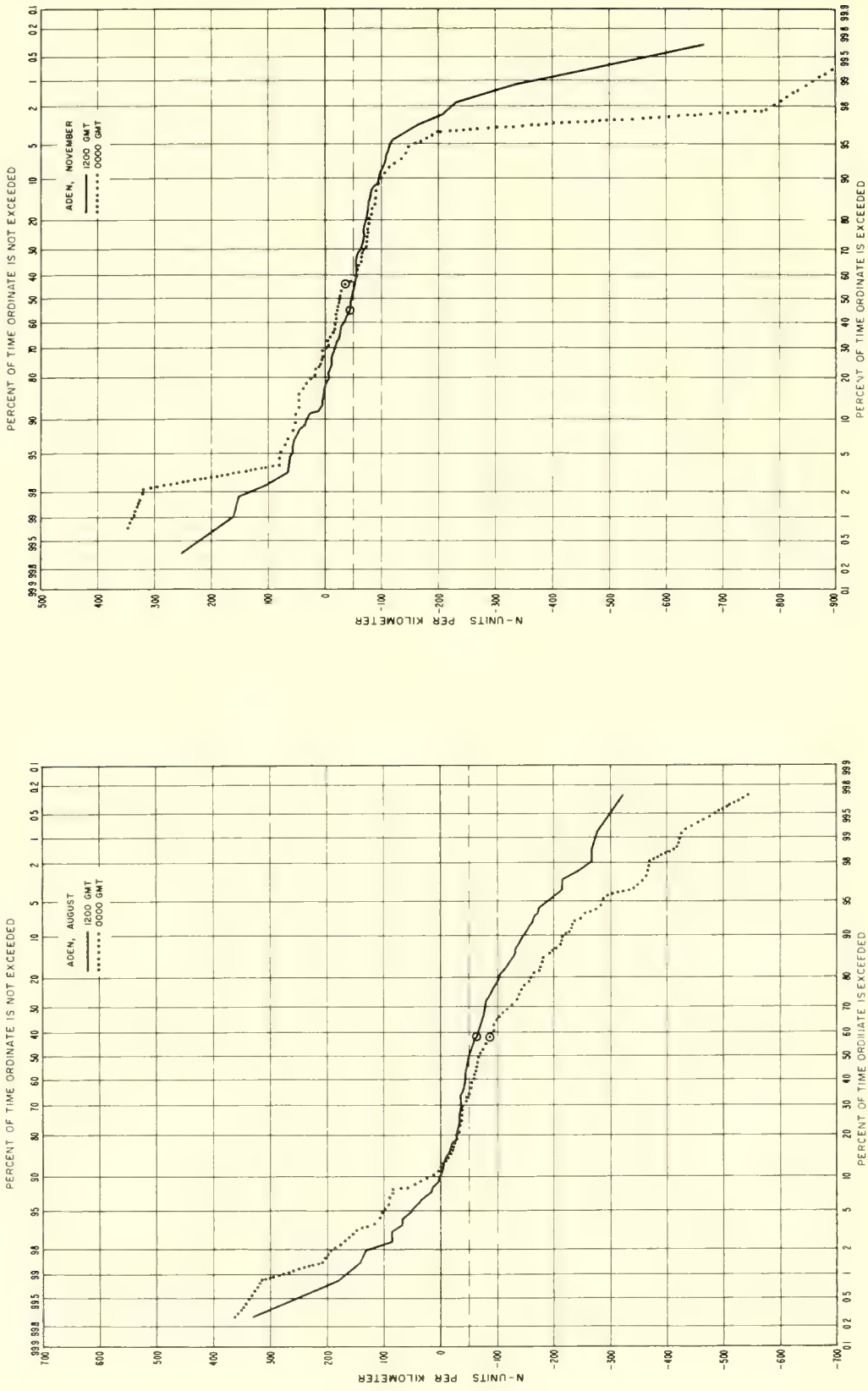

FIGURE C-57. (b) *Cumulative probability distributions of* dN/dh *for ground-based 100-m layer: Aden, Arabia (August, November).*

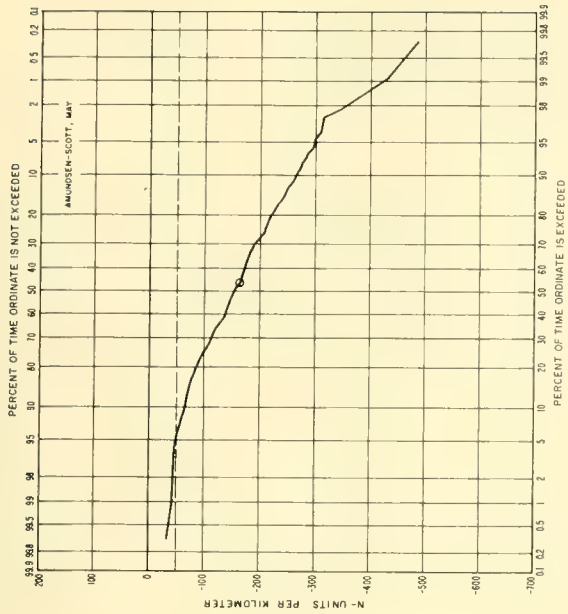

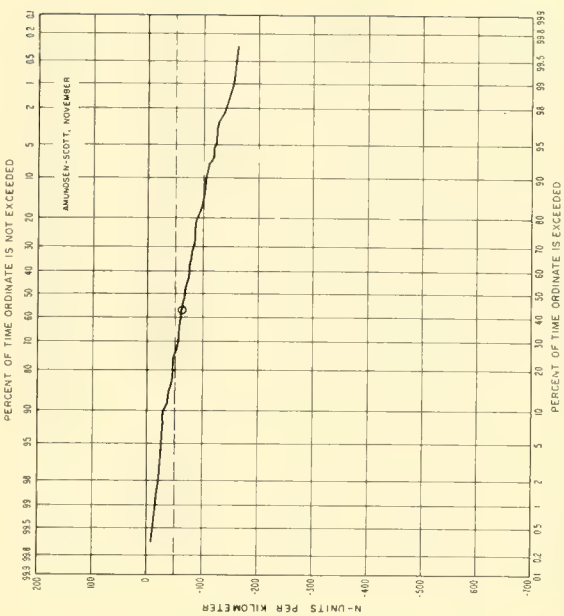

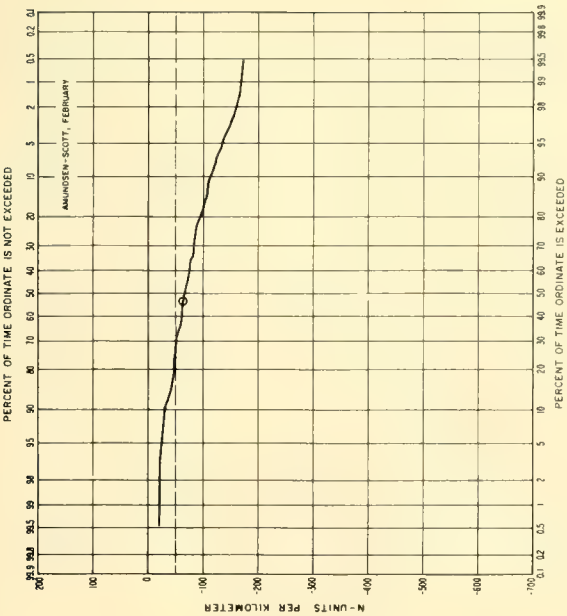

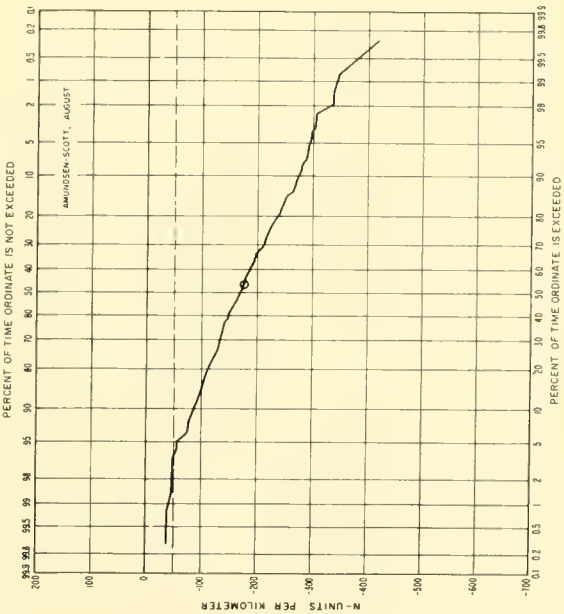

FIGURE C-58. *Cumulative probability distributions of* dN/dh *for ground-based 100-m layer: Amundsen-Scott, Antarctica.*

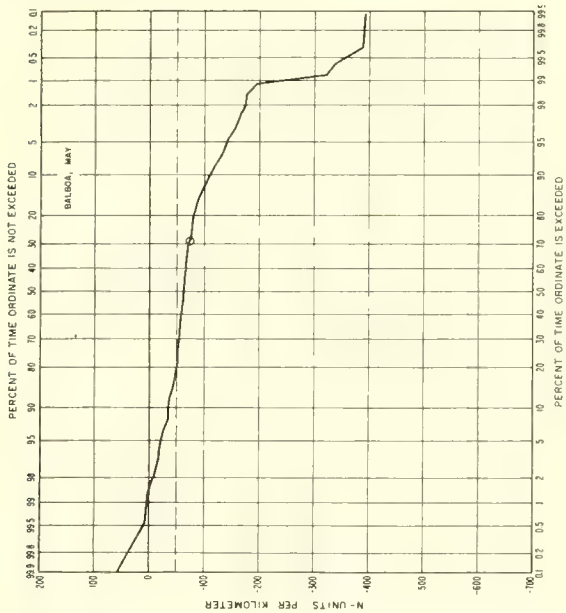

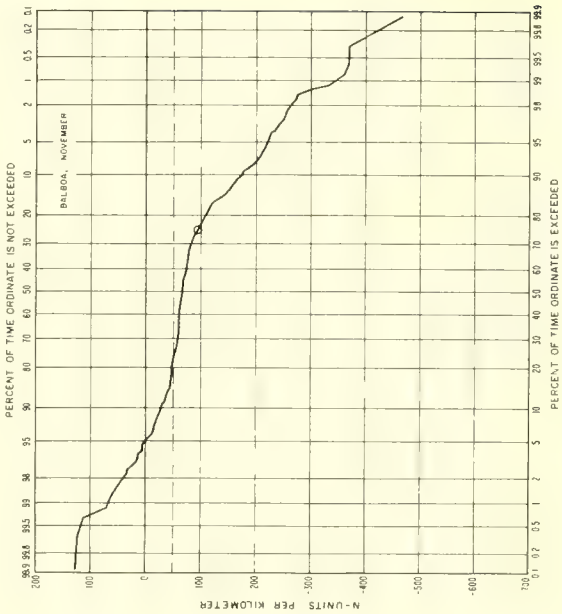

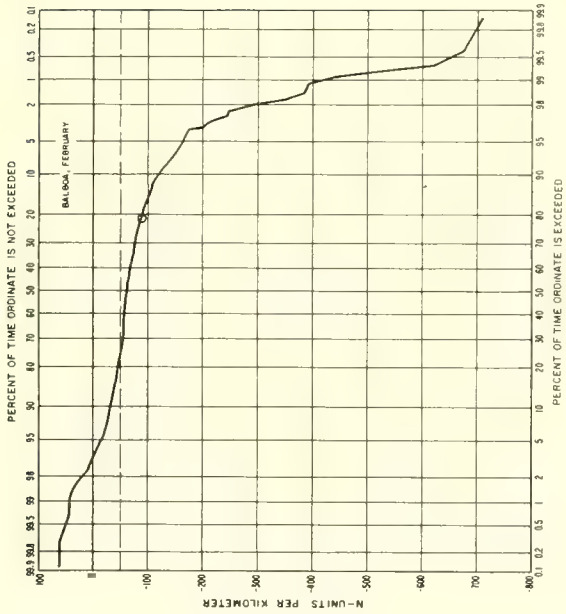

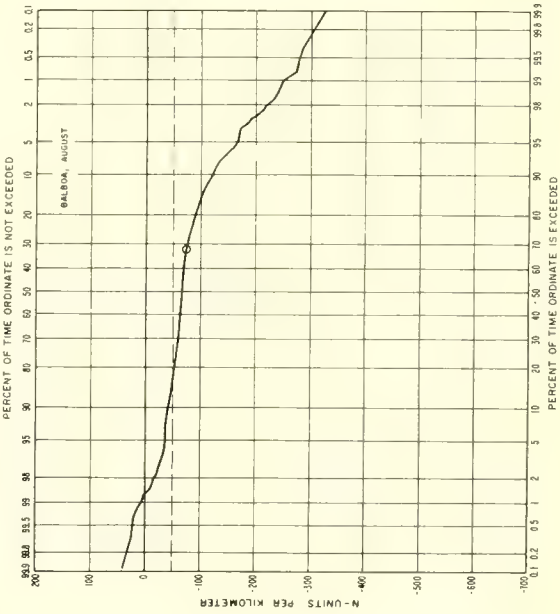

FIGURE C-59. *Cumulative probability distributions of* dN/dh *for ground-based 100-m layer: Balboa (Albrook), Panama C.Z.*

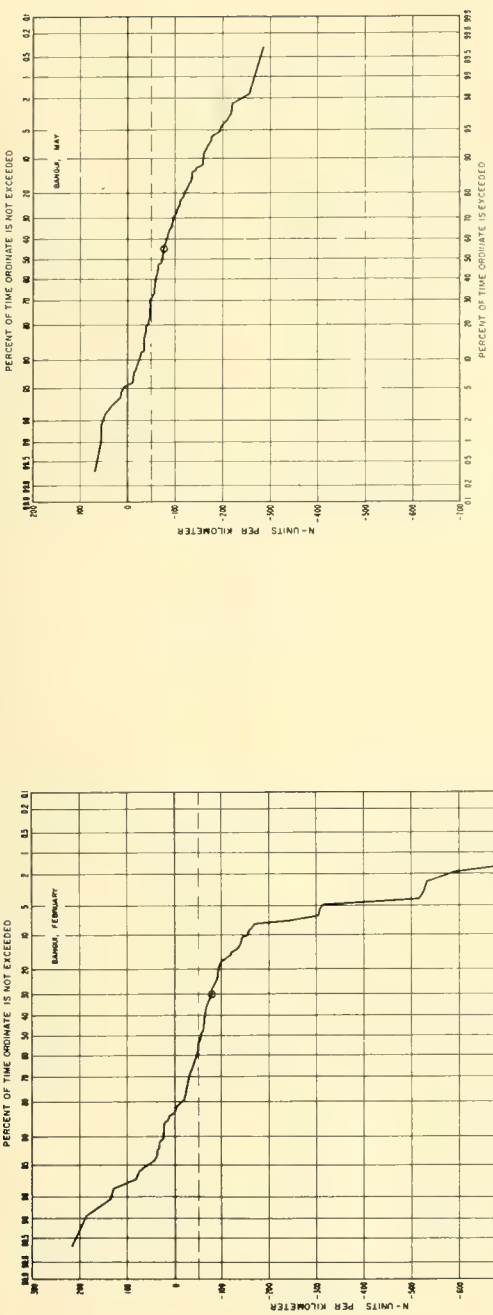

FIGURE C-60. *Cumulative probability distributions of* dN/dh *for ground-based 100-m layer: Bangui, Central African Republic.*

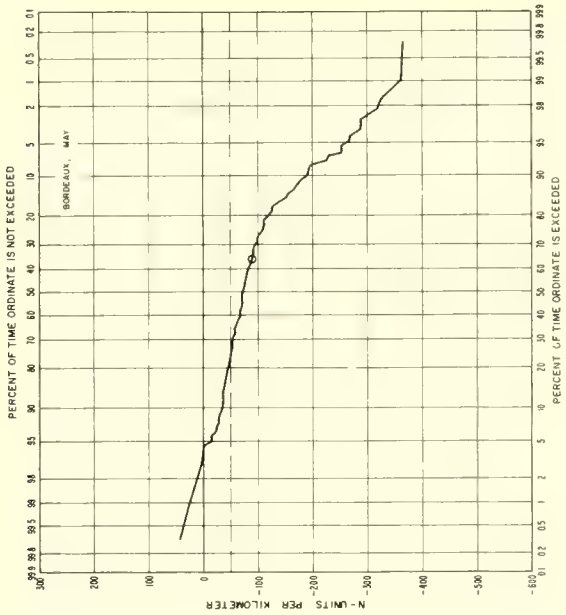

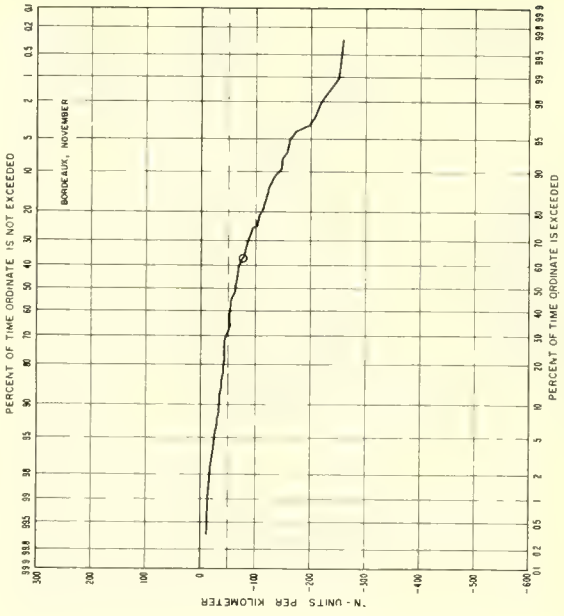

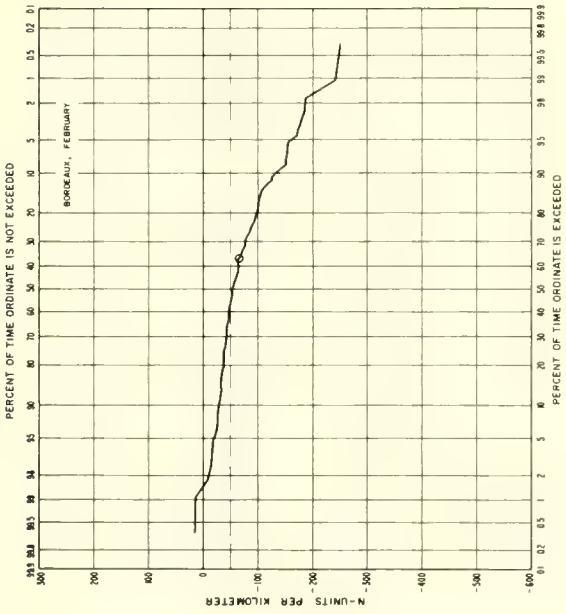

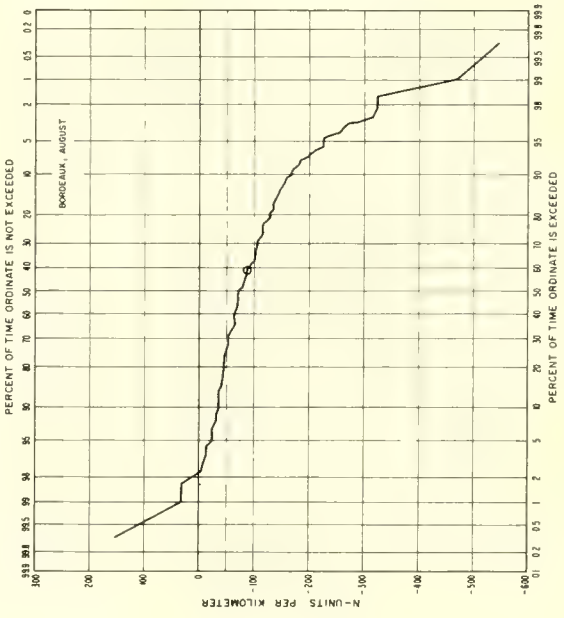

FIGURE C-61. *Cumulative probability distributions of* dN/dh *for ground-based 100-m layer: Bordeaux, France.*

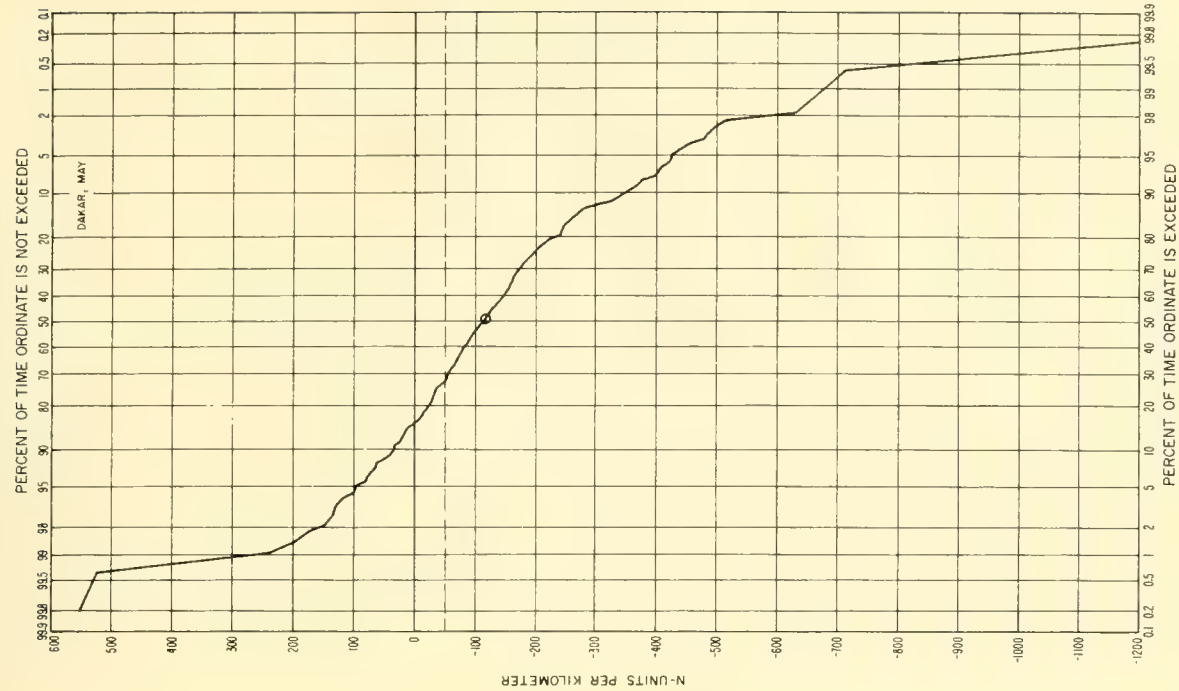

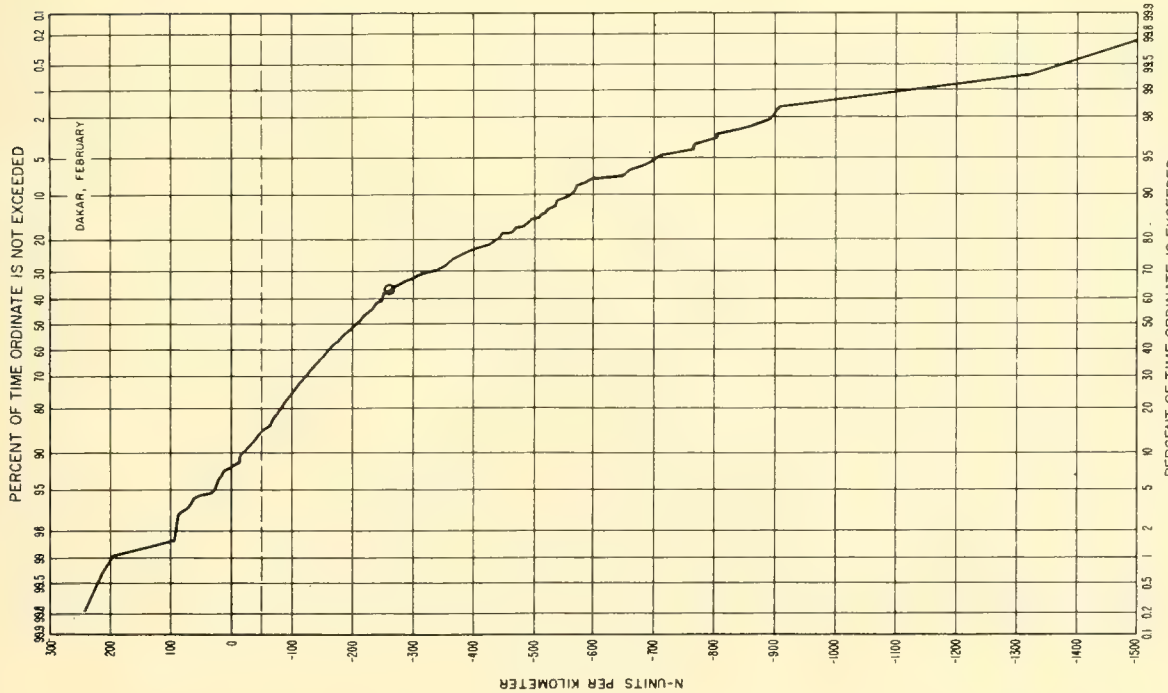

FIGURE C-62. *(a) Cumulative probability distributions of* dN/dh *for ground-based 100-m layer: Dakar, Republic of Senegal (February, May).*

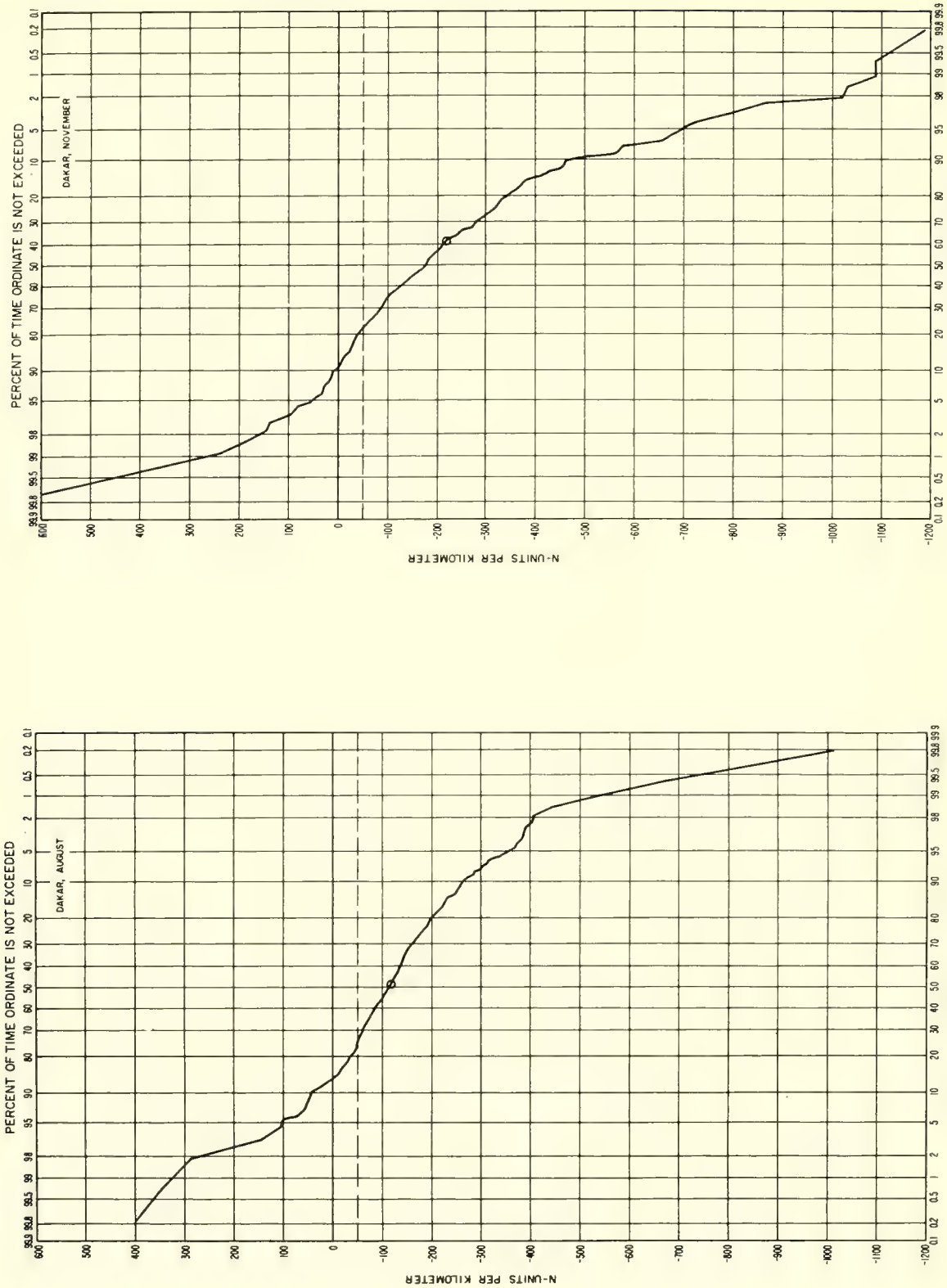

FIGURE C-62. (*b*) *Cumulative probability distributions of* dN/dh *for ground-based 100-m layer: Dakar, Republic of Senegal (August, November).*

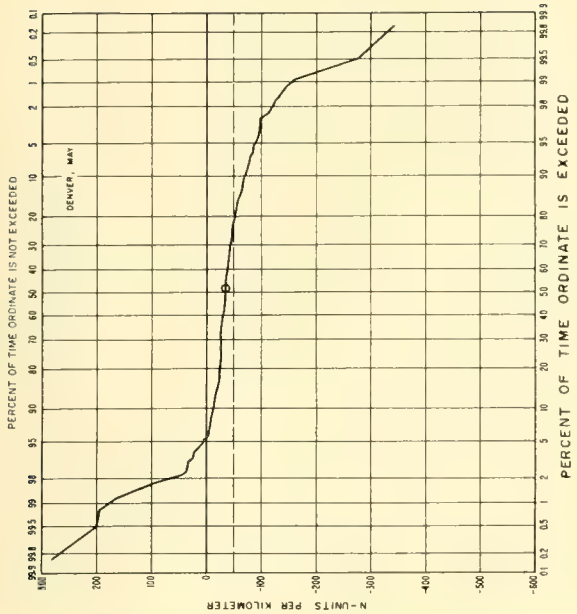

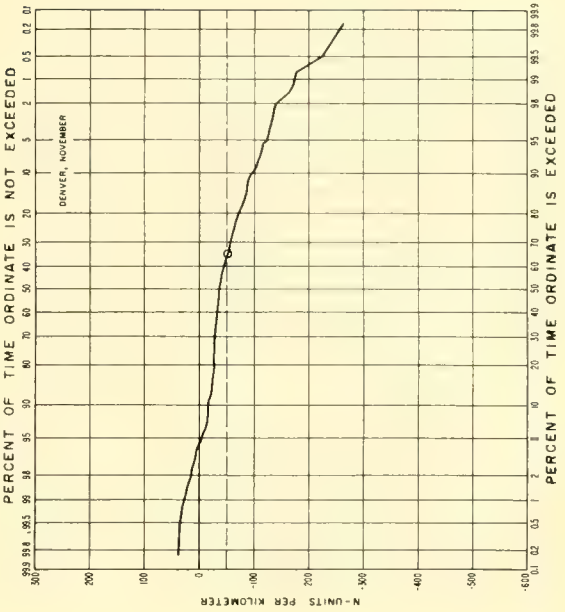

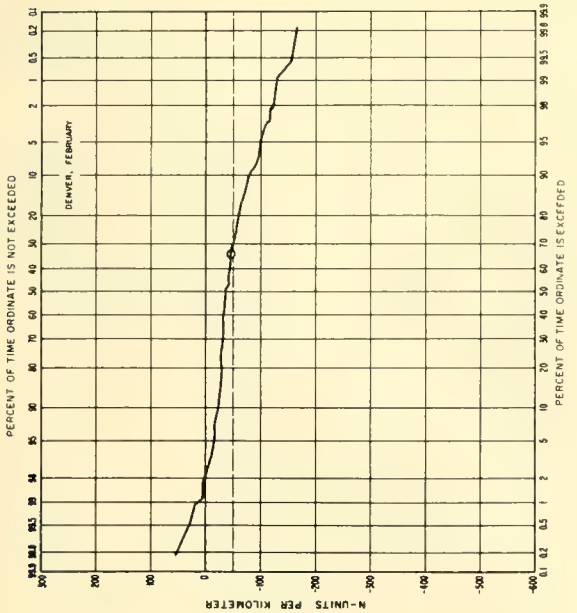

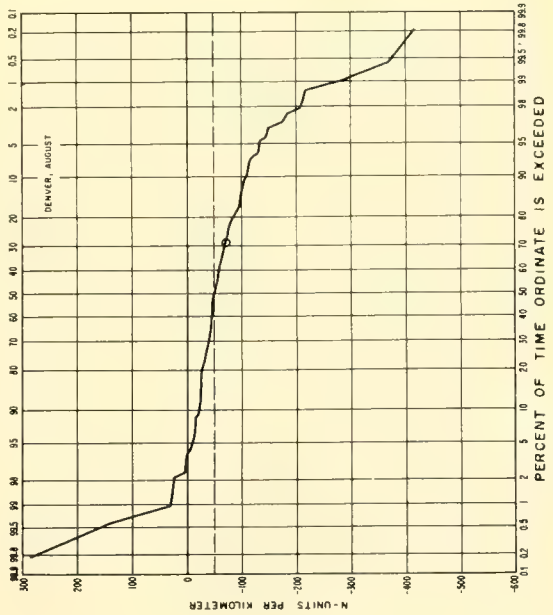

FIGURE C-63. *Cumulative probability distributions of* dN/dh *for ground-based 100-m layer: Denver, Colo.*

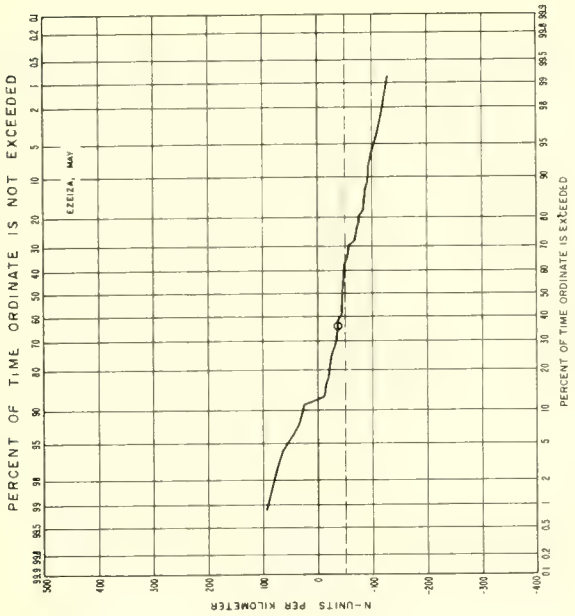

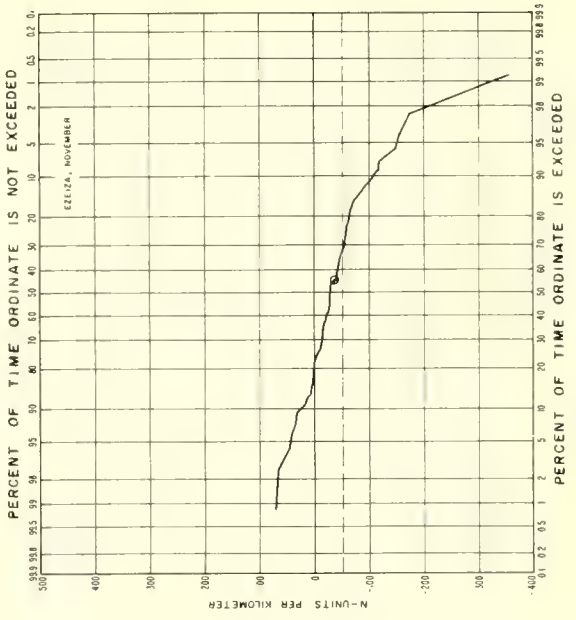

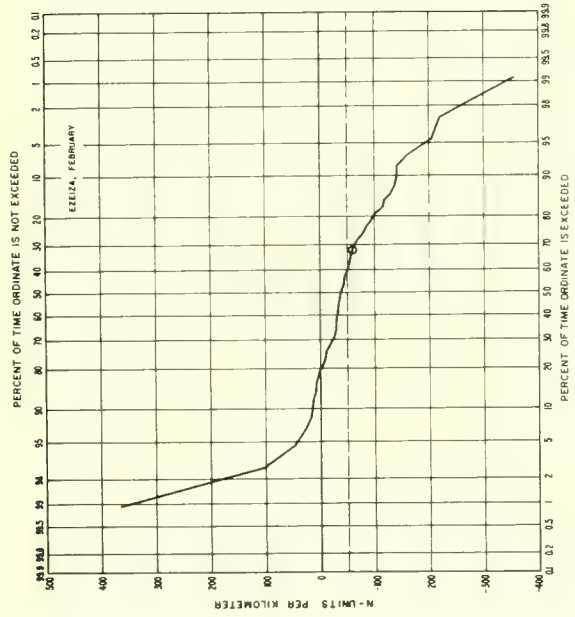

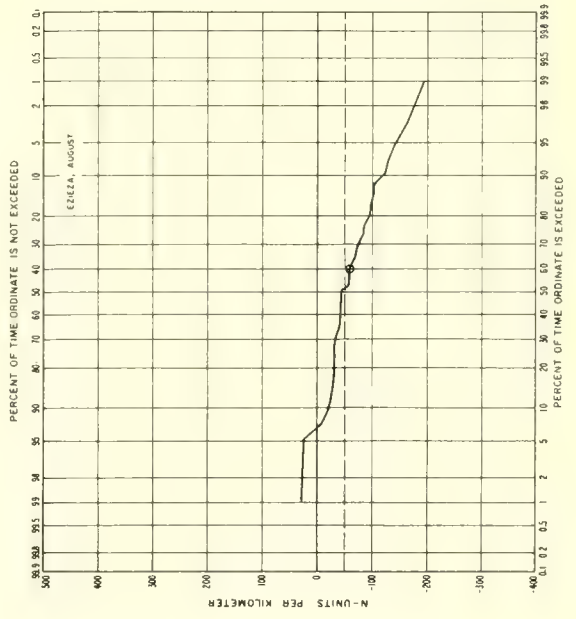

FIGURE C-64. *Cumulative probability distributions of* dN/dh *for ground-based 100-m layer: Ezeiza, Argentina.*

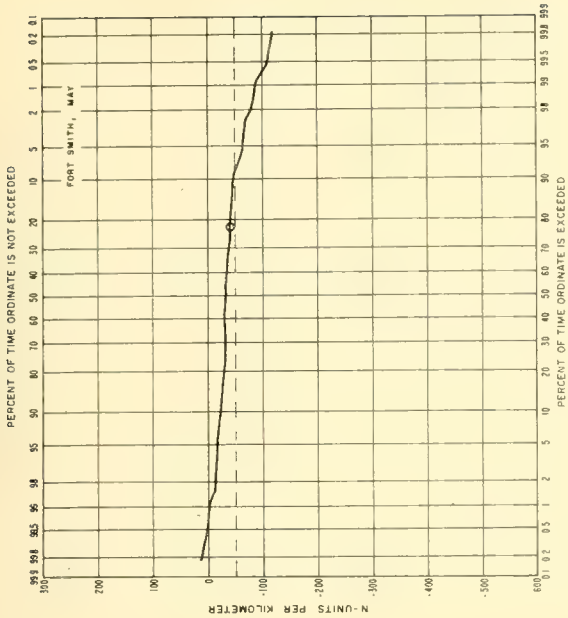

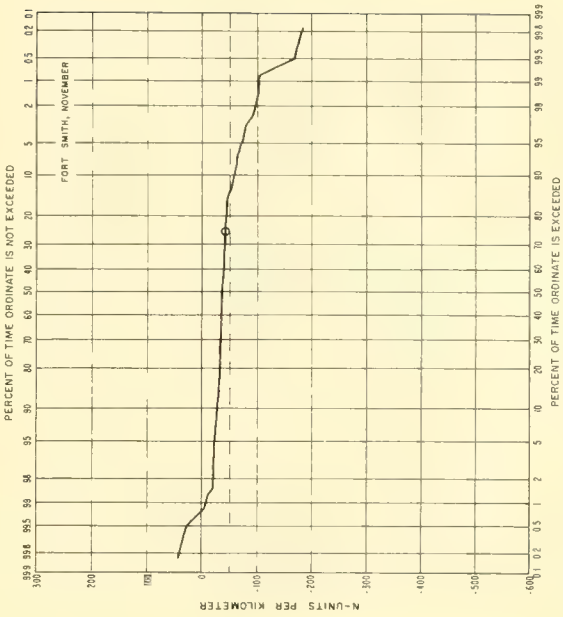

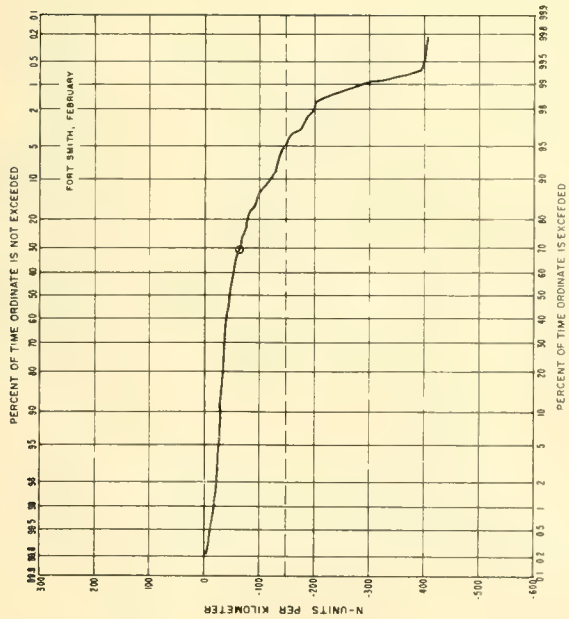

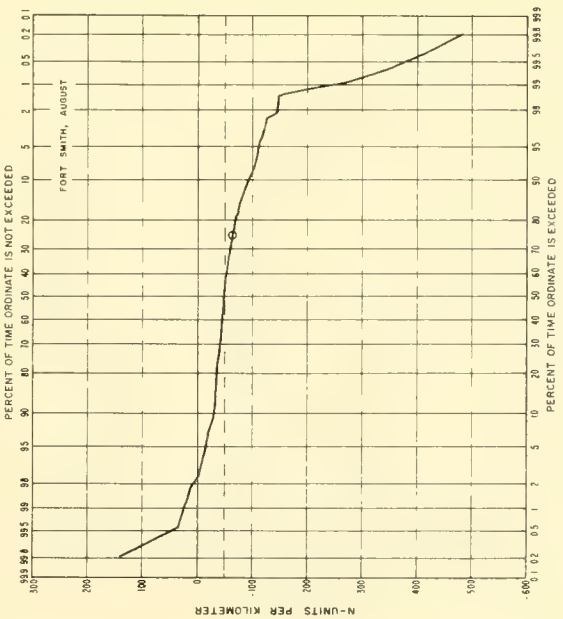

FIGURE C-65. *Cumulative probability distributions of* dN/dh *for ground-based 100-m layer: Fort Smith, Northwest Territories, Canada.*

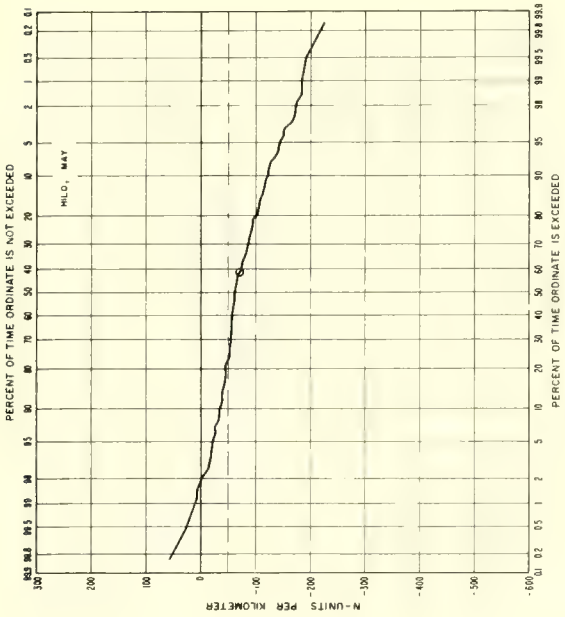

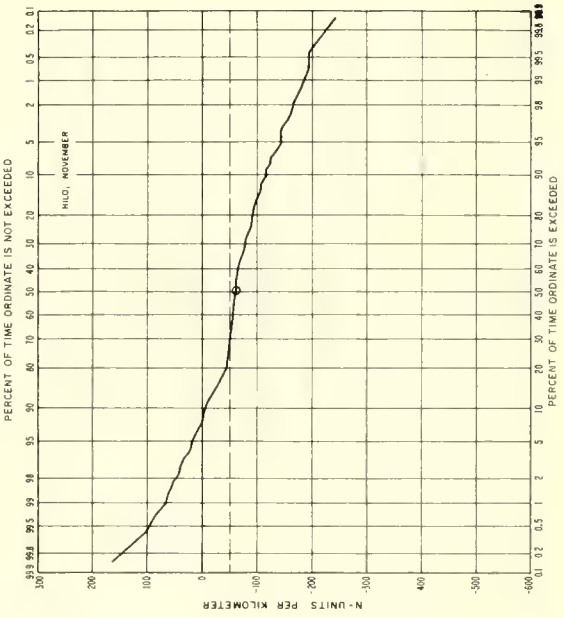

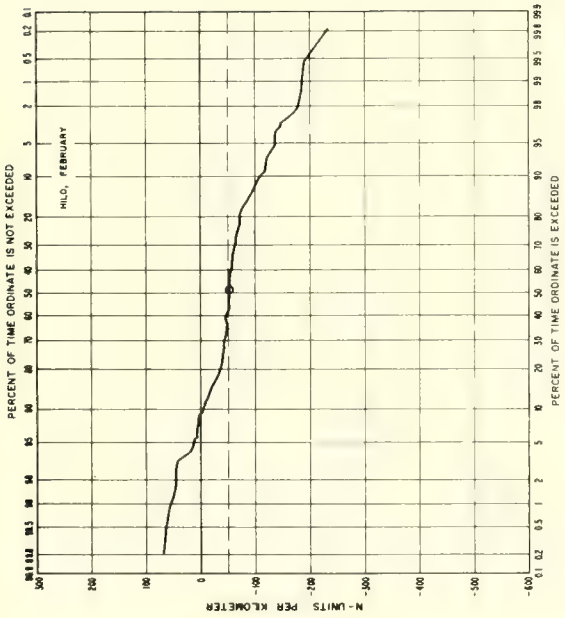

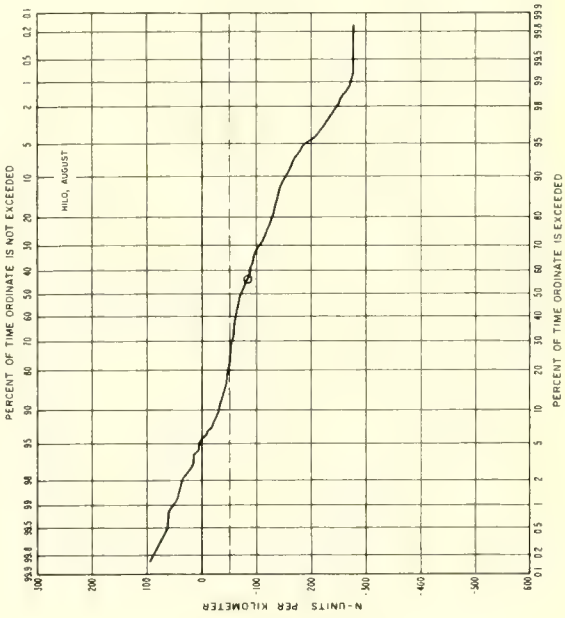

FIGURE C-66. *Cumulative probability distributions of* dN/dh *for ground-based 100-m layer: Hilo, Hawaii.*

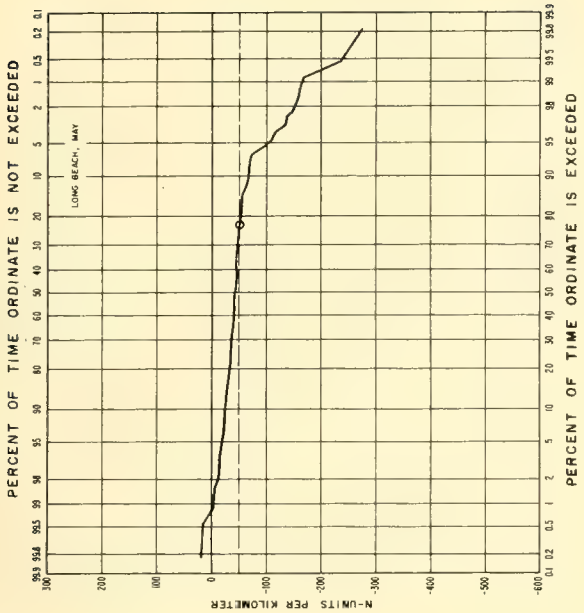

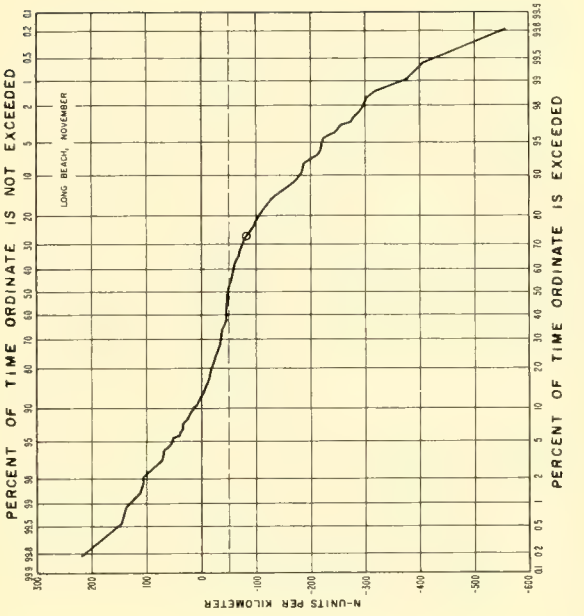

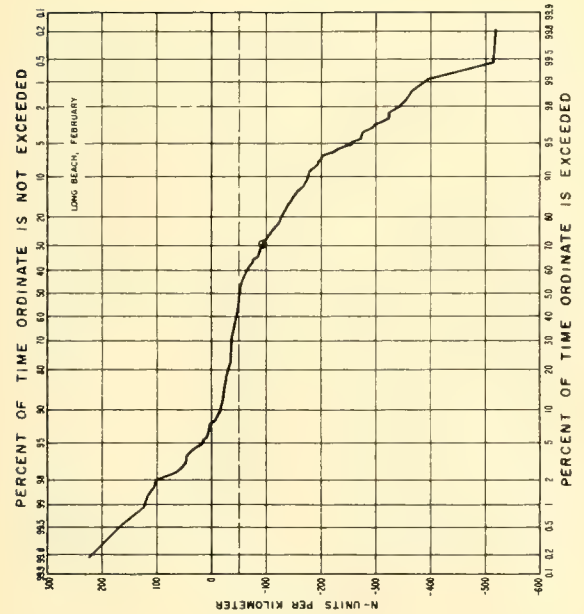

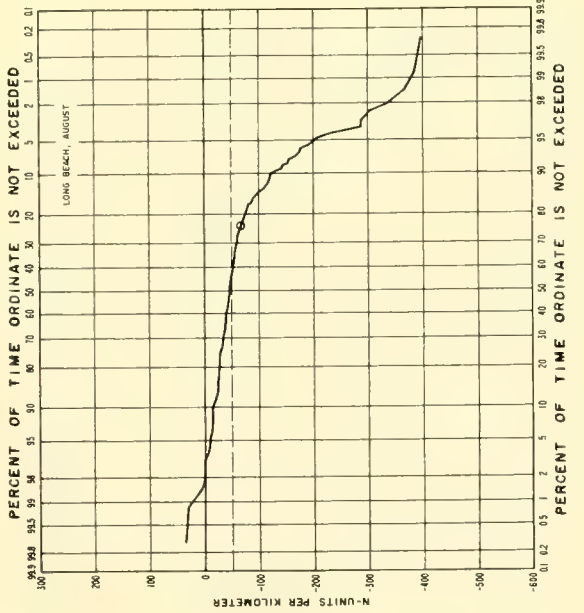

FIGURE C-67. *Cumulative probability distributions of* dN/dh *for ground-based 100-m layer: Long Beach, Calif.*

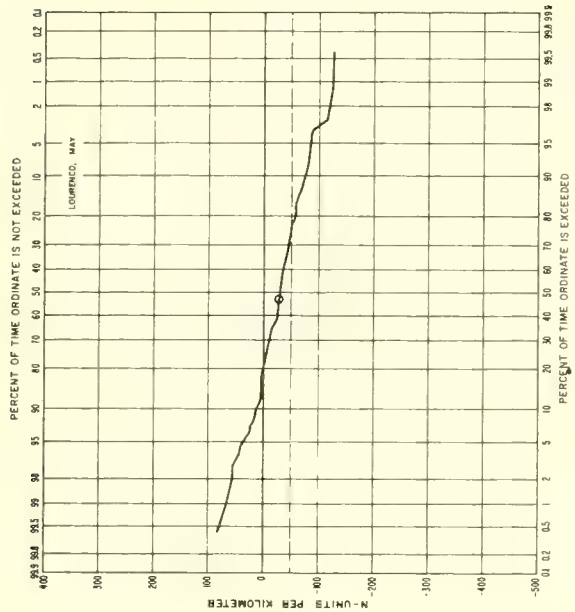

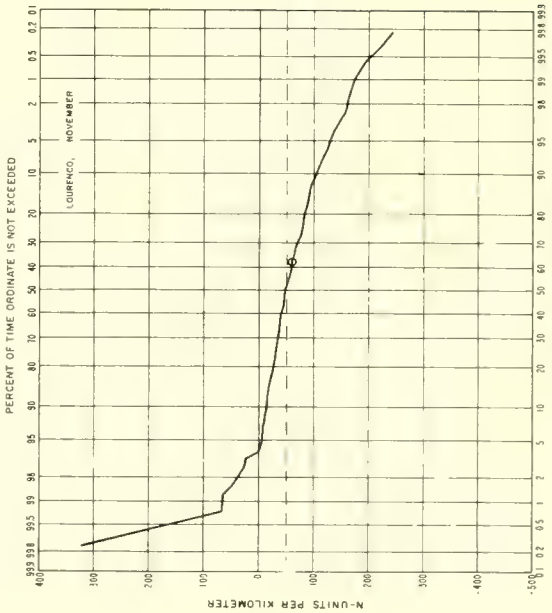

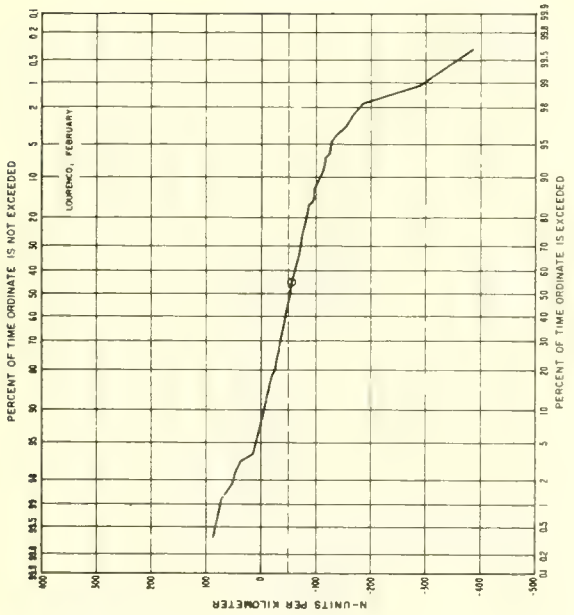

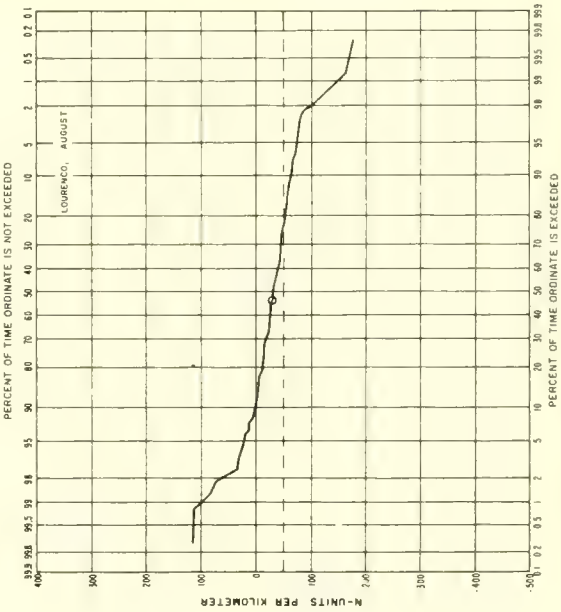

FIGURE C-68. *Cumulative probability distributions of* dN/dh *for ground-based 100-m layer: Lourenco Marques, Portuguese East Africa.*

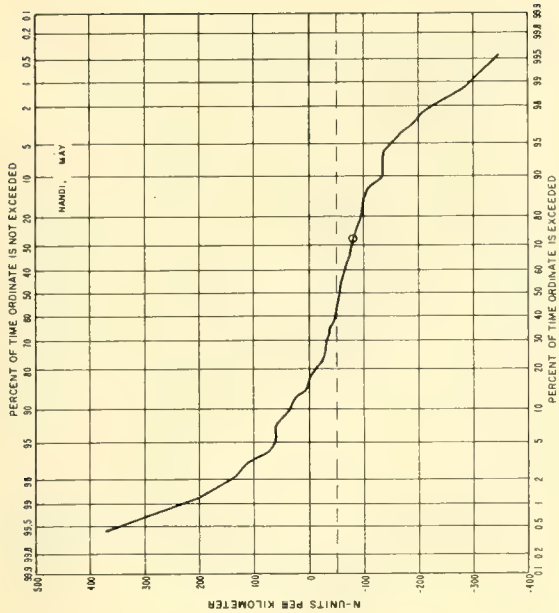

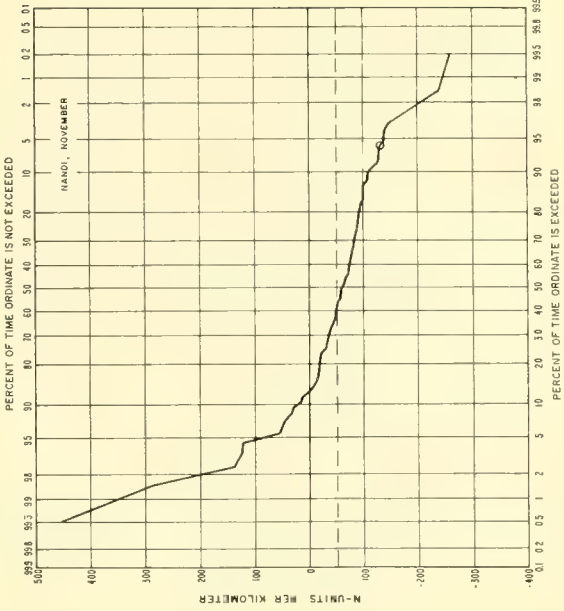

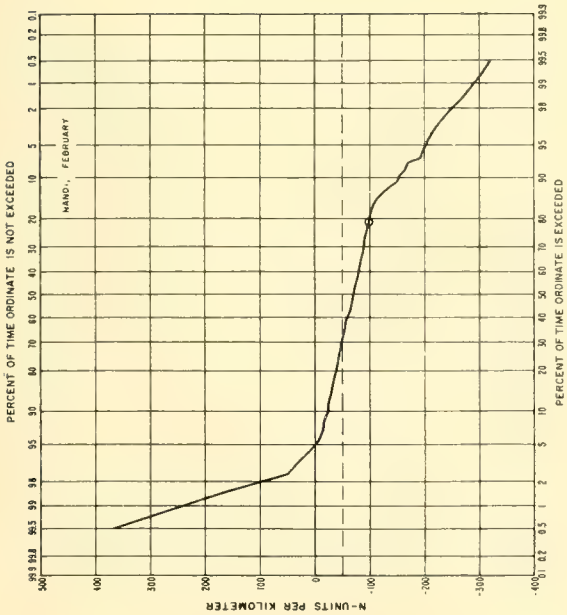

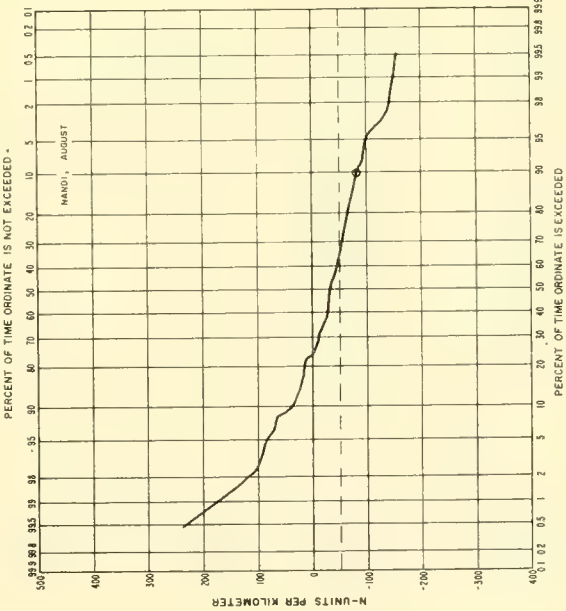

FIGURE C-69. *Cumulative probability distributions of* dN/dh *for ground-based 100-m layer: Nandi, Fiji Islands.*

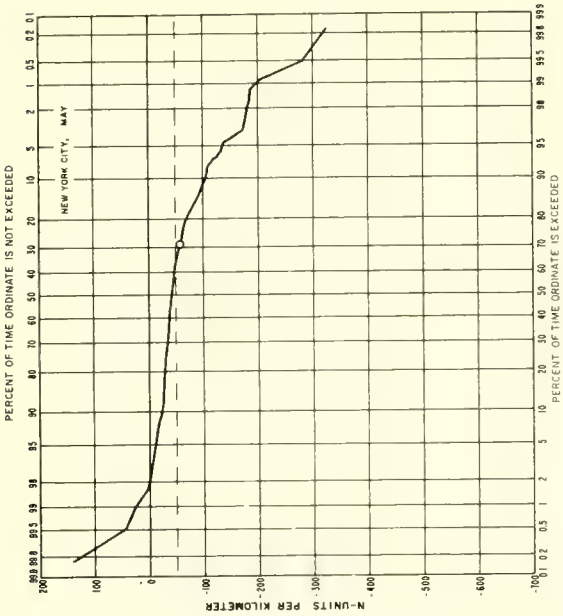

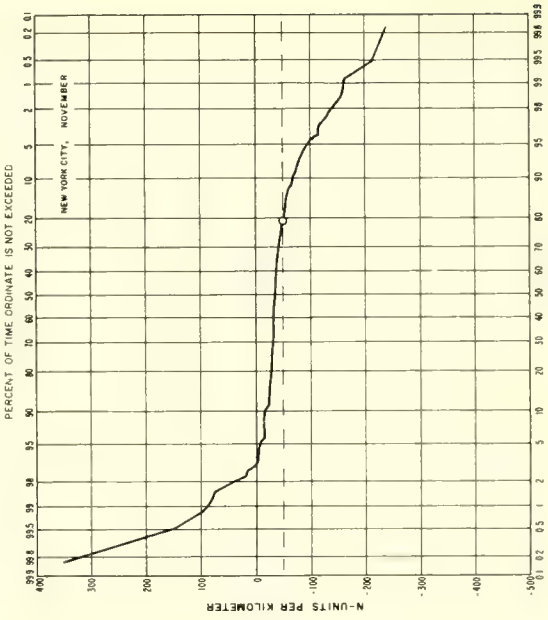

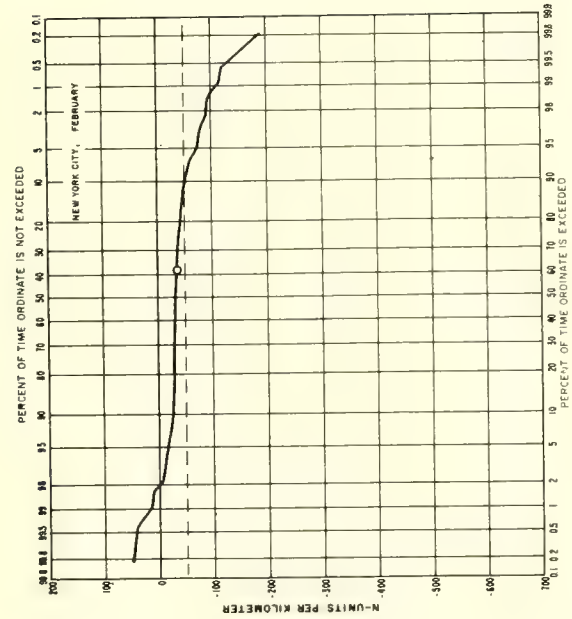

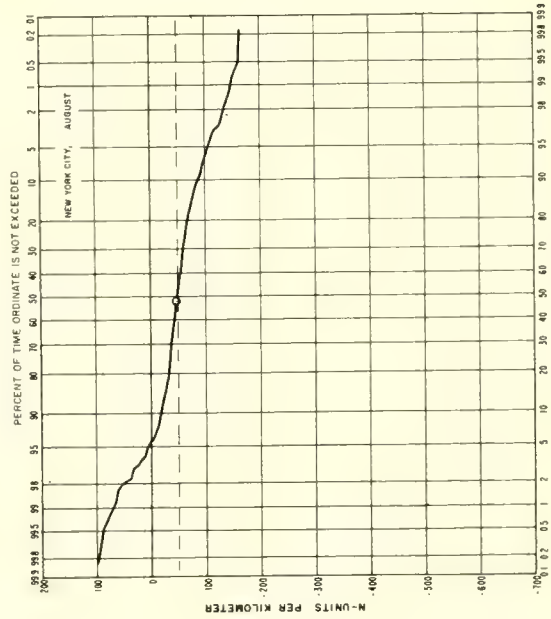

FIGURE C-70. *Cumulative probability distributions of* dN/dh *for ground-based 100-m layer: New York, N.Y.*

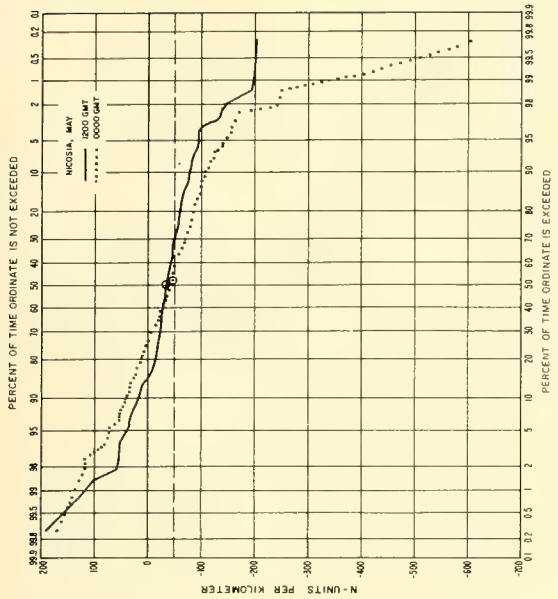

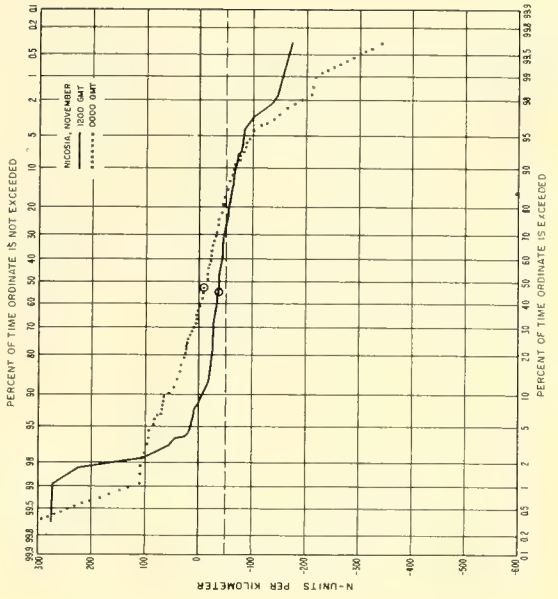

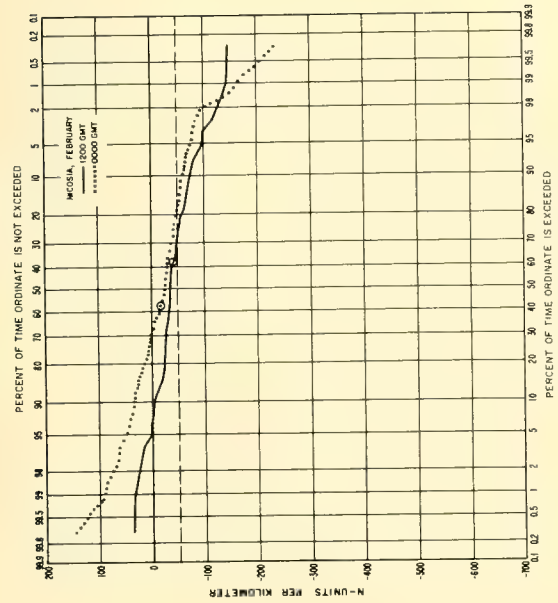

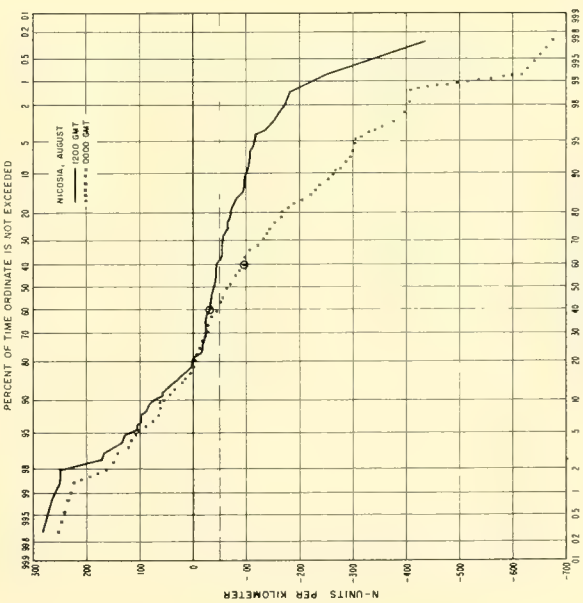

FIGURE C-71. *Cumulative probability distributions of* dN/dh *for ground-based 100-m layer: Nicosia, Cyprus.*

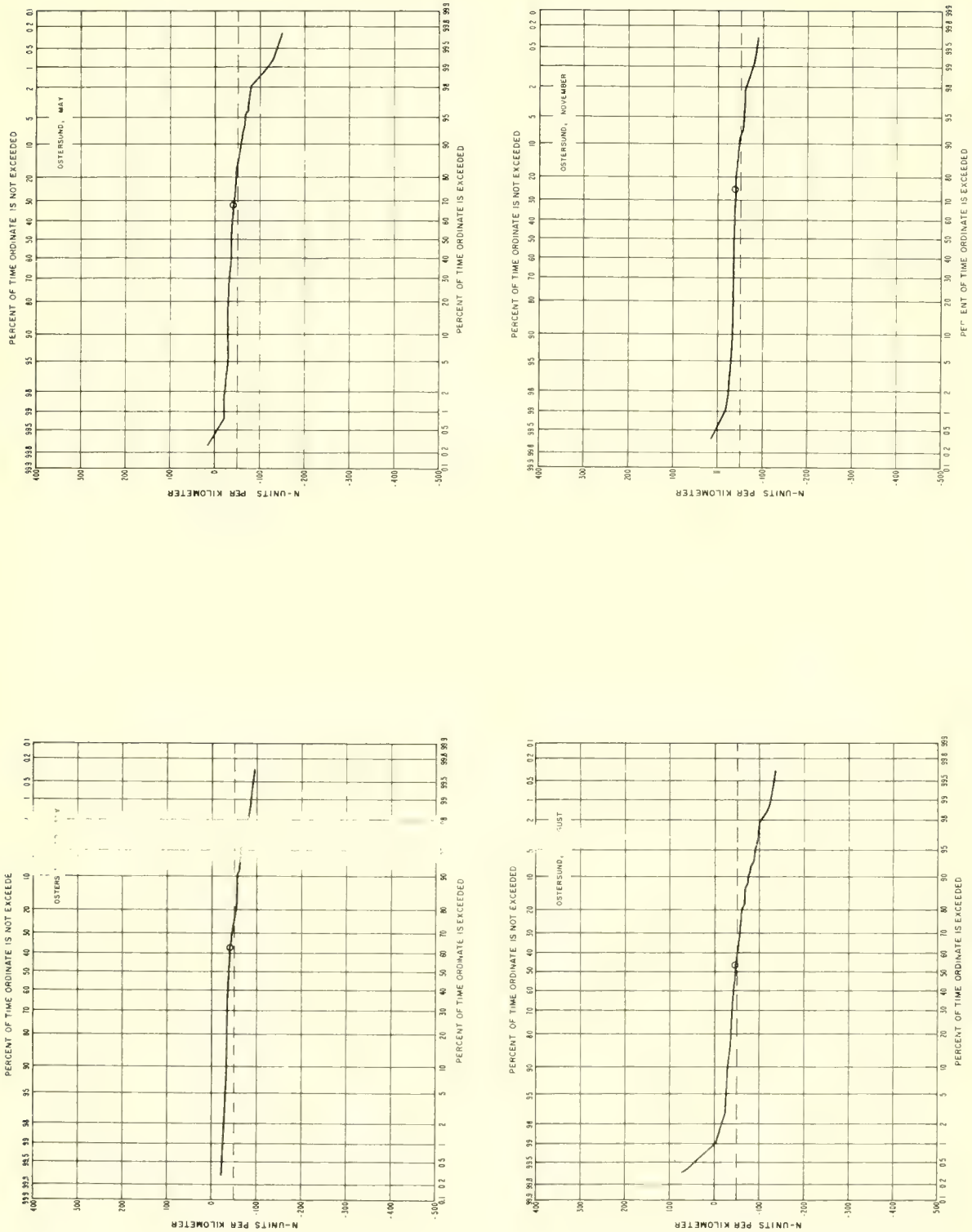

FIGURE C-72. *Cumulative probability distributions of* dN/dh *for ground-based 100-m layer: Ostersund, Sweden.*

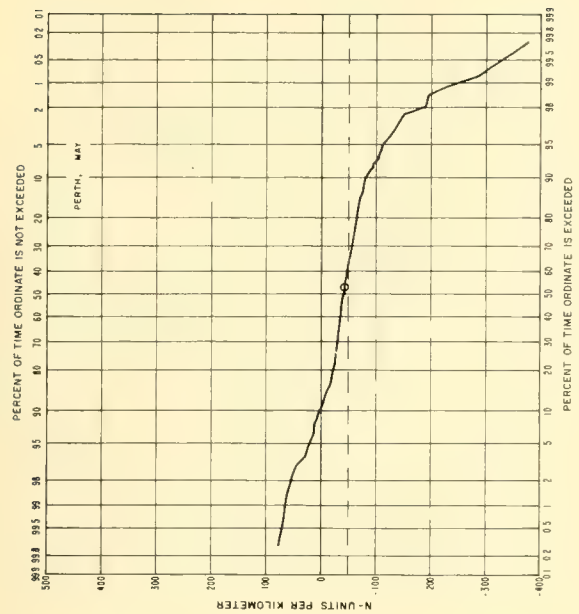

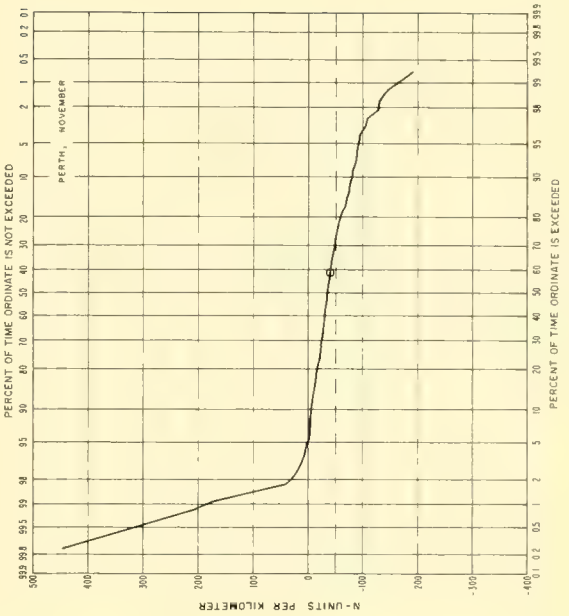

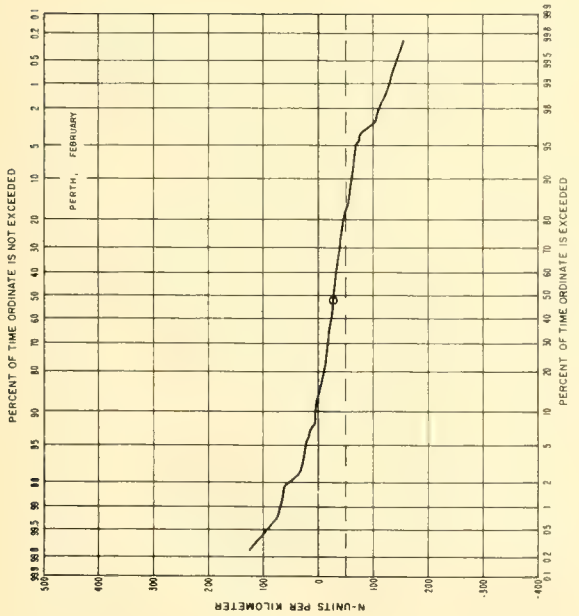

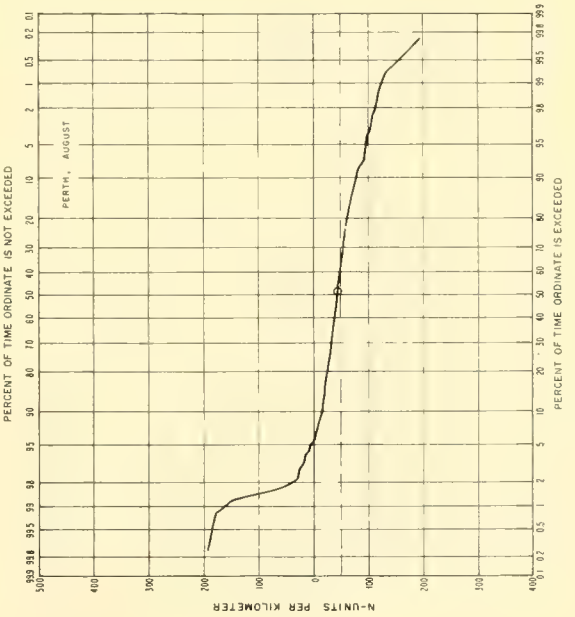

FIGURE C-73. *Cumulative probability distributions of* dN/dh *for ground-based 100-m layer: Perth, Australia.*

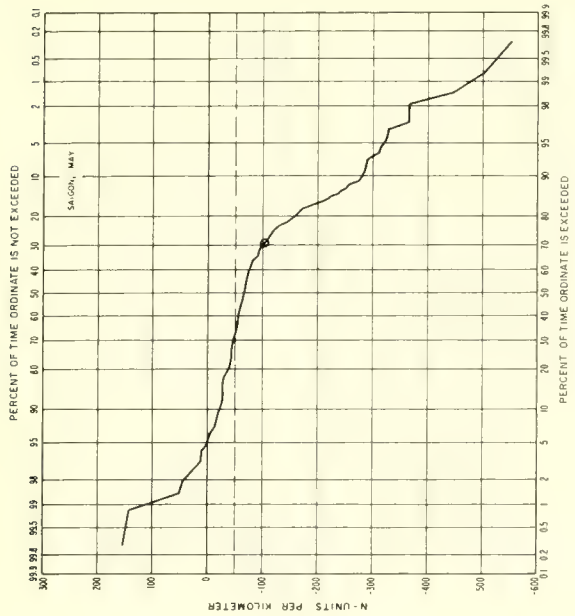

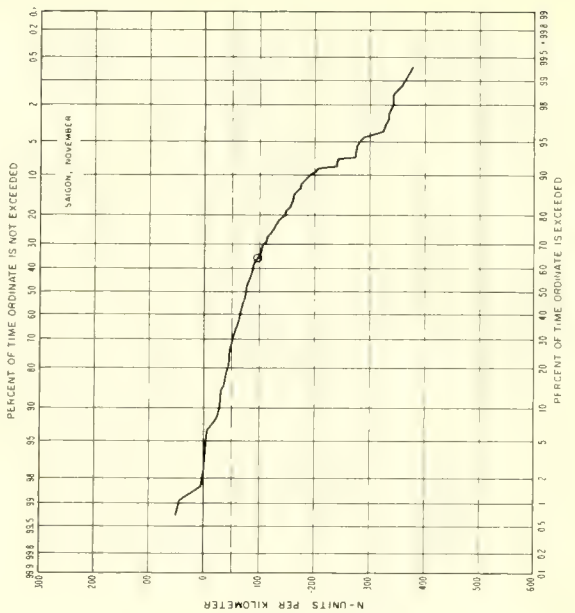

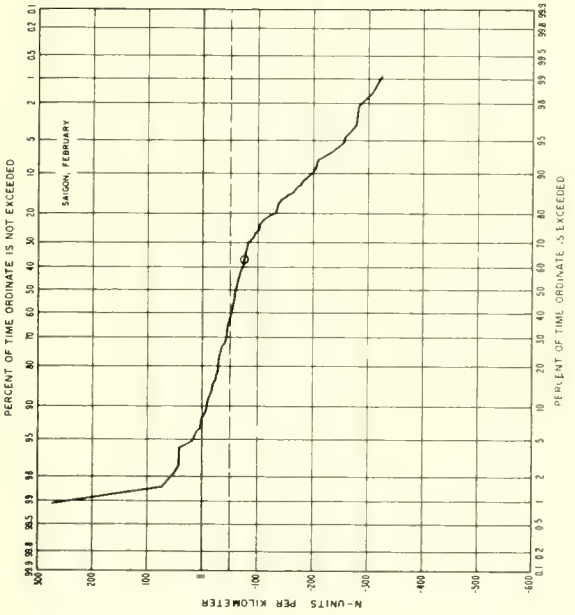

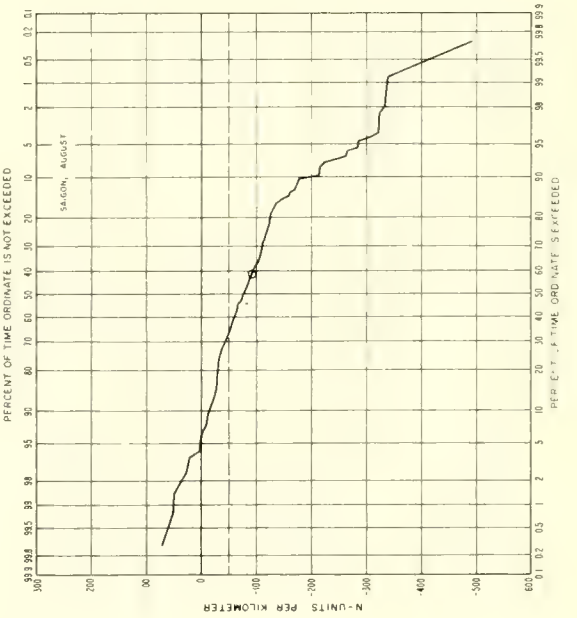

FIGURE C-74. *Cumulative probability distributions of* dN/dh *for ground-based 100-m layer: Saigon, Viet Nam.*

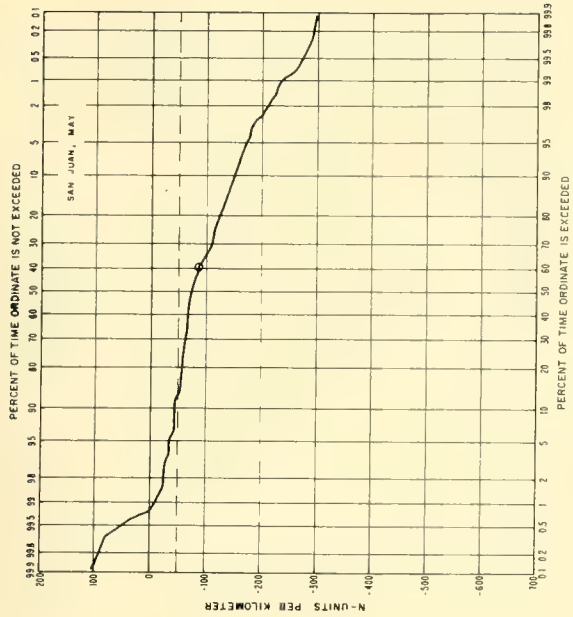

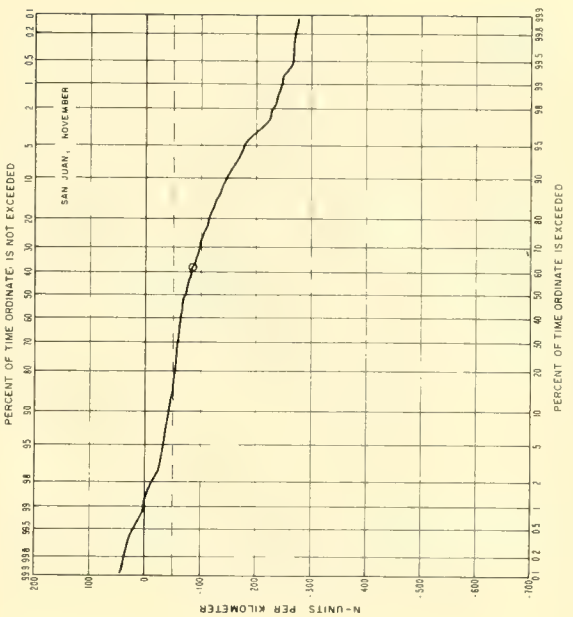

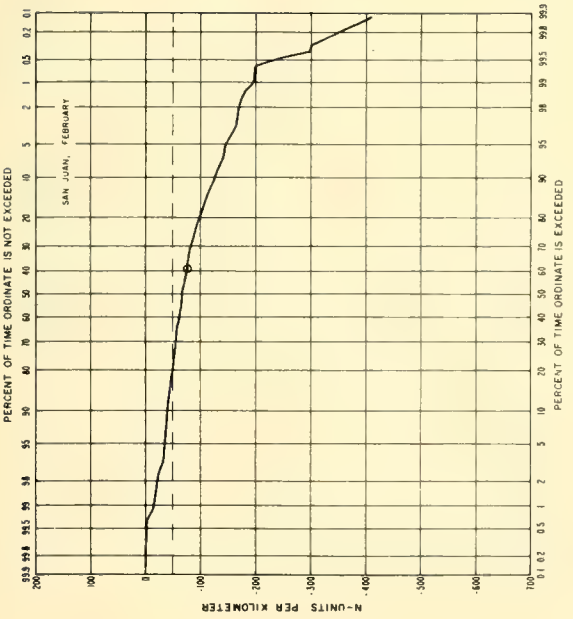

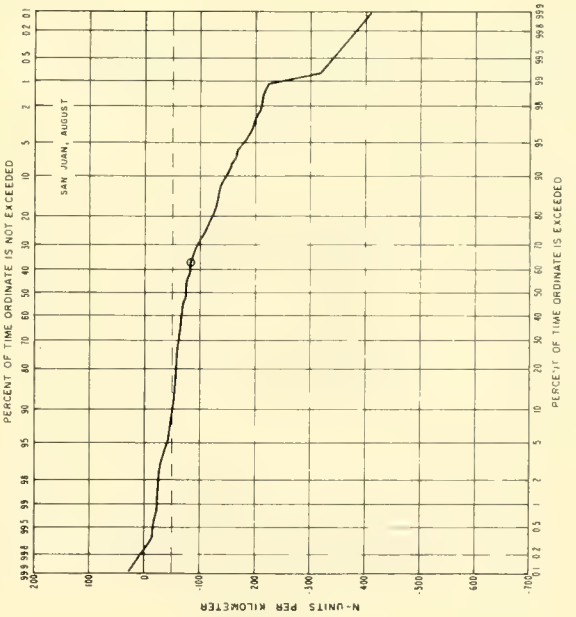

FIGURE C-75 *Cumulative probability distributions of* dN/dh *for ground-based 100-m layer: San Juan, P. R.*

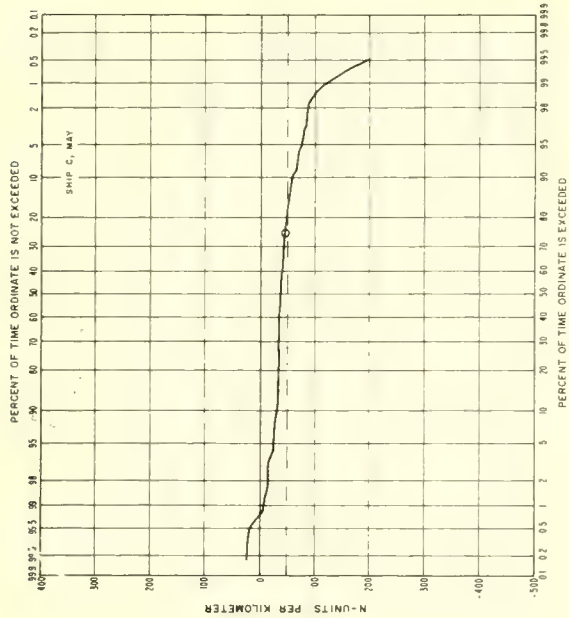

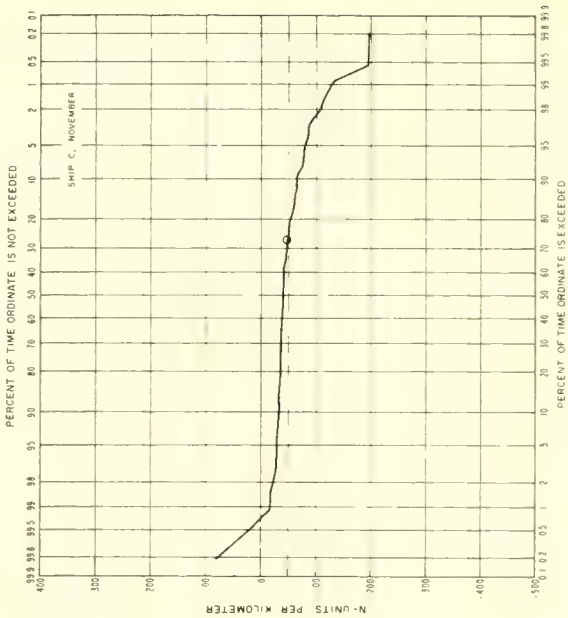

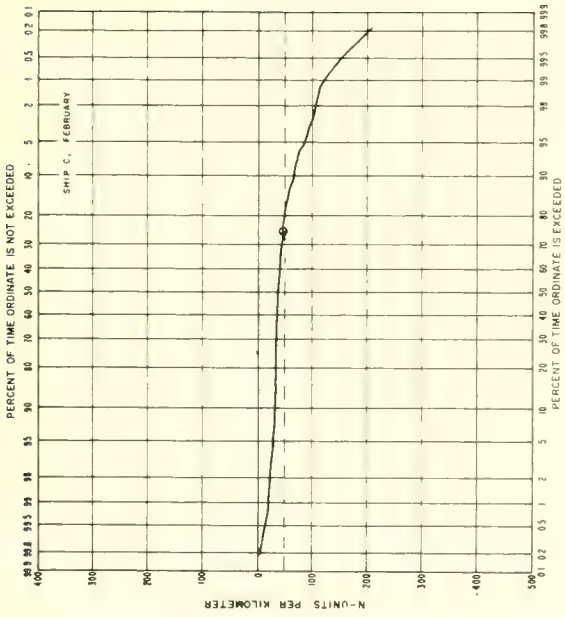

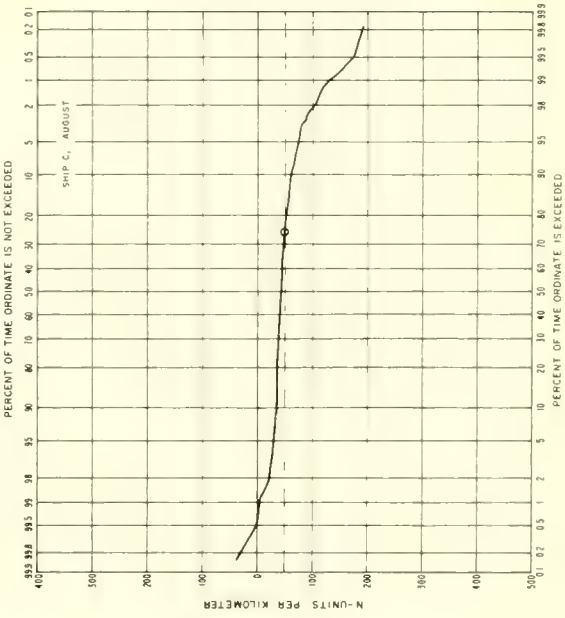

FIGURE C-76. *Cumulative probability distributions of* dN/dh *for ground-based 100-m layer: Ship Station "C."*

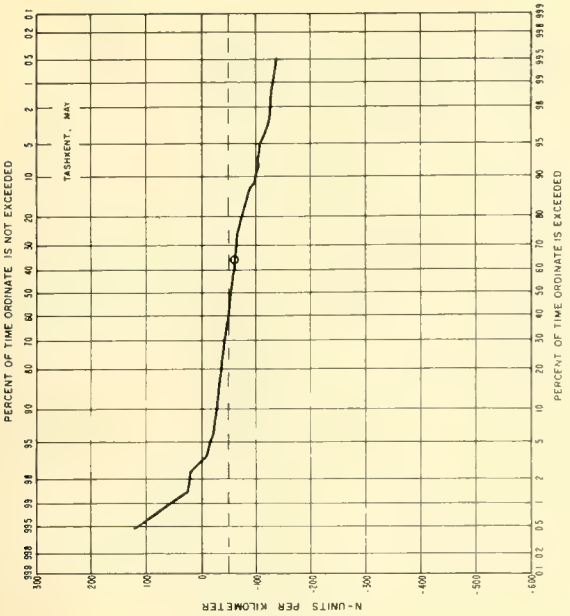

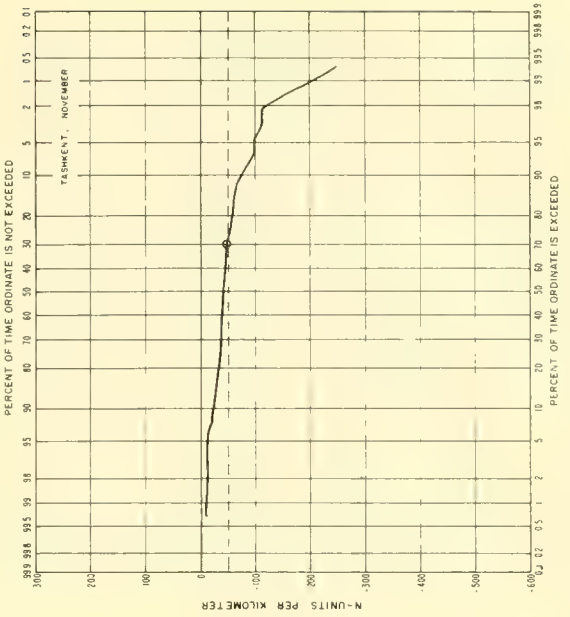

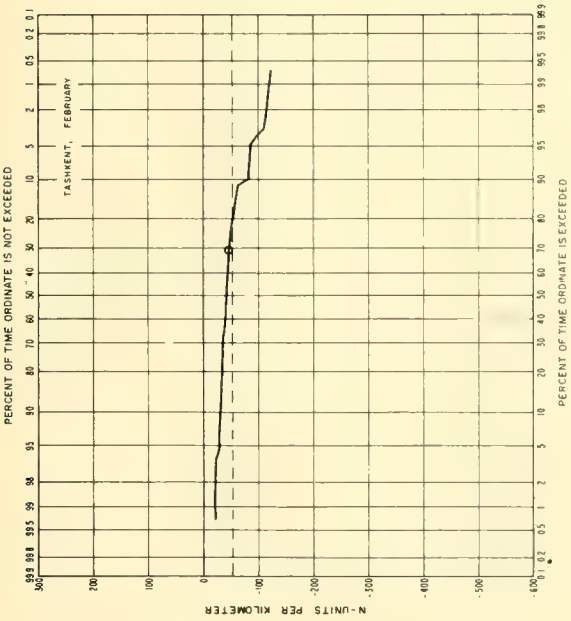

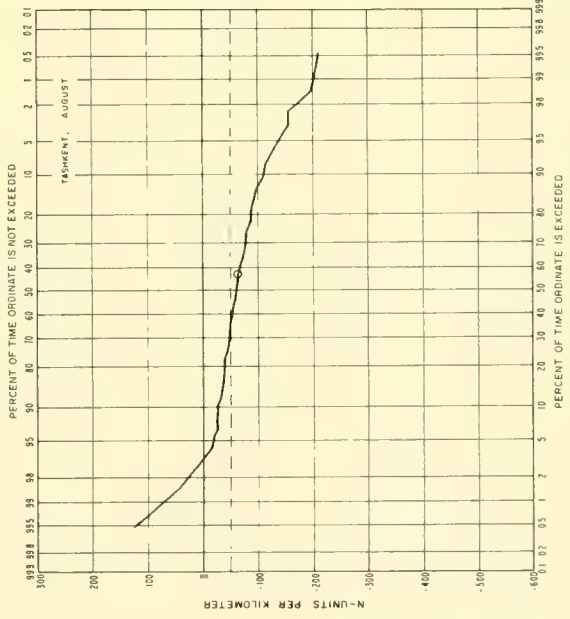

FIGURE C-77. *Cumulative probability distributions of* dN/dh *for ground-based 100-m layer: Tashkent, U.S.S.R.*

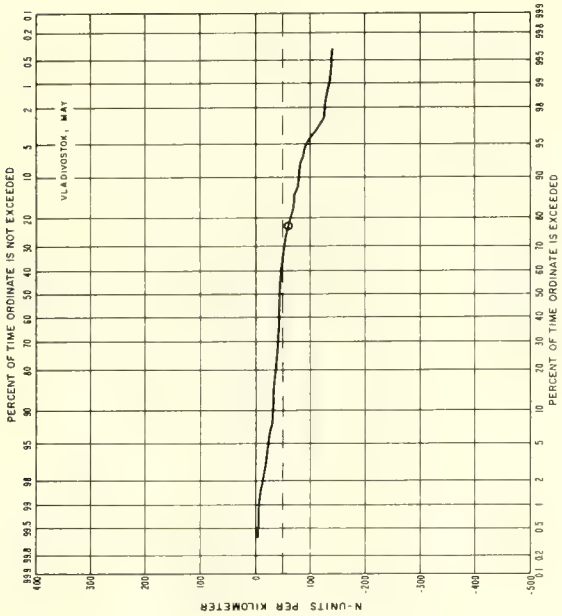

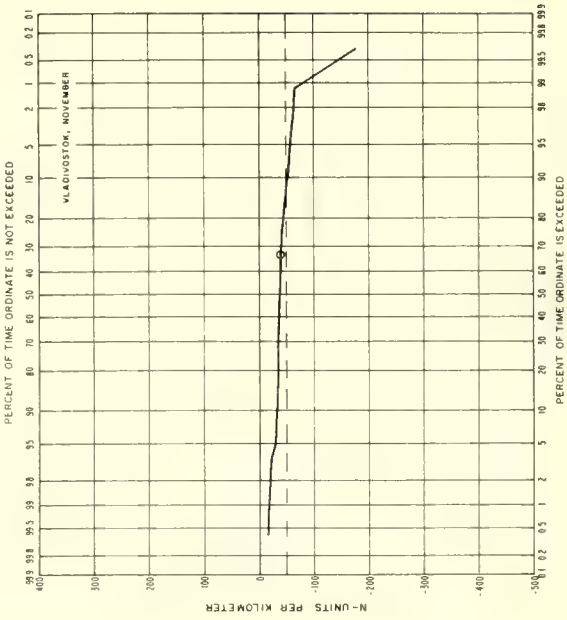

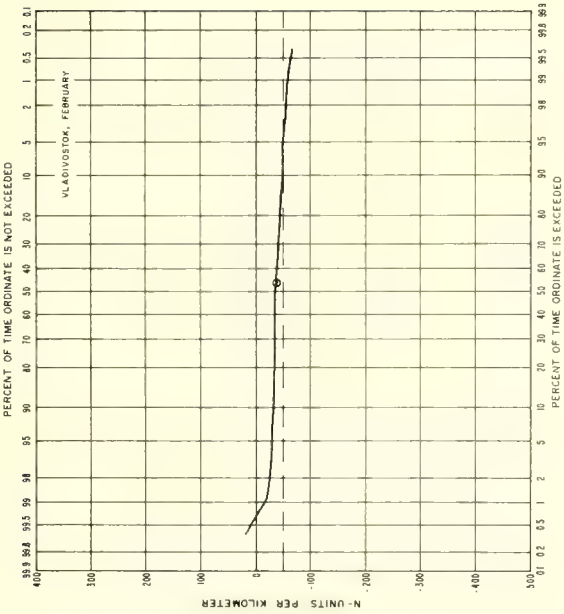

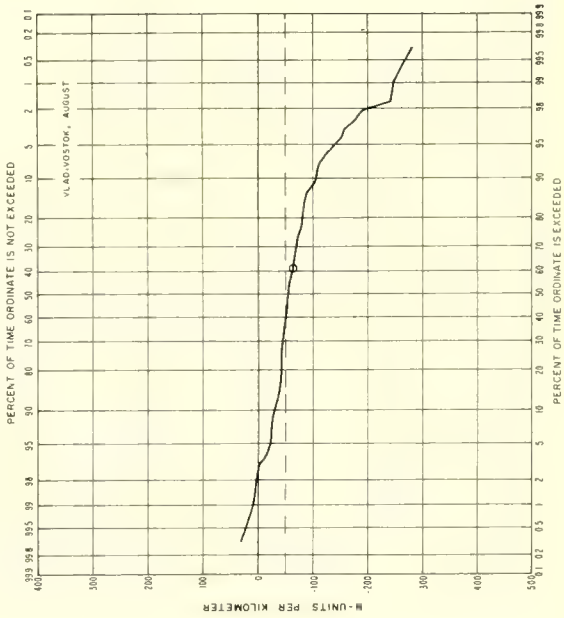

FIGURE C-78. *Cumulative probability distributions of* dN/dh *for ground-based 100-m layer: Vladivostok, U.S.S.R.*

13. Appendix D. World Charts of Tropopause Heights

Five-year mean tropopause heights obtained in the process of computing $N(z)$ parameters for February, May, August, and November at the 112 stations listed in table A-1 were plotted and contoured. Maps of these heights, given in figures D-1 through D-4, represent the average of all of the individual altitudes which marked the base of the first layer which had a thickness of at least 2 km and a temperature lapse rate of less than 2°C/km (see sec. 6).

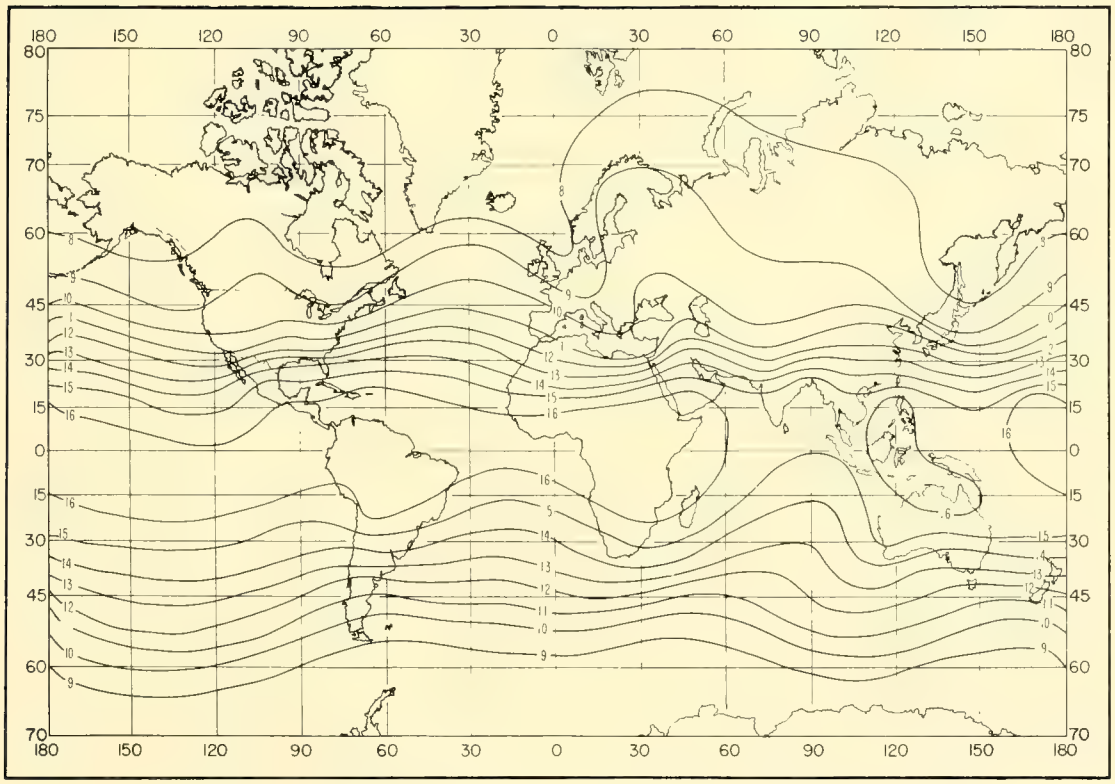

FIGURE D-1. *Tropopause heights (km), based on temperature lapse rate: February.*

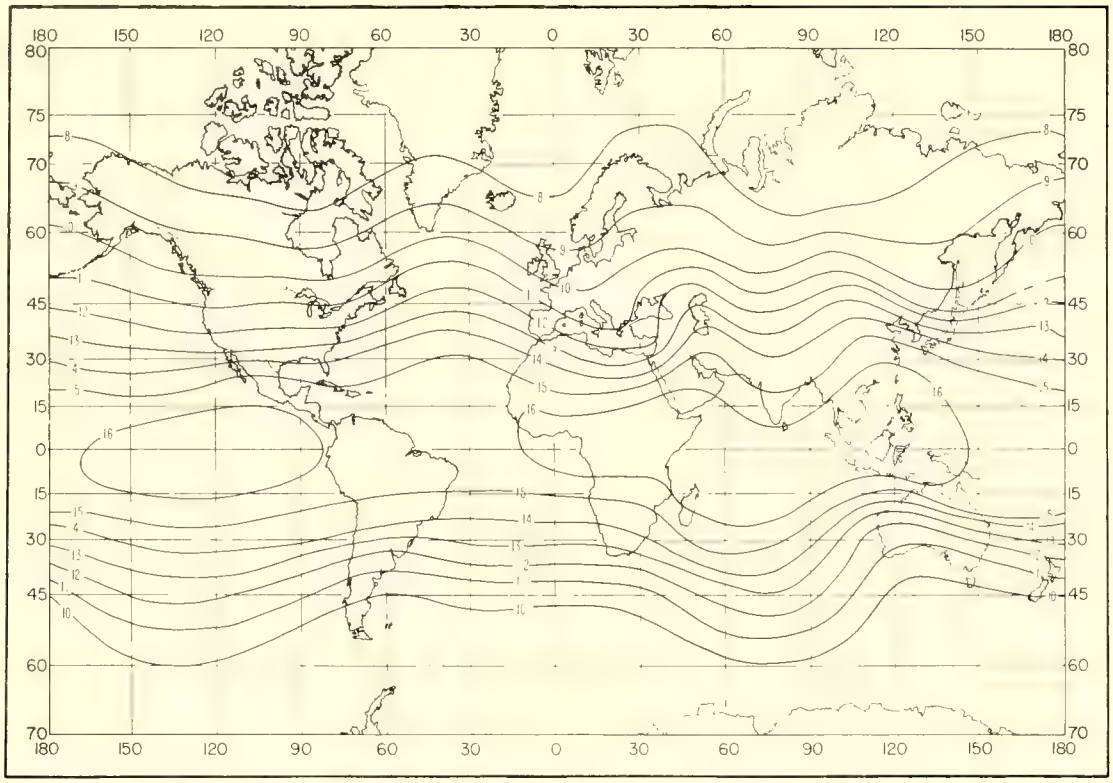

FIGURE D-2. *Tropopause heights (km), based on temperature lapse rate: May.*

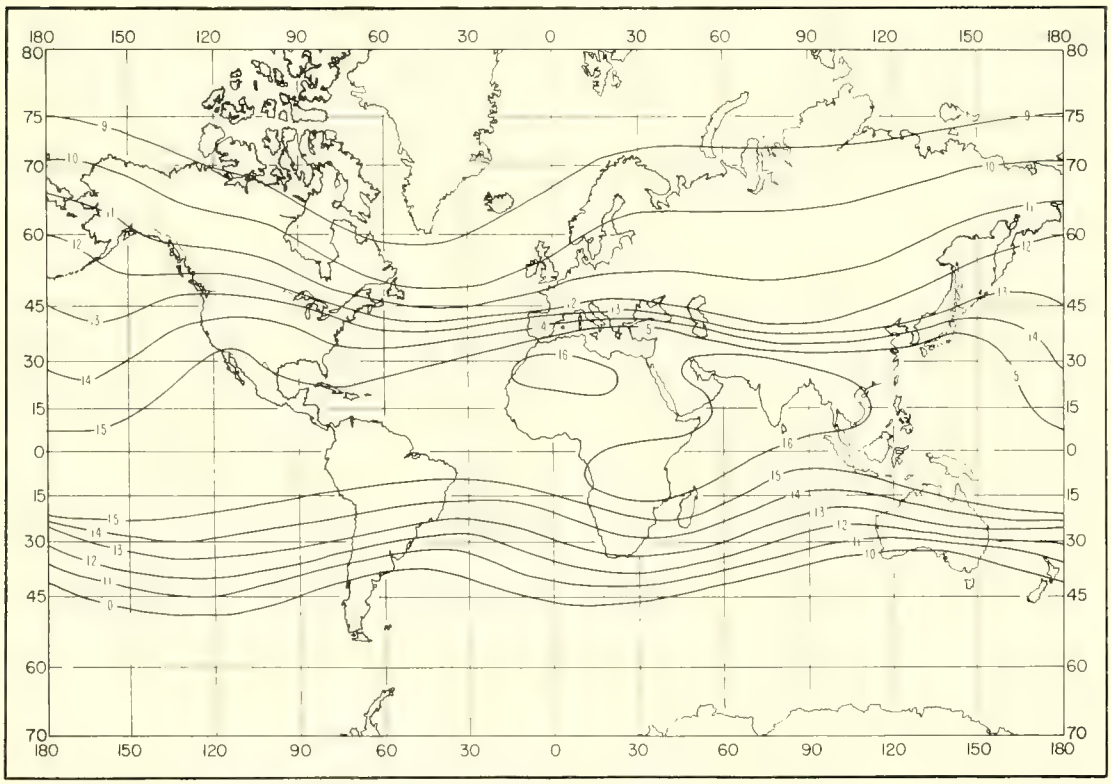

FIGURE D-3. *Tropopause heights (km), based on temperature lapse rate: August.*

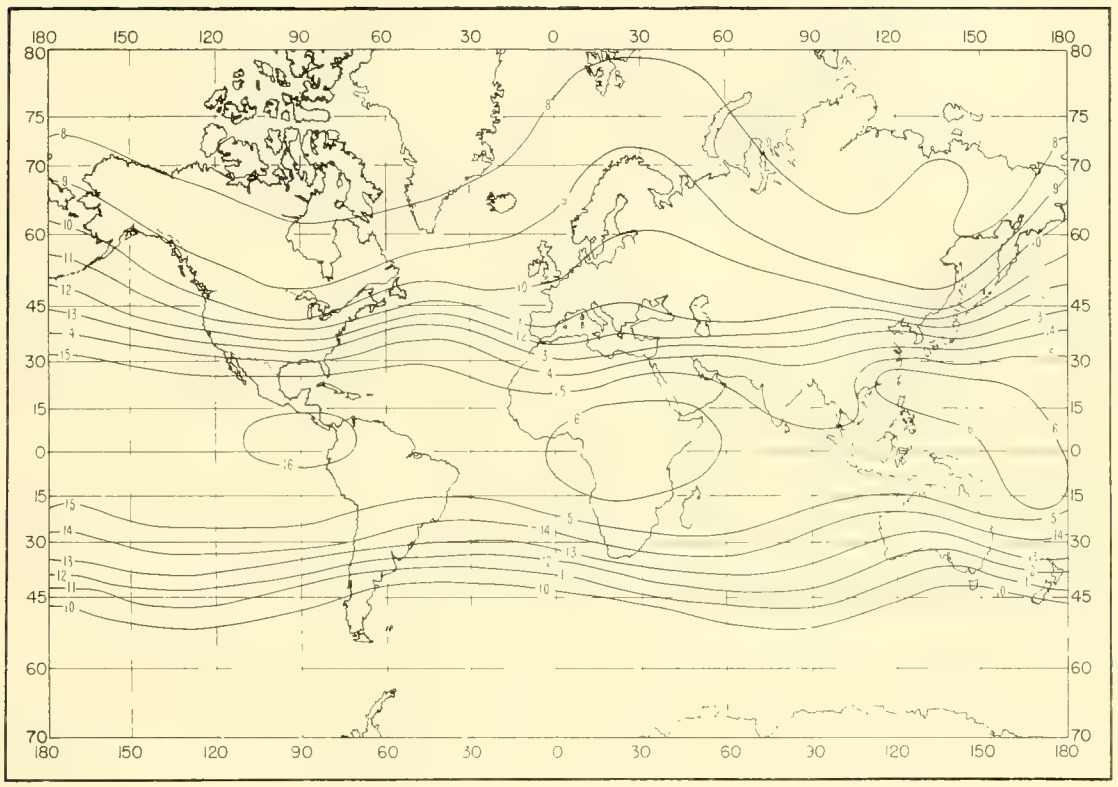

FIGURE D-4. *Tropopause heights (km), based on temperature lapse rate: November.*

14. Appendix E. Sample Listing of the Computer Output for San Juan, P.R., and Amundsen-Scott, Antarctica

A sample listing of the complete computer output of the mean N-profiles for February, May, August, and November at a subtropical and an arctic station is given in the first section of this appendix.

For instance, at station 11636 (San Juan, P. R.) in February (table E-1), the heading gives the number of pieces of data used to compute two types of tropopause height (based on two types of temperature criteria) :

(a) the mean heights where the extreme minimum temperature occurred in 320 individual profiles was 17.56 km ± a standard deviation of 0.65 km,

(b) the mean height of the bottom of the lowest atmospheric layer with a thickness $\geqq$ 2 km and a temperature gradient $\geqq$ —2°C/km in 307 temperature profiles was 16.44 km ± 0.96 km.

This February profile also gives refractivity information at 40 height levels ranging from 0 to 30 km. Following each height level is a listing of the values of total refractivity, gradient, dry and wet terms, and their respective standard deviations at that height above surface. For example, at 1 km, 383 radiosonde profiles were examined, and the refractivity was found to be 306.7 with a standard deviation of 8.22 N-units; the gradient at that level was —47.66 N/km with a standard deviation of 17.38 N/km; the dry term was 242.4 ± 1.19 N-units, and the wet term was 64.3 ± 8.52 N-units. The correlation coefficients for the data fit, within various height ranges, of the wet term (W) and the tropospheric (D_1) and stratospheric (D_2) dry terms to the line represented by a computed regression equation are found at the bottom of each month's listing. In this example, for the dry term equation (D_1), with a surface value of 271.9 and an exponential decay coefficient of —0.1088, the correlation coefficient is 0.999 and the standard deviation is 3.01 N-units. (These figures were based on 5 years of data from the surface to 15 km.)

At station 90001 (Amundsen-Scott, Antarctica) the wet-term value is so small at all heights during the months studied that the regression equation from 0 to 3 km becomes meaningless. Because the South Polar region is not shown on the ground-based gradient maps (figs. C-1 through C-56), a complete computer listing for Amundsen-Scott is included in this appendix. This also illustrates the form of the original station data which were used to plot the various values needed for the gradient maps. All gradients are in N-units/km and all frequencies are Mc/s. The "profiles skipped" represents the number of profiles which had gradients $>$ —100 N/km.

TABLE E-1. *Mean N-profiles: San Juan, P. R.*

Mean N–Profile, Station 11636, Month 2 — Number of Profiles Used in Calculating Tropopause 320. 307. Tropopause Height Min. Temp. 17.56 ±0.65, Lapse 16.44 ±0.96.

Height (KM)	Number	N	SDN	dN/dh	SDG	DRY	SDD	WET	SDW
0.	383	357.8	11.39	−75.67	42.11	265.3	1.66	92.5	11.22
0.050	383	354.0	11.04	−74.67	40.92	264.1	1.41	89.9	10.95
0.100	383	350.3	10.97	−72.30	38.26	262.9	1.24	87.5	10.98
0.250	383	341.6	12.05	−49.31	21.64	259.4	1.13	82.2	12.21
0.500	383	329.8	10.78	−46.09	10.62	253.7	1.18	76.1	11.09
0.750	383	318.3	9.77	−46.36	12.77	248.1	1.18	70.2	10.10
1.000	383	306.7	8.22	−47.66	17.38	242.4	1.19	64.3	8.52
1.500	383	282.9	10.09	−49.18	30.22	231.1	1.29	51.8	10.09
2.000	383	254.9	15.92	−59.71	74.26	219.2	1.64	35.6	15.13
2.500	383	230.1	15.52	−39.77	37.13	207.3	1.59	22.8	14.57
3.000	383	211.7	11.95	−30.40	22.38	196.5	1.44	15.2	11.04
3.500	380	197.7	8.93	−26.77	17.84	186.4	1.35	11.3	8.09
4.000	380	185.4	6.69	−22.94	11.16	176.9	1.25	8.4	5.94
4.500	379	174.6	5.04	−20.84	6.85	168.0	1.13	6.6	4.41
5.000	377	164.8	4.00	−18.44	5.13	159.6	1.08	5.2	3.45
5.500	376	155.8	3.36	−17.74	3.79	151.6	1.04	4.2	2.89
6.000	376	147.2	2.52	−16.71	3.23	143.9	0.94	3.3	2.21
6.500	375	139.2	1.85	−15.54	2.07	136.6	0.88	2.6	1.57
7.000	374	131.7	1.45	−14.48	1.39	129.7	0.84	2.0	1.16
7.500	374	124.7	1.18	−13.75	1.17	123.1	0.81	1.5	0.86
8.000	372	117.8	1.07	−13.25	1.17	116.7	0.75	1.1	0.74
8.500	372	111.3	0.91	−12.64	1.24	110.5	0.73	0.8	0.56
9.000	372	105.1	0.82	−12.04	1.17	104.6	0.72	0.5	0.43
9.500	372	99.2	0.76	−11.38	0.74	98.9	0.72	0.3	0.33
10.000	371	93.6	0.68	−11.01	0.85	93.5	0.69	0.1	0.22
11.000	371	83.2	0.69	−9.99	0.77	83.2	0.69	0.0	0.01
12.000	369	73.8	0.67	−9.09	0.67	73.8	0.67	0.	−0.
13.000	369	65.0	0.65	−8.46	0.76	65.0	0.65	0.	−0.
14.000	366	56.9	0.61	−7.79	0.64	56.9	0.61	0.	−0.
15.000	359	49.5	0.56	−7.00	0.53	49.5	0.56	0.	−0.
16.000	345	42.7	0.54	−6.48	0.55	42.7	0.54	0.	−0.
17.000	330	36.5	0.51	−5.98	0.60	36.5	0.51	0.	−0.
18.000	311	30.7	0.51	−5.68	0.67	30.7	0.51	0.	−0.
19.000	296	25.3	0.46	−5.02	0.53	25.3	0.46	0.	−0.
20.000	272	20.8	0.39	−4.00	0.39	20.8	0.39	0.	−0.
22.000	227	14.5	0.21	−2.52	0.20	14.5	0.21	0.	−0.
24.000	162	10.3	0.15	−1.73	0.12	10.3	0.15	0.	−0.
26.000	72	7.4	0.11	−1.23	0.06	7.4	0.11	0.	−0.
28.000	19	5.4	0.09	−0.87	0.04	5.4	0.09	0.	−0.
30.000	3	3.9	0.06	−0.61	0.02	3.9	0.06	0.	−0.

Exponential Profile Correlation	Equation	Range (KM)
0.982852	W = 99.92 Exp(−0.568658H) ±6.054419	0 = H = 3
0.998953	D_1 = 271.91 Exp(−0.108778H) ±3.011370	0 = H = 15
0.999385	D_2 = 662.57 Exp(−0.172110H) ±0.535157	17 = H = 30

Mean N–Profile, Station 11636, Month 5 — Number of Profiles Used in Calculating Tropopause 327. 313. Tropopause Height Min. Temp. 16.40 ±0.74, Lapse 15.17 ±0.83.

Height (KM)	Number	N	SDN	dN/dh	SDG	DRY	SDD	WET	SDW
0.	433	372.3	11.24	−88.57	47.92	262.8	1.92	109.5	11.19
0.050	433	367.8	10.88	−87.23	46.66	261.7	1.66	106.1	10.81
0.100	433	363.5	10.93	−84.31	44.29	260.7	1.47	102.9	10.92
0.250	433	354.5	10.33	−52.47	20.37	257.2	1.27	97.2	10.40
0.500	433	341.8	8.98	−48.10	12.27	251.4	1.16	90.3	9.08
0.750	433	329.2	8.46	−50.66	16.67	245.7	1.11	83.5	8.60
1.000	433	316.2	8.91	−51.94	20.71	240.0	1.06	76.2	9.08
1.500	433	291.1	10.60	−48.07	22.57	228.7	1.10	62.4	10.56
2.000	433	266.9	12.41	−45.77	27.31	217.6	1.14	49.3	12.14
2.500	433	244.2	12.54	−43.47	27.96	206.8	1.05	37.4	12.28
3.000	433	224.5	11.94	−34.29	25.71	196.4	0.96	28.1	11.59
3.500	433	208.6	9.99	−29.81	17.78	186.7	0.92	21.9	9.61
4.000	432	194.5	8.28	−26.27	20.12	177.4	0.85	17.1	7.94
4.500	431	181.9	7.14	−23.41	11.58	168.4	0.79	13.5	6.82
5.000	429	170.2	6.03	−22.74	10.60	159.8	0.76	10.4	5.76
5.500	429	159.9	4.99	−19.46	6.53	151.6	0.72	8.3	4.76
6.000	428	150.3	3.88	−18.68	5.39	143.8	0.69	6.5	3.71
6.500	428	141.3	2.95	−16.97	4.02	136.4	0.66	4.9	2.84
7.000	424	133.1	2.29	−15.77	2.48	129.4	0.63	3.7	2.22
7.500	422	125.5	1.81	−14.96	2.29	122.7	0.61	2.8	1.75
8.000	421	118.3	1.40	−13.66	1.74	116.3	0.55	2.0	1.33
8.500	419	111.7	1.09	−12.84	1.00	110.2	0.52	1.5	1.00
9.000	419	105.4	0.87	−12.14	0.77	104.4	0.49	1.0	0.74
9.500	417	99.5	0.72	−11.43	0.59	98.9	0.47	0.6	0.54
10.000	416	93.9	0.59	−10.85	0.51	93.6	0.45	0.3	0.38
11.000	413	83.6	0.46	−9.82	0.34	83.6	0.46	0.	−0.
12.000	412	74.3	0.49	−8.92	0.34	74.3	0.49	0.	−0.
13.000	411	65.8	0.53	−8.25	0.47	65.8	0.53	0.	−0.
14.000	407	57.8	0.59	−7.79	0.65	57.8	0.59	0.	−0.
15.000	384	50.2	0.66	−7.51	0.85	50.2	0.66	0.	−0.
16.000	348	42.9	0.66	−7.17	0.85	42.9	0.66	0.	−0.
17.000	311	36.1	0.61	−6.45	0.62	36.1	0.61	0.	−0.
18.000	287	30.0	0.54	−5.67	0.53	30.0	0.54	0.	−0.
19.000	269	24.8	0.44	−4.70	0.50	24.8	0.44	0.	−0.
20.000	251	20.6	0.32	−3.75	0.35	20.6	0.32	0.	−0.
22.000	212	14.5	0.19	−2.50	0.17	14.5	0.19	0.	−0.
24.000	134	10.4	0.12	−1.73	0.10	10.4	0.12	0.	−0.
26.000	55	7.5	0.11	−1.21	0.07	7.5	0.11	0.	−0.
28.000	6	5.5	0.14	−0.84	0.07	5.5	0.14	0.	−0.

Exponential Profile Correlation	Equation	Range (KM)
0.994961	W = 111.65 Exp(−0.433356H) ±3.006154	0 = H = 3
0.999393	D_1 = 268.22 Exp(−0.106109H) ±2.400332	0 = H = 14
0.999570	D_2 = 667.88 Exp(−0.172794H) ±0.457672	16 = H = 28

TABLE E-1. *(Continued)*

Mean N-Profile, Station 11636, Month 8 — Number of Profiles Used in Calculating Tropopause 376. 358. Tropopause Height Min. Temp. 16.32 ±0.69, Lapse 15.21 ±0.83.

Height (KM)	Number	N	SDN	dN/dh	SDG	DRY	SDD	WET	SDW
0.	434	378.6	7.30	−85.44	46.18	262.0	3.54	116.6	8.60
0.050	434	374.2	7.59	−84.22	44.59	260.8	2.41	113.3	8.33
0.100	434	369.9	8.05	−80.72	41.44	259.7	1.55	110.3	8.25
0.250	434	360.8	7.31	−54.12	12.16	256.1	1.16	104.7	7.37
0.500	434	347.4	6.37	−51.89	10.98	250.4	1.04	97.0	6.45
0.750	434	334.0	7.37	−52.22	11.84	244.7	1.01	89.2	7.49
1.000	434	320.5	7.69	−53.91	18.41	239.1	0.96	81.4	7.82
1.500	434	293.8	10.28	−52.05	23.00	227.9	0.95	65.9	10.23
2.000	434	266.2	13.77	−49.17	30.78	216.7	1.02	49.5	13.45
2.500	434	243.1	12.36	−41.81	26.83	206.1	0.92	37.1	12.11
3.000	434	224.4	10.76	−32.01	20.75	196.0	0.85	28.4	10.60
3.500	433	208.8	8.82	−29.30	17.99	186.4	0.86	22.4	8.77
4.000	433	195.2	7.94	−27.63	21.18	177.2	0.91	18.0	7.81
4.500	433	182.1	6.96	−25.23	14.04	168.2	0.90	13.9	6.75
5.000	431	170.1	5.74	−22.94	9.32	159.6	0.85	10.4	5.48
5.500	430	159.3	4.64	−20.16	6.19	151.4	0.72	7.9	4.39
6.000	430	149.6	3.60	−18.73	5.47	143.6	0.69	6.0	3.41
6.500	428	140.8	2.73	−16.85	3.92	136.2	0.61	4.6	2.62
7.000	428	132.7	2.03	−15.57	2.48	129.3	0.58	3.4	1.99
7.500	428	125.2	1.55	−14.67	2.12	122.7	0.60	2.6	1.54
8.000	426	118.0	1.35	−13.38	1.30	116.3	0.61	1.7	1.32
8.500	426	111.5	1.08	−12.71	0.88	110.2	0.56	1.2	1.00
9.000	426	105.3	0.86	−11.96	0.68	104.5	0.55	0.8	0.74
9.500	426	99.5	0.72	−11.31	0.52	99.0	0.53	0.5	0.53
10.000	425	94.0	0.60	−10.74	0.38	93.7	0.51	0.3	0.39
11.000	425	83.8	0.42	−9.76	0.30	83.8	0.42	0.0	0.03
12.000	422	74.6	0.40	−8.88	0.35	74.6	0.40	0.	−0
13.000	420	66.0	0.43	−8.39	0.58	66.0	0.43	0.	−0.
14.000	417	57.8	0.57	−8.01	0.79	57.8	0.57	0.	−0.
15.000	408	50.1	0.65	−7.53	0.75	50.1	0.65	0.	−0.
16.000	392	42.8	0.54	−7.02	0.68	42.8	0.54	0.	−0.
17.000	365	36.0	0.50	−6.48	0.65	36.0	0.50	0.	−0.
18.000	346	30.0	0.44	−5.52	0.45	30.0	0.44	0.	−0.
19.000	333	25.0	0.35	−4.52	0.32	25.0	0.35	0.	−0.
20.000	323	20.9	0.27	−3.66	0.26	20.9	0.27	0.	−0.
22.000	290	14.8	0.18	−2.49	0.18	14.8	0.18	0.	−0.
24.000	195	10.6	0.13	−1.75	0.11	10.6	0.13	0.	−0.
26.000	86	7.7	0.09	−1.24	0.08	7.7	0.09	0.	−0.
28.000	40	5.6	0.08	−0.89	0.05	5.6	0.08	0.	−0.
30.000	23	4.1	0.04	−0.63	0.04	4.1	0.04	0.	−0.

Exponential Profile Correlation	Equation	Range (KM)
0.994632	W = 120.48 Exp(−0.459425H) ±3.819615	0 = H = 3
0.999368	D_1 = 267.17 Exp(−0.105611H) ±2.388775	0 = H = 14
0.999661	D_2 = 614.01 Exp(−0.168039H) ±0.497345	16 = H = 30

Mean N Profile, Station 11636, Month 11 — Number of Profiles Used in Calculating Tropopause 369. 347. Tropopause Height Min. Temp. 16.95 ±0.70, Lapse 15.79 ±0.92.

Height (KM)	Number	N	SDN	dN/dh	SDG	DRY	SDD	WET	SDW
0.	420	371.1	12.75	−86.27	55.94	262.7	1.90	108.3	12.72
0.050	420	366.8	12.34	−85.01	54.69	261.5	1.64	105.3	12.36
0.100	420	362.7	12.29	−79.92	51.16	260.3	1.46	102.5	12.39
0.250	420	353.7	12.49	−51.29	14.93	256.7	1.29	97.0	12.68
0.500	420	341.0	11.34	−48.99	12.37	251.0	1.20	90.0	11.59
0.750	420	328.5	11.02	−49.36	23.88	245.3	1.18	83.1	11.31
1.000	420	315.7	10.44	−52.68	32.29	239.7	1.15	75.9	10.75
1.500	420	290.7	10.17	−49.13	19.09	228.6	1.12	62.1	10.42
2.000	420	266.7	11.54	−49.47	31.80	217.5	1.12	49.3	11.64
2.500	420	241.4	13.85	−47.58	37.82	206.4	1.02	35.1	13.67
3.000	420	220.5	12.35	−38.61	28.96	195.9	1.03	24.6	11.99
3.500	420	203.8	10.39	−29.54	18.67	186.0	0.98	17.8	9.93
4.000	420	190.2	8.41	−26.01	18.13	176.7	0.93	13.6	7.99
4.500	419	178.1	6.89	−23.39	10.29	167.7	0.86	10.4	6.54
5.000	419	166.9	5.33	−20.33	7.54	159.1	0.81	7.7	5.05
5.500	419	157.0	4.13	−19.23	6.04	151.0	0.78	6.0	3.91
6.000	419	147.9	3.12	−17.50	4.17	143.3	0.73	4.6	2.99
6.500	418	139.4	2.39	−16.13	2.96	136.0	0.68	3.5	2.30
7.000	418	131.7	1.74	−15.01	2.64	129.1	0.66	2.6	1.68
7.500	418	124.5	1.32	−14.19	2.27	122.5	0.70	2.0	1.27
8.000	418	117.4	1.17	−13.27	1.15	116.1	0.66	1.3	1.05
8.500	416	110.9	0.97	−12.58	0.95	110.0	0.60	0.9	0.79
9.000	416	104.8	0.81	−11.87	0.81	104.2	0.58	0.6	0.57
9.500	416	99.0	0.70	−11.19	0.45	98.7	0.56	0.4	0.41
10.000	416	93.6	0.59	−10.71	0.43	93.4	0.52	0.2	0.29
11.000	416	83.4	0.50	−9.78	0.38	83.4	0.50	0.	−0.
12.000	416	74.2	0.50	−8.89	0.47	74.2	0.50	0.	−0.
13.000	416	65.7	0.52	−8.25	0.39	65.7	0.52	0.	−0.
14.000	413	57.7	0.59	−7.68	0.55	57.7	0.59	0.	−0.
15.000	406	50.1	0.65	−7.35	0.60	50.1	0.65	0.	−0.
16.000	390	43.0	0.58	−6.86	0.68	43.0	0.58	0.	−0.
17.000	365	36.5	0.49	−6.32	0.66	36.5	0.49	0.	−0.
18.000	347	30.4	0.52	−5.84	0.65	30.4	0.52	0.	−0.
19.000	335	25.0	0.44	−4.86	0.54	25.0	0.44	0.	−0.
20.000	321	20.6	0.31	−3.82	0.36	20.6	0.31	0.	−0.
22.000	290	14.5	0.16	−2.47	0.18	14.5	0.16	0.	−0.
24.000	212	10.3	0.12	−1.71	0.10	10.3	0.12	0.	−0.
26.000	123	7.4	0.11	−1.20	0.07	7.4	0.11	0.	−0.
28.000	54	5.4	0.07	−0.86	0.06	5.4	0.07	0.	−0.
30.000	28	3.9	0.05	−0.60	0.04	3.9	0.05	0.	−0.
32.000	10	2.9	0.06	−0.45	0.03	2.9	0.06	0.	−0.
34.000	3	2.1	0.08	−0.34	0.01	2.1	0.08	0.	−0.

Exponential Profile Correlation	Equation	Range (KM)
0.989375	W = 112.72 Exp(−0.462755H) ±4.308167	0 = H = 3
0.999426	D_1 = 267.69 Exp(−0.106144H) ±2.280762	0 = H = 14
0.999400	D_2 = 594.38 Exp(−0.167133H) ±0.704327	17 = H = 34

TABLE E-2. *Mean N-profiles: Amundsen-Scott, Antarctica.*

Mean N–Profile, Station 90001, Month 2 — Number of Profiles Used in Calculating Tropopause 90. 90. Tropopause Height Min. Temp. 5.28 ±0.87, Lapse 4.93 ±0.51.

Height (KM)	Number	N	SDN	dN/dh	SDG	DRY	SDD	WET	SDW
0.	99	225.8	5.38	−66.37	32.89	225.8	5.42	0.0	0.15
0.050	99	222.2	4.26	−65.11	31.75	222.2	4.30	0.1	0.19
0.100	99	218.7	3.53	−62.54	30.30	218.6	3.57	0.1	0.26
0.250	99	212.3	2.70	−33.81	9.52	211.4	3.02	0.8	0.87
0.500	99	205.0	2.08	−28.06	7.42	203.4	2.52	1.5	1.09
0.750	99	198.5	1.75	−25.24	2.84	196.7	2.27	1.8	1.31
1.000	99	192.2	1.65	−24.07	2.02	190.5	2.06	1.7	1.29
1.500	98	180.5	1.60	−22.66	1.94	179.0	1.85	1.4	1.01
2.000	98	169.5	1.50	−20.95	1.02	168.5	1.65	1.1	0.86
2.500	98	159.2	1.28	−19.91	1.03	158.6	1.43	0.6	0.73
3.000	98	149.5	1.35	−18.85	0.81	149.2	1.34	0.3	0.56
3.500	98	140.4	1.27	−17.83	0.87	140.3	1.23	0.1	0.37
4.000	98	131.8	1.28	−16.88	0.97	131.7	1.21	0.0	0.21
4.500	98	123.5	1.29	−16.40	1.62	123.5	1.29	0.	−0.
5.000	97	115.2	1.75	−16.93	2.45	115.2	1.75	0.	−0.
5.500	96	106.5	2.41	−17.58	2.65	106.5	2.41	0.	−0.
6.000	95	97.8	2.73	−17.00	2.10	97.8	2.73	0.	−0.
6.500	94	89.8	2.53	−15.19	1.85	89.8	2.53	0.	−0.
7.000	94	82.6	2.07	−13.32	1.33	82.6	2.07	0.	−0.
7.500	94	76.3	1.72	−11.97	0.78	76.3	1.72	0.	−0.
8.000	93	70.7	1.53	−10.78	0.78	70.7	1.53	0.	−0.
8.500	91	65.4	1.27	−9.87	0.64	65.4	1.27	0.	−0.
9.000	91	60.7	1.19	−9.02	0.44	60.7	1.19	0.	−0.
9.500	91	56.4	1.13	−8.31	0.34	56.4	1.13	0.	−0.
10.000	91	52.4	1.05	−7.82	0.52	52.4	1.05	0.	−0.
11.000	91	45.1	0.84	−6.73	0.33	45.1	0.84	0.	−0.
12.000	90	38.9	0.69	−5.75	0.19	38.9	0.69	0.	−0.
13.000	90	33.5	0.58	−5.02	0.19	33.5	0.58	0.	−0.
14.000	89	28.9	0.46	−4.28	0.14	28.9	0.46	0.	−0.
15.000	88	24.9	0.36	−3.66	0.11	24.9	0.36	0.	−0.
16.000	85	21.5	0.28	−3.15	0.10	21.5	0.28	0.	−0.
17.000	80	18.6	0.21	−2.71	0.08	18.6	0.21	0.	−0.
18.000	79	16.0	0.17	−2.34	0.06	16.0	0.17	0.	−0.
19.000	77	13.8	0.14	−2.02	0.05	13.8	0.14	0.	−0.
20.000	70	11.9	0.10	−1.74	0.04	11.9	0.10	0.	−0.
22.000	51	8.9	0.09	−1.31	0.04	8.9	0.09	0.	−0.
24.000	42	6.6	0.07	−0.98	0.03	6.6	0.07	0.	−0.
26.000	35	4.9	0.06	−0.73	0.02	4.9	0.06	0.	−0.
28.000	19	3.7	0.05	−0.55	0.02	3.7	0.05	0.	−0.
30.000	5	2.7	0.02	−0.40	0.02	2.7	0.02	0.	−0.
32.000	2	2.0	0.03	−0.30	0.01	2.0	0.03	0.	−0.

Exponential Profile Correlation	Equation	Range (KM)
0.366453	W = 0.28 Exp(0.496583H) ±0.837504	0 = H = 3
0.997635	D_1 = 220.00 Exp(−0.130340H) ±2.578227	0 = H = 4
0.999997	D_2 = 229.11 Exp(−0.147761H) ±0.038209	10 = H = 32

Mean N Profile, Station 90001, Month 5 — Number of Profiles Used in Calculating Tropopause 38. 122. Tropopause Height Min. Temp. 15.66 ±5.00, Lapse 5.35 ±0.76.

Height (KM)	Number	N	SDN	dN/dh	SDG	DRY	SDD	WET	SDW
0.	164	244.6	6.97	−164.97	96.79	244.6	6.97	0.0	−0.
0.050	164	236.5	5.80	−147.27	69.41	236.5	5.81	0.0	0.02
0.100	164	229.4	5.13	−125.32	56.27	229.4	5.16	0.0	0.10
0.250	164	217.4	3.23	−50.18	21.57	217.3	3.35	0.2	0.28
0.500	164	208.0	2.67	−31.24	4.87	207.6	2.87	0.3	0.47
0.750	164	200.7	2.53	−27.06	2.66	200.3	2.73	0.4	0.54
1.000	164	194.2	2.47	−25.36	2.06	193.8	2.63	0.4	0.53
1.500	164	182.1	2.44	−23.00	1.26	181.7	2.55	0.3	0.48
2.000	164	170.9	2.37	−21.54	1.41	170.7	2.44	0.2	0.38
2.500	162	160.5	2.32	−20.01	0.94	160.4	2.36	0.1	0.24
3.000	162	150.8	2.23	−18.75	0.92	150.8	2.24	0.0	0.12
3.500	161	141.8	2.15	−17.76	1.03	141.8	2.15	0.	−0.
4.000	161	133.0	2.11	−17.02	1.04	133.0	2.11	0.	−0.
4.500	161	124.7	2.10	−16.29	1.24	124.7	2.10	0.	−0.
5.000	161	116.7	2.27	−16.00	1.75	116.7	2.27	0.	−0.
5.500	161	108.8	2.62	−15.68	1.67	108.8	2.62	0.	−0.
6.000	161	101.0	2.98	−15.59	1.99	101.0	2.98	0.	−0.
6.500	160	93.3	3.20	−14.93	1.56	93.3	3.20	0.	−0.
7.000	160	86.1	3.21	−14.09	1.51	86.1	3.21	0.	−0.
7.500	159	79.1	2.83	−13.31	1.62	79.1	2.83	0.	−0.
8.000	155	72.7	2.37	−12.08	1.31	72.7	2.37	0.	−0.
8.500	153	67.0	2.01	−10.85	1.02	67.0	2.01	0.	−0.
9.000	149	61.8	1.68	−9.81	0.80	61.8	1.68	0.	−0.
9.500	146	57.1	1.46	−9.01	0.67	57.1	1.46	0.	−0.
10.000	141	52.8	1.27	−8.29	0.51	52.8	1.27	0.	−0.
11.000	132	45.1	1.02	−7.06	0.31	45.1	1.02	0.	−0.
12.000	122	38.6	0.83	−6.05	0.29	38.6	0.83	0.	−0.
13.000	112	33.0	0.69	−5.25	0.20	33.0	0.69	0.	−0.
14.000	102	28.1	0.59	−4.50	0.15	28.1	0.59	0.	−0.
15.000	91	23.9	0.53	−3.88	0.14	23.9	0.53	0.	−0.
16.000	76	20.3	0.47	−3.34	0.13	20.3	0.47	0.	−0.
17.000	61	17.2	0.40	−2.87	0.13	17.2	0.40	0.	−0.
18.000	52	14.5	0.36	−2.45	0.10	14.5	0.36	0.	−0.
19.000	40	12.3	0.31	−2.08	0.09	12.3	0.31	0.	−0.
20.000	29	10.3	0.26	−1.76	0.07	10.3	0.26	0.	−0.
22.000	9	7.3	0.17	−1.28	0.05	7.3	0.17	0.	−0.
24.000	2	5.1	0.02	−0.91	0.00	5.1	0.02	0.	−0.
26.000	1	3.6	−0.	−0.63	−0.	3.6	−0.	0.	−0.

Exponential Profile Correlation	Equation	Range (KM)
0.	W = 1.00 Exp(0. H) ±1.000000	0 = H = 0
0.989730	D_1 = 229.70 Exp(−0.141651H) ±6.227127	0 = H = 4
0.999733	D_2 = 291.00 Exp(−0.167585H) ±0.579201	10 = H = 26

TABLE E-2. (*Continued*)

Mean N–Profile, Station 90001, Month 8 — Number of Profiles Used in Calculating Tropopause 50. 129. Tropopause Height Min. Temp. 14.35 ±1.30, Lapse 8.31 ±1.71.

Height (KM)	Number	N	SDN	dN/dh	SDG	DRY	SDD	WET	SDW
0.	185	246.7	6.10	—175.52	73.79	246.7	6.10	0.0	−0.
0.050	185	238.0	5.10	—167.74	67.82	238.0	5.10	0.0	−0.
0.100	185	230.0	5.54	—124.23	60.79	230.0	5.56	0.0	0.06
0.250	185	217.6	3.51	−52.07	27.00	217.5	3.53	0 0	0.14
0.500	185	208.1	2.56	−31.62	6.43	208.0	2.57	0.1	0.26
0.750	185	200.8	2.34	−27.27	2.57	200.7	2.32	0.1	0.29
1.000	185	194.2	2.23	−25.64	2.23	194.1	2.19	0.1	0.31
1.500	185	182.0	2.13	−23.08	1.52	181.9	2.11	0.1	0.30
2.000	185	171.0	2.06	−21.14	1.07	171.0	2.06	0.0	0.19
2.500	185	160.8	1.98	−19.74	1.06	160.8	1.98	0.0	0.11
3.000	185	151.2	1.91	−18.68	1.12	151.2	1.91	0.	−0.
3.500	183	142.2	1.92	−17.90	1.00	142.2	1.92	0.	−0.
4.000	183	133.4	1.91	−17.17	0.92	133.4	1.91	0.	−0.
4.500	183	125.0	1.95	−16.35	1.03	125.0	1.95	0.	−0.
5.000	183	117.0	2.05	−15.65	1.03	117.0	2.05	0.	−0.
5.500	182	109.3	2.19	−15.26	0.97	109.3	2.19	0.	−0.
6.000	182	101.8	2.30	−14.52	0.84	101.8	2.30	0.	−0.
6.500	182	94.7	2.36	−14.04	0.81	94.7	2.36	0.	−0.
7.000	178	87.8	2.41	−13.38	0.81	87.8	2.41	0.	−0.
7.500	177	81.3	2.36	−12.90	0.78	81.3	2.36	0.	−0.
8.000	175	75.0	2.26	−12.17	0.78	75.0	2.26	0.	−0.
8.500	174	69.1	2.06	−11.51	0.82	69.1	2.06	0.	−0.
9.000	173	63.5	1.82	−10.65	0.75	63.5	1.82	0.	−0.
9.500	170	58.4	1.58	−9.80	0.70	58.4	1.58	0.	−0.
10.000	168	53.7	1.35	−8.95	0.56	53.7	1.35	0.	−0.
11.000	155	45.5	1.07	−7.68	0.64	45.5	1.07	0.	−0.
12.000	141	38.4	0.88	−6.63	0.47	38.4	0.88	0.	−0.
13.000	119	32.3	0.70	−5.60	0.31	32.3	0.70	0.	−0.
14.000	91	27.2	0.57	−4.77	0.21	27.2	0.57	0.	−0.
15.000	62	22.8	0.46	−4.07	0.17	22.8	0.46	0.	−0.
16.000	41	19.0	0.39	−3.45	0.13	19.0	0.39	0.	−0.
17.000	24	15.9	0.32	−2.95	0.09	15.9	0.32	0.	−0.
18.000	10	13.1	0.29	−2.40	0.08	13.1	0.29	0.	−0.
19.000	1	10.8	−0.	−1.99	−0.	10.8	−0.	0.	−0.

Exponential Profile Correlation	Equation	Range (KM)
0.	W = 1.00 Exp(0. H) ±1.000000	0 = H = 0
0.995190	D_1 = 229.20 Exp(−0.136440H) ±6.117404	0 = H = 6
0.999715	D_2 = 322.60 Exp(−0.177505H) ±0.390122	10 = H = 19

Mean N–Profile, Station 90001, Month 11 — Number of Profiles Used in Calculating Tropopause 132. 132. Tropopause Height Min. Temp. 7.12 ±1.38, Lapse 5.71 ±0.82

Height (KM)	Number	N	SDN	dN/dh	SDG	DRY	SDD	WET	SDW
0.	161	226.7	5.11	−62.39	32.32	226.7	5.14	0.0	0.17
0.050	161	223.2	4.34	−66.64	32.10	223.2	4.37	0.0	0.18
0.100	161	219.8	3.75	−61.22	29.06	219.8	3.76	0.1	0.25
0.250	161	213.3	2.70	−37.47	10.63	212.6	3.12	0.7	0.85
0.500	161	205.4	2.48	−28.51	4.25	204.4	2.85	1.0	0.99
0.750	161	198.6	2.32	−26.25	3.18	197.6	2.64	1.0	1.02
1.000	161	192.3	2.01	−24.57	2.31	191.3	2.26	1.0	0.96
1.500	161	180.5	1.77	−22.31	0.99	179.7	1.89	0.8	0.80
2.000	161	169.6	1.56	−21.02	1.78	169.1	1.69	0.6	0.66
2.500	161	159.4	1.41	−19.64	0.82	159.2	1.49	0.3	0.47
3.000	161	149.9	1.29	−18.45	0.93	149.9	1.31	0.1	0.26
3.500	161	141.1	1.20	−17.39	0.82	141.1	1.20	0.0	0.12
4.000	161	132.6	1.15	−16.61	0.90	132.6	1.15	0.	−0.
4.500	161	124.5	1.20	−15.80	1.03	124.5	1.20	0.	−0.
5.000	160	116.8	1.42	−15.39	1.31	116.8	1.42	0.	−0.
5.500	158	109.1	1.70	−15.23	1.40	109.1	1.70	0.	−0.
6.000	156	101.6	2.04	−14.91	1.43	101.6	2.04	0.	−0.
6.500	154	94.2	2.28	−14.61	1.38	94.2	2.28	0.	−0.
7.000	153	87.0	2.40	−14.18	1.61	87.0	2.40	0.	−0.
7.500	152	80.0	2.25	−13.58	1.85	80.0	2.25	0.	−0.
8.000	149	73.5	1.99	−12.30	0.99	73.5	1.99	0.	−0.
8.500	144	67.6	1.73	−11.47	0.98	67.6	1.73	0.	−0.
9.000	143	62.1	1.48	−10.47	0.76	62.1	1.48	0.	−0.
9.500	141	57.1	1.30	−9.60	0.73	57.1	1.30	0.	−0.
10.000	141	52.5	1.14	−8.81	0.60	52.5	1.14	0.	−0.
11.000	135	44.4	0.96	−7.51	0.51	44.4	0.96	0.	−0.
12.000	132	37.5	0.85	−6.26	0.46	37.5	0.85	0.	−0.
13.000	129	31.9	0.80	−5.16	0.31	31.9	0.80	0.	−0.
14.000	126	27.1	0.78	−4.37	0.29	27.1	0.78	0.	−0.
15.000	119	23.1	0.81	−3.66	0.20	23.1	0.81	0.	−0.
16.000	108	19.7	0.84	−3.11	0.18	19.7	0.84	0.	−0.
17.000	100	16.9	0.84	−2.63	0.14	16.9	0.84	0.	−0.
18.000	86	14.4	0.89	−2.24	0.13	14.4	0.89	0.	−0.
19.000	76	12.3	0.91	−1.93	0.08	12.3	0.91	0.	−0.
20.000	71	10.5	0.88	−1.62	0.09	10.5	0.88	0.	−0.
22.000	55	7.7	0.81	−1.19	0.08	7.7	0.81	0.	−0.
24.000	45	5.6	0.66	−0.85	0.06	5.6	0.66	0.	−0.
26.000	21	4.0	0.48	−0.62	0.06	4.0	0.48	0.	−0.
28.000	8	2.9	0.25	−0.43	0.02	2.9	0.25	0.	−0.
30.000	4	2.2	0.26	−0.32	0.02	2.2	0.26	0.	−0.
32.000	1	1.9	−0.	−0.25	−0.	1.9	−0.	0.	−0.

Exponential Profile Correlation	Equation	Range (KM)
0.233854	W = 0.15 Exp(0.376075H) ±0.523091	0 = H = 3
0.997559	D_1 = 220.96 Exp(−0.130114H) ±2.602547	0 = H = 4
0.999344	D_2 = 239.21 Exp(−0.155433H) ±0.599881	10 = H = 32

TABLE E-3. *Cumulative distribution of ground-based gradients: Amundsen-Scott, Antarctica (gradient followed by percentage level).*

0–50 METERS, STATION 90001, MONTH 2

−20.7	0.51	−20.8	1.52	−22.3	2.53	−23.1	3.54	−24.8	4.55	−28.5	5.56	−28.7	6.57
−28.9	7.58	−30.5	8.59	−31.0	9.60	−32.8	10.61	−35.0	11.62	−37.2	12.63	−40.0	13.64
−41.6	14.65	−42.9	15.66	−43.3	16.67	−44.2	17.68	−44.2	18.69	−45.3	19.70	−46.9	20.71
−47.1	21.72	−47.7	22.73	−49.7	23.74	−50.1	24.75	−50.2	25.76	−50.3	26.77	−51.0	27.78
−51.3	28.79	−51.7	29.80	−52.8	30.81	−53.8	31.82	−54.0	32.83	−54.2	33.84	−56.0	34.85
−56.6	35.86	−57.5	36.87	−57.6	37.88	−61.5	38.89	−61.7	39.90	−62.4	40.91	−63.0	41.92
−63.5	42.93	−63.6	43.94	−63.9	44.95	−65.4	45.96	−67.6	46.97	−67.7	47.98	−67.8	48.99
−68.3	50.00	−68.4	51.01	−69.1	52.02	−70.7	53.03	−71.6	54.04	−72.5	55.05	−73.5	56.06
−73.8	57.07	−74.1	58.08	−74.5	59.09	−75.3	60.10	−75.7	61.11	−76.6	62.12	−76.7	63.13
−77.9	64.14	−79.5	65.15	−81.1	66.16	−81.9	67.17	−82.8	68.18	−83.9	69.19	−84.0	70.20
−84.4	71.21	−85.1	72.22	−85.4	73.23	−85.8	74.24	−86.1	75.25	−87.1	76.26	−89.2	77.27
−91.3	78.28	−93.7	79.29	−95.6	80.30	−97.9	81.31	−101.0	82.32	−102.4	83.33	−104.4	84.34
−107.2	85.35	−107.4	86.36	−107.5	87.37	−107.5	88.38	−109.7	89.39	−113.6	90.40	−114.6	91.41
−123.7	92.42	−125.1	93.43	−133.7	94.44	−137.2	95.45	−146.9	96.46	−154.4	97.47	−166.7	98.48
−171.8	99.49												

0–50 METERS, STATION 90001, MONTH 5

−33.8	0.30	−41.3	0.91	−42.4	1.52	−43.9	2.13	−45.1	2.74	−45.4	3.35	−45.6	3.96
−47.4	4.57	−48.7	5.18	−52.5	5.79	−53.3	6.40	−56.4	7.01	−57.4	7.62	−59.5	8.23
−63.1	8.84	−64.8	9.45	−65.2	10.06	−66.6	10.67	−68.1	11.28	−68.3	11.89	−69.5	12.50
−70.2	13.11	−70.8	13.72	−72.3	14.33	−73.1	14.94	−77.1	15.55	−78.2	16.16	−78.9	16.77
−80.6	17.38	−80.8	17.99	−82.0	18.60	−83.0	19.21	−83.7	19.82	−83.7	20.43	−89.5	21.04
−91.5	21.65	−92.0	22.26	−93.7	22.87	−94.1	23.48	−94.6	24.09	−97.6	24.70	−99.0	25.30
−102.3	25.91	−102.4	26.52	−105.8	27.13	−108.9	27.74	−110.4	28.35	−110.7	28.96	−111.4	29.57
−111.5	30.18	−113.9	30.79	−116.0	31.40	−116.7	32.01	−118.3	32.62	−119.7	33.23	−119.7	33.84
−120.7	34.45	−127.9	35.06	−131.9	35.67	−132.2	36.28	−132.2	36.89	−132.8	37.50	−134.4	38.11
−135.6	38.72	−137.1	39.33	−137.2	39.94	−137.4	40.55	−137.8	41.16	−138.1	41.77	−139.0	42.38
−140.7	42.99	−141.2	43.60	−144.5	44.21	−146.1	44.82	−147.3	45.43	−148.6	46.04	−150.3	46.65
−150.3	47.26	−150.4	47.87	−152.4	48.48	−153.3	49.09	−153.4	49.70	−153.6	50.30	−156.6	50.91
−157.1	51.52	−159.6	52.13	−164.0	52.74	−164.7	53.35	−165.1	53.96	−166.6	54.57	−166.7	55.18
−167.0	55.79	−168.4	56.40	−168.7	57.01	−170.5	57.62	−171.6	58.23	−172.4	58.84	−173.5	59.45
−173.6	60.06	−174.6	60.67	−175.1	61.28	−176.7	61.89	−177.4	62.50	−178.0	63.11	−178.5	63.72
−179.6	64.33	−180.1	64.94	−180.5	65.55	−183.4	66.16	−183.6	66.77	−183.7	67.38	−186.3	67.99
−186.9	68.60	−187.3	69.21	−189.7	69.82	−193.8	70.43	−197.3	71.04	−199.0	71.65	−199.7	72.26
−204.3	72.87	−204.9	73.48	−207.6	74.09	−208.9	74.70	−209.1	75.30	−210.1	75.91	−210.9	76.52
−211.2	77.13	−214.2	77.74	−214.4	78.35	−216.3	78.96	−217.0	79.57	−222.3	80.18	−226.8	80.79
−227.7	81.40	−229.2	82.01	−232.7	82.62	−233.4	83.23	−236.8	83.84	−238.9	84.45	−241.1	85.06
−244.1	85.67	−247.3	86.28	−247.6	86.89	−251.5	87.50	−255.0	88.11	−260.8	88.72	−263.3	89.33
−268.2	89.94	−270.8	90.55	−270.9	91.16	−275.0	91.77	−275.8	92.38	−282.8	92.99	−285.1	93.60
−297.8	94.21	−299.3	94.82	−299.8	95.43	−310.0	96.04	−311.1	96.65	−312.5	97.26	−341.2	97.87
−383.6	98.48	−429.0	99.09	−481.2	99.70								

0–50 METERS, STATION 90001, MONTH 8

−37.9	0.27	−39.3	0.81	−45.5	1.35	−47.9	1.89	−48.4	2.43	−49.5	2.97	−49.6	3.51
−58.3	4.05	−59.3	4.59	−59.3	5.14	−69.3	5.68	−74.6	6.22	−74.7	6.76	−74.9	7.30
−75.1	7.84	−80.4	8.38	−80.7	8.92	−82.9	9.46	−85.7	10.00	−89.9	10.54	−90.8	11.08
−92.6	11.62	−94.9	12.16	−95.4	12.70	−96.2	13.24	−96.6	13.78	−99.0	14.32	−100.4	14.86
−100.5	15.41	−100.6	15.95	−101.7	16.49	−105.6	17.03	−106.5	17.57	−108.2	18.11	−110.1	18.65
−112.4	19.19	−112.9	19.73	−114.7	20.27	−114.9	20.81	−115.1	21.35	−115.2	21.89	−116.0	22.43
−117.5	22.97	−118.6	23.51	−121.6	24.05	−123.9	24.59	−126.3	25.14	−126.3	25.68	−129.2	26.22
−129.6	26.76	−130.8	27.30	−131.9	27.84	−132.3	28.38	−132.7	28.92	−134.3	29.46	−134.8	30.00
−135.2	30.54	−135.5	31.08	−135.9	31.62	−137.3	32.16	−137.5	32.70	−137.6	33.24	−138.0	33.78
−138.7	34.32	−139.1	34.86	−139.3	35.41	−141.7	35.95	−143.6	36.49	−143.7	37.03	−143.7	37.57
−146.0	38.11	−146.6	38.65	−147.1	39.19	−147.2	39.73	−147.5	40.27	−149.8	40.81	−150.2	41.35
−151.4	41.89	−152.6	42.43	−154.7	42.97	−156.6	43.51	−156.8	44.05	−156.9	44.59	−157.6	45.14
−161.1	45.68	−163.3	46.22	−164.4	46.76	−164.6	47.30	−166.7	47.84	−166.9	48.38	−168.1	48.92
−169.2	49.46	−170.1	50.00	−171.3	50.54	−171.5	51.08	−171.8	51.62	−173.0	52.16	−174.4	52.70
−176.0	53.24	−176.2	53.78	−176.3	54.32	−177.8	54.86	−178.4	55.41	−180.4	55.95	−180.5	56.49
−180.9	57.03	−180.9	57.57	−183.8	58.11	−183.8	58.65	−184.4	59.19	−185.9	59.73	−186.3	60.27
−186.4	60.81	−189.5	61.35	−190.2	61.89	−191.7	62.43	−191.8	62.97	−192.0	63.51	−193.0	64.05
−193.8	64.59	−197.1	65.14	−198.3	65.68	−199.3	66.22	−200.8	66.76	−203.1	67.30	−204.5	67.84
−206.0	68.38	−208.6	68.92	−208.8	69.46	−211.2	70.00	−211.8	70.54	−212.0	71.08	−212.5	71.62
−215.4	72.16	−216.1	72.70	−216.1	73.24	−217.1	73.78	−218.3	74.32	−219.3	74.86	−221.4	75.41
−221.7	75.95	−225.2	76.49	−225.7	77.03	−227.7	77.57	−230.6	78.11	−230.7	78.65	−232.5	79.19
−238.2	79.73	−239.9	80.27	−240.9	80.81	−242.2	81.35	−242.6	81.89	−244.8	82.43	−245.4	82.97
−246.9	83.51	−249.6	84.05	−252.3	84.59	−252.9	85.14	−254.6	85.68	−262.2	86.22	−265.4	86.76
−266.3	87.30	−267.0	87.84	−267.1	88.38	−269.1	88.92	−272.4	89.46	−275.7	90.00	−277.6	90.54
−279.1	91.08	−279.2	91.62	−280.0	92.16	−289.3	92.70	−290.5	93.24	−290.7	93.78	−292.7	94.32
−293.7	94.86	−296.5	95.41	−298.7	95.95	−302.6	96.49	−305.8	97.03	−306.4	97.57	−314.4	98.11
−336.0	98.65	−346.2	99.19	−419.4	99.73								

TABLE E-3. (*Continued*)

0–50 METERS, STATION 90001, MONTH 11

−9.1	0.31	−16.1	0.93	−18.1	1.55	−21.3	2.17	−22.5	2.80	−24.9	3.42	−25.1	4.04
−25.8	4.66	−27.3	5.28	−27.6	5.90	−27.6	6.52	−27.7	7.14	−27.8	7.76	−28.0	8.39
−28.2	9.01	−29.1	9.63	−31.7	10.25	−35.1	10.87	−37.2	11.49	−38.4	12.11	−38.6	12.73
−39.5	13.35	−39.6	13.98	−39.7	14.60	−40.4	15.22	−40.7	15.84	−42.7	16.46	−43.6	17.08
−44.3	17.70	−45.4	18.32	−45.5	18.94	−46.5	19.57	−46.5	20.19	−46.6	20.81	−46.7	21.43
−47.3	22.05	−48.3	22.67	−49.1	23.29	−49.3	23.91	−49.3	24.53	−49.8	25.16	−49.9	25.78
−50.3	26.40	−51.7	27.02	−53.7	27.64	−53.7	28.26	−53.9	28.88	−54.6	29.50	−55.1	30.12
−55.4	30.75	−55.7	31.37	−55.9	31.99	−56.1	32.61	−56.3	33.23	−56.4	33.85	−56.8	34.47
−58.3	35.09	−58.6	35.71	−58.7	36.34	−58.8	36.96	−59.1	37.58	−59.7	38.20	−59.9	38.82
−60.2	39.44	−60.5	40.06	−61.1	40.68	−61.4	41.30	−61.9	41.93	−62.0	42.55	−62.3	43.17
−62.8	43.79	−62.8	44.41	−63.2	45.03	−64.1	45.65	−64.5	46.27	−65.0	46.89	−66.3	47.52
−66.3	48.14	−66.5	48.76	−67.2	49.38	−67.5	50.00	−67.7	50.62	−67.8	51.24	−68.2	51.86
−68.5	52.48	−68.6	53.11	−69.2	53.73	−69.7	54.35	−70.2	54.97	−73.0	55.59	−73.2	56.21
−73.4	56.83	−73.9	57.45	−74.2	58.07	−74.3	58.70	−74.6	59.32	−76.0	59.94	−76.3	60.56
−76.8	61.18	−77.1	61.80	−77.2	62.42	−77.2	63.04	−77.4	63.66	−77.8	64.29	−78.7	64.91
−79.0	65.53	−79.0	66.15	−79.5	66.77	−79.8	67.39	−80.5	68.01	−81.6	68.63	−81.8	69.25
−82.3	69.88	−84.0	70.50	−84.5	71.12	−84.7	71.74	−85.1	72.36	−86.0	72.98	−86.0	73.60
−86.0	74.22	−86.1	74.84	−86.6	75.47	−86.8	76.09	−87.3	76.71	−87.7	77.33	−88.9	77.95
−89.8	78.57	−90.2	79.19	−91.3	79.81	−92.4	80.43	−92.6	81.06	−96.0	81.68	−97.6	82.30
−98.9	82.92	−99.2	83.54	−99.4	84.16	−100.0	84.78	−100.7	85.40	−100.8	86.02	−100.9	86.65
−102.1	87.27	−102.3	87.89	−102.9	88.51	−103.7	89.13	−105.3	89.75	−106.1	90.37	−108.4	90.99
−110.2	91.61	−111.8	92.24	−111.9	92.86	−119.1	93.48	−119.1	94.10	−119.3	94.72	−122.4	95.34
−123.8	95.96	−124.1	96.58	−128.8	97.20	−139.4	97.83	−147.0	98.45	−155.9	99.07	−161.3	99.69

0–100 METERS, STATION 90001, MONTH 2

−20.6	0.51	−20.7	1.52	−22.1	2.53	−23.0	3.54	−24.7	4.55	−28.4	5.56	−28.6	6.57
−28.8	7.58	−30.3	8.59	−30.4	9.60	−32.7	10.61	−34.7	11.62	−37.1	12.63	−39.8	13.64
−41.1	14.65	−42.6	15.66	−43.0	16.67	−44.0	17.68	−44.0	18.69	−45.1	19.70	−46.6	2 .71
−46.7	21.72	−46.8	22.73	−47.4	23.74	−48.9	24.75	−49.9	25.76	−50.0	26.77	−50.7	27.78
−51.0	28.79	−51.4	29.80	−52.5	30.81	−53.5	31.82	−53.6	32.83	−53.8	33.84	−55.6	34.85
−56.2	35.86	−57.1	36.87	−57.3	37.88	−61.1	38.89	−61.3	39.90	−61.3	40.91	−62.6	41.92
−63.1	42.93	−63.1	43.94	−63.5	44.95	−64.9	45.96	−67.1	46.97	−67.2	47.98	−67.3	48.99
−67.8	50.00	−67.9	51.01	−68.5	52.02	−70.2	53.03	−71.1	54.04	−71.9	55.05	−72.9	56.06
−73.2	57.07	−73.5	58.08	−73.8	59.09	−74.7	60.10	−75.0	61.11	−76.0	62.12	−76.1	63.13
−77.3	64.14	−78.8	65.15	−80.3	66.16	−81.1	67.17	−82.0	68.18	−83.1	69.19	−83.2	70.20
−83.6	71.21	−84.3	72.22	−84.6	73.23	−85.0	74.24	−85.3	75.25	−86.2	76.26	−88.3	77.27
−90.4	78.28	−92.7	79.29	−93.0	80.30	−94.6	81.31	−96.8	82.32	−99.9	83.33	−101.3	84.34
−103.2	85.35	−106.2	86.36	−106.2	87.37	−106.2	88.38	−108.4	89.39	−112.2	90.40	−112.8	91.41
−113.1	92.42	−122.1	93.43	−131.8	94.44	−135.2	95.45	−144.6	96.46	−151.9	97.47	−163.8	98.48
−168.8	99.49												

0–100 METERS, STATION 90001, MONTH 5

−42.2	0.30	−43.7	0.91	−44.9	1.52	−45.2	2.13	−45.4	2.74	−47.2	3.35	−49.2	3.96
−56.1	4.57	−56.6	5.18	−57.1	5.79	−59.1	6.40	−62.7	7.01	−64.7	7.62	−66.1	8.23
−67.6	8.84	−70.2	9.45	−70.8	10.06	−71.8	10.67	−72.5	11.28	−74.0	11.89	−74.2	12.50
−77.3	13.11	−77.6	13.72	−79.9	14.33	−80.1	14.94	−83.0	15.55	−83.6	16.16	−86.1	16.77
−87.1	17.38	−90.3	17.99	−90.6	18.60	−91.1	19.21	−92.7	19.82	−93.2	20.43	−93.7	21.04
−96.6	21.65	−97.0	22.26	−98.0	22.87	−101.2	23.48	−101.3	24.09	−104.6	24.70	−107.6	25.30
−109.1	25.91	−109.5	26.52	−109.7	27.13	−110.1	27.74	−110.2	28.35	−110.8	28.96	−112.6	29.57
−114.7	30.18	−114.7	30.79	−115.0	31.40	−115.3	32.01	−116.8	32.62	−118.2	33.23	−118.2	33.84
−119.2	34.45	−126.3	35.06	−130.0	35.67	−130.4	36.28	−130.4	36.89	−131.0	37.50	−132.6	38.11
−134.6	38.72	−134.9	39.33	−135.2	39.94	−135.5	40.55	−135.9	41.16	−136.2	41.77	−138.7	42.38
−139.1	42.99	−141.0	43.60	−142.5	44.21	−144.0	44.82	−146.0	45.43	−146.5	46.04	−148.0	46.65
−148.1	47.26	−149.4	47.87	−150.0	48.48	−150.9	49.09	−151.2	49.70	−153.9	50.30	−154.6	50.91
−157.7	51.52	−158.8	52.13	−160.5	52.74	−161.2	53.35	−162.1	53.96	−162.3	54.57	−163.7	55.18
−163.8	55.79	−165.7	56.40	−165.8	57.01	−166.3	57.62	−168.2	58.23	−168.3	58.84	−169.6	59.45
−170.5	60.06	−170.6	60.67	−171.3	61.28	−171.5	61.89	−172.1	62.50	−173.1	63.11	−173.5	63.72
−174.2	64.33	−174.9	64.94	−175.3	65.55	−176.4	66.16	−177.2	66.77	−180.1	67.38	−180.3	67.99
−180.4	68.60	−182.8	69.21	−183.4	69.82	−183.7	70.43	−186.1	71.04	−186.2	71.65	−186.3	72.26
−193.4	72.87	−194.5	73.48	−195.1	74.09	−195.7	74.70	−196.1	75.30	−197.3	75.91	−197.4	76.52
−198.8	77.13	−200.1	77.74	−200.7	78.35	−203.3	78.96	−204.9	79.57	−205.5	80.18	−206.7	80.79
−208.9	81.40	−209.6	82.01	−209.7	82.62	−210.2	83.23	−212.0	83.84	−212.5	84.45	−217.3	85.06
−220.1	85.67	−221.1	86.28	−221.7	86.89	−222.6	87.50	−225.0	88.11	−227.5	88.72	−227.9	89.33
−229.4	89.94	−230.3	90.55	−234.0	91.16	−238.6	91.77	−239.8	92.38	−245.3	92.99	−248.1	93.60
−250.6	94.21	−252.3	94.82	−252.8	95.43	−263.5	96.04	−264.9	96.65	−270.7	97.26	−271.5	97.87
−277.4	98.48	−288.5	99.09	−290.9	99.70								

TABLE E-3. *(Continued)*

0–100 METERS, STATION 90001, MONTH 8

−37.7	0.27	−39.1	0.81	−45.2	1.35	−47.7	1.89	−48.2	2.43	−49.4	2.97	−57.9	3.51
−74.0	4.05	−74.2	4.59	−74.3	5.14	−79.5	5.68	−79.7	6.22	−80.0	6.76	−82.2	7.30
−84.2	7.84	−84.9	8.38	−89.1	8.92	−89.9	9.46	−91.7	10.00	−93.9	10.54	−94.4	11.08
−95.6	11.62	−97.9	12.16	−99.4	12.70	−99.6	13.24	−99.9	13.78	−105.3	14.32	−107.0	14.86
−108.9	15.41	−109.1	15.95	−111.1	16.49	−113.3	17.03	−113.6	17.57	−113.7	18.11	−113.8	18.65
−114.6	19.19	−115.1	19.73	−116.1	20.27	−116.9	20.81	−117.2	21.35	−120.1	21.89	−122.3	22.43
−124.7	22.97	−124.7	23.51	−126.8	24.05	−127.4	24.59	−127.9	25.14	−130.2	25.68	−130.4	26.22
−131.9	26.76	−132.1	27.30	−132.4	27.84	−132.9	28.38	−133.3	28.92	−133.6	29.46	−134.0	30.00
−135.4	30.54	−135.5	31.08	−135.5	31.62	−135.6	32.16	−136.7	32.70	−136.7	33.24	−137.1	33.78
−139.6	34.32	−139.8	34.86	−140.8	35.41	−141.5	35.95	−141.6	36.49	−141.7	37.03	−143.9	37.57
−145.0	38.11	−145.1	38.65	−145.3	39.19	−147.0	39.73	−147.6	40.27	−149.1	40.81	−150.3	41.35
−150.6	41.89	−152.2	42.43	−154.0	42.97	−154.5	43.51	−154.6	44.05	−156.0	44.59	−157.4	45.14
−158.1	45.68	−158.5	46.22	−161.1	46.76	−161.6	47.30	−161.8	47.84	−163.6	48.38	−164.1	48.92
−165.2	49.46	−166.3	50.00	−168.6	50.54	−169.3	51.08	−169.9	51.62	−170.7	52.16	−170.7	52.70
−170.9	53.24	−171.4	53.78	−172.9	54.32	−173.3	54.86	−175.5	55.41	−176.2	55.95	−177.2	56.49
−177.3	57.03	−177.7	57.57	−180.4	58.11	−180.5	58.65	−181.1	59.19	−182.5	59.73	−182.8	60.27
−182.9	60.81	−183.4	61.35	−183.5	61.89	−185.7	62.43	−185.9	62.97	−186.2	63.51	−186.5	64.05
−187.9	64.59	−188.4	65.14	−188.5	65.68	−189.2	66.22	−190.0	66.76	−190.4	67.30	−192.7	67.84
−192.8	68.38	−192.8	68.92	−196.1	69.46	−196.7	70.00	−198.7	70.54	−199.2	71.08	−203.3	71.62
−204.3	72.16	−204.4	72.70	−206.6	73.24	−207.4	73.78	−207.4	74.32	−207.6	74.86	−208.0	75.41
−210.6	75.95	−210.8	76.49	−211.4	77.03	−211.5	77.57	−213.7	78.11	−214.4	78.65	−215.8	79.19
−216.1	79.73	−218.3	80.27	−218.9	80.81	−219.3	81.35	−219.4	81.89	−220.0	82.43	−221.1	82.97
−221.2	83.51	−221.2	84.05	−222.5	84.59	−225.3	85.14	−231.0	85.68	−232.9	86.22	−233.5	86.76
−235.2	87.30	−235.6	87.84	−236.3	88.38	−238.5	88.92	−243.9	89.46	−244.8	90.00	−248.1	90.54
−252.9	91.08	−253.2	91.62	−255.4	92.16	−257.3	92.70	−260.0	93.24	−260.1	93.78	−260.2	94.32
−261.8	94.86	−262.9	95.41	−265.7	95.95	−271.5	96.49	−279.1	97.03	−279.7	97.57	−282.1	98.11
−293.5	98.65	−319.1	99.19	−328.5	99.73								

0–100 METERS, STATION 90001, MONTH 11

−9.0	0.31	−9.9	0.93	−17.9	1.55	−21.3	2.17	−22.5	2.80	−25.0	3.42	−25.7	4.04
−27.2	4.66	−27.5	5.28	−27.6	5.90	−27.7	6.52	−27.9	7.14	−28.1	7.76	−29.0	8.39
−29.8	9.01	−31.6	9.63	−34.9	10.25	−37.0	10.87	−38.2	11.49	−38.4	12.1	−39.4	12.73
−40.3	13.35	−40.5	13.98	−42.4	14.60	−44.1	15.22	−45.2	15.84	−46.3	16.46	−46.3	17.08
−46.3	17.70	−46.4	18.32	−48.1	18.94	−48.8	19.57	−49.0	20.19	−49.0	20.81	−49.5	21.43
−49.6	22.05	−50.0	22.67	−51.0	23.29	−51.1	23.91	−51.3	24.53	−51.4	25.16	−53.4	25.78
−53.4	26.40	−53.6	27.02	−54.3	27.64	−54.6	28.26	−54.7	28.88	−55.1	29.50	−55.3	30.12
−55.8	30.75	−56.0	31.37	−56.0	31.99	−56.5	32.61	−57.3	33.23	−57.9	33.85	−58.3	34.47
−58.4	35.09	−58.7	35.71	−58.8	36.34	−59.3	36.96	−59.5	37.58	−59.8	38.20	−60.1	38.82
−60.7	39.44	−61.0	40.06	−61.5	40.68	−61.6	41.30	−61.8	41.93	−62.4	42.55	−62.4	43.17
−62.8	43.79	−63.7	44.41	−64.0	45.03	−64.5	45.65	−65.6	46.27	−65.8	46.89	−66.0	47.52
−66.7	48.14	−67.0	48.76	−67.3	49.38	−68.1	50.00	−68.7	50.62	−69.2	51.24	−69.6	51.86
−72.4	52.48	−72.8	53.11	−73.3	53.73	−73.3	54.35	−73.5	54.97	−73.6	55.59	−73.7	56.21
−74.8	56.83	−75.4	57.45	−75.7	58.07	−76.1	58.70	−76.4	59.32	−76.5	59.94	−76.6	60.56
−76.7	61.18	−77.0	61.80	−78.0	62.42	−78.1	63.04	−78.3	63.66	−78.3	64.29	−78.8	64.91
−79.2	65.53	−79.8	66.15	−80.7	66.77	−80.8	67.39	−80.9	68.01	−81.1	68.63	−81.6	69.25
−83.2	69.88	−83.2	70.50	−83.8	71.12	−84.0	71.74	−84.1	72.36	−84.2	72.98	−84.3	73.60
−85.2	74.22	−85.2	74.84	−85.2	75.47	−85.3	76.09	−85.5	76.71	−85.8	77.33	−86.0	77.95
−86.0	78.57	−86.5	79.19	−86.9	79.81	−88.0	80.43	−88.9	81.06	−89.3	81.68	−89.8	82.30
−90.4	82.92	−91.6	83.54	−95.1	84.16	−96.6	84.78	−96.8	85.40	−98.2	86.02	−98.3	86.65
−98.9	87.27	−99.6	87.89	−99.7	88.51	−100.7	89.13	−100.9	89.75	−101.2	90.37	−101.7	90.99
−102.5	91.61	−104.1	92.24	−104.9	92.86	−107.1	93.48	−107.4	94.10	−110.4	94.72	−110.6	95.34
−114.8	95.96	−117.6	96.58	−120.7	97.20	−120.8	97.83	−122.1	98.45	−132.5	99.07	−158.5	99.69

TABLE E-4. *Analysis of ground-based superrefractive and ducting layers: Amundsen-Scott, Antarctica.*

FEBRUARY

87 Profiles Skipped
99 Profiles Read
Number of Ducts 2
Number of Superrefractive Layers 10

CUMULATIVE DISTRIBUTION OF DUCTING GRADIENTS, STATION 90001, MONTH 2

−157.500	25.00	−164.815	75.00

CUMULATIVE DISTRIBUTION OF DUCT THICKNESSES, STATION 90001, MONTH 2

0.120	25.00	0.108	75.00

CUMULATIVE DISTRIBUTION OF TRAPPING FREQUENCIES, STATION 90001, MONTH 2

3693.683	25.00	1191.104	75.00

CUMULATIVE DISTRIBUTION OF SUPERREFRACTIVE LAYER GRADIENTS, STATION 90001, MONTH 2

−100.000	5.00	−101.626	15.00	−103.922	25.00	−103.960	35.00	−117.391	45.00	−118.033	55.00	−124.793	65.00
−129.054	75.00	−138.182	85.00	−148.182	95.00								

TABLE E-4. *(Continued)*

CUMULATIVE DISTRIBUTION OF SUPERREFRACTIVE LAYER THICKNESSES, STATION 90001, MONTH 2

0.148	5.00	0.123	15.00	0.122	25.00	0.121	35.00	0.110	45.00	0.110	55.00	0.104	65.00
0.102	75.00	0.101	85.00	0.092	95.00								

MAY

45 Profiles Skipped
164 Profiles Read
Number of Ducts 79
Number of Superrefractive Layers 40

CUMULATIVE DISTRIBUTION OF DUCTING GRADIENTS, STATION 90001, MONTH 5

−157.396	0.63	−158.605	1.90	−158.929	3.16	−159.596	4.43	−159.873	5.70	−160.156	6.96	−161.207	8.23
−164.045	9.49	−165.248	10.76	−165.306	12.03	−165.789	13.29	−166.667	14.56	−167.290	15.82	−167.480	17.09
−167.925	18.35	−169.595	19.62	−170.732	20.89	−172.414	22.15	−173.810	23.42	−174.737	24.68	−175.163	25.95
−175.694	27.22	−176.119	28.48	−176.774	29.75	−176.800	31.01	−180.952	32.28	−182.906	33.54	−183.511	34.81
−187.629	36.08	−187.850	37.34	−188.095	38.61	−192.035	39.87	−192.105	41.14	−192.241	42.41	−196.241	43.67
−196.522	44.94	−198.742	46.20	−200.962	47.47	−202.778	48.73	−202.857	50.00	−203.175	51.27	−205.263	52.53
−206.542	53.80	−210.204	55.06	−210.959	56.33	−214.019	57.59	−219.231	58.86	−220.192	60.13	−221.429	61.39
−224.107	62.66	−224.762	63.92	−231.633	65.19	−231.818	66.46	−232.824	67.72	−233.333	68.99	−237.903	70.25
−239.583	71.52	−240.230	72.78	−244.706	74.05	−246.808	75.32	−250.000	76.58	−259.375	77.85	−263.265	79.11
−266.279	80.38	−266.327	81.65	−272.500	82.91	−275.000	84.18	−276.389	85.44	−284.615	86.71	−285.981	87.97
−298.947	89.24	−302.410	90.51	−306.383	91.77	−351.282	93.04	−375.000	94.30	−377.586	95.57	−405.128	96.84
−422.414	98.10	−789.655	99.37										

CUMULATIVE DISTRIBUTION OF DUCT THICKNESSES, STATION 90001, MONTH 5

0.215	0.63	0.196	1.90	0.188	3.16	0.178	4.43	0.171	5.70	0.169	6.96	0.164	8.23
0.159	9.49	0.157	10.76	0.155	12.03	0.153	13.29	0.152	14.56	0.148	15.82	0.144	17.09
0.141	18.35	0.134	19.62	0.133	20.89	0.131	22.15	0.128	23.42	0.126	24.68	0.126	25.95
0.126	27.22	0.125	28.48	0.124	29.75	0.123	31.01	0.120	32.28	0.117	33.54	0.116	34.81
0.116	36.08	0.116	37.34	0.115	38.61	0.113	39.87	0.112	41.14	0.112	42.41	0.108	43.67
0.107	44.94	0.107	46.20	0.107	47.47	0.107	48.73	0.107	50.00	0.106	51.27	0.105	52.53
0.105	53.80	0.105	55.06	0.104	56.33	0.104	57.59	0.104	58.86	0.099	60.13	0.098	61.39
0.098	62.66	0.098	63.92	0.098	65.19	0.097	66.46	0.096	67.72	0.096	68.99	0.095	70.25
0.095	71.52	0.094	72.78	0.087	74.05	0.086	75.32	0.085	76.58	0.083	77.85	0.078	79.11
0.076	80.38	0.076	81.65	0.075	82.91	0.073	84.18	0.072	85.44	0.066	86.71	0.060	87.97
0.058	89.24	0.058	90.51	0.049	91.77	0.048	93.04	0.047	94.30	0.039	95.57	0.039	96.84
0.029	98.10	0.028	99.37										

CUMULATIVE DISTRIBUTION OF TRAPPING FREQUENCIES, STATION 90001, MONTH 5

2429.613	0.63	2325.397	1.90	2227.842	3.16	1903.914	4.43	1718.862	5.70	1450.565	6.96	1439.236	8.23
1108.889	9.49	1107.595	10.76	1063.192	12.03	1054.213	13.29	1040.684	14.56	1037.927	15.82	980.129	17.09
961.749	18.35	957.395	19.62	954.692	20.89	913.759	22.15	847.641	23.42	838.695	24.68	820.140	25.95
816.260	27.22	810.394	28.48	777.463	29.75	764.293	31.01	712.759	32.28	710.191	33.54	662.327	34.81
646.673	36.08	610.797	37.34	603.274	38.61	592.484	39.87	586.278	41.14	582.761	42.41	573.161	43.67
563.175	44.94	553.068	46.20	538.194	47.47	534.227	48.73	530.990	50.00	528.221	51.27	522.541	52.53
515.639	53.80	512.172	55.06	507.723	56.33	506.381	57.59	502.051	58.86	494.731	60.13	484.498	61.39
483.106	62.66	482.604	63.92	482.287	65.19	481.507	66.46	476.108	67.72	472.742	68.99	465.027	70.25
450.911	71.52	449.615	72.78	449.164	74.05	448.447	75.32	445.739	76.58	439.734	77.85	437.183	79.11
435.225	80.38	424.335	81.65	412.328	82.91	394.994	84.18	390.938	85.44	390.912	86.71	387.054	87.97
370.600	89.24	340.803	90.51	338.249	91.77	302.637	93.04	299.088	94.30	290.004	95.57	287.878	96.84
282.840	98.10	266.106	99.37										

CUMULATIVE DISTRIBUTION OF SUPERREFRACTIVE LAYER GRADIENTS, STATION 90001, MONTH 5

−103.333	1.25	−103.347	3.75	−103.791	6.25	−106.587	8.75	−106.667	11.25	−111.515	13.75	−111.892	16.25
−112.632	18.75	−113.333	21.25	−114.465	23.75	−115.741	26.25	−120.084	28.75	−123.478	31.25	−125.253	33.75
−126.087	36.25	−126.214	38.75	−127.700	41.25	−127.835	43.75	−128.144	46.25	−130.000	48.75	−130.337	51.25
−130.469	53.75	−133.110	56.25	−133.588	58.75	−134.375	61.25	−135.714	63.75	−138.967	66.25	−139.655	68.75
−139.662	71.25	−140.845	73.75	−141.799	76.25	−142.938	78.75	−143.158	81.25	−147.183	83.75	−147.619	86.25
−148.980	88.75	−150.649	91.25	−155.208	93.75	−155.556	96.25	−155.797	98.75				

CUMULATIVE DISTRIBUTION OF SUPERREFRACTIVE LAYER THICKNESSES, STATION 90001, MONTH 5

0.300	1.25	0.299	3.75	0.240	6.25	0.239	8.75	0.239	11.25	0.237	13.75	0.213	16.25
0.213	18.75	0.213	21.25	0.211	23.75	0.206	26.25	0.198	28.75	0.189	31.25	0.185	33.75
0.184	36.25	0.178	38.75	0.177	41.25	0.174	43.75	0.167	46.25	0.167	48.75	0.165	51.25
0.159	53.75	0.154	56.25	0.147	58.75	0.142	61.25	0.138	63.75	0.131	66.25	0.128	68.75
0.126	71.25	0.120	73.75	0.115	76.25	0.108	78.75	0.098	81.25	0.097	83.75	0.096	86.25
0.096	88.75	0.095	91.25	0.095	93.75	0.090	96.25	0.080	98.75				

THICKNESS AND GRADIENT OF SUPERREFRACTIVE LAYERS OVER 300 METERS THICK

0.30000	−106.66667

TABLE E-4. *(Continued)*

AUGUST

31 Profiles Skipped
185 Profiles Read
Number of Ducts 104
Number of Superrefractive Layers 50

CUMULATIVE DISTRIBUTION OF DUCTING GRADIENTS, STATION 90001, MONTH 8

−157.059	0.48	−157.639	1.44	−157.843	2.40	−158.268	3.37	−159.236	4.33	−160.759	5.29	−161.881	6.25
−162.667	7.21	−163.265	8.17	−166.355	9.13	−167.262	10.10	−167.532	11.06	−168.033	12.02	−170.149	12.98
−170.248	13.94	−170.408	14.90	−172.308	15.87	−172.727	16.83	−172.727	17.79	−173.404	18.75	−173.984	19.71
−175.510	20.67	−175.949	21.63	−176.056	22.60	−176.111	23.56	−176.190	24.52	−176.786	25.48	−177.165	26.44
−177.922	27.40	−181.250	28.37	−182.292	29.33	−182.895	30.29	−182.993	31.25	−184.127	32.21	−184.536	33.17
−185.185	34.13	−185.315	35.10	−186.170	36.06	−190.816	37.02	−191.919	37.98	−194.286	38.94	−196.939	39.90
−198.889	40.87	−200.000	41.83	−200.000	42.79	−200.769	43.75	−202.062	44.71	−202.069	45.67	−202.083	46.63
−202.778	47.60	−203.738	48.56	−205.517	49.52	−205.674	50.48	−208.571	51.44	−210.526	52.40	−211.111	53.37
−211.702	54.33	−214.286	55.29	−214.943	56.25	−216.239	57.21	−218.584	58.17	−218.750	59.13	−220.619	60.10
−221.552	61.06	−222.078	62.02	−225.000	62.98	−230.645	63.94	−232.174	64.90	−232.941	65.87	−234.694	66.83
−236.842	67.79	−237.113	68.75	−239.175	69.71	−243.434	70.67	−243.750	71.63	−243.966	72.60	−245.977	73.56
−252.885	74.52	−255.652	75.48	−256.701	76.44	−257.843	77.40	−258.491	78.37	−264.935	79.33	−266.154	80.29
−266.279	81.25	−267.257	82.21	−268.817	83.17	−271.429	84.13	−277.586	85.10	−278.261	86.06	−281.395	87.02
−281.633	87.98	−282.558	88.94	−284.058	89.90	−284.211	90.87	−288.298	91.83	−289.189	92.79	−290.566	93.75
−295.349	94.71	−298.507	95.67	−302.941	96.63	−326.923	97.60	−332.653	98.56	−408.000	99.52		

CUMULATIVE DISTRIBUTION OF DUCT THICKNESSES, STATION 90001, MONTH 8

0.204	0.48	0.202	1.44	0.201	2.40	0.189	3.37	0.180	4.33	0.170	5.29	0.168	6.25
0.168	7.21	0.158	8.17	0.158	9.13	0.157	10.10	0.154	11.06	0.152	12.02	0.147	12.98
0.145	13.94	0.145	14.90	0.144	15.87	0.144	16.83	0.144	17.79	0.144	18.75	0.143	19.71
0.143	20.67	0.142	21.63	0.141	22.60	0.134	23.56	0.130	24.52	0.127	25.48	0.127	26.44
0.126	27.40	0.126	28.37	0.124	29.33	0.123	30.29	0.122	31.25	0.121	32.21	0.117	33.17
0.116	34.13	0.116	35.10	0.116	36.06	0.115	37.02	0.115	37.98	0.113	38.94	0.113	39.90
0.108	40.87	0.107	41.83	0.107	42.79	0.106	43.75	0.106	44.71	0.105	45.67	0.105	46.63
0.104	47.60	0.102	48.56	0.099	49.52	0.099	50.48	0.099	51.44	0.098	52.40	0.098	53.37
0.098	54.33	0.098	55.29	0.098	56.25	0.098	57.21	0.098	58.17	0.098	59.13	0.098	60.10
0.098	61.06	0.097	62.02	0.097	62.98	0.097	63.94	0.097	64.90	0.097	65.87	0.097	66.83
0.096	67.79	0.096	68.75	0.096	69.71	0.095	70.67	0.095	71.63	0.094	72.60	0.094	73.56
0.094	74.52	0.094	75.48	0.093	76.44	0.090	77.40	0.087	78.37	0.087	79.33	0.086	80.29
0.086	81.25	0.086	82.21	0.086	83.17	0.085	84.13	0.084	85.10	0.078	86.06	0.077	87.02
0.077	87.98	0.077	88.94	0.075	89.90	0.075	90.87	0.069	91.83	0.068	92.79	0.067	93.75
0.065	94.71	0.065	95.67	0.064	96.63	0.057	97.60	0.046	98.56	0.037	99.52		

CUMULATIVE DISTRIBUTION OF TRAPPING FREQUENCIES, STATION 90001, MONTH 8

4257.656	0.48	2532.044	1.44	2411.305	2.40	2246.992	3.37	1828.382	4.33	1707.076	5.29	1536.587	6.25
1452.918	7.21	1329.146	8.17	1250.981	9.13	1105.087	10.10	1094.283	11.06	1054.796	12.02	1015.818	12.98
963.952	13.94	959.732	14.90	898.651	15.87	836.497	16.83	793.512	17.79	788.227	18.75	774.572	19.71
773.430	20.67	762.783	21.63	748.876	22.60	689.477	23.56	686.622	24.52	679.791	25.48	667.047	26.44
665.675	27.40	645.208	28.37	612.670	29.33	608.351	30.29	605.451	31.25	590.511	32.21	586.965	33.17
585.818	34.13	583.745	35.10	581.916	36.06	576.303	37.02	571.701	37.98	557.462	38.94	555.015	39.90
554.666	40.87	552.839	41.83	550.368	42.79	536.565	43.75	535.535	44.71	511.758	45.67	509.624	46.63
508.428	47.60	507.829	48.56	496.512	49.52	493.191	50.48	491.071	51.44	486.291	52.40	484.535	53.37
456.489	54.33	455.120	55.29	454.290	56.25	450.911	57.21	441.075	58.17	439.567	59.13	439.536	60.10
434.024	61.06	433.891	62.02	429.227	62.98	422.651	63.94	420.691	64.90	418.707	65.87	413.111	66.83
412.601	67.79	410.449	68.75	400.787	69.71	398.659	70.67	396.399	71.63	394.077	72.60	393.639	73.56
387.321	74.52	385.794	75.48	383.099	76.44	374.394	77.40	369.326	78.37	365.419	79.33	363.385	80.29
362.590	81.25	361.955	82.21	360.014	83.17	355.321	84.13	351.509	85.10	347.118	86.06	341.917	87.02
323.797	87.98	322.623	88.94	321.650	89.90	321.337	90.87	320.504	91.83	317.181	92.79	308.929	93.75
306.892	94.71	298.083	95.67	298.050	96.63	292.426	97.60	274.025	98.56	272.166	99.52		

CUMULATIVE DISTRIBUTION OF SUPERREFRACTIVE LAYER GRADIENTS, STATION 90001, MONTH 8

−104.545	1.00	−105.093	3.00	−106.000	5.00	−109.016	7.00	−109.502	9.00	−110.687	11.00	−111.111	13.00
−112.500	15.00	−113.978	17.00	−118.902	19.00	−120.257	21.00	−120.556	23.00	−122.609	25.00	−124.409	27.00
−126.894	29.00	−127.362	31.00	−127.368	33.00	−127.962	35.00	−128.090	37.00	−128.495	39.00	−129.583	41.00
−130.380	43.00	−131.250	45.00	−131.902	47.00	−132.903	49.00	−133.047	51.00	−133.444	53.00	−133.673	55.00
−134.343	57.00	−135.052	59.00	−136.598	61.00	−136.813	63.00	−137.288	65.00	−138.378	67.00	−140.217	69.00
−140.645	71.00	−142.553	73.00	−144.253	75.00	−144.324	77.00	−144.545	79.00	−146.012	81.00	−146.980	83.00
−147.489	85.00	−151.402	87.00	−152.222	89.00	−153.247	91.00	−155.224	93.00	−156.081	95.00	−156.164	97.00
−156.627	99.00												

CUMULATIVE DISTRIBUTION OF SUPERREFRACTIVE LAYER THICKNESSES, STATION 90001, MONTH 8

0.311	1.00	0.307	3.00	0.302	5.00	0.279	7.00	0.264	9.00	0.244	11.00	0.240	13.00
0.233	15.00	0.232	17.00	0.224	19.00	0.221	21.00	0.220	23.00	0.219	25.00	0.216	27.00
0.211	29.00	0.200	31.00	0.198	33.00	0.194	35.00	0.186	37.00	0.185	39.00	0.185	41.00
0.184	43.00	0.182	45.00	0.180	47.00	0.178	49.00	0.177	51.00	0.174	53.00	0.166	55.00
0.164	57.00	0.163	59.00	0.163	61.00	0.158	63.00	0.155	65.00	0.155	67.00	0.149	69.00
0.148	71.00	0.146	73.00	0.134	75.00	0.131	77.00	0.127	79.00	0.117	81.00	0.115	83.00
0.110	85.00	0.107	87.00	0.098	89.00	0.097	91.00	0.095	93.00	0.094	95.00	0.090	97.00
0.077	99.00												

TABLE E-4. (*Coutinued*)

THICKNESS AND GRADIENT OF SUPERREFRACTIVE LAYERS OVER 300 METERS THICK

0.31100	−120.25723
0.30200	−133.44371
0.30700	−127.36157

NOVEMBER

144 Profiles Skipped
161 Profiles Read
Number of Ducts 0
Number of Superrefractive Layers 17

CUMULATIVE DISTRIBUTION OF SUPERREFRACTIVE LAYER GRADIENTS, STATION 90001, MONTH 11

−100.000	2.94	−100.000	8.82	−100.000	14.71	−101.786	20.59	−102.970	26.47	−106.504	32.35	−109.804	38.24
−111.972	44.12	−113.592	50.00	−115.254	55.88	−118.750	61.76	−120.690	67.65	−122.000	73.53	−131.667	79.41
−137.255	85.29	−151.852	91.18	−152.252	97.06								

CUMULATIVE DISTRIBUTION OF SUPERREFRACTIVE LAYER THICKNESSES, STATION 90001, MONTH 11

0.142	2.94	0.123	8.82	0.120	14.71	0.112	20.59	0.112	26.47	0.111	32.35	0.103	38.24
0.101	44.12	0.100	50.00	0.081	55.88	0.070	61.76	0.060	67.65	0.059	73.53	0.058	79.41
0.051	85.29	0.051	91.18	0.050	97.06								

☆ U.S. GOVERNMENT PRINTNG OFFICE: 1967—0 222-613